Magnetic Helicity Flow in the Sun and Heliosphere

Gareth Hawkes

Supervisors: Prof. Mitchell Berger
Dr Claire Foullon

College of Engineering, Mathematics and Physical Sciences
University of Exeter

Submitted by Gareth Hawkes to the University of Exeter as a thesis for the degree of

Doctor of Philosophy in Mathematics

in

February 2020.

(Signature) . . . .

Abstract

Magnetic helicity, the measure of entanglement within a magnetic field, has the capability to further our knowledge of the magnetic fields which are ubiquitous across the physical universe. Discovered half a century ago by Lodewijk Woltjer in 1958, it was only given physical meaning by Keith Moffatt in 1969. Progress was initially slow due to the constraints on its calculation: it is assumed that the volume within which we wish to measure helicity does not have any magnetic field crossing its boundaries. But, in 1984, Mitchell Berger and George Field provided a resolution to this problem which allowed it to be applied to open astrophysical fields. From there, and particularly in the last two decades, interest in magnetic helicity has grown exponentially within the research community, resulting in this thesis.

We will begin by providing a semi–formal introduction to the topic, in particular that of magnetohydrodynamics, which describes how a magnetic field and associated plasma co-interact. We provide a mathematical introduction to magnetic helicity, and demonstrate that unsolved problems remain in our understanding of the Sun's magnetic field that are associated with its magnetic helicity.

With this knowledge in hand, we first tackle the topic of predicting the Solar Cycle, which has been an unachieved goal of the solar physics community for longer than we care to remember. We show that magnetic helicity, which is intrinsically linked to the emergence of sunspots, is a statistically stronger candidate for the predictor of activity than that of the polar field strength, which is the current 'best of the worst' of the known predictors.

We then, for the first time, measure how much helicity is generated on the solar surface due to shear motions in a surface flux transport model, which is a method of modelling the magnetic field on the surface of the sun. We show that the results are not as obvious as we expect, and indeed that the flux of magnetic helicity within each hemisphere is carefully balanced between latitudes. We also provide an estimate of how much helicity is produced in a solar cycle, and correlate this with the dipole strength of that cycle.

This is followed by the main result of the thesis: we demonstrate that helicity can be completely generalised for any physical system in terms of a two–point correlation, and fully described in terms of spatial scales and locality using wavelet analysis. In particular, we show that our generalised measure of helicity offers a physical meaning to this localisation. Our methods are demonstrated to have some notable advantages to that of Fourier analysis, which is shown to sometimes produce spurious results.

Finally, we explore the hypothesis that the shape of a magnetic field domain can contribute to the magnetic helicity when using a toroidal–poloidal decomposition. Indeed, in some cases the asymmetry contains the entirety of the magnetic helicity, which we demonstrate numerically.

Acknowledgements

I would primarily like to thank my supervisor, Professor Mitchell Berger, without whom none of this work would have been possible. Also, my thanks go to Anthony Yeates and Chris Prior of Durham for being willing to collaborate with an occasionally foolish PhD student, and for teaching me to set myself to a higher standard. Credit should also be given to Andrew Hillier for providing a critical eye to this thesis, without which it half of it wouldn't make half as much sense as it should.

On a more personal note, I would like to thank my partner, Louise, for always making sure that one of us had the time to make the other laugh. Thanks also go to my long established friend Sam for being willing to discuss the widest possible range of topics, as well as for proof–reading numerically randomised sections of this thesis.

Finally, I would like to thank the UK Science and Technologies Funding Council (STFC) for their studentship funding (ST/N504063/1). No matter how interesting the subject matter, we researchers need to eat.

List of Publications

The research presented in Chapter 2 has been published in Solar Physics, as “Magnetic Helicity Flux as a Predictor of Solar Activity, Hawkes G. & Berger M.A., 2018", see Hawkes and Berger (2018).

The research presented in Chapter 3 has been published in Astronomy and Astrophysics, as “Hemispherical Injection of Magnetic Helicity by Surface Flux Transport, Hawkes G. & Yeates A.R, 2019", see Hawkes and Yeates (2019).

The research presented in Chapter 4 has been published in Astronomy and Astrophysics, as “Spatial Scales and Locality of Magnetic Helicity, Prior C., Hawkes G. & Berger M.A., 2020", see Prior et al. (2020).

Gareth Hawkes

Table of contents

List of figures

List of tables

Chapter 1

Introduction

1.1 The Sun

The Sun, an enormous ball of plasma (an ionised fourth state of matter), is held together by its own gravitational field. Consisting mainly of hydrogen, the temperatures at its centre allow fusion to occur, which forms helium from hydrogen, producing luminance. The Sun is by far our closest star, and thus its study is crucial for the development of our understanding of stars and of stellar objects in general.

The fusion–driven nuclear reactor is crucial to the continued existence of the Sun: it has been shown that if gravitational potential were its only source of energy, then the Sun's lifespan would be a mere 3×10^7 years. Given that the Sun has been luminous for around 4.6×10^9 years, it can thus be concluded that its lifespan has been greatly expanded by another energy source, which we take to be the existence of a nuclear reactor at its *core*. The core extends to about a quarter of the total solar radius, $r = 0.25 R_\odot$ where $R_\odot = 6.98 \times 10^9$ m, and is where the temperature and pressure are at their most extreme.

The energy produced by the reactor within the core is continuously removed through the *radiative zone* via high–energy photon diffusion. In the radiative zone, the temperature and pressure are no longer of the required intensity to create the regime needed for fusion.

At around $r = 0.7R_\odot$, the Sun becomes unstable to convective cell creation, so that convection overtakes diffusion as the dominant process of heat transport. This region is referred to as the *convection zone*, whose lower boundary with the radiative zone is known as the *tachocline*. Within the convection zone, collections of hot plasma rise and transport their energy, before cooling and falling back towards the radiative zone.

The edge of the convection zone, which we define as the visible surface as photons are free to escape into the solar exterior, is known as the *photosphere*, which defines the solar radius $R_\odot$. Above this layer (and above the *chromosphere*) is the *corona*, which extends above the solar surface. A pictorial figure showing these regions is given in Figure 1.1.

At the photosphere we see granulation formed by the convective cells in the convective zone. Giving a grainy appearance, there will typically be a central bright region with a dark region or line surrounding it. These brighter regions correspond to the hot, dense plasma

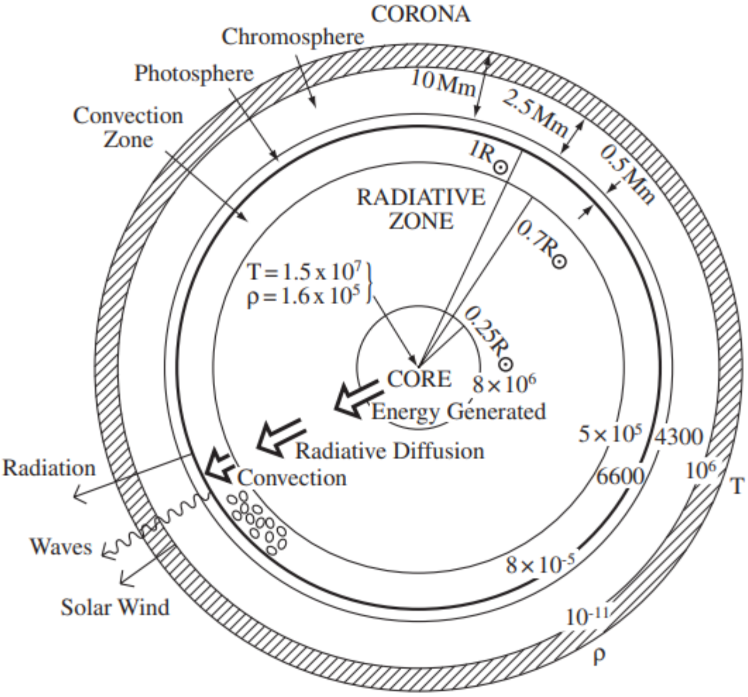

Fig. 1.1 Pictorial representation of the structure of the sun, showing features such as the radiative zone and convective zone etc. Reproduced from Priest (2014a) (their Figure 1.1).

emerging by the aforementioned convection, and the dark regions reveal the cooling of the plasma as it falls back into the convective zone. Convection is thought to occur on a range of scales: below (and rising up to) the photosphere the existence of so–called *supergranules* has been observed. As we move radially towards the photosphere, the length scale of these convection cells becomes gradually reduced. Supergranules have a typical length scale of $20-70$ Mm as compared to granules at 1 Mm. The critical parameters determining the physical behaviour within the Sun: temperature, pressure and density, can typically assumed to be functions of radius r alone - see Figure 1.2 for a simplistic model of their decays as a function of solar radius (reproduced from Priest (2014a), who also plot the sound speed).

The Sun is incredibly active. Indeed, the full region of influence of this activity, extending into the solar wind and beyond, is known as the *heliosphere*. The Earth sits well within this region, at a distance of 1 AU (1.495×10^{11} m), with the heliosphere extending to a distance of approximately 100 AU. We frequently observe a plethora of phenomena, including sunspots, coronal mass ejections, and flares, both lying on and being emitted from the surface of the Sun, which indicate a high–energy system. To understand these phenomena, and indeed to truly understand the Sun itself, we must study the *solar magnetic field*. Threading its interior, and stretching far into the solar atmosphere, the Sun's magnetic field is symbiotically coupled to the physical plasma of which the Sun is formed. The study

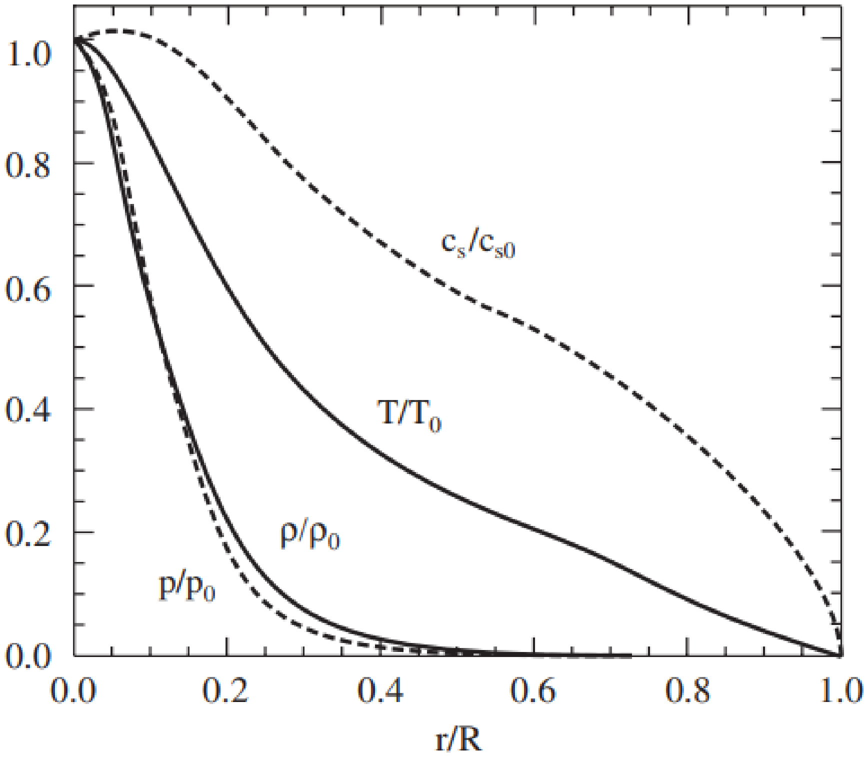

Fig. 1.2 A model of the temperature T, pressure p, density ρ and sound speed c_s as a function of the normalised radius within the sun, further normalised by their modelled value at the core. Core values are estimated as $c_{s0} = 5.05 \times 10^5\,\mathrm{ms}^{-1}$, $T_0 = 1.57 \times 10^7\,\mathrm{K}$, $\rho_0 = 1.54 \times 10^5\,\mathrm{kgm}^{-3}$ and $p_0 = 2.35 \times 10^{16}\,\mathrm{Nm}^{-2}$. Reproduced from Priest (2014a) (their Figure 1.4 - model is based on abundance of Helium and other heavy elements, see their work for full details).

of this relationship is known as *magnetohydrodynamics*: that is, the study of magnetised fluids and gases.

1.2 Magnetohydrodynamics

Magnetohydrodynamics is, in the simplest terms, a description of the interaction between electromagnetic fields **B** (magnetic) and **E** (electric), and their embedded plasmas. Magnetic fields in particular will be the subject of this thesis, and within the context of magnetohydrodynamics we can provide a clear physical motivation for their study. In this section we will provide a brief introduction to the topic of magnetohydrodynamics.

We begin by listing the Maxwell equations, which determine the evolution of a charged system. These are:

$$\nabla \times \mathbf{B} = \mu \mathbf{j} + \frac{1}{c^2}\frac{\partial \mathbf{E}}{\partial t}, \tag{1.1}$$

$$\nabla \cdot \mathbf{B} = 0, \tag{1.2}$$

$$\nabla \times \mathbf{E} = -\frac{\partial \mathbf{B}}{\partial t}, \tag{1.3}$$

$$\nabla \cdot \mathbf{E} = \frac{\rho_c}{\varepsilon}, \tag{1.4}$$

where $\mathbf{E}$ and $\mathbf{B}$ are the electric and magnetic fields respectively, ρ_c is the charge density, μ and ε are magnetic and electric permeabilities of free space (respectively), c is the speed of light constant and $\mathbf{j}$ is the current density.

Qualitatively, the first (1.1) of the listed Maxwell equations demonstrates that either time-varying electric fields or electric currents can generate a magnetic field. However, throughout this thesis we will not take account of the second term of the right hand side of this equation, associated with time varying electric fields, due to its negligibility. To see this, we first define that our study of the Sun will be highly non-relativistic. That is, the characteristic speeds, v_0, with which we shall be working are of order $v_0 << c$.

Now, consider the scales associated with (1.3). We have

$$[\nabla \times \mathbf{E}] = \frac{E_0}{l_0} = \frac{B_0}{t_0} = \left[-\frac{\partial \mathbf{B}}{\partial t}\right], \tag{1.5}$$

(taken to be assumed as an approximation) where E_0, B_0, l_0 and t_0 are characteristic values of $\mathbf{E}$, $\mathbf{B}$, length and time respectively for the systems we shall study. By applying the same process to the time–varying electric fields in (1.1), we find

$$\begin{aligned}\left[\frac{1}{c^2}\frac{\partial \mathbf{E}}{\partial t}\right] &= \frac{E_0}{c^2 t_0}\\ &= \frac{B_0 l_0}{c^2 t_0^2} \text{ (by 1.5)}\\ &= \frac{v_0^2 B_0}{c^2 l_0} \text{ (by } v_0 = \frac{l_0}{t_0}\text{)}\\ &= \frac{v_0^2}{c^2}[\nabla \times \mathbf{B}], \end{aligned} \tag{1.6}$$

for which $\nabla \times \mathbf{B}$ is exactly the left–hand–side of (1.1). Given our assumption of $v_0 << c$, we can thus neglect the formation of currents by time–varying electric fields.

The second equation (1.2) is the mathematical formulation of the no magnetic monopole rule, or equivalently that a magnetic field is divergence–free: there will never be a fixed source from which the magnetic field emerges (unlike some electric fields). In symmetry to the first equation, the third (1.3) and fourth (1.4) expressions demonstrate that a time varying magnetic field, or an electric charge, can generate an electric field.

Ohm's Law, relating the current density to the electric and magnetic fields, is given by

$$\mathbf{j} = \sigma(\mathbf{E} + \mathbf{v} \times \mathbf{B}), \tag{1.7}$$

where $\mathbf{v}$ is the velocity of the plasma, and σ is electric conductivity. Ohm's Law demonstrates that current density is proportional to the sum of the electric field produced by a moving magnetic field ($\mathbf{v} \times \mathbf{B}$) and the electric field $\mathbf{E}$ (the sum of these is known as the *total* electric field).

A particularly useful expression can be found by taking the curl of Ohm's law. Rearranging (1.7) to make $\mathbf{E}$ the subject, we have

$$\mathbf{E} = -\mathbf{v} \times \mathbf{B} + \frac{\mathbf{j}}{\sigma}. \tag{1.8}$$

Taking the curl of (1.8) then gives

$$\frac{\partial \mathbf{B}}{\partial t} = \nabla \times (\mathbf{v} \times \mathbf{B}) - \nabla \times (\eta \nabla \times \mathbf{B}), \tag{1.9}$$

using (1.1), where $\eta = 1/(\mu\sigma)$ is the ohmic magnetic diffusivity. Assuming that diffusivity is constant across space, we then have

$$\frac{\partial \mathbf{B}}{\partial t} = \nabla \times (\mathbf{v} \times \mathbf{B}) + \eta \nabla^2 \mathbf{B}, \tag{1.10}$$

which is known as the *induction equation*. For a prescribed $\mathbf{v}$, we are able to determine the evolution of the magnetic field subject to $\nabla \cdot \mathbf{B} = 0$. The study of this type of evolution is known as a flux transport model. In the case of the Sun, where it is difficult to obtain measurements of the magnetic field beneath the surface, a surface flux transport model typically follows the evolution of the radial magnetic field at the surface, B_r, alone due to surface motions.

The final equation of motion, the momentum equation,

$$\rho \frac{\mathrm{D}\mathbf{v}}{\mathrm{Dt}} = -\nabla p + \mathbf{j} \times \mathbf{B} + \mathbf{F}, \tag{1.11}$$

where ρ is the plasma density and D/Dt is the material derivative, describes how the system changes due to the action of forces: ∇p is a pressure gradient associated with plasma pressure p, the *Lorentz* force $\mathbf{j} \times \mathbf{B}$ and $\mathbf{F}$. $\mathbf{F}$ decomposes into contributions from gravity and viscosity, $\mathbf{F} = \mathbf{F}_g + \mathbf{F}_\upsilon$, respectively. The gravity force is given by

$$\mathbf{F}_g = -\rho g(r)\hat{\mathbf{r}}, \tag{1.12}$$

where g gives the gravitational acceleration as a function of radius. The gravity force the acts towards the centre of the Sun, hence the minus sign. We will not consider viscous forces for the purpose of this thesis.

1.2.1 Ideality

Magnetohydrodynamics (MHD), for the purpose of this thesis, can be subdivided into two regimes: ideal MHD, and non–ideal MHD. The more ideal an MHD system is, the more frozen the magnetic field is to the plasma.

This qualitative description can be quantified by taking a ratio of the scales associated with the two terms on the right hand side of (1.10). Naturally,

$$[\nabla\times(\mathbf{v}\times\mathbf{B})] = \frac{B_0 v_0}{l_0},$$
$$[\eta\nabla^2\mathbf{B}] = \frac{\eta_0 B_0}{l_0^2},$$

where square brackets again denote the units associated with a quantity. Taking the ratio of these approximations, we obtain

$$R_m = \frac{[\nabla\times(\mathbf{v}\times\mathbf{B})]}{[\eta\nabla^2\mathbf{B}]} = \frac{v_0 l_0}{\eta_0} \equiv \frac{\text{Advection}}{\text{Diffusion}}, \tag{1.13}$$

which is known as the *magnetic* Reynolds number. At the limit of an infinite magnetic Reynolds number ($\eta = 0$) our magnetohydrodynamical system is ideal, whilst a low R_m indicates that the system could exhibit non–ideal behaviour: i.e., an MHD system is ideal if the field evolution is dominated by advection.

In an ideal regime, Ohm's Law (1.7) reduces to $\mathbf{E} = -\mathbf{v}\times\mathbf{B}$ ($\sigma\to\infty$ indicates that the medium is perfectly conducting), and the magnetic field is frozen into the plasma. In this case, we preserve magnetic flux as posed by Alfvén's Frozen Flux theorem (Alfvén, 1942):

"Suppose that we have a homogeneous magnetic field in a perfectly conducting fluid... In view of the infinite conductivity, every motion (perpendicular to the field) of the liquid in relation to the lines of force is forbidden because it would give infinite eddy currents. Thus the matter of the liquid is "fastened" to the lines of force. . . ",

which states that for ideal (perfectly conducting ≡ non–resistive) magnetohydrodynamics, the flux of an individual flux tube is constant in time.

To be precise, a flux tube can be qualitatively described as a cylinder which is deformed to fit the shape of local bunch of magnetic field lines within a finite width ε of a central axis, for which $\mathbf{B}$ does not cross the side boundaries of the cylinder. The magnetic flux, Φ, of a flux tube is equal to the integral sum over the cross section of the cylinder:

$$\Phi = \int_S \mathbf{B}\cdot\hat{\mathbf{n}}\,\mathrm{dS}, \tag{1.14}$$

and is constant throughout the flux tube by $\nabla\cdot\mathbf{B} = 0$.

Thus, Alfvén's frozen flux theorem states that in an ideal system, the magnetic field moves exactly with the plasma. To see this (following Priest (2014a)), consider a flat surface S (as in 1.14) moving within the plasma with velocity $\mathbf{v}$, whose boundary can be described by a closed curve C. Then, within time dt, an element $d\mathbf{l}$ along the curve C

carves out an area $\mathbf{v} \times d\mathbf{l}\,\mathrm{dt}$. Thus, the change in magnetic flux due to a motion $\mathbf{v}$ in time dt is given by

$$\frac{\mathrm{d}}{\mathrm{dt}} \int_S \mathbf{B} \cdot \mathrm{d}\mathbf{S} = \int_{\mathrm{S}} \frac{\partial \mathbf{B}}{\partial \mathrm{t}} \cdot \mathrm{d}\mathbf{S} + \oint_{\mathrm{C}} \mathbf{B} \cdot \mathbf{v} \times \mathrm{d}\mathbf{l}. \tag{1.15}$$

Thus, as time passes, the magnetic flux through S changes due to either changes in the magnetic field, or because the boundary C moves in line with the plasma. Then, application of Stokes theorem gives

$$\frac{\mathrm{d}}{\mathrm{dt}} \int_S \mathbf{B} \cdot \mathrm{d}\mathbf{S} = \int_{\mathrm{S}} \left(\frac{\partial \mathbf{B}}{\partial \mathrm{t}} - \nabla \times (\mathbf{v} \times \mathbf{B}) \right) \cdot \mathrm{d}\mathbf{S}, \tag{1.16}$$

which is exactly zero in the ideal limit of (1.10), which itself reduces to

$$\frac{\partial \mathbf{B}}{\partial t} = \nabla \times (\mathbf{v} \times \mathbf{B}). \tag{1.17}$$

Alfvén's Frozen Flux theorem has important consequences for magnetic helicity, which is the main topic of this thesis, and will be fully introduced in Section 1.5.

1.3 An Active Sun

With the mathematical formulation describing how a plasma interacts with a local magnetic field, we can properly describe how the phenomena associated an active Sun with are generated.

Alongside the granular pattern, at the photospheric surface we observe *active regions* (bipolar magnetic regions), the more mature of which are referred to as *sunspots*. These regions represent intense toroidal magnetic flux tubes which have 'bubbled' up from the convective zone. In a solar physics context, the poloidal field refers to the component which follows a meridional circulation (along lines of constant longitude), whilst the toroidal component refers to the azimuthal component. The magnetic flux tubes rise from the convection zone due to magnetic buoyancy, a process which we describe below.

1.3.1 Magnetic Flux Emergence

First, consider the Lorentz force of (1.11) describing the action of the magnetic field on the plasma. We can expand the Lorentz force in terms of two different physical effects:

$$\begin{aligned}
\mathbf{F}_L &= \mathbf{j} \times \mathbf{B} \\
&= \frac{1}{\mu} (\nabla \times \mathbf{B}) \times \mathbf{B} \\
&= \frac{(\mathbf{B} \cdot \nabla)\mathbf{B}}{\mu} - \frac{1}{2\mu} \nabla (B^2).
\end{aligned} \tag{1.18}$$

The first term of the expansion (1.18) is the force applied to the plasma due to magnetic tension, and the second term is that due to magnetic pressure. The magnetic tension force is the effect of tension along the fieldlines associated with $\mathbf{B}$ of magnitude B^2/μ. The magnetic pressure force has magnitude $B^2/2\mu$ along the gradient of $\mathbf{B}$. Note that the form of $\mathbf{F}_L = \mathbf{j} \times \mathbf{B}$ indicates that the components parallel to $\mathbf{B}$ are internally cancelled out.

Now, suppose that a magnetic flux tube in the convective zone has internal pressure p_i, a magnetic field of magnitude B_i along its axis, and the external pressure is given by p_e. If this system were stable in terms of a pressure balance, it would require

$$p_e = p_i + \frac{B_i^2}{2\mu}, \tag{1.19}$$

where $B_i^2/2\mu$ is the pressure associated with the internal magnetic field. Using the ideal gas law

$$p = \frac{k_B T \rho}{m}, \tag{1.20}$$

where k_B is the Boltzmann constant, T is the temperature associated with the system and m is the average particle mass, we can write (1.19) as

$$\frac{k_B T \rho_e}{m} = \frac{k_B T \rho_i}{m} + \frac{B_i^2}{2\mu}, \tag{1.21}$$

and as such we must have $\rho_e \geq \rho_i$ by the absolute positivity of B^2 and μ. The flux tube will then experience a buoyancy force equal to the weight of the background plasma replaced by the flux tube, which is determined by their relative densities: a buoyancy force of $(\rho_e - \rho_i)g$ per unit volume, where g denotes the magnitude of gravitational acceleration.

Returning to the expanded Lorentz force (1.18), suppose we take $\mathbf{B} = B\hat{\mathbf{s}}$, where $\hat{\mathbf{s}}$ is the unit vector along a fieldline. We can then expand the magnetic tension force as

$$\begin{aligned}
\frac{(\mathbf{B} \cdot \nabla)\mathbf{B}}{\mu} &= \frac{1}{\mu}(B\hat{\mathbf{s}} \cdot \nabla)B\hat{\mathbf{s}} \\
&= \frac{B}{\mu}\frac{\mathrm{dB}\hat{\mathbf{s}}}{\mathrm{ds}} \\
&= \frac{1}{\mu}\frac{\mathrm{dB}^2}{\mathrm{ds}}\hat{\mathbf{s}} + \frac{B^2}{2\mu}\frac{\hat{\mathbf{n}}}{R_c},
\end{aligned} \tag{1.22}$$

where $\hat{\mathbf{n}}$ is the normal to $\hat{\mathbf{s}}$, and R_c is the radius of curvature of $B(s)$ (for each individual field line), describing how far the flux tube has deviated from having a linear directionality. We neglect the term parallel to $\hat{\mathbf{s}}$ due to the orthogonality of $\mathbf{F}_L$. Thus, the tension component of the Lorentz force $\mathbf{F}_L$ acts to straighten a curved fieldline, with magnitude $B^2/2\mu R_c$.

Balancing the magnetic tension force (1.22) with that associated with pressure-buoyancy, we can assert that a flux tube will rise buoyantly if

$$(\rho_e - \rho_i)g > \frac{B_i^2}{2\mu R_c}. \tag{1.23}$$

Qualitatively, the magnetic flux tube will rise if either the density differential is sufficiently large, or if the magnetic field is sufficiently weak. Note that this equation constitutes an instability: if the flux tube begins to rise buoyantly, then R_c will grow and allow continued rising through suppression of the $B_i^2/2\mu R_c$ term.

Having established the various pressures involved in an MHD system, we can also introduce another dimensionless parameter, the plasma beta,

$$\beta = \frac{2\mu p}{B_0^2}, \tag{1.24}$$

which measures the ratio of strengths of the plasma and magnetic pressures. The value of the plasma beta can indicate which regime we are in: if $\beta >> 1$, then the plasma dominates, whilst if $\beta << 1$ then the magnetic force dominates.

1.3.2 Sunspots

The magnetic intensity of emergent flux tubes acts to suppress convection. In particular, emergent flux tubes are known to have a $\beta << 1$, which suppresses the granulation process, and as such they typically appear dark upon the photosphere. The flux tubes making up an active region are typically of an Ω shape, and as such as they rise they give the appearance of moving apart, assuming that their footpoints are fixed within the convection zone. Naturally, these flux tubes possess a positive and negative pole, which denote the regions in which the magnetic flux tube exits and then re-enters the photospheric layer respectively. A basic pictorial demonstration of active region emergence is shown in Figure 1.3 (reproduced from Centeno (2012) with minor changes).

Magnetic emergence occurs on a wide range of scales, dependent on the interactions of the flux tube with the surrounding material, and the current state of the overlying photosphere. As the flux tube rises it is subject to the Coriolis force (Parker, 1955). The Coriolis force, acting on the apparent stretching of the flux tube due to its rising with magnetic buoyancy, acts to tilt the orientation of the flux tube between its polarities (D'Silva and Choudhuri, 1993): see Figure 1.4. The degree of tilting is dependent upon the latitude of emergence, a phenomena which is known as Joy's law.

The line along which the radial magnetic field changes direction is known as the polarity inversion line. The polarity that lies to the east of the polarity inversion line is referred to as the *leading* pole, and its counterpart the *trailing* pole. The trailing pole is typically referred to as possessing the tilt angle with respect to the leading pole, relative to the equatorial line.

The appearance and global translation of sunspots occurs over the course of the *solar cycle*: see Figure 1.5. As we can see, a solar cycle will last roughly 11 years, over which time the latitude of emergence of a sunspot decreases towards the equator. Over the course of many solar cycles, the latitudinal translation of the emergence of sunspots exhibits the famous butterfly pattern (Figure 1.5, top).

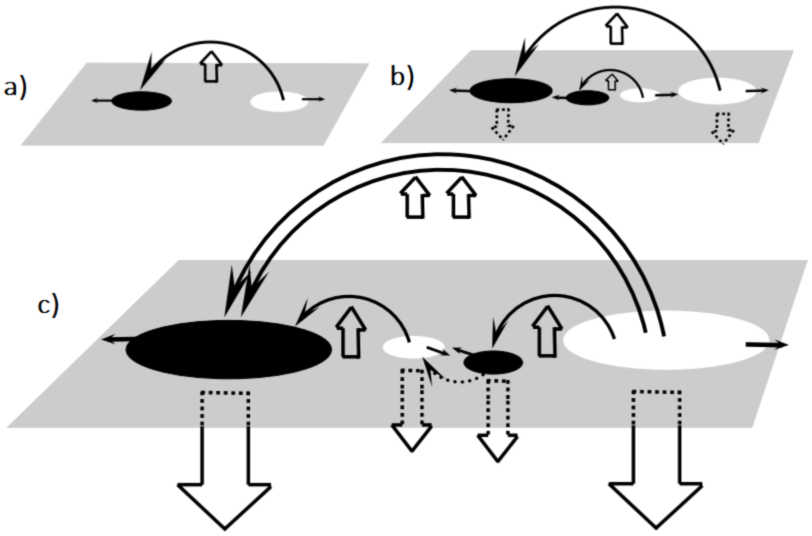

Fig. 1.3 Pictorial representation of the emergence and spread of a solar active region. In (a) we see the classic emergence of a dipolar field structure, typically in the form of an Ω loop (this produces the initial appearance that the poles are separating). In (b) we continue to see smaller sub-structures of magnetic flux appear, which will typically go on to decay or reconnect with the larger polar structures. In (c) we see further substructures emerge, whose magnetic fields reconnet with the larger structure. Figure reproduced and slightly altered from Centeno (2012) (their Figure 10).

Further, the emergence of a sunspot-generating flux tube will follow a series of empirical laws, which are obeyed around 97% of the time (Priest, 2014a):

1. The hemisphere in which a sunspot emerges will decide the polarity of the leading sunspot, which is fixed for a full 11–year cycle (Hale's law)
2. The latitude at which the sunspot emerges decreases as the cycle progresses
3. At the end of each solar cycle, the polarity of the leading and trailing sunspot is reversed
4. The leading polarity lies closest to the equator (Joy's law), with the trailing polarity experiencing the tilt angle
5. The tilt angle varies between around 0° and 35°, dependent upon the latitude of emergence.

We observe a gradual increase in sunspot number on the solar disk up until the half way point of a cycle (Figure 1.5, bottom), at which time the Sun's large–scale poloidal field reverses. There is then a gradual decline in sunspot number until the next minima, indicating the end of a cycle.

The leading pole will typically be of the same sign as that of the polar magnetic field at the beginning of the solar cycle. The sign of this pole only reverses at the end of a solar cycle, not when the polar field reverses sign. The process by which the poloidal field

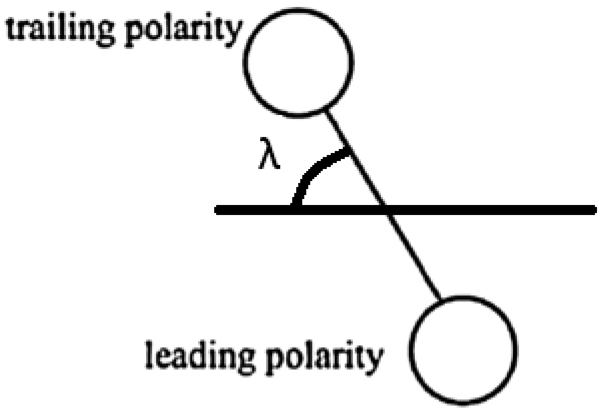

Fig. 1.4 Pictorial digram showing the tilt angle associated with a sunspot pair with tilt angle λ. The horizontal line from which the angle is measured is an E-W line(left to right).

reverses by the mass emergence of flux tubes is managed by a combination of the alpha effect, Ω effect, and the Babcock-Leighton mechanism, which we will now detail.

1.4 The Solar Cycle

1.4.1 Differential Rotation: The Ω effect

To begin, we must first introduce the concept of the Ω-effect, produced by differential rotation. On the Sun, the equatorial regions rotate at a rate exceeding that at the poles. Between these regions, the azimuthal velocity decreases with increasing latitude. As such, the synodic period of the rotation (as viewed from the Earth) at the equator is 26.24 days, corresponding to a speed around $2\mathrm{kms}^{-1}$. Compare this to latitudes of 60°, where the period is around 31 days. The latitudinal nature of the rotation is enabled by the fact that the Sun is a non–solid body, and is caused by a combination of conservation of angular momentum from its formation, and large scale convective motion. The first observations of differential rotation originated from watching the transition of sunspots across the solar disk. However, we now know that such transitions are not necessarily indicative of the actual differential rotation profile at the photosphere, as they will typically be anchored at a sub–surface layer.

At the beginning of a solar cycle, the Sun's large scale magnetic field is typically assumed (and observed) to be roughly dipolar, in that it can be approximated as a poloidal field which is highly concentrated in the polar regions. As the solar cycle progresses, this poloidal field descends towards lower latitudes, and is slowly wrapped around the centre of rotation through a combination of differential rotation and meridional velocity. Meridional velocity acts to transport flux from the equatorial region to the poles at the photospheric level, and then through the convective zone back towards the equator. The magnitude of

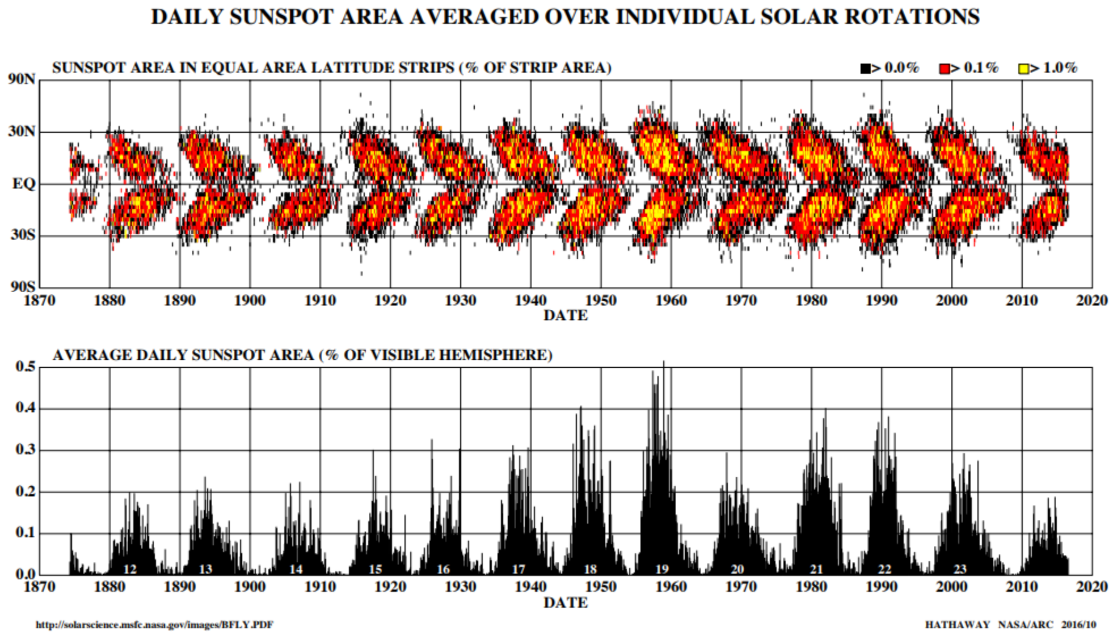

Fig. 1.5 The classical sunspot butterfly diagram as a function of time over 12 complete solar cycles (top) alongside a measure of the average daily sunspot area normalised by total visible solar surface (bottom), indicating the variability of the intensity of solar cycles (courtesy of D. Hathaway, NASA/MSFC; see http://solarscience.msfc.nasa.gov/images/bfly.gif).

meridional velocity is much smaller than that of differential rotation, at around 20ms^{-1}, and only gets slower at reduced radii as it circulates.

This wrapping of the initially dipolar field acts to convert the magnetic field from a poloidal dominated form to a field which is mostly toroidal. This process shown in figures 1.6(a-c). The poloidal field which has been submerged by the Ω effect is thought to go on to form the flux tubes which buoyantly rise through the convection zone and emerge as bipolar magnetic regions, producing the solar activity we observe. However, the exact process by which the Sun's magnetic field returns to a primarily poloidal state from a toroidal field is as of yet unclear. There are two clear contenders: the α–effect, and the Babcock–Leighton mechanism.

1.4.2 The Babcock–Leighton Mechanism

The Babcock–Leighton mechanism is shown pictorially in figures 1.6(h-j). As we described in the previous section, bipolar magnetic regions are thought to emerge from the underlying toroidal field. And, as we have already stated, the two emerging poles are tilted with respect to the equator, where the pole whose sign corresponds to that of the background mean field will typically lie closer to the equator.

By the effects of differential rotation, meridional velocity, and gradual emergence of a Ω shaped loop, these two poles will separate, and their magnetic flux will diffuse according to the appropriate diffusive effects. After the active region has decayed, either by

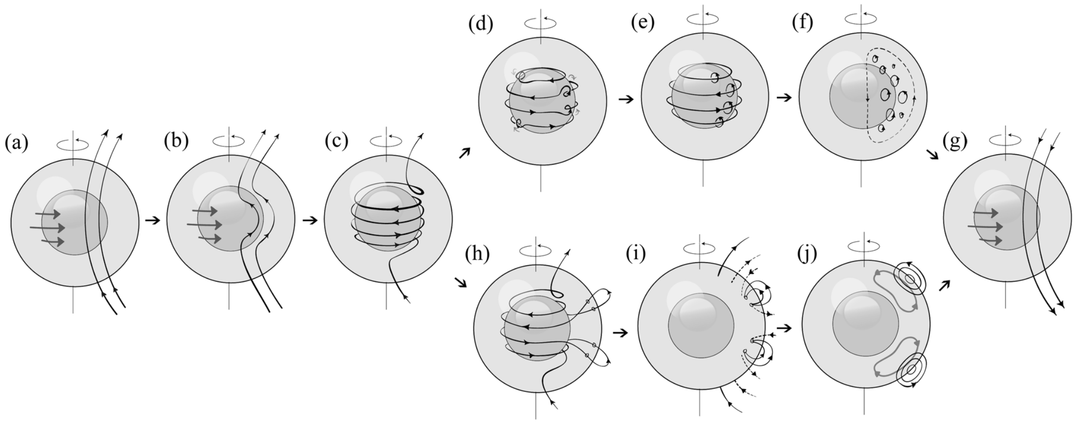

Fig. 1.6 Pictorial representation of the process by which the Sun's poloidal field is reversed over the course of a solar cycle. (a) shows a poloidal field, which circulates from pole to pole. In (b) and (c), we see the transition of this poloidal field towards a toroidal field due to the twisting motions associated with differential rotation (Ω-effect). In (d)-(f), we see a pictorial representation of the α-effect, which through cyclonic motions acting on rising toroidal field acts (on average) to create a large scale poloidal field opposite in sign to that of (a). Simultaneously, the Babcock-Leighton process is shown in (h)-(j), whereby the emergence and decay of bipolar active regions over the whole cycle acts to reverse the poloidal field. The result of these combined effects, in the form of a reversed poloidal field, is shown in (g). Reproduced from Sanchez and Fournier (2014) (their Figure 1).

submerging back into the photosphere, flux cancellation, or in certain cases by eruption, the remaining magnetic flux of the leading polarity is assumed to approximately cancel across the equator with an oppositely signed counterpart from the other hemisphere. The magnetic flux from the trailing pole is free to diffuse towards the polar region which, we recall, is typically of opposite sign to that of the polar field at the beginning of the solar cycle. Cumulatively, the diffused magnetic flux from many bipolar regions gradually decays the poloidal field at the magnetic poles. At the height of the solar cycle, the polar field will flip sign, and then continue to be strengthened by this same diffused flux (recall that the orientation of sunspots in a hemisphere is fixed for the entire solar cycle). As such, at the end of the solar cycle, the polar flux will have reversed sign and have a strength somewhat correlated with the sunspot number during that cycle. How strong this correlation is, and how important differential rotation is to the formation of the toroidal field which produces active regions, will be the topic of study in Chapter 2. In Figure 1.7, we present a pictorial figure showing how these velocities work together, reproduced from Choudhuri (2010).

1.4.3 The Alpha (α) Effect

The second theorised contribution to a regeneration of the solar poloidal field is that of the *alpha (α) effect*. The alpha affect, like the Babcock–Leighton mechanism, is concerned with the average effect of many magnetic flux tubes emerging from the photosphere.

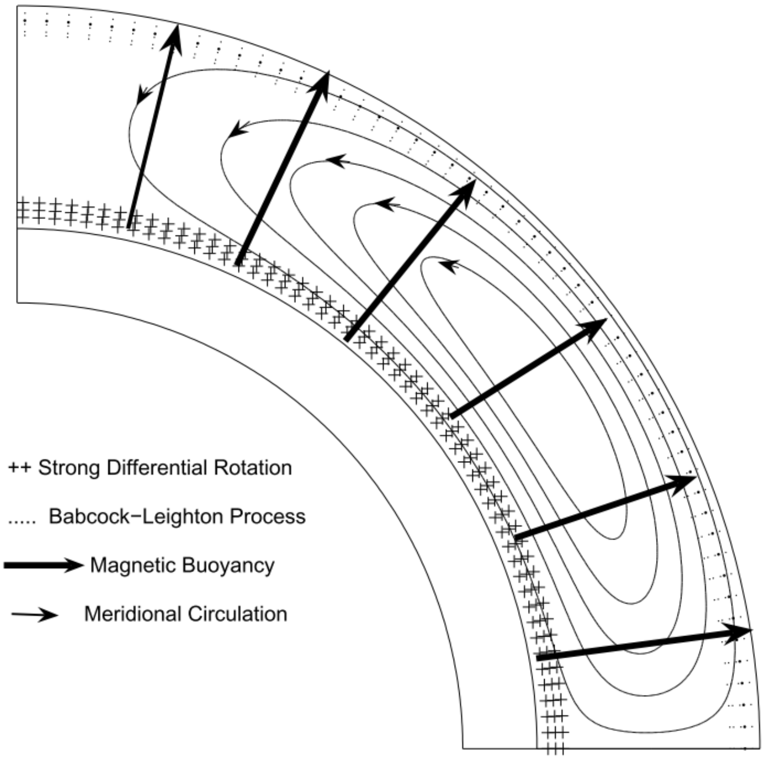

Fig. 1.7 A pictorial diagram showing the shear layer generated by differential rotation, the meridional circulation, and the expected direction of magnetic buoyancy. The region in which the Babcock–Leighton process occurs is also shown. Reproduced from Choudhuri (2010) (their Figure 1).

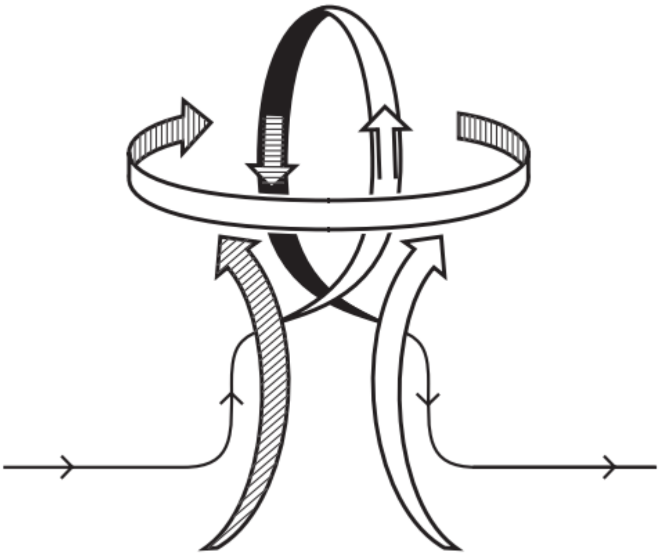

Fig. 1.8 A pictorial diagram showing how the twisting of emerging flux tubes into an α shape due to the Coriolis effect. Reproduced from Priest (2014b).

As we have described, the Coriolis force causes the tubes to twist as they undergo magnetic buoyancy. We show this pictorially in Figure 1.8 (reproduced from Priest (2014b)). With proper application of the right–hand rule, we can see that the magnetic current produced by the twisting of these flux loops is toroidal in nature, anti-parallel to the orientation of the rising toroidal field, and is thus associated with a poloidal magnetic field (the curl of a poloidal field is toroidal, and the curl of a toroidal field is poloidal). Further, whilst the toroidal field in the two hemispheres of the Sun are of opposing sign (due to the opposing sign of the initially poloidal field), the cyclonic motions producing the α–effect will also have opposing sign. These doubly opposing signs have the overall effect that the α loops in either hemisphere have the same orientation, and thus produce identically orientated magnetic current.

Averaged over the whole solar disk, these loops act to produce a poloidal field from many twisted toroidal fields, as shown in figures 1.6(d-g). Note that this concept applies only to *emerging* loops: loops which are *descending* would have an oppositely signed twist orientation. As such, there is an inherent assumption that there are more emerging loops than descending loops, or rather that the magnetic field in the ascending loops is on average more intense.

1.4.4 Mean Field Magnetohydrodynamics

The cyclonic motions driving the twisting motions associated with the alpha affect are turbulent, in that they are a departure from the large scale motions observed on the Solar surface, such as differential rotation. It is possible to describe these mean and turbulent processes in the context of mean field MHD. This is a complex and wide–ranging topic, and so we do not claim to offer anything close to a proper introduction, but hope that such a viewpoint can provide clarity to the topics we will discuss within this thesis.

Following Charbonneau (2005), suppose we take our mean magnetic field to be an azimuthal average, which we write as $\langle \mathbf{B} \rangle$, and similarly for mean velocity field $\langle \mathbf{v} \rangle$. The turbulent component is then given by the departure of the original field from this mean at any time, such that the original field is the sum of the mean and varying components:

$$\mathbf{B}' = \mathbf{B} - \langle \mathbf{B} \rangle, \tag{1.25}$$

$$\mathbf{v}' = \mathbf{v} - \langle \mathbf{v} \rangle, \tag{1.26}$$

where $'$ here denotes a varying/turbulent quantity (departure from the mean). As such, we would expect the fluctuating components to themselves have a zero azimuthal average: $\langle \mathbf{B}' \rangle = \langle \mathbf{v}' \rangle = 0$.

For this separation of scales, we find that the induction equation (1.10) can be written as (Charbonneau, 2005)

$$\frac{\partial \langle \mathbf{B} \rangle}{\partial \mathrm{t}} = \nabla \times \Big(\langle \mathbf{v} \rangle \times \langle \mathbf{B} \rangle + \langle \mathbf{v}' \times \mathbf{B}' \rangle \Big) + \eta \nabla^2 \langle \mathbf{B} \rangle, \tag{1.27}$$

which describes how the mean magnetic field changes in time due to ohmic magnetic diffusion η and large–scale advection, but also has the addition of a mean electromotive force associated with a mean turbulent effect

$$\langle \mathscr{E} \rangle = \langle \mathbf{v}' \times \mathbf{B}' \rangle. \tag{1.28}$$

Assuming that $\langle \mathbf{B} \rangle$ varies on scales much larger than its turbulent counterpart, (1.28) can be written as (Blackman and Brandenburg, 2002)

$$\langle \mathscr{E} \rangle = \alpha \langle \mathbf{B} \rangle - \eta_t \langle \nabla \times \mathbf{B} \rangle, \tag{1.29}$$

for which η_t is the turbulent diffusivity, and α is the mathematical expression of the alpha effect. As such, the induction equation describing the evolution of the mean field (1.27) becomes

$$\frac{\partial \langle \mathbf{B} \rangle}{\partial \mathrm{t}} = \nabla \times (\langle \mathbf{v} \rangle \times \langle \mathbf{B} \rangle) + \nabla \times (\alpha \langle \mathbf{B} \rangle) + (\eta + \eta_t) \nabla^2 \langle \mathbf{B} \rangle, \tag{1.30}$$

The effect of turbulent motions on the diffusion of large scale fields often exceeds the ohmic diffusive effects, $\eta_t >> \eta$, and are often associated with the convective motions within large–scale structures such as supergranules.

In a kinematic regime, where one fixes the velocity (it is assumed that the magnetic field $\mathbf{B}$ is unable to change $\mathbf{v}$), according to some original treatments of α, we can write (Charbonneau, 2005)

$$\alpha = -\frac{\tau_c}{3} \langle \mathbf{v}' \cdot \nabla \times \mathbf{v}' \rangle = -\frac{\tau_c}{3} \langle \omega' \cdot \mathbf{v}' \rangle, \tag{1.31}$$

where τ_c is the correlation time of the turbulent motions (the correlation between the motions as a function of time), and ω is the fluid vorticity such that $\mathbf{v} \cdot \omega$ is the turbulent fluid helicity density, which measures the local entanglement of fluid lines in terms of their twisting and linking. Thus, the effectiveness of the α effect depends on there being a non-zero twisting motion with a preferred direction, as would be the case from the Coriolis force.

The Sun is typically referred to as an $\alpha\Omega$ dynamo, as it is by the joint effort of these physical effects that the magnetic field is reversed every eleven years. Indeed, turbulence–induced effects are thought to be highly desirable for any dynamo. However, the Sun does not lie within a kinematic regime, and thus there are additional terms to take account of when determining α. We discuss this further in Section 1.5.9.

1.5 Magnetic Helicity

Magnetic helicity, H, a measure of the entanglement of a magnetic field, was first proposed by Woltjer (1958), who showed that for a closed ideal system within V ($\mathbf{B} \cdot \hat{\mathbf{n}} = 0$),

$$H = \int_V \mathbf{A} \cdot (\nabla \times \mathbf{A})\, \mathrm{d}^3\mathrm{x} = \int_\mathrm{V} \mathbf{A} \cdot \mathbf{B}\, \mathrm{d}^3\mathrm{x} = \mathrm{const}, \tag{1.32}$$

for a suitably chosen magnetic vector potential, $\mathbf{A}$:

$$\mathbf{B} = \nabla \times \mathbf{A}. \tag{1.33}$$

This integral quantity was then first given topological meaning by Moffatt (1969) as the linking of magnetic field lines. To see this, we first consider the Gauss linking number, which proposes that the net linking number of two closed curves $\mathbf{x}(\sigma)$ and $\mathbf{y}(\tau)$ with radial distance $\mathbf{r}(\tau, \sigma) = \mathbf{x}(\sigma) - \mathbf{y}(\tau)$ can be written as

$$\mathscr{L}_{\mathbf{xy}} = -\frac{1}{4\pi} \oint_{\mathbf{x}} \oint_{\mathbf{y}} \frac{\mathrm{d}\mathbf{x}}{\mathrm{d}\sigma} \cdot \frac{\mathbf{r}}{r^3} \times \frac{\mathrm{d}\mathbf{y}}{\mathrm{d}\tau}\, \mathrm{d}\sigma\, \mathrm{d}\tau, \tag{1.34}$$

(originally inspired by the crossing of asteroid paths). Berger and Prior (2006) list many of the useful properties of $\mathscr{L}$, including

1. $\mathscr{L}$ is invariant to ideal deformations in either curve, assuming neither curve crosses through the other,
2. $\mathscr{L}$ is unchanged by the reversal of an axial direction, assuming both curves are equally affected.

1.5.1 Crossing Number

To determine linking number (1.34) qualitatively, we could project the three dimensional curves $\mathbf{x}$ and $\mathbf{y}$ onto a two-dimensional plane, and count how often these lines of projection cross one another, which is known as the crossing number. The signed crossing number associated with an individual crossing is as shown in Figure (1.9), where the direction of traversal of the two curves determines the sign.

To avoid problems such as non-injective mappings of the curve onto the plane, which could occur for (for example) a curve that is sinusoidal in the direction perpendicular to the plane, it is often necessary to rotate the curve and subsequently change its projection. The total crossing number is a simple sum over all crossings between the curves. If we define $\mathscr{C}_{\mathbf{xy}}$ to be the *total* crossing number between curves **x** and **y**, then

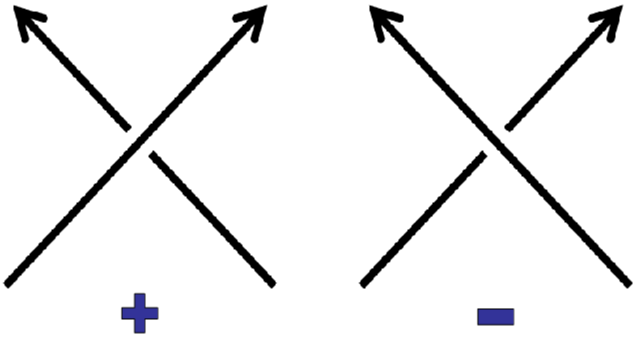

Fig. 1.9 Pictorial representation of the differing signatures of crossings in a plane projected curves

$$\mathscr{L}_{\mathbf{xy}} = \frac{1}{2}\langle \mathscr{C}_{\mathbf{xy}} \rangle = \frac{1}{2}\langle n_+ - n_- \rangle, \tag{1.35}$$

where n_+ is the number of positive crossings, n_- the number of negative crossing and $\langle\rangle$ now denotes an averaging procedure over all possible viewing angles.

1.5.2 Flux Tubes

To see how this concept of linking applies to a magnetic field, let us first assume that our magnetic field is composed of two closed flux tubes having magnetic fluxes $\Phi_{\mathbf{x}}$ and $\Phi_{\mathbf{y}}$ respectively. In this case their mutual helicity is given by

$$H = 2\mathscr{L}_{\mathbf{xy}}\Phi_{\mathbf{x}}\Phi_{\mathbf{y}}, \tag{1.36}$$

as the field–weighted linking number. Note that we require $\mathbf{B}\cdot\hat{\mathbf{n}} = 0$ on the edges of our boundaries, in accordance with the nature of closed curves established in (1.34).

Now suppose that the magnetic field **B** can be decomposed into a finite number, N, of such flux tubes. In this case, (1.36) is written as

$$H = \sum_{i,j=0}^{N} \mathscr{L}_{ij}\Phi_i\Phi_j, \tag{1.37}$$

where i, j denote each pair of curves $\mathbf{x}$, $\mathbf{y}$.

1.5.3 Self Helicity

There is a subtlety to (1.37) when $i = j$ – can a flux tube link itself? In fact, the self–helicity measures how the flux tube's inner field goes on to link itself in two ways: twist and writhe. Unlike total helicity, the individual components $\mathscr{T}$ (twist) and $\mathscr{W}$ (writhe) are not individually conserved, as helicity can be transferred between the two forms. Naturally their sum, which is equal to the total helicity, is conserved:

$$H = \Phi^2(\mathscr{T} + \mathscr{W}). \tag{1.38}$$

Writhe

Qualitatively, writhe is the kinking and winding that can be observed in physical objects such as DNA, which must be highly coiled, and thus a large quantity of winding is observed. Quantitatively, the writhe is exactly the linking number $\mathscr{L}$, in terms of the crossing number above for a single curve threading the flux tube's central axis. The mathematical statement of this concept is given by,

$$\mathscr{W} = -\frac{1}{4\pi}\oint_x \oint_{x'} \mathbf{T}(s) \cdot \frac{\mathbf{r}(\mathbf{x}, \mathbf{x}')}{r(\mathbf{x}, \mathbf{x}')^3} \times \mathbf{T}(s')\ \mathrm{ds}\ \mathrm{ds}', \tag{1.39}$$

following (1.34), where $\mathbf{T}$ is the tangential vector to the curve $\mathbf{x}(s)$: $\mathbf{T} = \mathrm{d}\mathbf{x}/\mathrm{ds}$.

Twist

The twist, $\mathscr{T}$, is given by

$$\mathscr{T} = \frac{1}{2\pi}\oint_x \mathbf{T}(s) \cdot \mathbf{N}(s) \times \frac{\mathrm{d}\mathbf{N}(\mathrm{s})}{\mathrm{ds}}\ \mathrm{ds}, \tag{1.40}$$

where $\mathbf{N}$ is the vector normal to the tangent vector $\mathbf{T}$. Following the traversal of $\mathbf{x}$, the tip of $\mathbf{N}$ defines a secondary curve $\mathbf{n}$, such that a surface defined by their joining is a ribbon. Assuming that we take $|\mathbf{N}| < \varepsilon$, where ε is the radius of the flux tube, then we can interpret the twist number as the winding of the fieldlines defined by $\mathbf{n}$ within the flux tube around their central axis $\mathbf{x}$.

An alternative mathematical definition is given by

$$\mathscr{T} = \frac{1}{2\pi}\oint_{\mathbf{x}} \left(\tau + \frac{\mathrm{d}\Theta}{\mathrm{ds}}\right)\ \mathrm{ds}, \tag{1.41}$$

where τ is the torsion of the curve, and Θ is the *twist angle*, i.e. the angle the tangent to the curve $\mathscr{C}$ makes with the axis curve. One could also simply define $\mathscr{T} = \frac{H}{\Phi^2} - \mathscr{W}$.

1.5.4 Classical Magnetic Helicity

It is, however, rarely the case that we can neatly decompose our magnetic field into a series of well–defined flux tubes: a magnetic field will typically be composed of a set of co–interacting scale–based structures. Thus, as a complete generalisation, we regard each field line as an individual flux tube with vanishing magnetic flux. Taking the limit $N \to \infty$ and $\Phi_{i,j} \to 0$ of (1.37), we obtain (Arnol'd and Khesin, 1998)

$$H = -\frac{1}{4\pi} \int \int \mathbf{B}(\mathbf{x}) \cdot \frac{\mathbf{r}}{r^3} \times \mathbf{B}(\mathbf{y}) \, \mathrm{d}^3\mathrm{x} \, \mathrm{d}^3\mathrm{y}, \tag{1.42}$$

where

$$\mathbf{r} = \mathbf{x} - \mathbf{y}, \tag{1.43}$$

and $\mathbf{x}$ and $\mathbf{y}$ now represent copies of the region of interest, V. Crucially, we still assume that $\mathbf{B} \cdot \hat{\mathbf{n}} = 0$, for which $\hat{\mathbf{n}}$ defines the normal to the boundaries of V. As compared to (1.34), the magnetic field vector has taken the place of the curve gradient, and each individual point along the field lines has its linking measured with every other individual point in space. With the proper use of the Coulomb vector potential via the Biot-Savart law, we can write

$$\mathbf{A}(\mathbf{x}) = -\frac{1}{4\pi} \int \frac{\mathbf{r}}{r^3} \times \mathbf{B}(\mathbf{y}) \, \mathrm{d}^3\mathrm{y}, \tag{1.44}$$

such that $\mathbf{B} = \nabla \times \mathbf{A}$ and $\nabla \cdot \mathbf{A} = 0$, we once again obtain

$$H = \int_V \mathbf{A} \cdot \mathbf{B} \, \mathrm{d}^3\mathrm{x}. \tag{1.45}$$

1.5.5 Gauge Invariance

The requirement that $\mathbf{B} = \nabla \times \mathbf{A}$ leads to a gauge freedom:

$$\mathbf{A}' = \mathbf{A} + \nabla \psi, \tag{1.46}$$

for some potential field $\nabla \psi$, as one still obtains

$$\begin{aligned} \nabla \times \mathbf{A}' &= \nabla \times (\mathbf{A} + \nabla \psi) \\ &= \nabla \times \mathbf{A} \\ &= \mathbf{B}. \end{aligned} \tag{1.47}$$

The magnetic helicity associated with $\mathbf{A}'$ and $\mathbf{B}$ $(= \mathbf{B}')$ is then given by

$$\begin{aligned} H' &= \int_V (\mathbf{A} + \nabla \psi) \cdot \mathbf{B} \, \mathrm{d}^3\mathrm{x} \\ &= \int_V (\nabla \psi \cdot \mathbf{B} + \mathbf{A} \cdot \mathbf{B}) \, \mathrm{d}^3\mathrm{x} \\ &= H + \int_V \nabla \psi \cdot \mathbf{B} \, \mathrm{d}^3\mathrm{x}. \end{aligned} \tag{1.48}$$

The second component can be expanded as so:

$$\begin{aligned}\int_V \nabla\psi\cdot\mathbf{B}\,\mathrm{d}^3\mathrm{x} &= \int_S \nabla\psi\mathbf{B}\cdot\hat{\mathbf{n}}\,\mathrm{d}^2\mathrm{x} - \int_{\mathrm{V}} \psi\nabla\cdot\mathbf{B}\,\mathrm{d}^3\mathrm{x} \\ &= \int_S \nabla\psi\mathbf{B}\cdot\hat{\mathbf{n}}\,\mathrm{d}^2\mathrm{x}, \qquad (1.49)\end{aligned}$$

by the no magnetic monopoles rule ($\nabla\cdot\mathbf{B}=0$). Thus, for a **closed** magnetic field, where $\mathbf{B}\cdot\hat{\mathbf{n}}=0$, the gauge invariance of helicity is ensured, as originally proposed by Woltjer (1958).

1.5.6 Relative Magnetic Helicity

It is, however, also rarely the case that the magnetic field is closed. As we have described in previous sections, magnetic flux is constantly emerging through the photosphere of the Sun. In this case, the physical meaningfulness of magnetic helicity retained by (1.49) is lost.

A solution to this, posed by Berger and Field (1984), is to measure the magnetic helicity of our open field relative to a minimum–energy, potential field. To show how such a relative helicity retains gauge invariance, we follow the intuitive arguments presented in Berger (1999).

Suppose that we split the entire space V_s for which we have measured the magnetic field into two components, V and V'. V is the region of interest, within which we want to measure the magnetic helicity, but its magnetic field threads the boundaries of V into an external region V'. In this case, it has been shown that there is a unique potential field $\mathbf{B}_0$ (Berger and Field, 1984) such that

$$\mathbf{B}\cdot\hat{\mathbf{n}}_V = \mathbf{B}_0\cdot\hat{\mathbf{n}}_V = -\mathbf{B}_0\cdot\hat{\mathbf{n}}_{V'}. \qquad (1.50)$$

We can then define a closed magnetic field as

$$\mathbf{B}_{cl} = \mathbf{B} - \mathbf{B}_0, \qquad (1.51)$$

with an associated magnetic vector potential $\mathbf{A}_{cl} = \mathbf{A} - \mathbf{A}_0$. We can see that $\mathbf{B}_{cl}$ is closed from the matching condition (1.50) between the potential field $\mathbf{B}_0$ and $\mathbf{B}$. A pictorial representation of the two fields $\mathbf{B}$ and $\mathbf{B}_0$ is given in Figure 1.10 (reproduced from Berger and Field (1984) with some modifications).

We can then calculate the helicity of the two fields making up $\mathbf{B}$, $\mathbf{B}_{cl}$ and $\mathbf{B}_0$, independently, and add on a cross–helicity term between them to give the relative helicity. The self-helicity of the closed magnetic field is given as

$$H(\mathbf{B}_{cl}) = \int_V \mathbf{A}_{cl}\cdot\mathbf{B}_{cl}\,\mathrm{d}^3\mathrm{x}, \qquad (1.52)$$

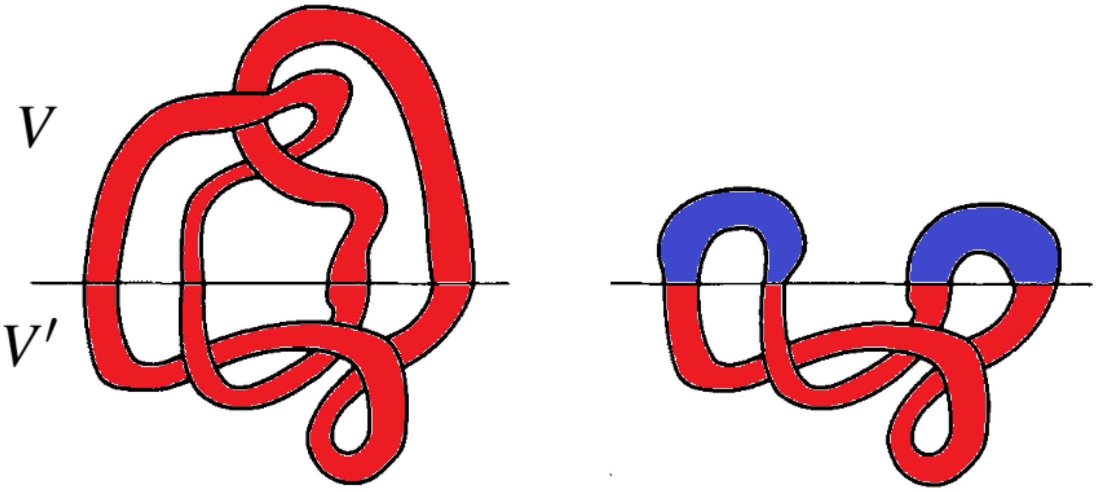

Fig. 1.10 Pictorial diagram showing how a magnetic field **B** (red) which is not closed within a volume V can be used to define a potential field $\mathbf{B_0}$ (blue) within V, based on the field at the boundary between V and V'. Reproduced from Berger and Field (1984) with some modifications.

as it possesses the necessary boundary conditions on V for the classical definition $H = \int \mathbf{A} \cdot \mathbf{B}$ to be applicable. Similarly, the linking of the closed field **B** and the potential field $\mathbf{B}_0$ is well defined as their linking inside the volume of interest V,

$$H(\mathbf{B}_{cl}, B) = 2 \int_V \mathbf{A}_0 \cdot \mathbf{B}_{cl} \, \mathrm{d}^3\mathrm{x}, \tag{1.53}$$

as $\mathbf{B}_{cl}(\mathbf{x}) = 0 \forall \mathbf{x} \in V'$, so that we need not consider their linking outside of V. The above expression (1.53) takes account of both the linking of the open with the closed field, and that of the closed with the open field, hence the factor of two. Finally, as is common throughout the literature, we set the self–helicity of the potential field to be zero, as a minimum–energy and minimum–helicity state subject to the above boundary conditions. A minimum helicity field has $H = 0$, as it is a signed quantity.

As such, the total relative helicity is given by

$$\begin{aligned} H_R &= \int_V (\mathbf{A}_{cl} \cdot \mathbf{B}_{cl} + 2\mathbf{A}_0 \cdot \mathbf{B}_{cl}) \, \mathrm{d}^3\mathrm{x} \\ &= \int_V \Big((\mathbf{A} - \mathbf{A}_0) \cdot (\mathbf{B} - \mathbf{B}_0) + 2\mathbf{A}_0 \cdot (\mathbf{B} - \mathbf{B}_0) \Big) \, \mathrm{d}^3\mathrm{x} \\ &= \int_V (\mathbf{A} + \mathbf{A}_0) \cdot (\mathbf{B} - \mathbf{B}_0) \, \mathrm{d}^3\mathrm{x}, \end{aligned} \tag{1.54}$$

which is in the form posed by (Finn and Antonsen, 1985). Crucially, H_R is **independent** of the field outside of V.

1.5.7 Gauges

In Section 1.5.5, we demonstrated that if $\mathbf{B}\cdot\hat{\mathbf{n}} \neq \mathbf{0}$, then we obtain a gauge term in the expression for classical magnetic helicity. This of course reduces the physical meaningfulness of the quantity, but there are a few choice gauges which are used throughout the literature which are designed to offer the most physicality. One popular choice is the so–called 'DeVore–Coulomb' gauge, introduced in DeVore (2000), given by

$$\mathbf{A}^D = \mathbf{A}_0 - \int_{z_0}^{z_1} \hat{\mathbf{z}} \times \mathbf{B}\ \mathrm{dz}, \tag{1.55}$$

for which $\mathbf{A}_0$ is a Coulomb potential field ($\nabla\cdot\mathbf{A}_0 = 0$) which matches the radial field at the boundary. This particular gauge was proposed by DeVore to measure the helicity at radial regions exterior to the photosphere (such that the first layer of field data we have on the Sun is at the photosphere). Studies of photospheric helicity flux will be a large component of this thesis, in particular Chapters 2 and 3, where we will typically use a Coulomb gauge.

A more recent gauge was posed by Prior and Yeates (2014), who propose a Winding Gauge $\mathbf{A}^w$, given by

$$\begin{aligned} \mathbf{A}^w(x,y,z) &= \frac{1}{2\pi}\int_{S_z} \frac{\mathbf{B}(x',y',z)\times\mathbf{r}}{r^2}\,\mathrm{dx'}\ \mathrm{dy'}, \\ \mathbf{r} &= (x-x', y-y', 0). \end{aligned} \tag{1.56}$$

which the authors demonstrate measures the average winding number between all fieldlines with respect to a *fixed axis*, assuming that $\mathbf{B}\cdot\hat{\mathbf{n}} = 0$ on the side boundaries. In this case, they demonstrate that any other gauge choice is equivalent to choosing an *unfixed axis* for the reference of rotation, which is demonstrably less physical. The definition of helicity in terms of fieldline winding will be the basis for our work in Chapter 4, within which we will describe the notion of winding in more detail.

1.5.8 Conservation and Flux

The time dependence of magnetic helicity is given by

$$
\begin{aligned}
\frac{\mathrm{d}H}{\mathrm{dt}} &= \int_V \frac{\partial \mathbf{A}}{\partial \mathrm{t}} \cdot \mathbf{B}\,\mathrm{d}^3\mathrm{x} + \int_{\mathrm{V}} \mathbf{A} \cdot \frac{\partial \mathbf{B}}{\partial \mathrm{t}}\,\mathrm{d}^3\mathrm{x} \\
&= \int_V \frac{\partial \mathbf{B}}{\partial \mathrm{t}} \cdot \mathbf{A}\,\mathrm{d}^3\mathrm{x} - \int_{\mathrm{S}} \left(\frac{\partial \mathbf{A}}{\partial \mathrm{t}} \times \mathbf{A} \right) \cdot \hat{\mathbf{n}}\,\mathrm{d}^2\mathrm{x} + \int_{\mathrm{V}} \mathbf{A} \cdot \frac{\partial \mathbf{B}}{\partial \mathrm{t}}\,\mathrm{d}^3\mathrm{x} \\
&= 2\int_V \mathbf{A} \cdot \frac{\partial \mathbf{B}}{\partial \mathrm{t}}\,\mathrm{d}^3\mathrm{x}\ [\mathrm{by}\ \nabla \cdot \mathbf{A} = 0] \\
&= 2\int_V \mathbf{A} \cdot (-\nabla \times \mathbf{E})\,\mathrm{d}^3\mathrm{x} \\
&= -2\int_V (\nabla \times \mathbf{A}) \cdot \mathbf{E}\,\mathrm{d}^3\mathrm{x} + 2\int_{\mathrm{S}} (\mathbf{A} \times \mathbf{E}) \cdot \hat{\mathbf{n}}\,\mathrm{d}^2\mathrm{x} \\
&= -2\int_V \mathbf{E} \cdot \mathbf{B}\,\mathrm{d}^3\mathrm{x} + 2\int_{\mathrm{S}} \mathbf{A} \times \mathbf{E} \cdot \hat{\mathbf{n}}\,\mathrm{d}^2\mathrm{x}, \qquad (1.57)
\end{aligned}
$$

by Gauss' divergence theorem. The first of these terms describes volume dissipation, which we can see is zero for ideal MHD where $\mathbf{E} = -\mathbf{v} \times \mathbf{B}$. Berger (1984) also demonstrated that for a magnetic field representative of the solar corona, magnetic helicity remains well–conserved, despite the non–ideal conditions. Indeed, it is shown that this approximate conservation against dissipation is stronger than that of magnetic energy (Berger, 1984)

$$
\left| \int_V \mathbf{E} \cdot \mathbf{B}\ \mathrm{d}^3\mathbf{x} \right| \leq \left(2\eta \mathrm{E} \left| \frac{\mathrm{dE}}{\mathrm{dt}} \right| \right)^{\frac{1}{2}}, \qquad (1.58)
$$

where E is the magnetic energy:

$$
E = \frac{1}{2} \int_V \mathbf{B}^2\,\mathrm{d}^3\mathrm{x}. \qquad (1.59)
$$

The strength of magnetic helicity conservation can be assumed to be associated with the inverse cascade of helicity (Frisch et al., 1975) from the small dissipative scales towards the large scales, which is opposite to the cascade of, say, magnetic energy. A simple illustrative experiment can be performed to demonstrate the inverse cascade of helicity using a ribbon of paper. If we take each end of the ribbon and begin to rotate them with an opposite handedness, then the paper will begin to twist (small–scale helicity) before eventually kinking (large–scale helicity). Such an experiment also demonstrates that the two components of self–helicity, writhe and twist, are not individually conserved as there can be a transfer between forms.

The second term of (1.57) describes the flux of helicity through the boundary by either the emergence of flux through said boundary, or by surface motions along the boundary. If $\hat{\mathbf{B}} \cdot \hat{\mathbf{n}} = \hat{\mathbf{v}} \cdot \hat{\mathbf{n}} = 0$ then helicity is exactly conserved (bar negligible dissipative processes), but this is rarely the case. From (1.8), we can expand the boundary flux term as

$$
\frac{\mathrm{dH_V}}{\mathrm{dt}} = 2\int_S (\mathbf{A} \cdot \mathbf{v}) B_n\,\mathrm{d}^2\mathrm{x} - 2\int_{\mathrm{S}} (\mathbf{A} \cdot \mathbf{B}) \mathrm{v_n}\,\mathrm{d}^2\mathrm{x}, \qquad (1.60)
$$

for which the first term describes the flux of helicity due to surface shear, and the second due to the removal of field from within the volume.

The strength of the helicity conservation law is such that we can restrict the evolution of a magnetohydrodynamic system according to the total magnetic helicity in its initial state, as posed by Taylor (1974) in his seminal letter. There, it was shown that the evolution from a complex magnetic field to that of a minimal energy state (a force–free system) can be found by constraining said evolution by the conservation of magnetic helicity. Berger and Prior (2006) also show how a winding number (which has been shown to be related to helicity, described in Chapter 4) is conserved within a tubular domain, provided that there is no motion on either the top or bottom boundary. The consequences of Alfvén's Frozen Flux theorem are also clear here: if the flux within each flux tube is conserved, regardless of how infinitesimal it is, then the helicity as posed by (1.37) is conserved.

Throughout the course of this thesis, we will study the flows of magnetic helicity, and in particular try to gain an understanding of the structures causing the localised entanglement which are responsible for the global helicity.

1.5.9 Alpha Quenching

We have discussed the concept of the α effect aiding the reconstruction of a reversed poloidal field by cyclonic twisting of emerging flux tubes in Section 1.4.3. Further, in this section we have discussed how magnetic helicity is well–conserved even in a non–ideal regime. Thus, it is fair to assume that this turbulent writhing of the toroidal flux tubes should, to conserve the total helicity, also induce an equal and oppositely signed helicity. It is also assumed that this oppositely signed helicity will be on the smaller spatial scales associated with twist–helicity, given that the produced writhe seems unopposed. Note the distinction between the mean writhe of flux tubes by *twisting motions* describing the α effect, and *twist* describing the local winding of field lines in Section 1.5.3.

How this injection of small–scale twist affects the progression of the solar dynamo has been fundamental to the development of our theoretical understanding. To obtain an expression of α in terms of the kinetic helicity (1.31), we assumed that the system which we are studying is kinematic. In actuality, this is highly inaccurate: the back–reaction from the magnetic field onto the velocity field must be taken account of. First posed by Pouquet et al. (1976), we can write

$$\alpha = \alpha_K + \alpha_M, \tag{1.61}$$

$$\alpha_K = -\frac{\tau_c}{3}\langle \omega' \cdot \mathbf{v}' \rangle, \tag{1.62}$$

$$\alpha_M = \frac{\tau_c}{3}\langle \mathbf{j}' \cdot \mathbf{B}' \rangle, \tag{1.63}$$

which is a combination of the original kinematic expression, with the addition of a term determined by the small–scale current helicity $\mathbf{j}' \cdot \mathbf{B}'$. But what does this mean? First, note that the two terms are oppositely signed. This means that the magnetic component of the α effect acts to oppose the averaged cyclonic (kinetic) motions. The back reaction is quantified by the mean small–scale current helicity density $\langle \mathbf{j}' \cdot \mathbf{B}' \rangle$, which measures the linking of lines of current. Whilst less physically meaningful than magnetic helicity, the two helicities have been shown, for these small–scale variations, to be intrinsically linked (Hubbard and Brandenburg, 2012):

$$\langle \mathbf{j}' \cdot \mathbf{B}' \rangle \simeq k_f^2 \langle \mathbf{A}' \cdot \mathbf{B}' \rangle, \tag{1.64}$$

where k_f is the wave–vector corresponding to the length scale of the turbulent motions (Fourier spectra will be detailed further in Chapter 4). As such, mean field theory indicates that the mean small–scale magnetic helicity is a quencher of the production of large–scale twist by turbulent motions.

The magnetic energy has also been shown to be key to the quenching of the alpha effect (Charbonneau, 2005):

$$\alpha(\langle \mathbf{B} \rangle) = \frac{\alpha_0}{1 + (\langle \mathbf{B} \rangle / B_{eq})^2}, \tag{1.65}$$

where B_{eq} is the equipartition strength of the magnetic field, and α_0 is as given in (1.61). B_{eq} gives an indication of the magnitude of the magnetic field when kinetic energy is balanced with magnetic energy, where the system reaches an equilibrium. A qualitative description of (1.65) is that the tubulent motions move kinetic energy to magnetic energy by the net production of writhe, which can be quenched by a constraint on the transfer of energies. We can see that the more the magnetic field's energy exceeds that of the equipartition value (such that magnetic and kinetic energy are unbalanced), then $\alpha \to 0$.

Thus, by the above theoretical result, we can see that that the poloidal regeneration of the α–effect, which is necessary for the continued function of the solar dynamo, is actually counteracted by the generation of small scale twist that comes from the very writhe it acts to create. This twist acts to trap energy in the magnetic field, as it is not easily converted to further writhe by the constraint of magnetic tension once the toroidal field reaches an appropriate strength $|\langle \mathbf{B} \rangle| > B_{eq}$.

Even the expression given by (1.65) has been challenged as too lenient (Cattaneo and Hughes, 1996; Vainshtein and Cattaneo, 1992), and it is thought that we should instead write

$$\alpha(\langle \mathbf{B} \rangle) = \frac{\alpha_0}{1 + R_m (\langle \mathbf{B} \rangle / B_{eq})^2}, \tag{1.66}$$

to take account of the equipartition between the small scale turbulence and kinetic energy. Given that R_m near the photosphere can take values of up to 10^8, this could imply that quenching of the solar magnetic field's occurs before it has the chance to grow. One solution to is the so-called *interface dynamo*, posed by Parker (1993), where the regions in which the toroidal field is stored, and the region in which the α effect occurs, are separated. Specifically, the toroidal field is assumed to be stored around the tachocline, where the radial and latitudinal shear which produces the toroidal field is strongest. As such, the region in which the α effect operates has a lower magnetic energy, and will be less constrained by the quenching effect.

1.6 Outline

Over the course of this introductory chapter we have established that the Sun consists of a highly complex set of interacting regions, with vastly different physical parameters, which require different assumptions in their modelling. Key to their collaborative function is the solar dynamo, which operates within a specific parameter space. Crucial to the function of this dynamo is magnetic helicity, a measure of twisting and writhing of the magnetic field. We have seen that the conservation of magnetic helicity both aids our understanding of the dynamo, whilst seemingly constricting it via the α-effect.

In an attempt to take further advantage of the constraining invariance of magnetic helicity, and its flux, we shall test in Chapter 2 whether magnetic helicity flux can be used to predict the strength of the large–scale 11 year solar cycle. In particular, we shall test how strongly correlated the twisted large–scale poloidal field is to the sunspot number in a cycle, which we use to quantify the strength of the toroidal field.

Then, in Chapter 3, we for the first time measure the photospheric helicity flux associated with each of the terms in a surface flux transport model, at a much higher spatial resolution than in Chapter 2. More specifically, we will look at a two–dimensional surface flux transport model, which determines how the magnetic field on the photosphere changes due to advection and diffusion effects. We will discuss the latitudinal dependencies of magnetic helicity, and again study the correlation between solar cycle strength and helicity flux.

It appears to be key to the function of the solar dynamo that helically twisted magnetic structures are ejected from the solar interior, or surface, wherever they may form, to minimise the value of mean small–scale current helicity. There is currently, however, no additive way to measure where the helicity is within a volume of interest, nor classify what scale it is on (the latter typically requires the assumption of periodicity). In Chapter 4, the main result of the thesis, we show that localisation is possible using wavelets, and we define a gauge–invariant measure of helicity which has a physically meaningful definition of locality.

Finally, in Chapter 5, we look at other, simpler ways of measuring helicity density in asymmetric volumes, with a particular focus on how that asymmetry affects the value of helicity.

Chapter 2

Magnetic Helicity Flux as a Predictor of Solar Activity

The research presented in this chapter has been published in the journal Solar Physics, under the title "Magnetic Helicity Flux as a Predictor of Solar Activity" in July 2018 (the point at which the data analysis halts): see Hawkes and Berger (2018) . I performed the data analysis, wrote the numerical codes, produced the figures and wrote the article's text. Section 2.4 did not appear in the publication.

2.1 Introduction

In this chapter we investigate the suitability of magnetic helicity flux as a predictor of solar activity. Solar activity and its associated phenomena and drivers are known to have wide-ranging effect on the heliosphere, including on (for example) how cosmic rays pass through said regions (Ferreira and Potgieter, 2004). Indeed, measurements of solar activity are one of the few ways that we have of taking direct measurements of the Sun, which in turn is the only star close enough for us to fully and reliably observe. The magnetic field produced by the solar dynamo is utterly fundamental to furthering this understanding (Cameron and Schussler, 2015; Charbonneau, 2005), and is the cause of solar activity. Solar dynamos are in a rare class where we see a self-sustained and reinforced magnetic field (Moffatt, 1978). This, and other conditions on the Sun (for example, sustained nuclear fusion), are not currently reproducible on the Earth, making it an excellent laboratory for studying more exotic and extreme physical phenomena.

Observations of the Sun have been occurring for hundreds of years. Sunspot records are semi-reliably available back to 1610 (Hoyt and Schatten, 1998), although there is evidence of observations being made as early as the year 939 (Vaquero and Gallego, 2002). Other activity indices include solar radio flux index (F10.7), interplanetary magnetic field (IMF), flare index, polar faculae (N. R. Sheeley, 2008), and coronal index (Fe XIV emission) (Usoskin, 2005).

There have been many attempts to make predictions of the strength of a solar-activity cycle, which itself tends to be quantified by either sunspot/active region number or area, a convention we shall follow. To see this, first recall that a sunspot is formed from an emergent flux tube from within the convective zone (perhaps near the tachocline). Thus, the sunspot number, which is a measure of the number of emergent flux tubes, should give an indication of the amount of magnetic field which is emerging, and thus an indication of the activity of the solar cycle (Balogh et al., 2016).

Prediction methodologies can be split into three subsets: extrapolation methods, precursor methods, and model-based predictions (Munoz-Jaramillo et al., 2013). An extrapolation method would take advantage of, for example, a sunspot data series, and any mathematical relations that can be derived from them, whilst a precursor method takes advantage of other observables such as poloidal field strength during solar minima. Finally, a model-based prediction (arguably a combination of the two methods) takes a range of data sets in an attempt to model the solar cycle, which are then passed through evolution equations. A model based prediction could include physical affects such as the $\alpha\Omega$ dynamo. Two recent reviews are Hathaway (2009) and Petrovay (2010).

One notable example is the work of Choudhuri et al. (2007), who use a mean field dynamo model. In that article, they gave a prediction of the strength of Cycle 24, using a dynamo model based prediction system, which has now been revealed to be accurate in at least an amplitude sense (a large reduction from Cycle 23). An earlier prediction for the same cycle, made in Dikpati et al. (2006), using a surface flux transport model, which had been successful in re-predicting previous solar cycles, predicted that Cycle 24 would in fact exceed Cycle 23 by a similar percentage to the decrease predicted by the Choudhuri et al. (2007) article. This variability in results demonstrates the difficulties in predicting solar cycles, even when using similar methods.

The work of this chapter fits within the definition of a precursor method, taking advantage of the magnetic helicity flux during the preceding solar minima. We will attempt to display a relationship between this quantity and the strength of the following solar maxima, which is quantified here by sunspot number. We hope such a relationship would give us the ability to predict the strength of the cycle approximately five years in advance.

As we described in Chapter 1, magnetic helicity H quantifies the degree of entanglement of a magnetic field. Recall that for open magnetic fields, a gauge invariant relative helicity can be defined by

$$H_{\mathrm{V}} = \int_V (\mathbf{A}+\mathbf{A}_0)\cdot(\mathbf{B}-\mathbf{B}_0)\ \mathrm{d}^3x, \tag{2.1}$$

where $\mathbf{B}_0$ is typically a current-free (potential) field ($\nabla\times\mathbf{B}_0 = 0$), such that $\mathbf{B}_0 = \nabla\times\mathbf{A}_0$. $\mathbf{A}_0$ is the vector potential of the current-free field. Relative helicity also demanded that the boundary conditions of the potential reference field match that to the field we wish to measure: $\mathbf{B}\cdot\hat{\mathbf{n}} = \mathbf{B}_0\cdot\hat{\mathbf{n}}$, where $\hat{\mathbf{n}}$ is the normal vector associated with V. On the Sun, the northern hemisphere generates and ejects negative helicity, and the southern hemisphere positive (Ding et al., 1987).

We showed that magnetic helicity is a well-conserved quantity in ideal and low resistivity magnetohydrodynamics. This conservation means that the change in helicity with respect to time is essentially restricted to two mechanisms: helicity flow due to motions parallel and perpendicular to a boundary (having neglected dissipation). We were then able to write (Berger and Ruzmaikin, 2000)

$$\frac{\mathrm{dH}}{\mathrm{dt}} = 2\int_S (\mathbf{A}_0 \cdot \mathbf{v}) B_n \,\mathrm{d}^2\mathrm{x} - 2\int_S (\mathbf{A}_0 \cdot \mathbf{B}) \mathrm{v}_\mathrm{n} \,\mathrm{d}^2\mathrm{x}, \tag{2.2}$$

where $\mathbf{v}$ is the fluid velocity flow on the solar surface. The first integral determines the flux of helicity due to tangential surface motions such as differential rotation (the shear term). The second component of this integral describes helicity rising through the convective zone and being ejected into the corona, with a velocity component in the direction of $\hat{\mathbf{n}}$. Indeed, for the Sun we are only able to reliably calculate $\mathbf{A}_0$ at the surface itself. In this chapter (and throughout the thesis in general) we choose to neglect the second component, and we focus on the contribution due to the Omega effect, which is thought to be the main contributor to large scale helicity flux. For $\mathbf{v}$, we shall use the profile as given in Berger and Ruzmaikin (2000).

As we have described, the Omega effect is typically attributed to the polar magnetic field lines, which move slower than those at the equator due to differential rotation. As a consequence, they wrap themselves around the solar axis, generating toroidal field. Thus, by measuring the strength of the polar field at solar minimum, we would hope to get an estimate of how much toroidal flux is being stored for the production of sunspots in the next solar cycle. However, polar field (in this work and similarly in others) is defined only as a field average over a fifteen degree polar cap, whilst our helicity flux takes accounts of all the field lines on a hemisphere. We believe this makes helicity flux a better measure of the Omega-effect than the polar field.

The Sun's activity minimum is defined as the period in which we see very few sunspots, in between long periods of notable activity. At this time the Sun's poloidal field is observed to be maximal. The action of differential rotation on the poloidal field (the Omega effect) then causes a maximal helicity flux in line with this maximum poloidal field.

Large scale helicity flux associated with the solar dynamo is typically modelled via a three-stage process which traces the flow of positive helicity. Negative helicity flux is ejected by the northern hemisphere into the corona, which can be interpreted as positive helicity flowing into the interior. Positive helicity then flows through an equatorial slice into the southern hemisphere at a rate exceeding that of the inflow from the corona into the northern hemisphere, resulting in a negative helicity build-up in the northern hemisphere. Equivalently, a relatively small flow of positive helicity exits the southern interior, which gives an overall build-up of positive helicity in the southern hemisphere. This model can be succinctly described by the following formulae (Berger and Ruzmaikin, 2000)

$$\frac{\mathrm{dH}_{\mathrm{VN}}}{\mathrm{dt}} = \dot{H}(C_\mathrm{N} \to V_{\mathrm{N})} - \dot{H}(V_\mathrm{N} \to V_\mathrm{S}), \quad \frac{dH_{\mathrm{CN}}}{\mathrm{dt}} = -\dot{H}(C_\mathrm{N} \to V_\mathrm{N}), \tag{2.3}$$

$$\frac{\mathrm{dH_{VS}}}{\mathrm{dt}} = \dot{H}(V_{\mathrm{N}} \to V_{\mathrm{S}}) - \dot{H}(V_{\mathrm{S}} \to C_{\mathrm{S}}), \quad \frac{\mathrm{dH_{CS}}}{\mathrm{dt}} = \dot{H}(V_{\mathrm{S}} \to C_{\mathrm{S}}), \tag{2.4}$$

where V and C denote the solar interior and corona respectively, with N and S denoting North and South. In this chapter, when we refer to a sum of hemispheres, we will sum the absolute values of these quantities. The helicity, having built up within the hemispheres, can be ejected through CMEs and flares etc (van Driel-Gesztelyi et al., 2003).

There have been studies into the effectiveness of measuring the build up of magnetic helicity to measure the likelihood of a solar eruption (see e.g. Pariat et al. (2017)). This is admittedly restricted to singular events, rather than a study of helicity flow and build up over the whole Sun. However, one advantage of their type of study is that one can take account of the scale of the active region, rather than assuming uniformity.

In Section 2.2 we first provide the mathematical basis for the magnetic field used within this chapter. Then, in Section 2.3 we perform a preliminary analysis on the magnetic field data provided by the Wilcox Observatory using a variety of techniques described within. Section 2.4 has us study whether it might be better to take the square root of helicity. Then, in Section 2.5 we look at how splitting sunspot number by hemisphere can improve our results. There is limited sunspot data that is split hemispherically, and so we study a reconstruction of past data in Section 2.6. Section 2.7 is where, to ensure our analysis is meaningful, we also test the inverse of our hypothesis: whether helicity is in fact predicted by solar activity.

The predictive power of polar field strength, which is currently the most commonly used precursor indicator of the solar cycle is ranked against our methods in Section 2.8 (this is also a recurring theme throughout the other, earlier sections). We attempt to overcome the small sample size inherent in this study in Section 2.9 by studying reconstructed magnetic field data published in Makarov and Tlatov (2000), to which we apply the same analytical techniques. Finally, in Section 2.10 we attempt a prediction of the characteristics of Solar Cycle 25, before concluding in Section 2.11.

2.2 Magnetic and Vector Potential Fields

2.2.1 The Photospheric Field

In this chapter we will use the spherical harmonic expansion provided by the Wilcox Solar Observatory as our photospheric radial field. Spherical harmonics are a set of orthogonal functions on the surface of a sphere, which allow us to write the signed radial photospheric magnetic field, B_r, as

$$B_r = \sum_l \sum_m P_l^m(\cos(\theta))(g_l^m \cos(m\phi) + h_l^m \sin(m\phi)) = \sum_{lm} b_{lm} Y_l^m, \tag{2.5}$$

for which P_l^m are the associated Legendre functions of order m and degree l, b_{lm} is a co–efficient determining the relative strength of each harmonic component (dipole, quadrupole etc), θ is the colatitude and ϕ is the longitude. The relation between Legendre functions and spherical harmonics is given by

$$Y_l^m = \frac{(l-m)!}{(l+m)!} P_l^m(\cos(\theta))\exp(im\phi). \tag{2.6}$$

Given that we want to measure the helicity flux associated with large scale magnetic fields, we limit ourselves to $l = 4$. The co–efficients determining the strength of each harmonic within the expansion are given by

$$g_l^m = \frac{2l+1}{2\pi}\frac{(l-m)!}{(l+m)!}\int_0^{2\pi}\cos(m\phi)\int_0^{\pi} B_{r0}(\theta,\phi)P_l^m(\cos\theta)\sin(\theta)\,\mathrm{d}\phi\mathrm{d}\theta, \tag{2.7}$$

and

$$h_l^m = \frac{2l+1}{2\pi}\frac{(l-m)!}{(l+m)!}\int_0^{2\pi}\sin(m\phi)\int_0^{\pi} B_{r0}(\theta,\phi)P_l^m(\cos\theta)\sin(\theta)\,\mathrm{d}\phi\mathrm{d}\theta, \tag{2.8}$$

where B_{r0} is the $r$adial approximation of the magnetic field, obtained by taking

$$B_{r0} = \frac{B_r^{los}}{\sin(\theta)}, \tag{2.9}$$

from the line–of–sight approximation B_r^{los}, by assuming that the photospheric field is entirely radial (else B_r^{los} could arguably contain other components). The $\sin(\theta)$ term acts to correct for the fact that observations would indicate that the equatorial radial field is stronger than the polar fields. This approximation will be applicable for the large–scale fields being employed here. When sunspots emerge, their field is typically non–radial, but their resolution is below that of which we are interested in here. There are superior approximations (such as that described within Leka et al. (2017)) when one is interested in fields with a higher complexity.

2.2.2 A magnetic vector potential

The reference magnetic vector potential field, $\mathbf{A}_0$, as described above, depends only on the radial component of the magnetic field. Within the gauge invariance of relative helicity, we choose (following Berger and Ruzmaikin (2000))

$$\nabla\cdot\mathbf{A}_0 = 0, \tag{2.10}$$

$$\mathbf{A}_0\cdot\hat{\mathbf{n}} = 0, \tag{2.11}$$

(these conditions increase in complexity for non–spherical or planar surfaces). In this case

$$\mathbf{A}_0 = \hat{\mathbf{n}}\times\nabla\Psi, \tag{2.12}$$

such that

$$\mathbf{A}_0 = \sum_{lm} \frac{-R_\odot b_{lm}}{l(l+1)} \mathbf{r} \times \nabla Y_l^m, \tag{2.13}$$

as required.

2.3 Data and Analysis Techniques

In Figure 2.1, we compare magnetic helicity flux due to differential rotation through the northern hemisphere against total sunspot number, averaged over each Carrington Rotation (CR) from the daily value. We take sunspot number over the entire solar disc due to restrictions in data availability, although in later sections we do analyse the two hemispheres separately. Magnetic helicity flux is calculated using data from the Wilcox Solar Observatory according to equation (2.2), and sunspot data are provided by the WDC-SILSO, Royal Observatory of Belgium, Brussels. The helicity of the two hemispheres are not exact sign opposites, but are closely aligned enough that comparing a single hemisphere's helicity to sunspot number over the disc should make little difference. Throughout this article, we normalise all data with respect to the highest peak contained within it, starting from the first relevant cycle. This would mean we would not include, for example, a sunspot cycle before our first helicity cycle. It is possible to normalise these quantities using other techniques (such as taking $|\Phi|^{-2}\mathrm{dH}\,/\,\mathrm{dt}$, where Φ is the magnetic flux through a hemisphere), but we found these methods to be less intuitive.

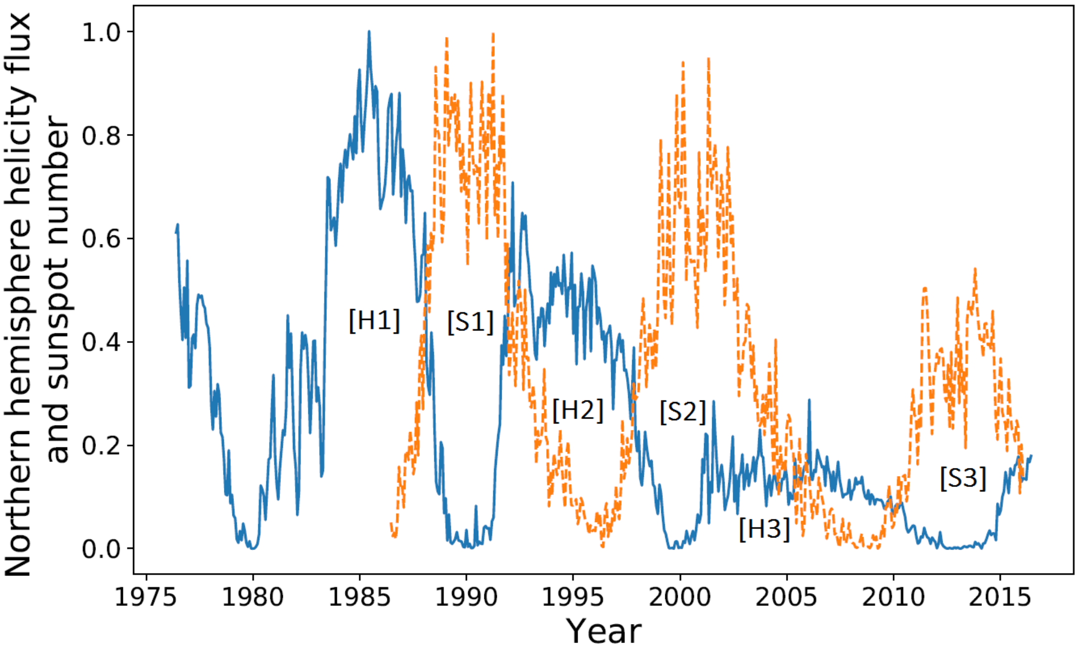

Fig. 2.1 Sunspot number (dashed orange) and helicity flux through the northern hemisphere (solid blue), normalised by the amplitude of the largest cycle within their respective data sets. Cycles have been labelled according to the number system used in this chapter, with H denoting helicity and S denoting sunspot.

The data display a clear resemblance between the helicity flux cycles during solar decline/minima and the following solar-activity cycle. If we were to take account of the relationship between helicity flux and magnetic flux ($\sim \Phi^2$) versus that between sunspot strength and magnetic flux ($\sim \Phi$), the differences in amplitude are somewhat accounted for. This is not, however, physically meaningful, as the sunspot number used here does not distinguish between regions with strong and weak flux. Regardless, we briefly examine the possibility of dimension matching in Section 2.4.

The similarities seem to be much weaker for the weaker cycle (the third pair of peaks (Cycle 24), 2000 onwards). This cycle is also distinctive in that the helicity maximum lies at around 20 % that of the previous cycle. The cause of this anomaly could be the recent extended solar minimum (Frohlich, 2013). Regardless, both cycles are anomalously low within their own set, which is an inherent similarity.

The conclusion drawn is that a larger set of data is required. Magnetic field data, however, are largely unavailable before the dates already graphed. We perform an analysis on the available data, with this restriction in mind.

2.3.1 Dynamic Linear Modelling and Kalman Smoothing

Both data sets of Figure 2.1 have high frequency noise, making it difficult to identify similar overall trends. In an attempt to smooth the data, we employ two data analysis tools: dynamic linear modelling (DLM) and Kalman smoothing (KS). Smoothed data is commonly used when working with sunspot number, for the purposes of prediction (Petrovay, 2010).

A dynamic linear model is described by two equations:

$$y_t = F_t x_t + a_t, \tag{2.14}$$

$$x_t = G_t x_{t-1} + \omega_t, \tag{2.15}$$

where G_t and F_t are matrices, a_t and ω_t are vectors of Gaussian (normal) distributions (indexed by t), y_t are the observations and x_t is the (assumed) underlying model. Equation (2.14) is known as the observation equation, and (2.15) is known as the state equation (Petris et al., 2009). This state space model assumes that the process (in this case the flux of magnetic helicity or sunspot number) is governed by some underlying process which we cannot measure directly (the state equation), but has an output that we can measure (the observation equation). This type of model is typically used to predict future data points, within an error given by the aforementioned Gaussian distributions. The underlying process (which is assumed to govern our observations) is found using maximum-likelihood estimation, based on the observations that we input (the data). In simple terms, we find the variables that are *most likely* to generate the data set we observe, with associated distributions.

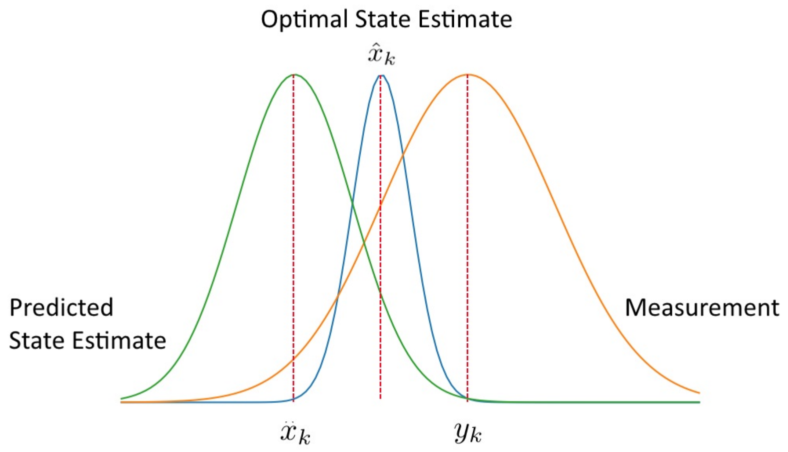

Fig. 2.2 Pictorial representation of the Kalman smoothing process at an individual time step $t = k$. The optimal state estimate, in blue, is found by multiplying the red and green curves together, which represent our predicted state estimate and measurement distributions respectively.

Figure 2.2 shows how this model works, for an individual time step $t = k$. The optimal state estimate, shown by the blue curve, is calculated by multiplying the two distributions together (red and green), and is assumed to be more accurate than either the measurement or state estimator. Calculating these optimum values for every time step t, once the entire data set is known, is referred to as Kalman Smoothing (KS).

In figures 2.3 and 2.4, we give the smoothed data produced by applying the KS to magnetic helicity flux and sunspot number respectively. The red line indicates the smoothed data, and the green bars represent a 90 % confidence interval.

The smoothed plot of Figure 2.4 in particular reveals an interesting underlying double peak structure, known as Gnevyshev gaps (Gnevyshev, 1963). It is possible that this is due to a disparity in the specific timings of the sub–dynamos governing each hemisphere. Evidence for this can be seen in Figure 2.5, where we have plotted sunspot number for the two hemispheres separately (for which data is available from 1992). This two-peak structure is particularly notable in the final sunspot cycle, due to the disparity between the height of the two peaks, and the structures of the cycles.

2.3.2 Pearson Correlation Coefficient

One standardized method for testing how well two data sets are correlated is the Pearson correlation coefficient, which we denote by P. The discrete data form of the Pearson correlation coefficient is employed, given by

$$P = \mathrm{corr}(\mathrm{X},\mathrm{Y}) = \frac{\mathrm{cov}(\mathrm{X},\mathrm{Y})}{\sigma(\mathrm{X})\sigma(\mathrm{Y})}, \tag{2.16}$$

where X and Y are the two data sets being studied, $\mathrm{cov}(\mathrm{X},\mathrm{Y})$ is the covariance of the two sets, and $\sigma(X)$ and $\sigma(Y)$ are their standard deviations.

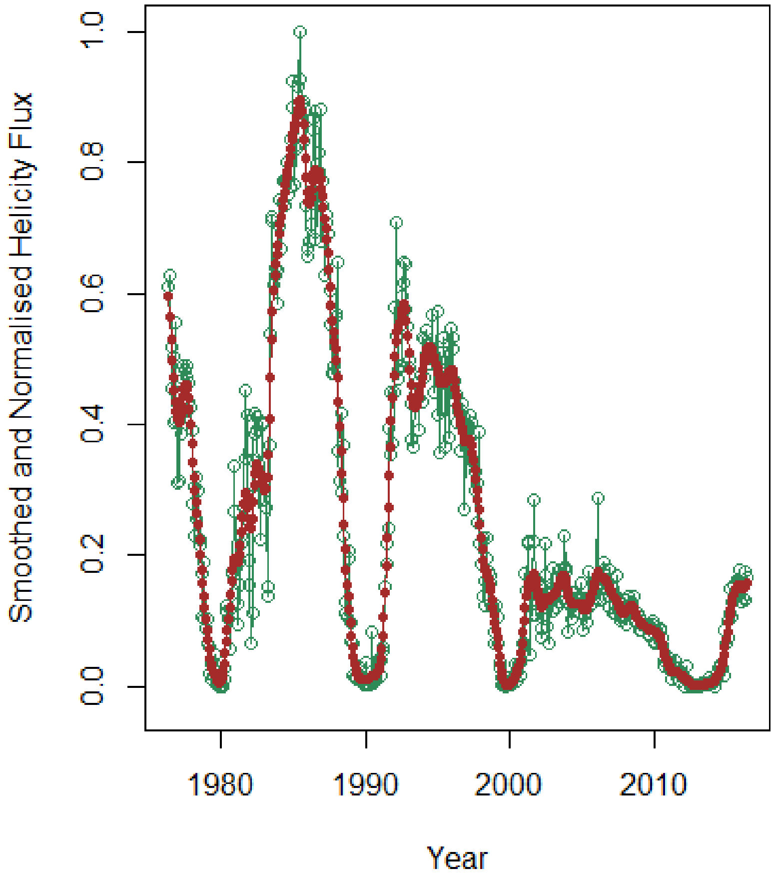

Fig. 2.3 Normalised helicity flux (northern hemisphere) data processed using Kalman smoothing and dynamic linear modelling (red) with uncertainties (green)

To find the phase shift between the two cycles, we calculate the correlation co-efficient for all possible phase shifts (within the limit of our data) and take the shift which offers the strongest $|P|$. We find that there is a clear difference between the optimum lag times, with the first (larger) peaks having a phase shift of 60 Carrington Rotations (4.5 years), whilst the second peaks are shifted by 92 Carrington rotations (6.9 years). These shifts give values of P corresponding to their relevant cycle pairs of 0.88 and 0.84 respectively, both of which indicate strong positive correlation. In all cases, unless otherwise stated, we use all data points that define the cycle to calculate the correlation between each successive minima. We will also use the minima between sunspot cycles to denote the beginning and end of a solar cycle.

Figure 2.6 shows helicity flux shifted by the above time periods plotted on the same axis as normalised sunspot number (unshifted). The visual correlation offered by either of these phase shifts have both positive and negative attributes. For the latter, we see a good correlation of minima (lowest points between cycles), and excellent correlation for the second pair of peaks. The first pair of peaks is less well aligned (in the region between the minima). This is could be due to the sudden drop observed in the helicity flux around the fiftieth (CR 1692) Carrington rotation, which is not reflected in the sunspot number. The 4.5 year phase shift gives a stronger correlation for the first pair of peaks, although

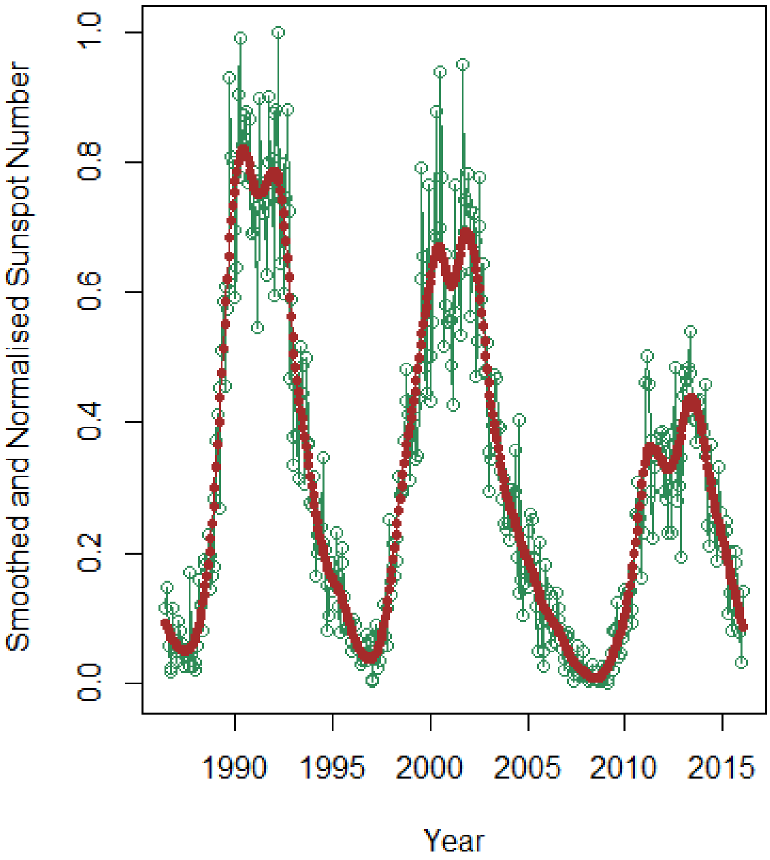

Fig. 2.4 Normalised monthly sunspot number data processed using Kalman smoothing and dynamic linear modelling (red) with uncertainties (green).

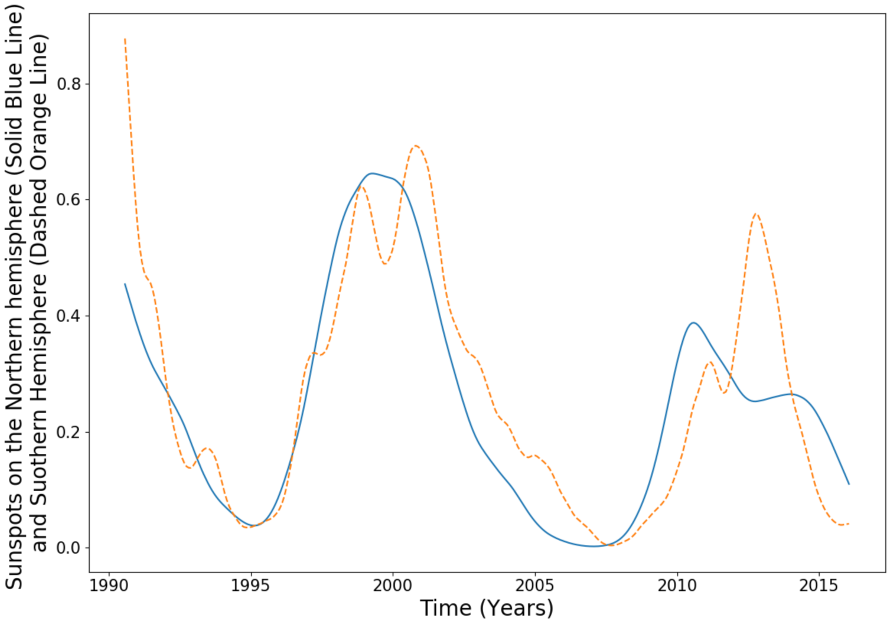

Fig. 2.5 Smoothed sunspot numbers for the northern (blue) and southern (orange) hemispheres from 1992 – 2017.

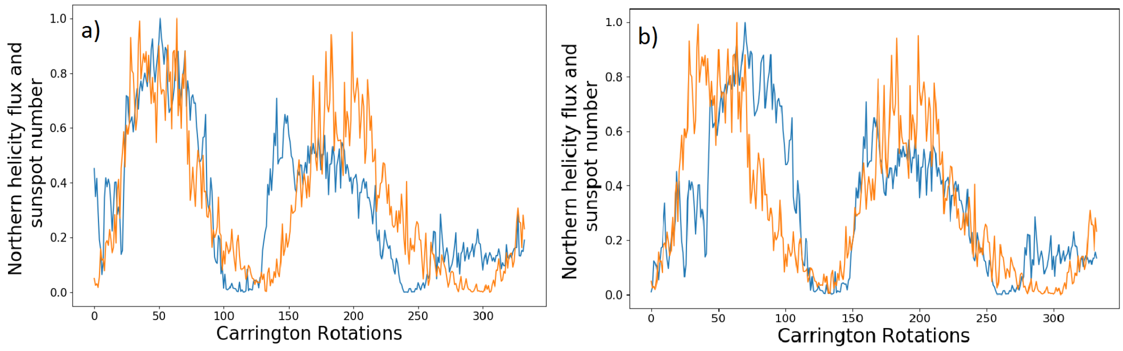

Fig. 2.6 Phase shifted normalised helicity data (blue) by 60 Carrington rotations (a) and 92 Carrington rotations (b), with normalised sunspot number (orange).

the minima are no longer as well aligned. In the left figure, the second pair of peaks is less well aligned between the minima. Note that the third pair of peaks is not very well correlated in either figure, nor do we attempt to perform an optimisation on those data sets (we demonstrated their distinct nature in Figure 2.1).

We also plot the smoothed versions of the figures 2.6(a) and (b), with identical phase shifts, in Figure 2.7. The results of this are mostly unchanged. Visually, the peaks appear less correlated. The values of P, however, are greater for the two optimised cycles (unsurprisingly). The left of Figure 2.7 corresponds to the phase shift of 60, and gives a P of 0.938 for the first cycles, and on the right we have a phase shift of 92 with $P = 0.904$ for the second pair of cycles. This is a marked improvement for the latter in particular. The comments made on Figure 2.6 regarding the structural differences continue to apply here.

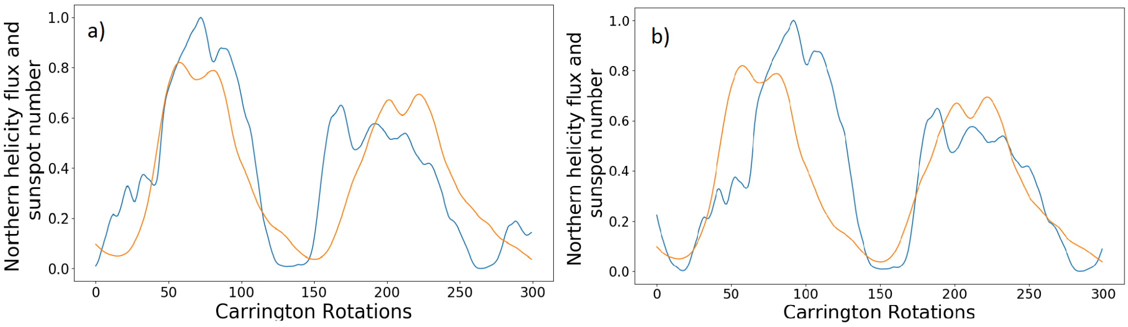

Fig. 2.7 Phase-shifted smooth normalised helicity data (blue) by 98 Carrington rotations (a) and 68 Carrington rotations (b), with normalised smooth sunspot number (orange).

2.3.3 Integration

In the previous section we found that whilst it was possible to align Solar Cycles 22 and 23, cycle 24 in particular offers only weak indications of correlation, both in terms of length and amplitude. We therefore look for a comparison technique that disregards structure, reducing large sets of data to single points. This work is concerned with comparisons of

Peak Pair	Helicity Data Integrated	Sunspot Number Integrated	Ratio of Integrations
1	59.50 CR	55.15 CR	94 %
2	42.39 CR	52.40 CR	81 %
3	17.5 CR	26.50 CR	66 %

Table 2.1 Values of integrated helicity flow and sunspot number, and their ratio.

overall activity, and we thus compare the area under adjacent peaks. It should be noted that these areas have been calculated after the normalisation procedure, and therefore have units of Carrington rotations. The first example of this is shown in Table 2.1.

Integrating helicity flux (dH / dt) over time clearly gives the total helicity H that passed through the photosphere in a given time period. For sunspot number, however, a temporal integral is less physically meaningful. There is, however, a known relation between sunspot size, activity, and its period of existence (Henwood et al., 2010). For recurring sunspots (those that traverse the entire solar disc and re-appear in a following sunspot cycle), the temporal integral should then take account of their increased size and activity.

The ratio column of Table (2.1) (and all subsequent tables) is obtained by dividing the smaller quantity by the larger, regardless of association (whether the larger value be of integrated helicity flux, or sunspot number), as a measure of similarity. The closer the ratio is to 100%, the more similar the two areas of interest are: we don't seek to distinguish between cases where the area of the predicting quantity exceeds or falls short of the quantity which we aim to predict. We see that, for the second peak in particular, the area under the curves is very similar. Again, the weakest comparison comes from the third pair of peaks. All three results match with a 66 % threshold, but with an average of 80 %, indicating good activity matching.

2.4 Square Root of Magnetic Helicity

In Section 2.3, we noted if we were comparing helicity flux with a sunspot number which took account of the flux, Φ, of the active regions, then the differences between the two data series might be taken account of by taking the square root of helicity. In particular, the SI units of helicity flux are

$$\left[\frac{\mathrm{dH}}{\mathrm{dt}}\right] = \frac{G^2 m^4}{s} \equiv [\Phi]^2 s^{-1}, \tag{2.17}$$

whilst sunspot number is a unit-free quantity, but it could be thought to be associated with $[\Phi]$. In this section, we will perform our data analysis techniques as if this unit comparison were physically meaningful, by taking the square root of magnetic helicity.

We plot the normalised square–root of helicity flux against sunspot number in Figure 2.8 (in the style of Figure 2.1). We find in this case that the amplitude of the peaks could be argued to be slightly better matched for the second cycle pair, although the helicity

Peak Pair	Square Root of Helicity Data Integrated	Sunspot Number Integrated	Ratio of Integrations
1	81.10 CR	55.15 CR	68.0 %
2	68.57 CR	52.40 CR	76.4 %
3	51.32 CR	26.50 CR	51.6 %

Table 2.2 Values of the integrated square–root of absolute helicity flux, and sunspot number, and their ratio.

flux peak might now be too large, dependent on how we define a peak's maxima. We do, however, see a notable improvement in the matching of peaks for the third cycle.

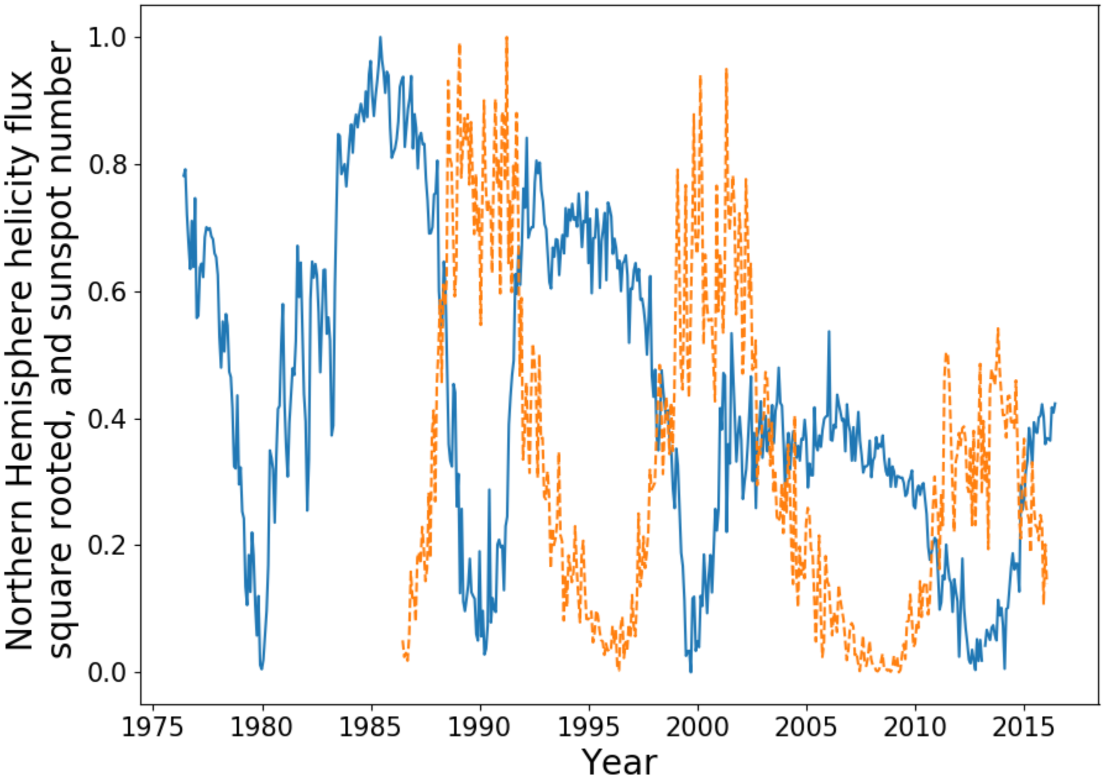

Fig. 2.8 Square root of absolute helicity flux (blue) versus sunspot number (dashed orange) for the period.

In Table 2.2, we give the values of integrated helicity flux, for which we take the absolute root before normalising. For each of the three cycles, the ratio of integration measure is lower than that for which the helicity flux which is not rooted (Table 2.1). We further found that the values for correlation were unchanged, as one might expect.

We choose not to continue with taking the square–root of helicity flux, due to the lack of physicality established in Section 2.3, and the notably worse integration values. It is, however, of future interest to determine whether there is a physicality behind the square–root improving mainly the final cycle's peak–matching.

2.5 Hemispherical Helicity and Sunspots

In figures 2.9 and 2.10 we plot sunspot number for each hemisphere against the helicity flow for the northern and southern hemispheres respectively. Internationally recognised sunspot number data that is split by hemisphere is only available from 1992 onwards, restricting data analysis. The limited results do indicate a stronger relationship than that when the hemispheres are combined. In particular, if we look at the final two cycles of Figure 2.9, they appear to be more closely related than what we observe in Figure 2.1. The most recent cycle in particular is much closer in amplitude for the northern hemisphere. This is however not reflected in the southern hemisphere (see Figure 2.10).

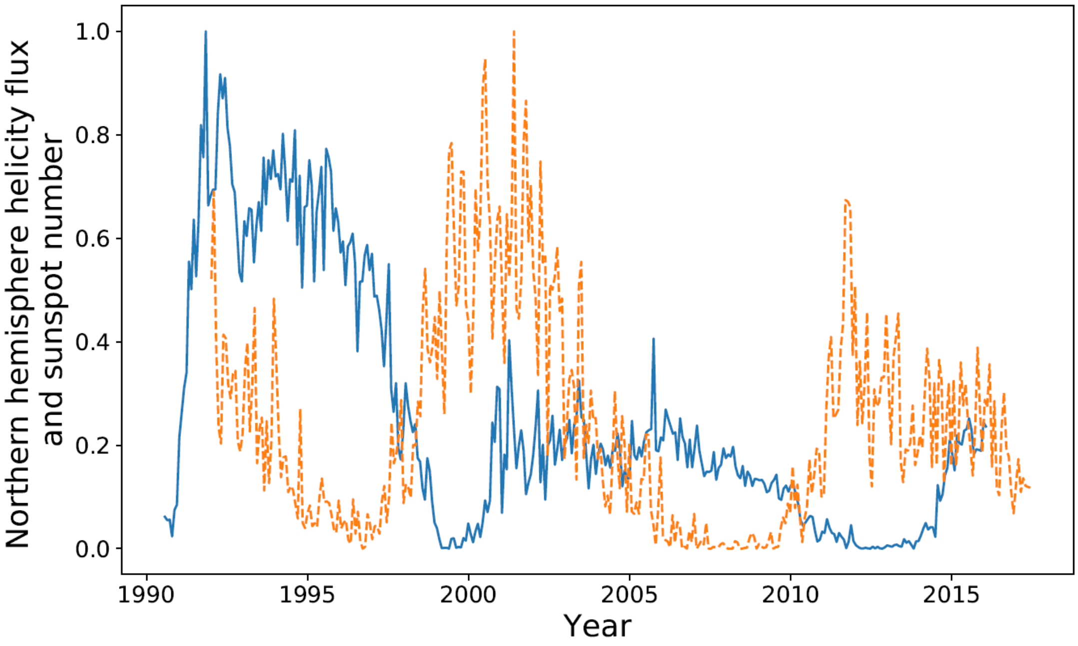

Fig. 2.9 Northern hemisphere helicity flow (blue) and northern sunspot number (dashed orange).

Peak Pair	Integration Ratio (North)	Integration Ratio (South)	Ratios of Sums
2	73.5 %	98.7 %	94.9 %
3	93.2 %	78.0 %	83.1 %

Table 2.3 Ratios of the values of integrated helicity flow and sunspot number separated by hemisphere.

Table 2.3 shows the results of calculating the ratios of the areas for cycles when we split sunspot number by hemisphere. We see better results (on average) here than in Table 2.1, with an average ratio of 85.9 %, indicating a strong correlation between the area enclosed by each cycle. Additionally, the final column shows the result of the integration ratio when we take the sum of absolute helicity flux from both hemispheres, giving results stronger than the aforementioned average.

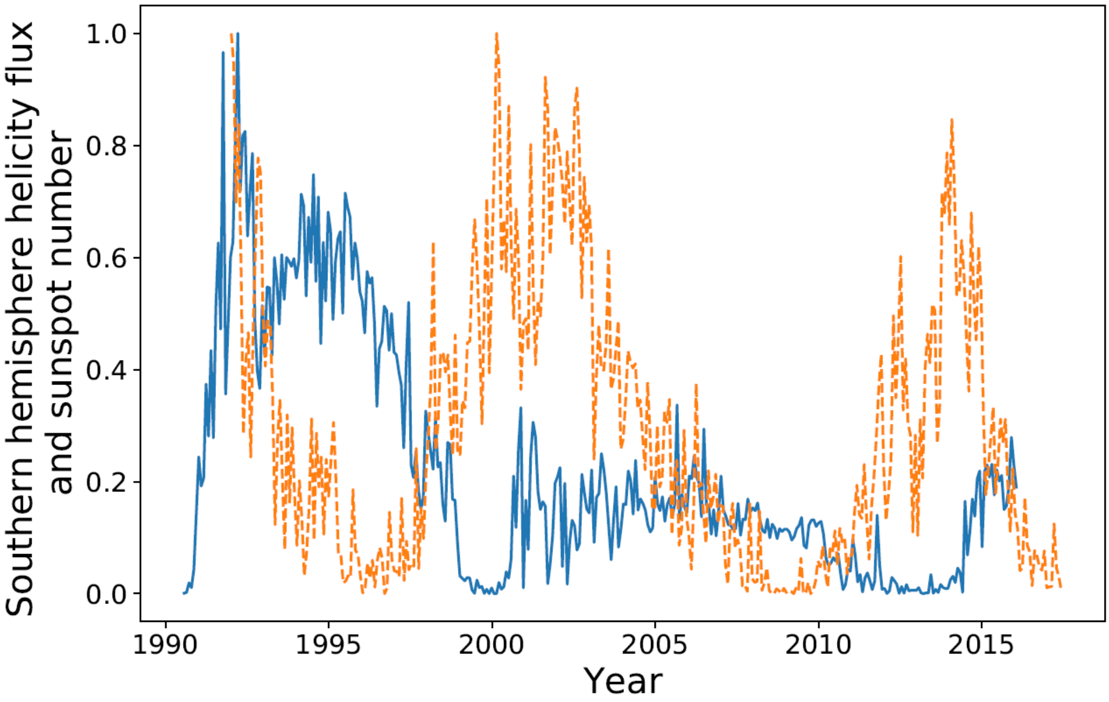

Fig. 2.10 Southern hemisphere helicity flow (blue) and southern sunspot number (dashed orange).

The value of the integration ratio for the second pair of peaks associated with the southern hemisphere isn't improved by taking the square root of helicity flux as described in Section 2.4. In this case, we find a ratio of 47.5%. The corresponding plot is given in Figure 2.11. Indeed, we find that every integration ratio decreases for a square–rooted helicity flux. There is some improvement with the agreement between the southern hemisphere's second cycle peaks, but this improvement is not strong as in Figure 2.8.

Performing our correlation maximisation procedure for the first pair of peaks for each hemisphere gives $P = 0.76$ with a lag of 77 CR in the North, and $P = 0.72$ and a 88 CR lag in the South. We encounter a problem when attempting to map the second helicity cycle onto its sunspot counterpart, as the shifted helicity has a length exceeding the sunspot data range. Correlating the minima gave a lag of 94 CR for the northern hemisphere and 98 for the southern. This fits in with our pattern of varying lag time. The two values of P obtained again indicate strong positive correlation between the cycles.

In Figure 2.12 and Table 2.4 we also make comparisons with the predictively capabilities of the polar field, defined as the absolute value of the average radial field in the $0 \leq \theta \leq 15$ range for the northern pole, and similarly for the south. Visually, the polar field is less well correlated with the sunspot number than helicity flux, and we see almost consistently lower integration ratios. The large integration ratio for the second peak in the northern hemisphere is a relative anomaly. However, this unusually high value is still lower than that offered by magnetic helicity flux.

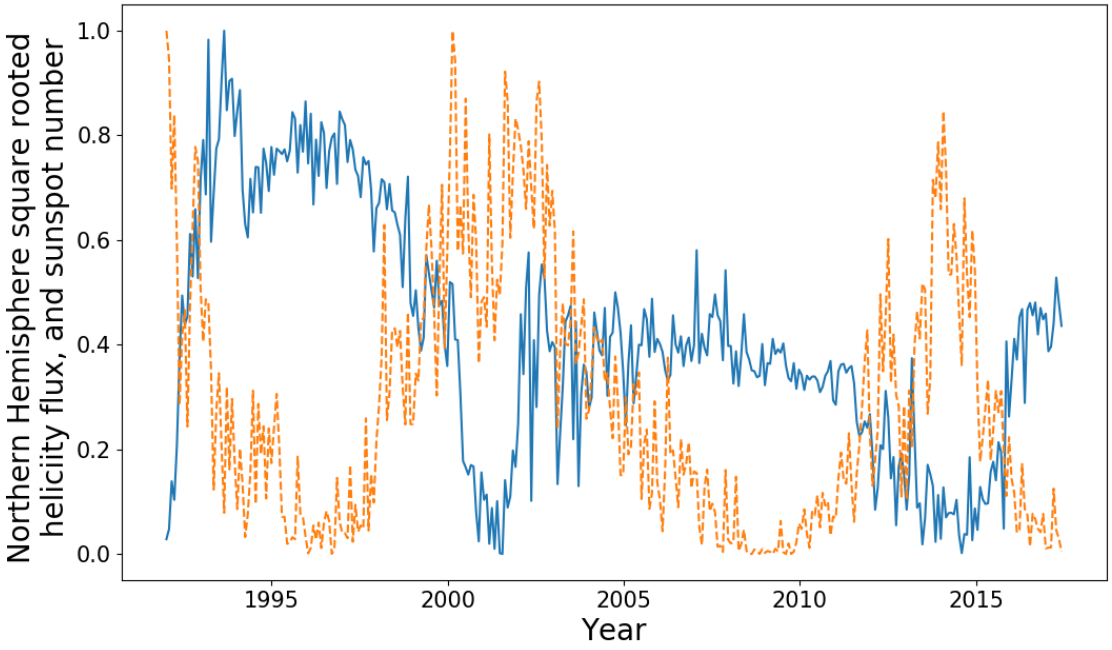

Fig. 2.11 Southern hemisphere square rooted helicity flow (blue) and southern sunspot number (dashed orange).

Peak Pair	Integration Ratio (North)	Integration Ratio (South)
2	54.8 %	90.4 %
3	41.1 %	55 %

Table 2.4 Ratios of the values of integrated polar field and sunspot number separated by hemisphere.

2.5.1 Summation of hemispheres

In Table 2.3, we saw that when using a summation over the two hemispheres, we obtain slightly improved integration ratios. Recall that a summation over hemispheres is, for helicity flux, an absolute sum. Here we perform this same summation over the north and south, inclusive of the first cycle. Figure 2.13 gives the result of normalising the summation of the helicity fluxes and polar fields within both hemispheres. We obtain correlation values of $P = 0.86$ and $P = 0.83$ for the helicity flux cycles (when compared to sunspots cycles), and $P = 0.85$ and $P = 0.80$ for the polar fields, which is approximately equivalent to the result obtained when observing the northern hemisphere only. The results of cycle integration are given in Table 2.5. Polar field is seen to occasionally outperform helicity flux as a precursive quantity only in terms of amplitude, and then only if we do not split sunspot number by hemisphere.

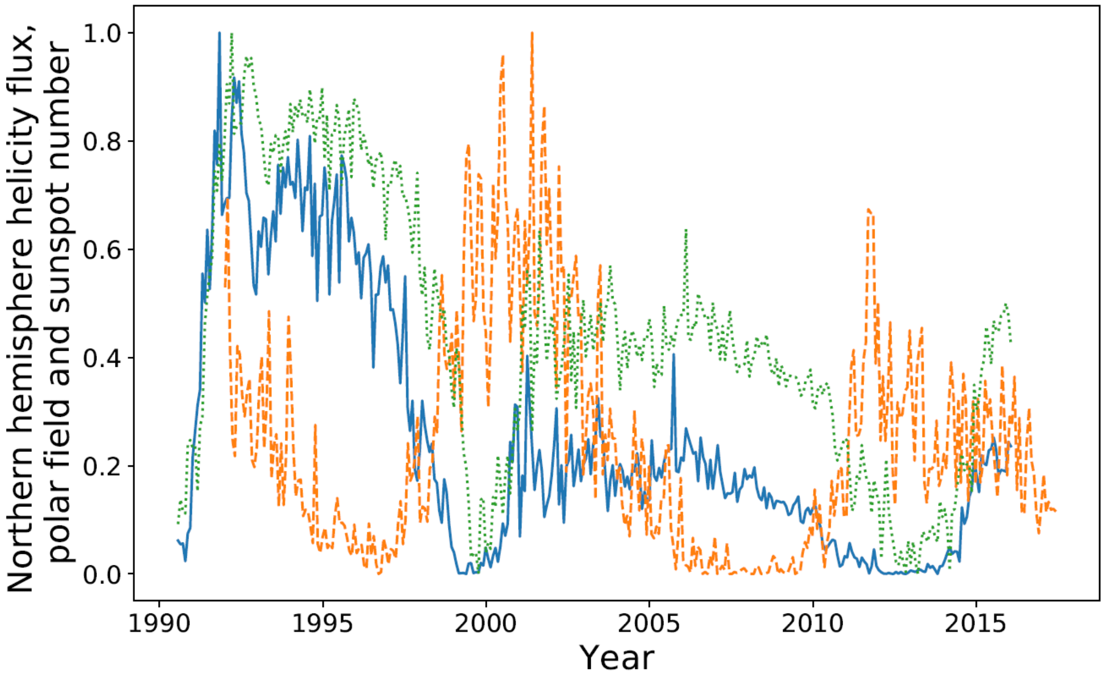

Fig. 2.12 Northern hemisphere: helicity flux (blue), sunspot number (orange dashed), and polar field (green dotted).

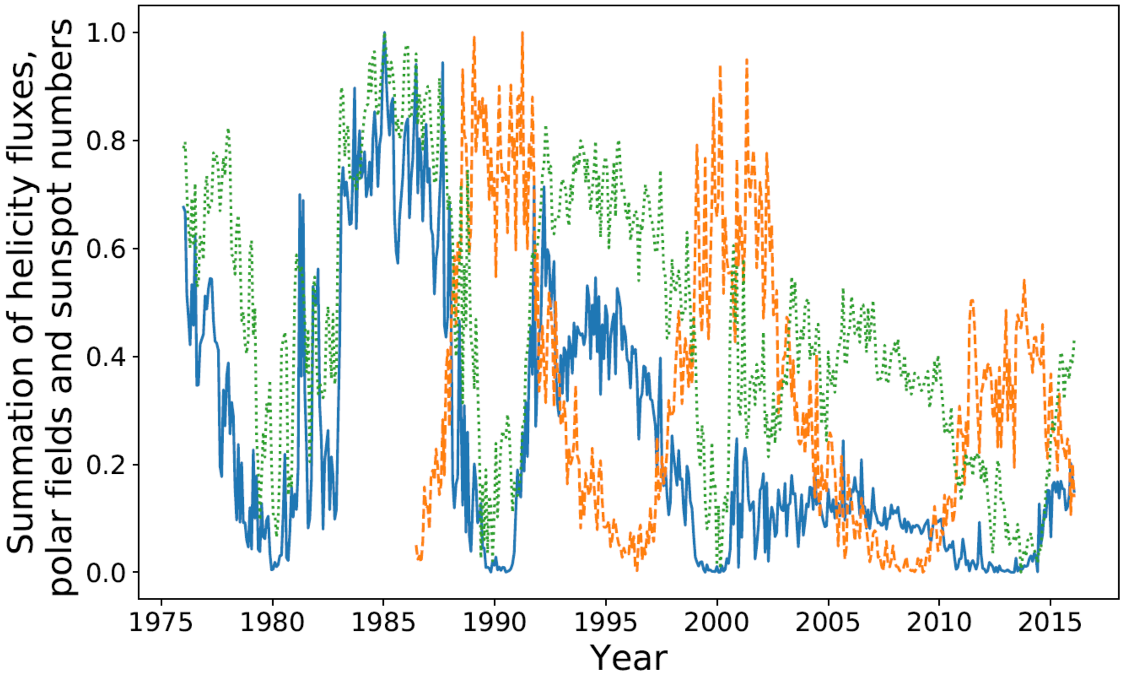

Fig. 2.13 Summation of hemispheres: helicity flux (blue), polar field (green dotted), and sunspot number (orange dashed).

2.5.2 Sunspot area

The limited extent of the hemispherical sunspot number data can be partially overcome with publicly available hemispherical sunspot area, which is recorded dating back to

Peak Pair	Helicity Integration Ratio	Polar Field Integration Ratio
1	90.0 %	67.9 %
2	75.4 %	72.3 %
3	58.4 %	45.2 %

Table 2.5 Integrated helicity flux and sunspot number with summation over hemispheres.

1874, available from NASA (solarscience.msfc.nasa.gov/greenwch.shtml). In Figure 2.14, we plot helicity flux against sunspot area for the northern hemisphere, from 1976 onwards. Sunspot-area data is highly noisy, and has thus been smoothed and compared to the smoothed helicity flux. The first pair of cycles, for which we could not obtain hemispherical sunspot number, gives an integration ratio of 88.8 %. The visual correlations are approximately equivalent to that of Figure 2.12, except for a slight amplitude increase in the final sunspot cycle (although this could be an artefact of the smoothing process).

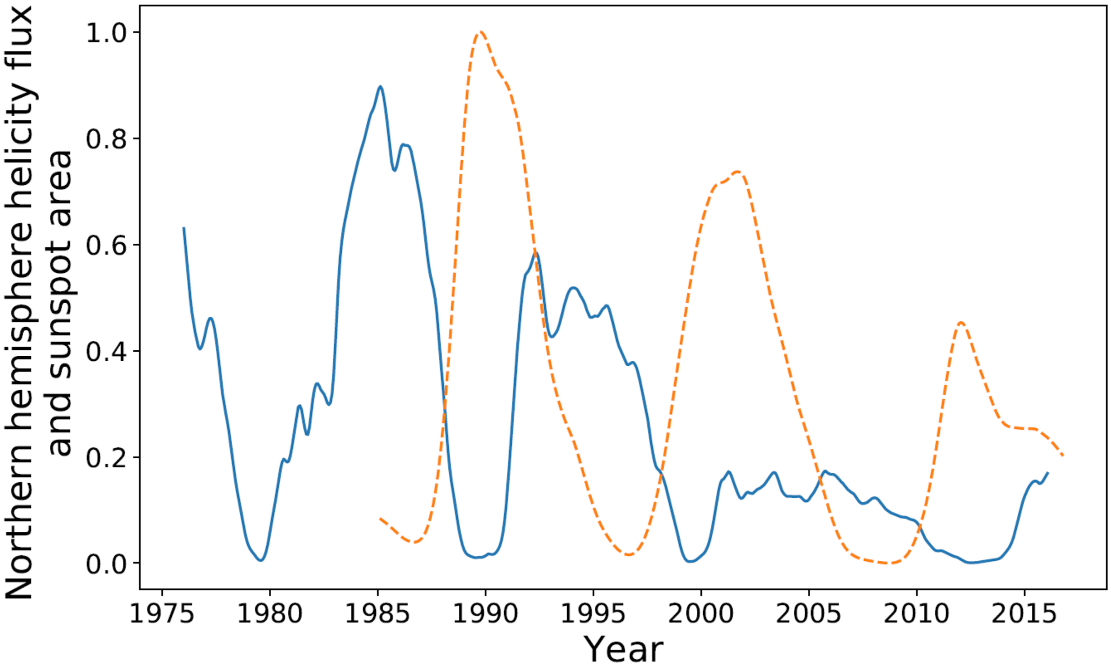

Fig. 2.14 Northern hemisphere: helicity flux (blue) and sunspot area (dashed orange).

2.6 Interpolated Sunspot Data

Temmer et al. (2006) have generated a catalogue of sunspot data, split by hemisphere, for the years 1945 – 2004. To obtain this result, the authors analysed daily sunspot drawings from two observatories, Kanzelhohe Solar Observatory (KSO) and Skalnate Pleso Observatory (SPO). The drawings from the SPO were analysed from 1945 – 1988, at which point they they change their source to the Stara Lesna Observatory. Drawings from KSO were analysed from 1952 onwards, due to fact that additional details on the drawings before this point made sunspot number calculation difficult. They found that the coverage of the observatories is 58% and 72% for the SPO and KSO respectively, giving an overall coverage of 84%. A simple averaging procedure was used to combine the results of the two observatories.

To ensure that their reconstruction is in agreement with the SIDC (international sunspot number) for that day, they take the normalised fraction

$$n'_{int} = \frac{n_{int}}{n_{int} + s_{int}}, \tag{2.18}$$

where n_{int} is the northern hemispherical sunspot number calculated according to their regime (and similarly for the south). Their final value is then given by

$$S_n = n'_{int} S_{SIDC}, \tag{2.19}$$

for the sunspot number over the whole disc according to the SIDC, and similarly for the southern hemisphere.

Hemispherical data being calculated on a daily cadence allows us to determine the means over a Carrington rotation, as is done throughout this chapter. Normalising this series gives the data set shown in Figure 2.15, which we compare directly with the observed WDC data as an indication of accuracy, both taken from the Northern hemisphere. We choose to apply this data only to our initial helicity cycle, given that this is the only cycle for which we do not have already existing hemispherical sunspot data. The normalisation

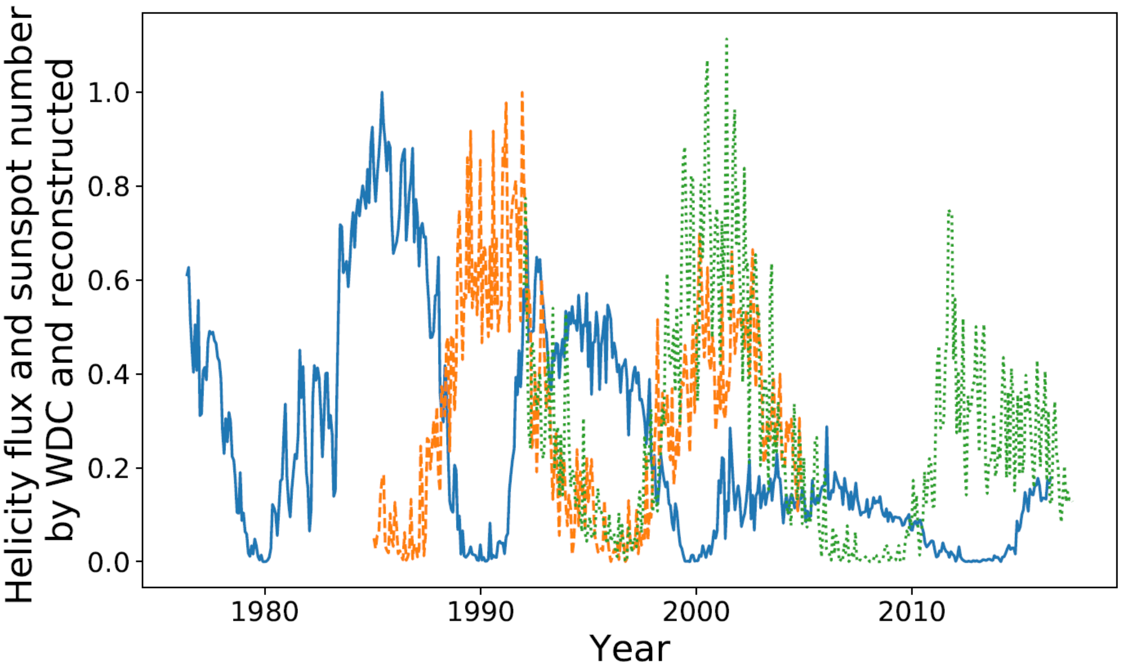

Fig. 2.15 Helicity flow (blue), WDC sunspot number (dotted green), and reconstructed sunspot number (dashed orange) in the Northern hemisphere.

procedure for the hemispherical sunspot data would thus be centred around the cycle encompassing 1985 – 1998.

Calculating the integration ratios for the North gives a value of 74 % for the North and 82 % for the South. These values have a median of 78 %, which is considerably lower than that obtained when one uses sunspot number over the entire solar disk (90 %). This could be due to the reconstruction, given the improvements observed in the ratios when using the WDC data (especially in the case of the final cycle).

2.7 Sunspots Predicting Helicity Flow

In order to assert statistically that it is indeed helicity predicting the behaviour of the sunspot cycle, and not the converse, we must test the strength of said converse. Therefore, in this section we look at the strength of the theory that sunspot number predicts helicity flow. We note that by including an additional sunspot cycle, the normalisation of the sunspot number data set is changed slightly.

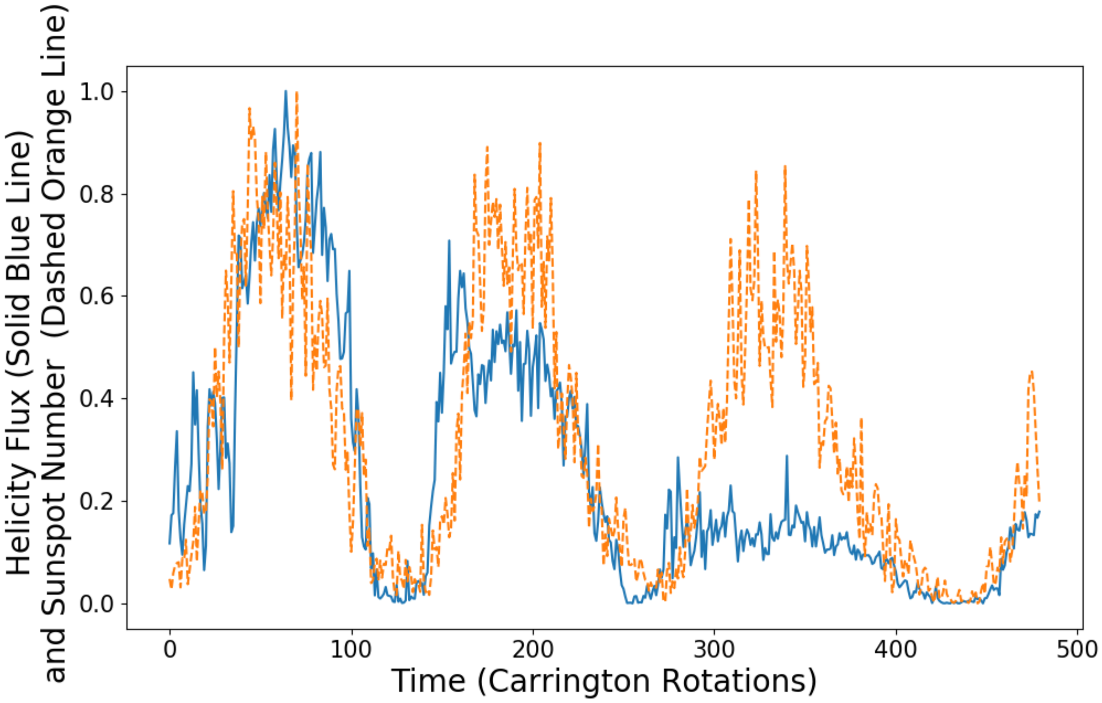

Fig. 2.16 Northern hemisphere helicity flow (solid blue), and sunspot number (dashed orange) shifted forward by approximately 3.33 years.

Figure 2.16 shows sunspot number on the same axes as helicity flow, where sunspot number has been shifted forwards by approximately 4.2 years. This value was chosen using the same process of correlation maximisation described in the previous section.

We notice that the minima in particular are very well matched, as opposed to the changing phase shift of the helicity flux → sunspot number results. In particular, the minima of the final pair of peaks, where we saw an elongated helicity cycle, are well correlated.

We see very weak correlation for the final pair of peaks in terms of amplitude. This weakness is quantified in Table 2.6, where we have performed the same procedure as described for Table 2.1. The ratio is worse for the first pair of peaks ($-4\,\%$), slightly improved for the second ($+6\,\%$), and drastically worse for the final pair ($-29\,\%$). We also find that, excluding the final pair of peaks, a value of $P = 0.804$ is achieved.

Peak Pair	Helicity Data Integrated	Sunspot Number Integrated	Ratio of Integrations
1	59.5 CR	53.50 CR	90.0 %
2	42.39 CR	48.90 CR	87.2 %
3	17.5 CR	46.79 CR	37.4 %

Table 2.6 Integrated helicity flux and sunspot number for the case where sunspot number predicts helicity flux.

One possible explanation for these results is that cycle influence works not only in one direction, but both. Indeed, our results indicate that the cycle amplitude/strength (where strength is indicated by the integrated area) of a sunspot cycle being dictated by helicity flow, whilst the length of a helicity flux cycle is strongly correlated with that of the previous activity cycle.

2.8 Comparisons with Polar Field

The strength of the polar field during solar minima has often been used to predict the strength of the following solar maxima (Jiang et al., 2007). The dipole moment has also been used (such as in the predictions made in Choudhuri et al. (2007)), back to 1978 (Schatten et al., 1978). However, given that the polar field is more directly related to the Omega effect being described by our helicity flux, as well as a good measure of the dipole moment, we choose to compare the effectiveness of magnetic helicity predictions with this benchmark. Helicity flux, as stated earlier, is a arguably more rigorous measure of the Omega effect than polar field, making it likely to be more strongly correlated with sunspot number.

In Figure 2.17, we plot magnetic helicity flux through the northern hemisphere compared with total sunspot number and the averaged north pole magnetic-field strength. We continue to define the northern pole as the region $0 \leq \theta \leq 15°$, for which we take an absolute value of the average field. The southern pole is defined similarly. Visually, the polar field appears to be a slightly weaker precursor for the strength of the solar minima, except in the case of the final pair of peaks, where it performs much better than magnetic helicity.

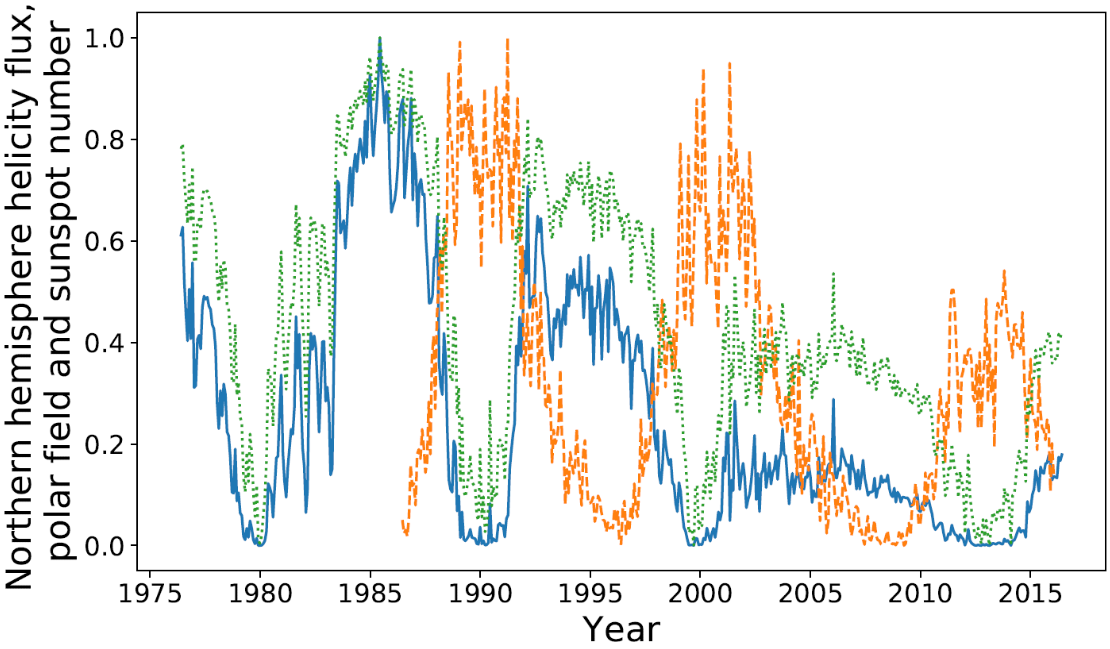

Fig. 2.17 Normalised magnetic helicity flux (blue) and polar field (dotted green) for the northern hemisphere compared with normalised sunspot number (dashed orange).

Of note is the amplitude differences between the polar field and magnetic helicity. Given that the expression used to calculate magnetic helicity flux is directly dependent upon the poloidal field, we would expect a closer relation in amplitude. These differences could be due to the distribution of flux being more concentrated at mid to low latitudes.

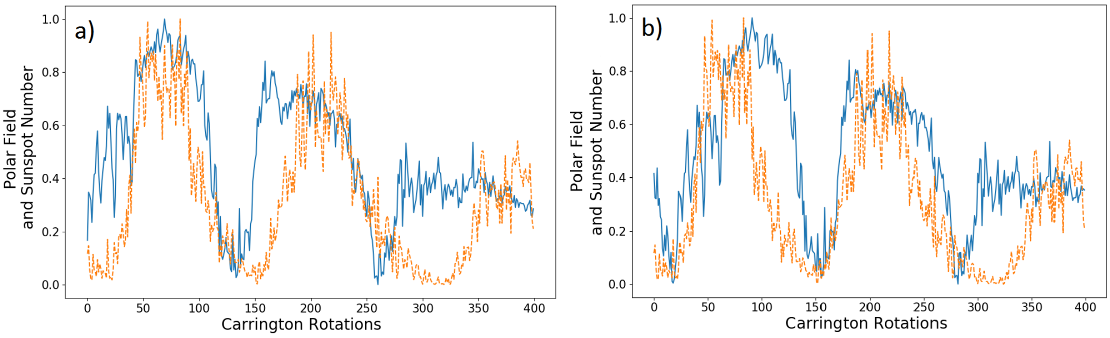

Fig. 2.18 Normalised northern polar field (blue) with a phase shift of 60 CR (a) and 92 CR (b) plotted alongside sunspot number (dashed orange).

In Figure 2.18, we plot polar field strength against sunspot number with optimised phase shifts. Here, we found that correlating the first pair of peaks required a phase shift of 60 Carrington rotations, the second peaks had a shift of 92 rotations. These shifts corresponded to correlation coefficients of 0.824 and 0.795 respectively. For the first pair of peaks, this is a slight decrease when compared to helicity ($\Delta P = -0.06$), and a negligible change in the second case ($\Delta P = 0.045$).

Peak Pair	Polar Field Integration Ratio	Helicity Flux Integration Ratio
1	68 %	94 %
2	77 %	81 %
3	52 %	66 %

Table 2.7 Integrated polar field and helicity flux ratios with integrated sunspot number.

Visually, the helicity-flux cycles appear to have a better fit than polar field (with the exception of the third pair of cycles). It is however difficult to quantify this. We perform the same integration procedure as performed on magnetic helicity flux in tables 2.1 and 2.6. Table 2.7 shows the results of the integration process. The results are more consistent than the aforementioned tables, with the ratio fluctuating close to 65 %. At the time of writing, the final sunspot cycle was incomplete, meaning that its integrated value is likely to increase.

The ratios are consistently below those of Table 2.1, which have been included in the rightmost column. This indicates a larger disparity between the strength and structure of the polar-field cycles, when compared to that of sunspots. The structural comments made earlier continue to apply, which is expected, given the presence of B_n in the expression for magnetic helicity flux.

2.9 Reconstructed Magnetic Field Harmonics

There have been attempts to recreate measurements of the large-scale solar magnetic field using a variety of proxies. One example of this is described by Makarov and Tlatov (2000), who used Hα maps to calculate a spherical-harmonic decomposition of said field, up to degree $l = 9$ (the same as that used by Wilcox). They have reconstructed the largest scale magnetic fields using H_α and Ca_{II} charts from Kodaikanal observatory, for which they assign a value radial field of ±1G to the magnetic field distribution according to the sign of the leading and trailing sunspot polarities expected for a given solar cycle. This distribution then undergoes the same procedure as described in Section 2.2. The assumed magnitude of $|B_r| = 1G$ is rendered unimportant by the normalisation procedure employed here. The authors have generously provided their decomposition data over the period (in years) 1958 – 2015, covering Carrington rotations 1400 – 2161. This period contains two additional solar cycles that are not available in the Wilcox data. We must, however, take care when using reconstruction data due to possible inaccuracies, and we therefore suggest that any conclusions drawn from this work are taken as secondary to that in the previous sections.

Markarov and Tlatov have also provided data covering Rotations 800 – 1400 (1913 – 1958), although they have made it clear this second, earlier data set is more likely to be inaccurate than the more recent reconstructions. We therefore split our analysis into two sections, each dealing with one of the two periods.

2.9.1 1958 – 2015

In Figure 2.19, we plot helicity flux through the northern hemisphere on the same axes as sunspot number, for the reconstructed period 1958–2015. Both data sets continue to have a cadence of one Carrington rotation. The helicity-flux data calculated from the reconstructed spherical harmonics are noisier than that provided by the Wilcox Observatory, likely due to their nature as an indirect measurement. Applying the KS as described earlier gives the data sets shown in Figure 2.20. The cycles appear much more correlated when smoothed, particularly in terms of their amplitude. Maximising the correlation of the two data sets over their entire range gave $P = 0.72$ with a phase shift of 84 Carrington rotations for the smoothed data, and $P = 0.56$ over a 87 Carrington-rotation shift for the unprocessed data (again over the whole data set). The difference in the phase shift is likely due to the noise, not any underlying change in structure.

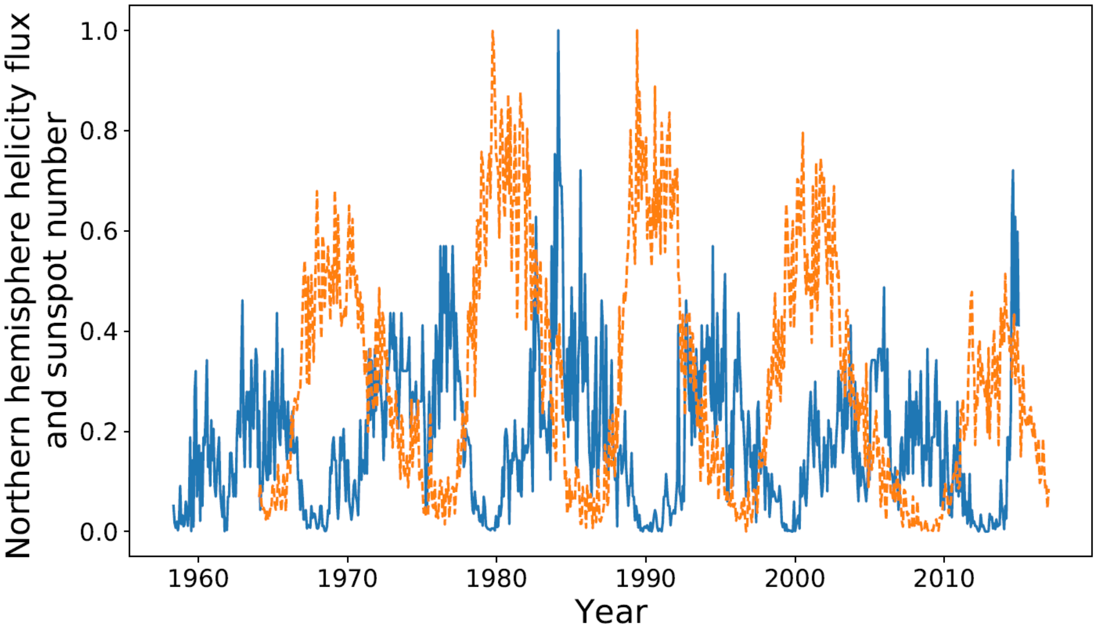

Fig. 2.19 Northern hemisphere helicity flow (blue) and sunspot number (dashed orange) for the reconstructed 1958–2015 period.

Maximising the correlation between each pair of peaks individually gives a small range of phase shifts: $85, 84, 81, 84$, and 87 Carrington rotations, respectively. This corresponds to a range of 0.44 years. Given the small range, we choose to use a mean of these values: 84 CR. The result of shifting our entire helicity flux data set forwards by this amount is shown in Figure 2.21. We see a fairly strong correlation in terms of structure, albeit weaker than that of the previous sections. Notably, the final cycle is quite well correlated, which

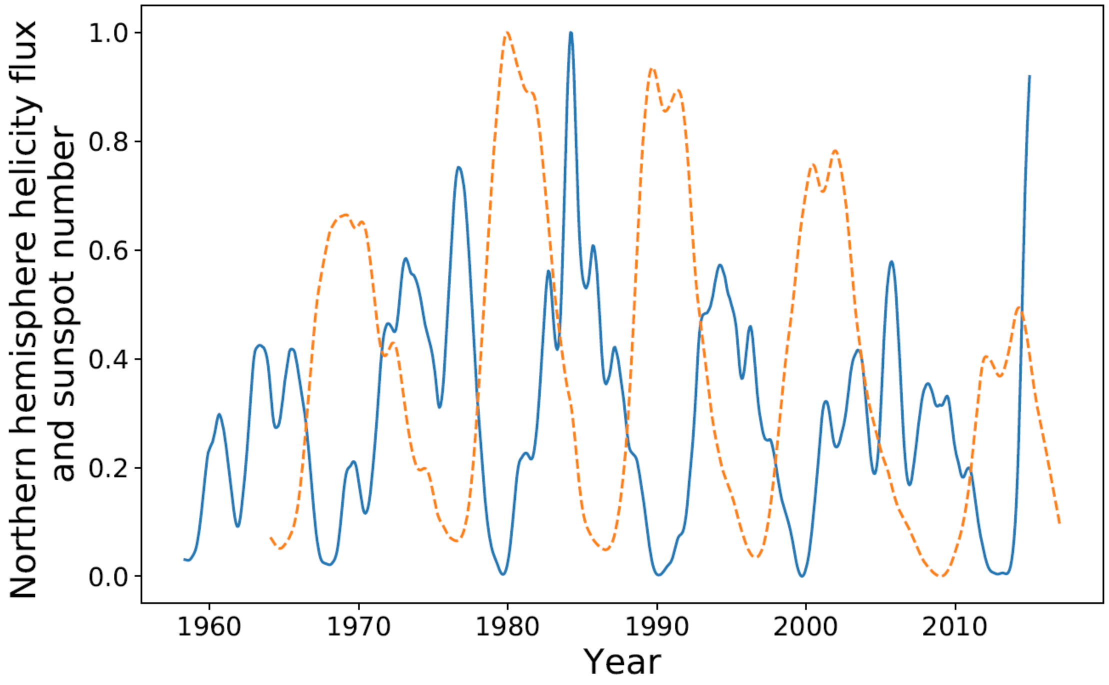

Fig. 2.20 Smoothed, reconstructed–harmonic northern helicity flux (blue) and smoothed sunspot number (dashed orange)

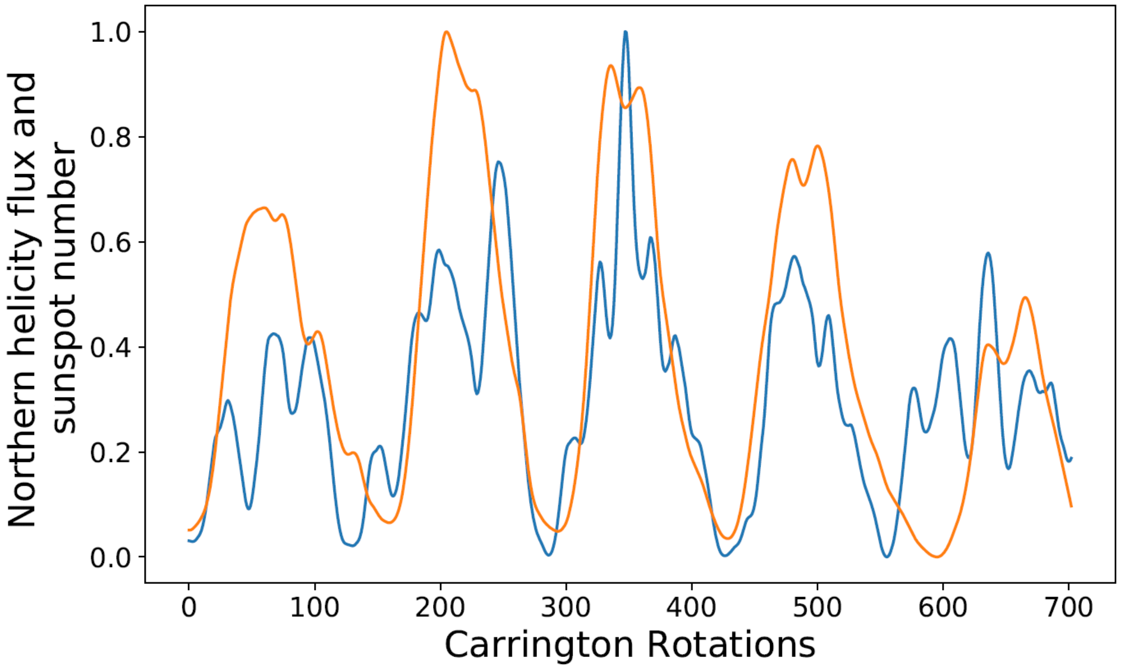

Fig. 2.21 Shifted helicity flux (blue) by 84 CR, compared with sunspot number (orange) for the reconstructed 1958–2015 period.

is where the Wilcox Data performed notably less well. This is discussed further in the coming sections.

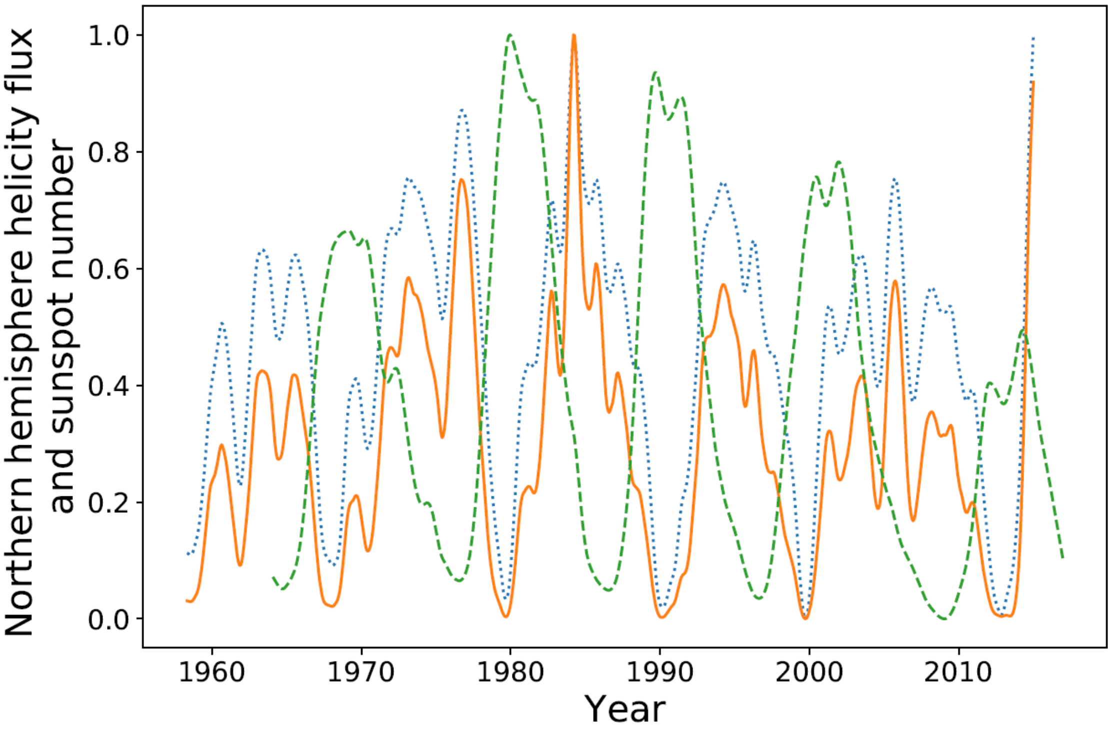

Fig. 2.22 Helicity flux (orange) and polar field (blue) in the northern hemisphere compared with sunspot number (green) for the reconstructed 1958–2015 period.

Peak Pair	Helicity Flux Ratio (Smooth)	Polar Field Ratio (Smooth)
1	39.60 % (51.89 %)	96.20 % (90.20 %)
2	59.57 % (80.69 %)	97.69 % (83.40 %)
3	63.44 % (83.57 %)	81.98 % (83.66 %)
4	46.30 % (60.23 %)	99.40 % (94.86 %)

Table 2.8 Integrated polar field and helicity flux integration ratios for the reconstructed 1958–2015 period. Values taken from smoothed data sets are shown in brackets.

Polar Field

In Figure 2.22, we plot polar field, helicity flux and sunspot number, all of which have been smoothed. In Table 2.8, we perform the same integration procedure as described during earlier analyses. The integration procedure has been performed on the unprocessed data. For the reconstructed data, Figure 2.22 indicates that the polar field instead is an (albeit slightly) superior precursor to the following solar cycle, except in the case of the final cycle. This is contrary to the results of the previous section, which used more direct measurement. This is reflected in the table of integration ratios, where we see helicity performing much more poorly than polar field. However, note that the helicity flux fluctuated quite chaotically on short time scales, which has skewed our integration measure. Errors when integrating over a helicity cycle were seen to be as high as 13 %.

Peak Pair	Helicity Flux (Smooth)	Sunspot Number (Smooth)	Integration Ratio (Smooth)
1	18.32 (29.99)	41.90 (59.17)	43.7% (50.6%)
2	32.80 (54.21)	42.29 (61.66)	77.6% (88.0%)
3	30.91 (51.29)	38.10 (54.53)	81.1% (94.1%)
4	21.55 (35.40)	31.56 (45.28)	68.3% (78.2%)

Table 2.9 Northern integrated sunspot number and helicity flux integration ratios using hemispherical splitting, for the reconstructed 1958–2015 period.

Polar field is taken as an average over a fifteen-degree latitude cap, and would therefore be less subject to fast fluctuations in space.

The advantages of smoothing are shown in the bracketed values, making the most notable difference for the helicity-flux ratio. For the two central cycles, we note that smoothing brings the ratios of the polar field and helicity flux to almost equal values.

Hemispherical Sunspot Number

In this subsection we compare the reconstructed helicity flux with the reconstructed hemispherical sunspot number. We note that we are comparing two reconstructed data sets, meaning that any inaccuracies are likely to be compounded.

Table 2.9 shows the integration ratios for these helicity and sunspots data series in the northern hemisphere. These have slight improvements for the smoothed data sets, and noticeable improvements when we use the “raw" data. The median of the helicity-integration ratios when we took sunspot number over the whole disk was 69.1 %, whilst when we split the data by hemisphere we get a mean of 77 %: an improvement of 10 %.

Comparisons with Wilcox Data

In this subsection, we compare the outputs of the harmonics in the reconstructed data with the outputs produced by the Wilcox data sets. This will give a measure of the accuracy of the reconstructed data, indicating how firmly we can make conclusions from the results it provides.

In Figure 2.23, we plot helicity flux through the northern hemisphere using both Wilcox Data and the reconstructed data. The relationship between the two sets of data for was almost identical in the southern hemisphere, and we thus choose to analyse only the north.

There is a strong correlation between the two sets of helicity flux for Cycle 23, but differences remain. Notable differences include the amplitude of the final observed cycle, and the smoothness of the cycles, particularly notable during 1980 – 1990. These differences are mostly removed using the KS process described in earlier sections. These differences in structure are what likely caused the integration procedure of the previous section to be skewed, and they are strongest during the aforementioned cycle.

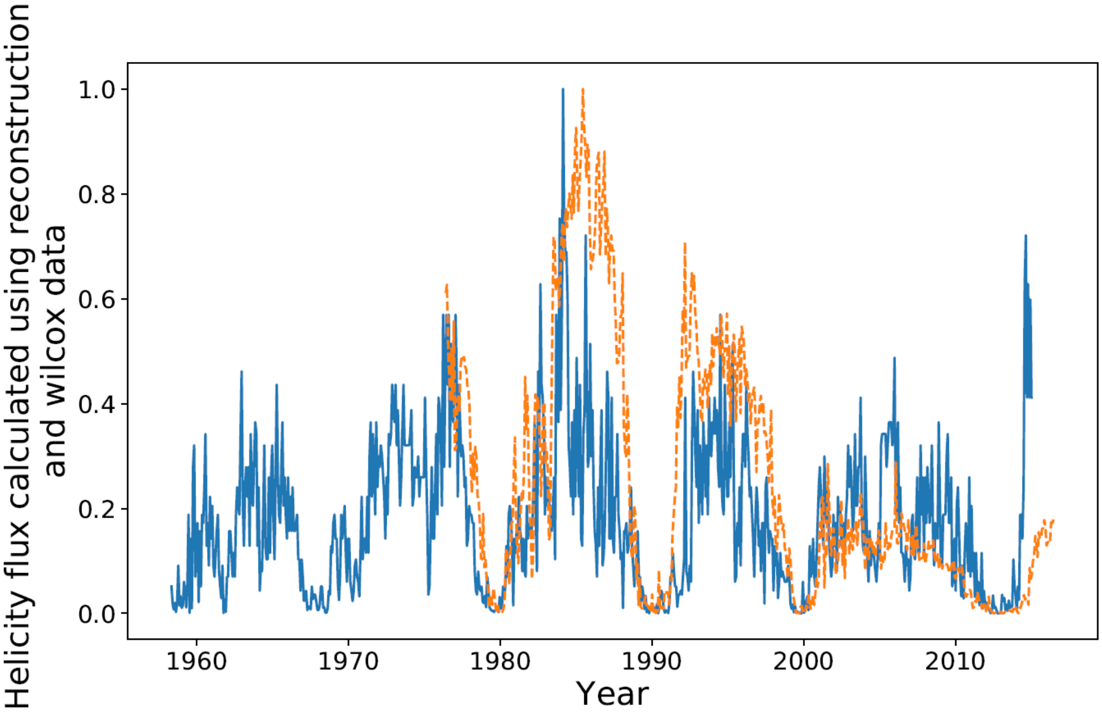

Fig. 2.23 Helicity flux through the Northern Hemisphere calculated using Wilcox (dashed orange) and reconstructed spherical harmonics (blue).

Cycles 22 and 24 have the strongest dissimilarities between their respective series. The length of the cycles are the same for the two sets, but the amplitude is notably (approximately two times) larger in the reconstructed data. The amplitude differences

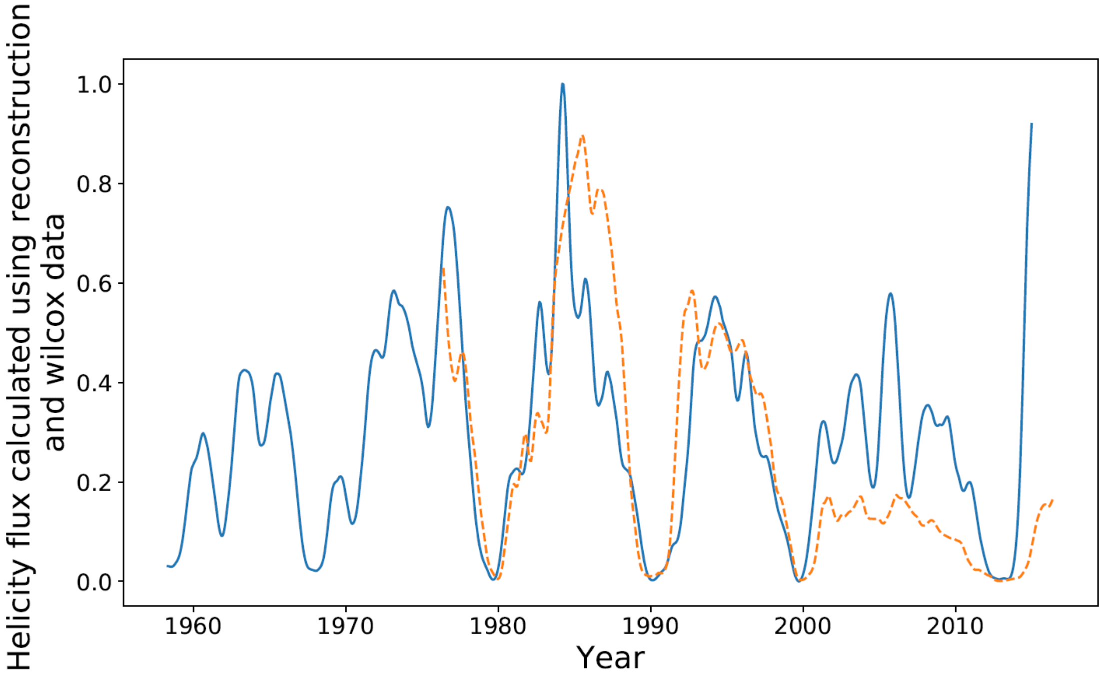

Fig. 2.24 Helicity flux through the Northern Hemisphere calculated using Wilcox (dashed orange) and reconstructed spherical harmonics (blue), all smoothed.

could be due to an issue with the Hα maps used to determine the magnetic harmonics. In the case of Cycle 24, there could also be some underlying physical mechanism linked to the elongated solar minima experienced during this period that has affected the reconstruction. More likely is that the reconstruction technique is simply not as accurate as real-time data taken by the Wilcox Observatory, and should thus be considered as less accurate.

Figure 2.24 gives a comparison of the two smoothed data sets. Here, we see that the structures are quite similar, but we continue to observe the amplitude differences for the final cycle.

The reconstructed data also has a different relationship with its polar field than that of the Wilcox Data. For Wilcox, we see an increasing cycle-amplitude difference between the two quantities with decreasing cycle strength. In the reconstructed data, however, the difference between helicity flux and polar field is fairly constant from cycle to cycle. The exact reasons for the differences described are not known, but they are worthy of further investigation, being of particular importance for the helicity cycles of 1980 – 1990 and 2000 – 2012.

2.9.2 1913 – 2015

In figures 2.25 and 2.26 we plot reconstructed helicity flux and polar field compared with sunspot number from 1913 onwards. Although there is a good correlation between helicity and sunspot number for dates preceding 1958, we note that the polar field of Figure 2.26 exhibits conjoined cycles, indicating inaccuracies in their data processing (as was

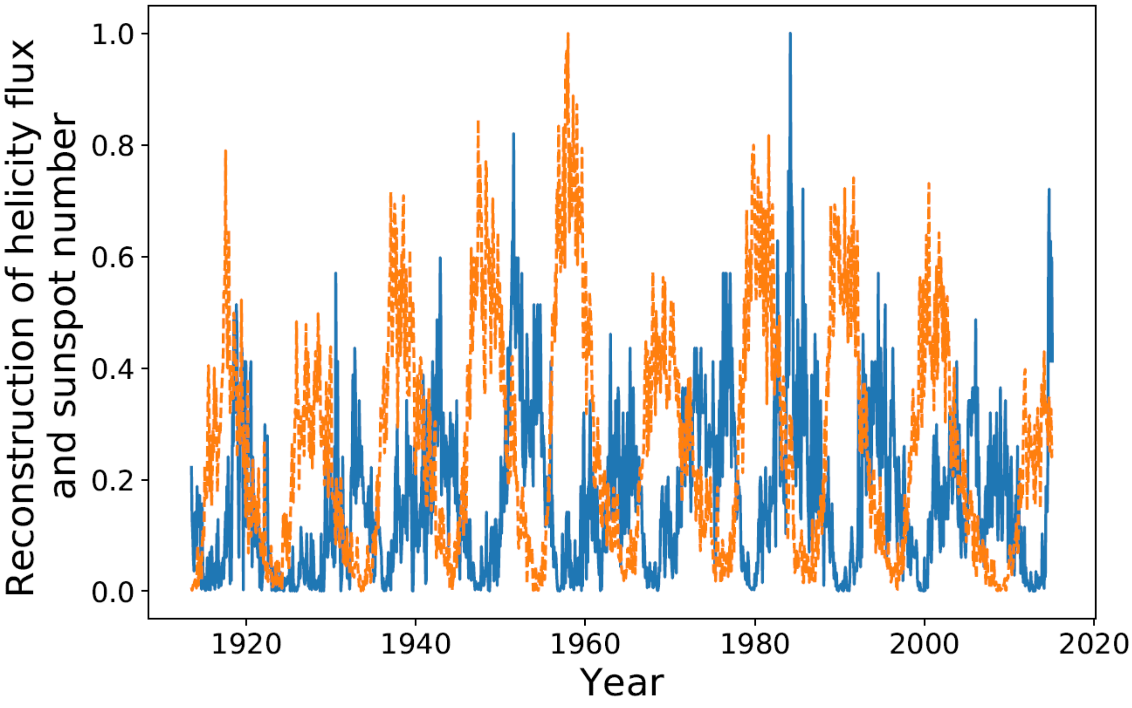

Fig. 2.25 Helicity flux (blue) through the northern hemisphere and sunspot number (dashed orange) for the reconstructed 1913–2015 period.

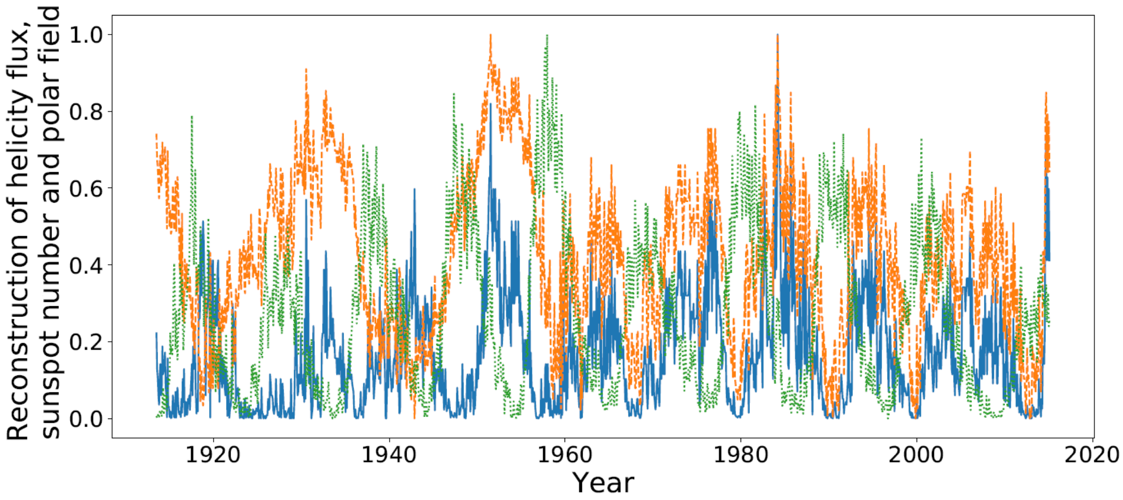

Fig. 2.26 Helicity flux (blue), polar field (dashed orange) in the northern hemisphere, and sunspot number (dotted green) for the reconstructed 1913–2015 period.

indicated when the data were provided). We therefore do not perform further data analysis on this period. We note only that there continues to be a fairly noticeable visual correlation between the helicity flux and sunspot number.

2.10 Predicting Solar Cycle 25

In this section we make a short prediction of the upcoming solar cycle 25. Figure 2.27 gives the northern hemispherical helicity flow, and total sunspot number, up to 2018 (making it more recent than other data used within this chapter). We are unfortunately not at a point where we can be sure that the helicity flux of associated with the current solar cycle has reached its peak, making the accuracy of any prediction lower than we would like.

Over the course of this article we have demonstrated statistically that the helicity flux cycle is a good predictor of the following activity cycle. With this in mind, based on the assumption that Cycle 25's preceding helicity flux cycle has reached its maxima, we predict that the amplitude of Cycle 25 will be only slightly higher than that of Cycle 24.

Using our three existing cycles, we estimate Cycle 25 will have an amplitude of 117 (given as the max value of sunspots per Carrington rotation over a cycle), 50% that of Cycle 22, calculated by performing regression analysis. This was calculated using regression analysis on peak–to–peak amplitude comparison of the data shown in Figure 2.27 (between sunspot number and helicity flux). The result is quite similar to that of Cycle 24's amplitude of 104. With only three data points, the standard statistical error was found to be quite un-realistic, and we therefore do not include it here.

Previous sections have also indicated that helicity flux as a prediction mechanism is best when we compare the areas under curves. At the time of writing, the current helicity

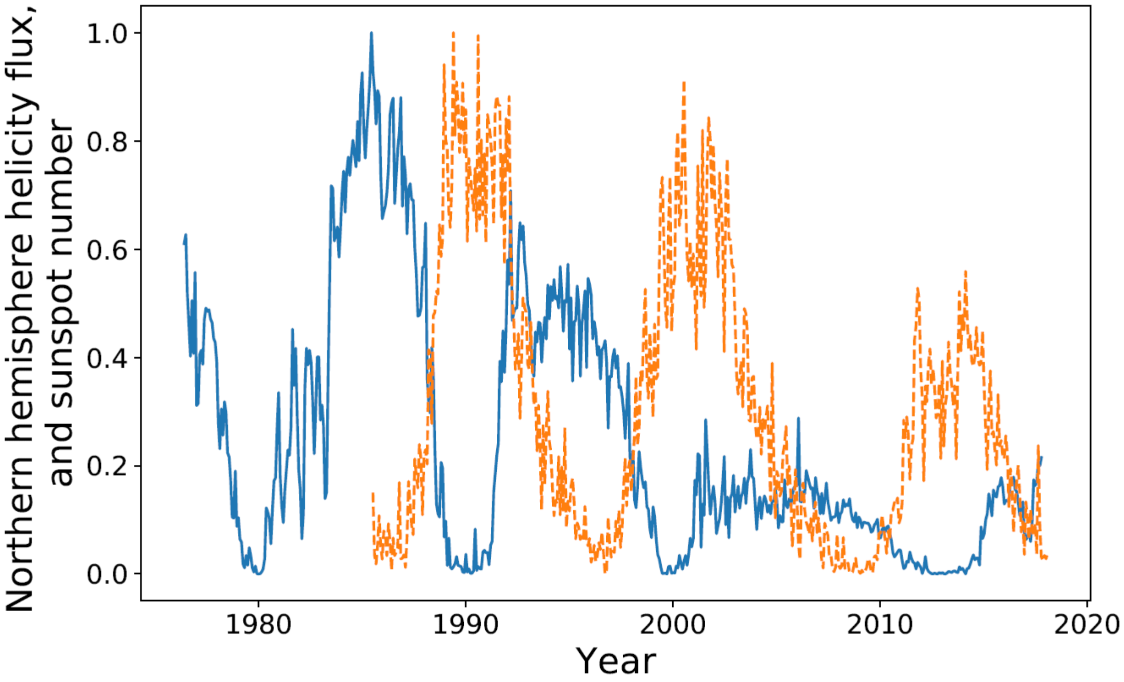

Fig. 2.27 Helicity flux (blue) through the northern hemisphere against sunspot number (dashed orange).

flux cycle has an area of 5.63 CR. If we again assume that the helicity flux cycle has reached its halfway point, this would give us a total area of ~ 11.26 CR.

Performing regression analysis on the areas, as an indication of the overall strength of the cycle (as in Table 2.1) gives a predicted normalised area of 24.48 CR for Cycle 25. This is again approximately equivalent to the area of Cycle 24 (26.50 CR). Errors have once again been neglected. Gopalswamy et al. (2018) similarly found that Cycle 25 will be akin to Cycle 24.

2.11 Summary and Conclusion

We have completed a fairly comprehensive statistical analysis of the hypothesis that helicity flux during solar minima can be used to predict the strength of the following solar maxima. We found a strong indication of causation between the two sets of data. This was most noticeable when we performed our analysis on a hemispherical basis, where we saw ratios consistently outperforming those calculated over the entire solar disc. In some cases, this ratio was more than doubled (41.1 % to 93.2 %) when using helicity flux as opposed to polar field. Notably, the suitability of the polar field as a precursor seemed to decrease when we looked at individual hemispheres. This result indicates that future attempts to predict the strength of solar cycles should use a hemispherical model. In particular, the relationship between helicity flux and sunspot number appears stronger than that offered by the polar field, which is currently the most popular precursor indicator of solar activity. The only advantage that we found when using polar field was that it seemed to occasionally excel in terms of more-exact amplitude prediction. However, this only occurred when the analysis was performed over the entire disc, rather than with respect to hemispheres. Helicity flux outperforming polar field indicates that magnetic-field activity in regions beyond the polar cap is important for the progression of the solar dynamo into its next maxima.

In an attempt to strengthen our result, we obtained reconstructed data, but this was found to imply that polar field was the stronger indicator, even if helicity flux still offered a high correlation. However, these data were found to contain large inaccuracies when compared to direct measurements, and were notably chaotic. Some underlying structure of solar cycles appeared to be absent. The reconstruction then, with the necessary amount of trepidation, does also indicate a causal relationship between helicity flux and sunspot number.

In conclusion, we believe that we have demonstrated the statistical link between these two physical quantities, using two different data sets over a period covering approximately fifty years. Additionally, we made a speculative guess as to the amplitude of the forthcoming solar cycle 25, which we believe would have approximately the same (perhaps slightly greater) amplitude and strength as Cycle 24.

In April 2019, after this analysis was performed, the “Solar Cycle 25 Prediction Panel", which is comprised of scientists representing NOAA, NASA, the International Space Environment Services amongst others cross referenced multiple predictive estimates. Based on this collective information, they came to the conclusion that Solar Cycle 25 will have a peak magnitude of sunspot number between 95 to 130 (NOA, 2019), for which our prediction of 117 lies squarely within.

Chapter 3

Hemispheric Injection of Magnetic Helicity by Surface Flux Transport

The research presented in this chapter has been published in the journal Astronomy and Astrophysics, under the title "Hemispheric Injection of Magnetic Helicity by Surface Flux Transport": see Hawkes and Yeates (2019). I was involved in developing the research idea, performed the data analysis, produced the figures and wrote large sections of the article's text. Sections 3.5 and 3.6 were not part of this publication.

3.1 Introduction

In this chapter, we consider the global-scale injection of helicity due to surface flux transport, from large-scale solar rotation and meridional flow, as well as the relatively small-scale from supergranular diffusion. Previously, Berger and Ruzmaikin (2000) estimated that $4 \times 10^{46}\,\mathrm{Mx}^2$ of magnetic helicity were injected into each coronal hemisphere by solar rotation over a 22–year period from 1976 to 1998 (Solar Cycles 21 and 22), using low resolution magnetogram data from Wilcox Solar Observatory. We extended this calculation in Chapter 2 to 2018, where we found that the injected helicity in Solar Cycle 23 was lower than in the previous two cycles. In this chapter, we use surface flux transport modelling to extend this calculation to many solar cycles, and consider magnetic flux distributions with higher spatial resolution, including also the helicity flux from meridional flow and supergranular diffusion.

DeVore (2000) estimated the helicity flux from differential rotation based on an analytical MHD calculation of the shearing of a single bipolar active region. Extrapolation of this calculation to an estimated number of similar regions in a full solar cycle gave a final estimate of $10^{46}\,\mathrm{Mx}^2$ of helicity injected during Solar Cycle 21. However, this approach neglects the contribution from weaker, but of greater spatial extent, high-latitude magnetic fields. In this chapter, the use of a surface flux transport model allows us to consistently include both the injection measured by DeVore (2000) as well as the contribution from large-scale fields that was captured by the approach of Berger and Ruzmaikin (2000).

In the approaches discussed so far, as well as in this chapter, the electric field $\mathbf{E}$ on the solar surface is approximated by imposing an analytical flow and/or diffusion (see Section 3.2). By contrast, LaBonte et al. (2007) and Georgoulis et al. (2009) used correlation tracking in high-cadence magnetograms to estimate the electric field pattern in individual observed active regions, and hence calculate their associated helicity flux. Using magnetograms from SoHO/MDI, the authors have estimated the helicity flux in the 393 largest active regions during Solar Cycle 23. Accounting for unobserved regions and uncertainties in the correlation tracking, they estimate a total helicity flux of $6.6 \times 10^{45}\,\mathrm{Mx}^2$ over Solar Cycle 23. Only about 20% of this flux came from differential rotation. However, it has not been possible to apply this technique outside of active regions due to the high resolution required when taking magnetograms.

Brandenburg and Sandin (2004) and Brandenburg (2009) calculated that the solar dynamo must shed around $10^{46}\mathrm{Mx}^2$ of magnetic helicity per cycle, based on analytical calculation on the catastrophic alpha quenching caused by a build up of small-scale magnetic helicity. From the viewpoint of the heliosphere, Bieber and Rust (1995) estimated a helicity ejection rate of $2 \times 10^{45}\,\mathrm{Mx}^2$ through coronal mass ejections by considering toroidal magnetic flux, while DeVore (2000) gave a higher estimate of $10^{46}\,\mathrm{Mx}^2$ by modelling the magnetic structure of interplanetary magnetic clouds. More recently, Démoulin et al. (2016) extrapolated data from 107 observed magnetic clouds to estimate a total ejection rate of $2.5 \times 10^{46}\,\mathrm{Mx}^2$ over Solar Cycle 23, and a similar value was obtained independently by Lowder and Yeates (2017) through non-potential modelling of flux rope formation and ejection in the low corona.

All of these estimates are broadly consistent, but they are all still approximations. It is a question of ongoing interest to study how much helicity is contributed by different physical processes, and particularly how this varies between solar cycles. In Section 3.2 we describe the two surface flux transport models used in this chapter to estimate the helicity flux, before presenting the results for Solar Cycles 21 to 23 in Section 3.3, and for earlier solar cycles in Section 3.4. We also compare the helicity fluxes calculated in this chapter with helicity fluxes that we calculate from a higher resolution set of Wilcox Solar Observatory co-efficients (used in Chapter 2). We extend some results of DeVore (2000) in Section 3.6, and perform some analytical measures of solar helicity injection in Section 3.7. Finally, we present our conclusions in Section 3.8.

3.2 Methods

The helicity flux through the photosphere is not a directly observable quantity, so instead we estimate $\mathbf{A}_0 \times \mathbf{E} \cdot \hat{\mathbf{n}}$ numerically. In this chapter, we do so using a pair of surface flux transport models as will be outlined in this section. The surface flux transport model (Jiang et al., 2014) evolves the photospheric radial magnetic field, $B_r(R_\odot, \theta, \phi, t)$ following the radial component of the induction equation

$$\frac{\partial B_r}{\partial t} = -\hat{\mathbf{r}} \cdot \nabla \times \mathbf{E} + S(\theta, \phi, t) - D(\theta, \phi, t), \tag{3.1}$$

where $S(\theta, \phi)$ is a source term representing the emergence of new magnetic flux, and $D(\theta, \phi, t)$ is an additional decay term that accounts for the effect of radial (inward) diffusion, that cannot be properly assessed in such a two–dimensional model. The electric field, assuming a purely radial magnetic field, takes the form

$$E_\theta(\theta, \phi, t) = -v_\phi B_r + \frac{\eta}{R_\odot \sin\theta} \frac{\partial B_r}{\partial \phi}, \tag{3.2}$$

$$E_\phi(\theta, \phi, t) = v_\theta B_r - \frac{\eta}{R_\odot} \frac{\partial B_r}{\partial \theta}. \tag{3.3}$$

These represent the evolution of B_r due to both advection by large-scale horizontal flows $\mathbf{v}(\theta)$ and horizontal (turbulent) diffusion due to supergranular convection, with coefficient η. Note that in Chapter 1, turbulent diffusion was referred to as η_t, but we choose here to refer to it as *the* diffusion, η, due to its vastly increased magnitude. We have assumed that the velocity flows are neither time nor longitudinally dependent.

To estimate the helicity flux, we take the electric field (3.2), (3.3) as an approximation of the horizontal electric field on the solar photosphere. We thus neglect any electric field arising from flux emergence ($\mathbf{v} \cdot \hat{\mathbf{n}}$), as well as from localised flows on a smaller length scale (such as those within individual active regions). We also neglect the contribution from the decay term (we justify this in the following subsection).

We also need to calculate $\mathbf{A}_0$ from B_r at each time. This is done by expressing $\mathbf{A}_0 = -\nabla\psi \times \hat{\mathbf{r}}$, where ψ satisfies a two-dimensional Poisson equation

$$B_r = -\hat{\mathbf{r}} \cdot \nabla \times \nabla \times (\psi \hat{\mathbf{r}}) = -\nabla_h^2 \psi = \nabla \times \mathbf{A}_0. \tag{3.4}$$

The two flux transport models used here differ both in the choice of imposed flow parameters $\mathbf{v}$ and η and in the form of the source term S, as we now describe.

3.2.1 Finding the magnetic vector potential field

We will solve directly for $\mathbf{A}_0$ (3.4), using a finite–difference grid. We are in a spherical co-ordinate system, and as such

$$\mathbf{r} = r\sin(\theta)\cos(\phi)\hat{\mathbf{x}} + r\sin(\theta)\sin(\phi)\hat{\mathbf{y}} + r\cos(\theta)\hat{\mathbf{z}}, \tag{3.5}$$

in which case the co-ordinate scale factors (e.g. $h_r = |d\mathbf{r}/dr|$) are given by

$$h_r = 1, \tag{3.6}$$

$$h_\theta = r, \tag{3.7}$$

$$h_\phi = r\sin(\theta), \tag{3.8}$$

and, likewise, the surface area co-efficient

$$S_A = r\sin^2(\theta)\delta\theta\delta\phi, \tag{3.9}$$

where $\delta\theta = \pi/n_\theta$ and $\delta\phi = 2\pi/n_\phi$. We find the values of A_θ and A_ϕ along each vertex line between vertices (on their respective co-ordinate lines), and B_r is taken to be at the centre of the face. We index by i in θ and j in ϕ.

At each vertex, our gauge condition $\nabla \cdot \mathbf{A}_0 = 0$ offers one constraint, whilst Stokes' theorem at each face tells us that the line integral along the vertices surrounding each face gives the magnetic flux ($B_r S_A$) gives the second constraint. In which case, we have

$$\frac{A_\theta^{i+1,j} - A_\theta^{i,j}}{2r\delta\theta} + \frac{A_\phi^{i,j+1} - A_\theta^{i,j}}{2r\sin(\theta)\delta\phi} = 0, \tag{3.10}$$

$$r\sin(\theta)\delta\phi\left(A_\phi^{i,j+1} - A_\phi^{i,j}\right) + r\delta\theta\left(A_\theta^{i+1,j} - A_\phi^{i,j}\right) = B_r^{i,j} S_A^{i,j}, \tag{3.11}$$

for all $1 \leq i \leq n_\theta - 1$ and $0 \leq j \leq n_\phi$. At the poles, where we experience a co-ordinate singularity, we treat the system slightly differently.

First note that if we have a divergence free vector field at all but one vertex, then we must also have a divergence free vector field at all vertices. We then have a "spare" condition, which we will use to ensure we take account of the polar flux. This will take the form

$$\sum_j r\sin(\delta\theta)A_\phi^{0,j} = B_r P_A, \tag{3.12}$$

where P_A is the polar area. These expressions (3.10, 3.11, 3.12) provide a complete algebraic system for determining $\mathbf{A}_0$, as required.

3.2.2 Model driven by observed active regions (W18)

For Solar Cycles 21 to 23, we use the flux transport model of Yeates et al. (2015), in which the source term $S(\theta, \phi, t)$ comprises of individual active regions assimilated from synoptic magnetogram observations. These regions were selected from US National Solar Observatory radial-component magnetograms based on a flux threshold ($\geq 39.8\,\mathrm{G}$), for which Figure 3.1 (reproduced from Yeates et al. (2015)) shows how these regions are assimilated from a synoptic map. The exact process of assimilation (involving Gaussian smoothing and flux balancing) is detailed in the appendix of Yeates (2015). Regions with

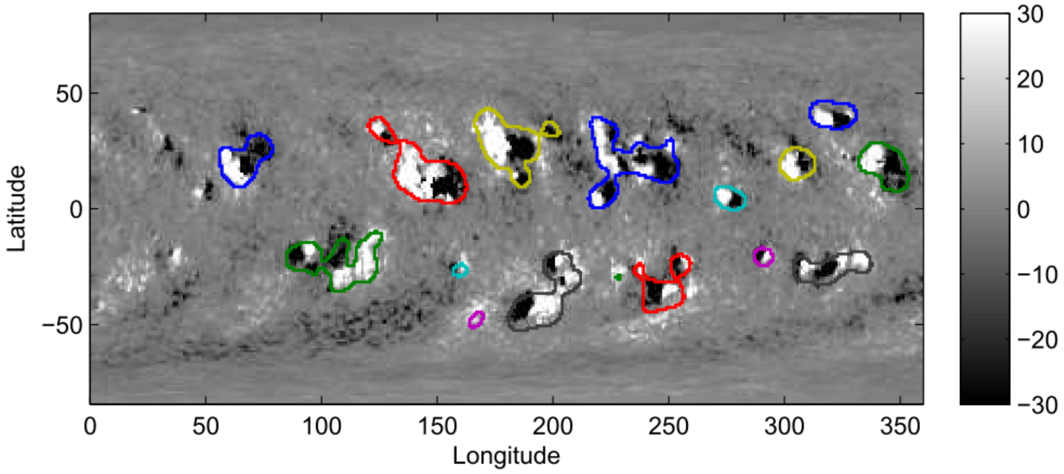

Fig. 3.1 Indicative figure showing how bipolar magnetic regions are sourced from a GONG synoptic map (taken at CR2132). Note the W18 model did not use GONG maps. Reproduced from Yeates et al. (2015) (their Figure 2).

sufficiently balanced flux are inserted instantaneously into the simulation by replacing the corresponding grid points of B_r, with correction to ensure that flux balance is maintained. This technique best represents individual emerging regions without approximating them as idealized magnetic bipoles. The disadvantage is that systematic magnetogram observations are required, which are not available for earlier cycles. The replacement of the B_r at the location of the bipole (rather than simple addition) ensures that strong bipoles which appear in multiple synoptic maps are not doubly–represented.

The initial condition was set to

$$B_r(\theta,\phi) = B_0|\cos\theta|^7\cos\theta. \tag{3.13}$$

The azimuthal velocity was

$$v_\phi(\theta) = R_\odot\Omega(\theta)\sin\theta, \tag{3.14}$$

with angular velocity

$$\Omega(\theta) = \Omega_0 + \Omega_2\cos^2\theta + \Omega_4\cos^4\theta. \tag{3.15}$$

The meridional velocity took the form

$$v_\theta(\theta) = -\frac{v_0}{v_{\max}}\sin^p\theta\cos\theta, \tag{3.16}$$

where $v_{\max} = \max_\theta\left(\sin^p\theta\cos\theta\right)$. The decay term in this model took the form of a simple exponential decay $D(\theta,\phi,t) = B_r/\tau$.

The particular simulation used here, henceforth denoted W18, was published by Whitbread et al. (2018), who determined the parameters through systematic optimization against the observed magnetic butterfly diagram for Cycles 21 to 23, which they define

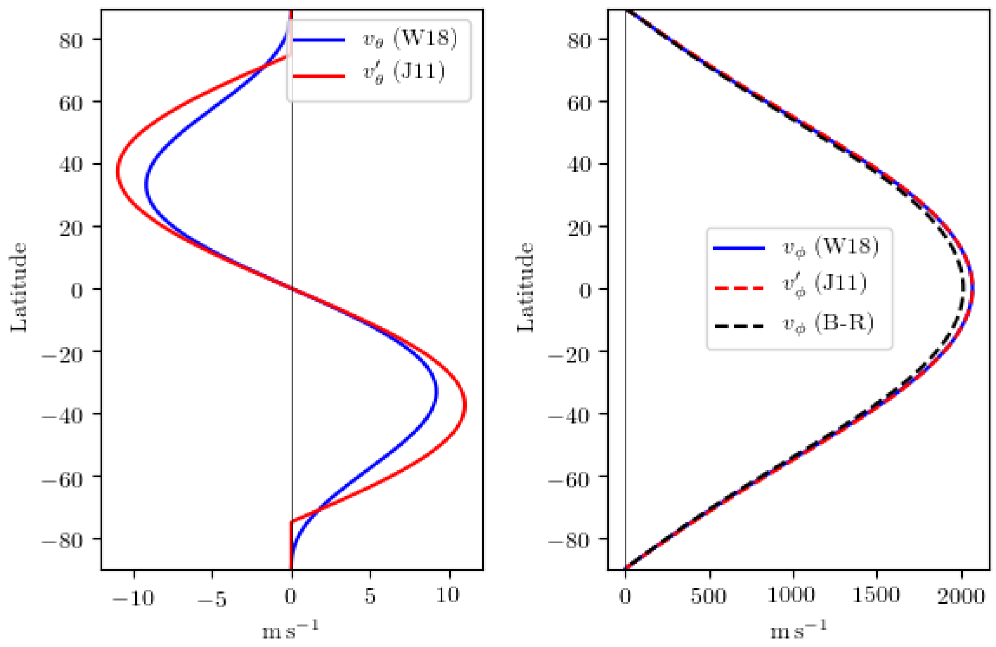

Fig. 3.2 Velocity profiles as a function of latitude for meridional velocity v_θ (left), and differential rotation v_ϕ (right), in W18 and J11. The black dashed curve for v_ϕ shows the profile used by Berger and Ruzmaikin (2000) (and in Chapter 2).

as 19767 May 1 to 2008 October 23, using a genetic algorithm. This involved running a series of simulations with parameters constrained within a minima and maxima, for the parameters η, v_0, p, τ, B_0 for a two–dimensional model in (θ, ϕ) (they also studied longitudinally averaged one–dimensional models). A fitness statistic was used to quantify the level of success of an individual, which was measured in time and space. The statistic measured the degree of similarity between the simulation data and an observational ground–truth taken from magnetograms produced by Kitt Peak, averaged over Carrington rotations (with some smoothing), with a variance assumed in the observation data associated with its nature as a line–of–sight measurement (as we did in Chapter 2). The optimum values (which best represented the true solar cycles (21-23)) were given as $B_0 = 6.7\,\mathrm{G}$, $v_0 = 9.2\,\mathrm{m\,s^{-1}}$, $p = 2.33$, $\eta = 466.8\,\mathrm{km^2\,s}$ and $\tau = 10.1\,\mathrm{yr}$.

The rotation profile $\Omega(\theta)$ was fixed with $\Omega_2 = -2.396\,\mathrm{deg\,day^{-1}}$ and $\Omega_4 = -1.787\,\mathrm{deg\,day^{-1}}$ as determined by Snodgrass and Ulrich (1990). The original W18 simulation was performed in the Carrington frame, but for computing the helicity flux, we include not only the contribution from differential rotation in the Carrington frame but also that from uniform rotation of this frame with respect to the fixed stars. Thus we set $\Omega_0 = 14.713\,\mathrm{deg\,day^{-1}}$ (the sidereal rotation rate at the equator). The v_θ and v_ϕ profiles are shown in Figure 3.2.

For a simple comparison of the magnitude of the various terms, note that the peak flow speed of rotation is $|v_\phi| \approx 2\,\mathrm{km\,s^{-1}}$, compared to the maximum meridional flow speed of $|v_\theta| \approx 9.2\,\mathrm{m\,s^{-1}}$. To calculate an effective diffusion speed, we must define a characteristic length scale; given the signed nature of helicity, we choose this to be of the order of a unipolar structure, which corresponds to 10 degrees, or approximately $0.17R_\odot$. In this

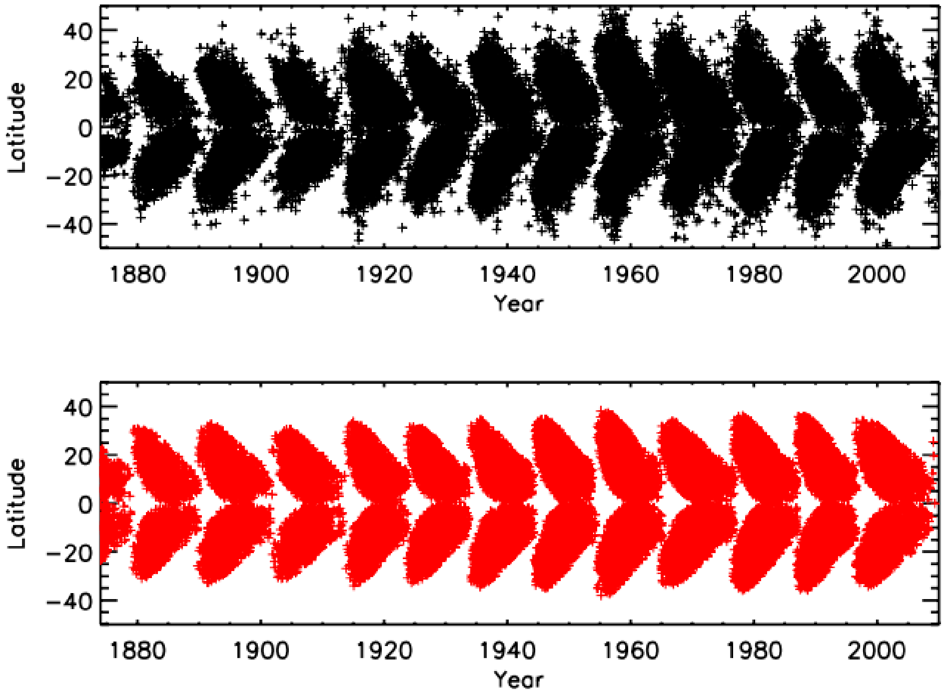

Fig. 3.3 Butterfly diagrams comparing the true sunspot number (top) to the semi–synthetic sunspot numbers (bottom) used for the J11 simulation. Reproduced from Jiang et al. (2011) (their Figure 13).

case, we calculate an effective diffusion speed of $|v_\eta| \approx \eta/0.17R_\odot = 3.97$ ms^{-1}. We do not calculate the helicity flux solely attributable to the decay term $D(\theta,\phi,t)$ - calculating its effective decay speed (at the same characteristic length scale) gives $|v_D| \approx 0.17R_\odot/\tau = 0.37$ ms^{-1}, which is an order of magnitude below that of $|v_\eta|$, and is thus neglected. It is also not immediately clear how to calculate the helicity flux associated with such a decay. We see in Section 3.3 that this ordering determines the relative contribution of each of these terms to the helicity flux.

3.2.3 Model driven by statistical active regions (J11)

In order to estimate the helicity flux over a larger range of solar cycles, we also employ a flux transport simulation by Jiang et al. (2011), who simulated the solar magnetic field evolution continuously over the period 1700 to 2009 using the model introduced in Cameron et al. (2010). Henceforth denoted J11, this model has several differences compared to the W18 model. Most significantly, the flux emergence term $S'(\theta,\phi,t)$, where primes denote parameters associated with the J11 simulation, consists of bipolar active regions determined semi-synthetically from statistical distributions modulated by observed sunspot numbers (Jiang et al., 2011) (see Figure 3.3, reproduced from their paper). These bipolar regions are described by the formula

$$B^{\pm}(\lambda,\phi) = B_{\max}\left(\frac{0.4\Delta\beta}{\delta}\right)\exp\left(-\frac{2[1-\cos(\beta_{\pm}(\lambda,\phi))]}{\delta^2}\right), \tag{3.17}$$

for which λ is the latitude ($\lambda = \theta - \pi/2$), $\beta_{\pm}(\lambda,\phi)$ is the angle between the center of a given bipolar region, and the two polarities of defining the individual sunspot $(\lambda_{\pm},\phi_{\pm})$. $\delta\beta = 0.45A_{AR}^{1/2}$, for which A_{AR} is the total area of the sunspot group, defined as the sum of the umbral, penumbral and facular areas making up the bipolar magnetic region, calculated by an empirical formula determined by Chapman et al. (1997). $\delta = 4$ is the width of each polarity, and they choose $B_{\max} = 374G$. These active regions are inserted instantaneously according to the form

$$S'(\lambda,\phi,t) = \delta(t-t_n)(B^{+}(\lambda,\phi) - B^{-}(\lambda,\phi)), \tag{3.18}$$

where $\delta(t-t_n)$ is the Dirac delta function.

The flow profiles are also different: J11 uses a lower supergranular diffusivity $\eta' = 250\,\mathrm{km}^2\,\mathrm{s}^{-1}$, which is compensated by a slightly faster meridional flow with a slightly sharper gradient at the equator, given by

$$v'_{\theta}(\theta) = \begin{cases} -v'_0\sin(2.4\lambda) & \lambda < 1.31 \\ 0 & \text{otherwise} \end{cases}, \tag{3.19}$$

where $\lambda = \pi/2 - \theta$ and $v'_0 = 11\,\mathrm{m\,s}^{-1}$. The differential rotation profile was also slightly different from W18, with $\Omega'_2 = -2.30\,\mathrm{deg\,day}^{-1}$ and $\Omega'_4 = -1.62\,\mathrm{deg\,day}^{-1}$. Again we set $\Omega'_0 = 14.713\,\mathrm{deg\,day}^{-1}$. Finally, the decay term $D(\theta,\phi,t)$ in J11 is of a more sophisticated form, following Baumann et al. (2006), where different spherical harmonic components of the solution decay at different rates. The strength of convection zone diffusivity used here gives an effective decay time of about 20 yr, a little longer than the W18 model.

To compute the helicity flux, we once again compute $\mathbf{A}_0$ from B'_r, using the same finite-difference method as for W18. The electric field, however, would be determined using v'_{ϕ}, v'_{θ} and η', but we do not calculate it ourselves: J11 data was provided as a series of snapshots of B_r.

Figure 3.4(a) shows that J11 produces a larger unsigned magnetic flux in each cycle than W18, as we would expect with the lower diffusivity. On the other hand, Figure 3.4(b) shows that the relative strength of their axial dipole moments (and hence polar fields) varies from cycle to cycle, in agreement with the differences in flux transport, and particularly in the source term. The axial dipole strength used here is given by

$$D_2 = \frac{3}{2}\oint B_r\cos(\theta)\sin(\theta)\,\mathrm{d}\theta\mathrm{d}\phi, \tag{3.20}$$

following Whitbread et al. (2018).

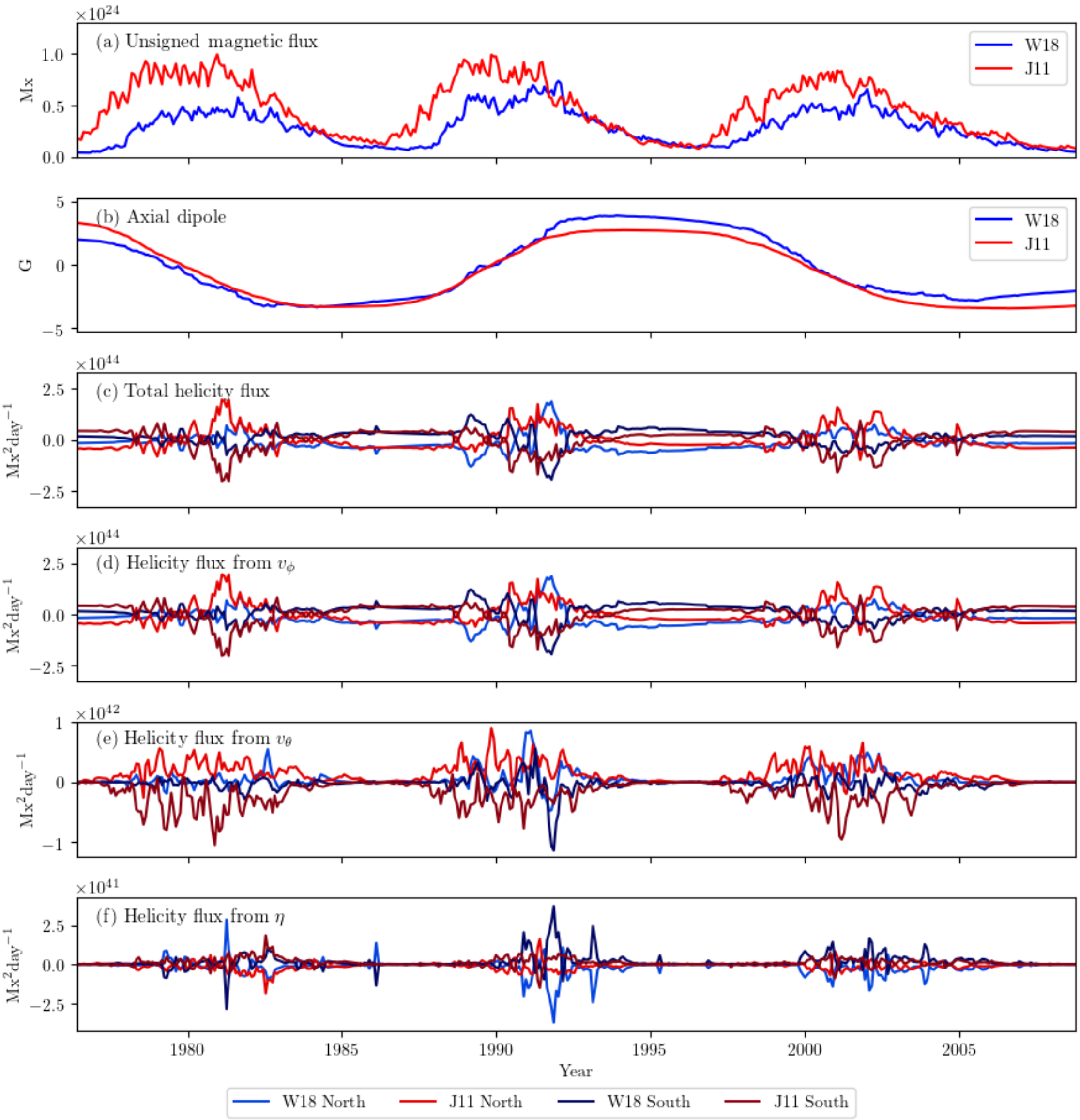

Fig. 3.4 Time variation of unsigned magnetic flux (a), axial dipole moment (b), and hemispheric helicity fluxes (c)-(f) for the W18 and J11 models over Solar Cycles 21 to 23. The net helicity flux $F_{N/S}$ (c) is the sum of those due to solar rotation $F_{v_\phi,N/S}$ (d), meridional velocity $F_{v_\theta,N/S}$ (e) and supergranular diffusion $F_{\eta,N/S}$ (f) for both W18 (blue shades) and J11 (red shades).

3.3 Results for Solar Cycles 21 to 23

3.3.1 Relative contributions of different terms

We first consider the period covered by both flux transport models: Solar Cycles 21 to 23. Figure 3.4(c) shows the net helicity flux out of the solar surface in each hemisphere as a function of time, whilst figures 3.4(d)-(f) show the separate contributions from differential rotation, meridional velocity and supergranular diffusion respectively, for both W18 and J11. Throughout this chapter, line plots associated with W18 are shaded blue, while those describing J11 are shaded red. The contributions from the Northern hemisphere N are defined as

$$F_{v_\phi,N}(t) = -2\int_N A_{0\phi} v_\phi B_r \,\mathrm{d}^2x, \tag{3.21}$$

$$F_{v_\theta,N}(t) = -2\int_N A_{0\theta} v_\theta B_r \,\mathrm{d}^2x, \tag{3.22}$$

$$F_{\eta,N}(t) = 2\eta\int_N \mathbf{A}_0\cdot\nabla B_r \,\mathrm{d}^2x, \tag{3.23}$$

with their sum giving the net hemispheric flux

$$F_N = -2\int_N \mathbf{A}_0\times\mathbf{E}\cdot\hat{\mathbf{r}}\,\mathrm{d}^2x = F_{v_\phi,N} + F_{v_\theta,N} + F_{\eta,N}. \tag{3.24}$$

The fluxes are defined similarly for the Southern hemisphere, denoted S. The net helicity fluxes in north and south need not be exactly equal and opposite, although they remain so to a good approximation. In fact, in Section 3.7 we prove that this is true mathematically for the helicity flux from supergranular diffusion, and true to first order for differential rotation (uniform rotation).

Figure 3.4 shows clearly that the contributions from differential rotation dominate the flux overall, followed by meridional velocity and supergranular diffusion, in that order, for both simulations. To quantify the difference in magnitude between the helicity fluxes, we compute the ratio

$$f_{v_\phi}(t) = \frac{1}{2}\left(\frac{|F_{v_\phi,N}|}{|F_{v_\phi,N}|+|F_{v_\theta,N}|+|F_{\eta,N}|} + \frac{|F_{v_\phi,S}|}{|F_{v_\phi,S}|+|F_{v_\theta,S}|+|F_{\eta,S}|}\right), \tag{3.25}$$

and similarly for the other two fluxes. Table 3.1 shows the mean, maximum and minimum values of these ratios, over the course of the W18 and J11 simulations. The mean magnitude of each term is roughly separable by an order of magnitude, consistent with the magnitudes of the shear velocities associated with each term (in the same order), as described in Section 3.2.2.

We note that W18 and J11 agree in the ordering of contributions in Table 3.1, although there can be substantial differences between their actual individual helicity fluxes at any given time, as seen in Figure 3.4. Around Solar Maximum, differences between the helicity

	Mean	Maximum	Minimum
f_{v_ϕ} (W18)	0.99	1.00	0.82
(J11)	*0.99*	*1.00*	*0.64*
f_{v_θ} (W18)	0.0037	0.15	0.00
(J11)	*0.0076*	*0.17*	*0.00*
f_η (W18)	0.0014	0.069	0.00
(J11)	*0.0013*	*0.19*	*0.00*

Table 3.1 Mean, maximum and minimum values of the ratios in Equation (3.25), indicating the relative size of the three different contributions to the helicity flux for the W18 and J11 (italic) simulations.

fluxes in W18 and J11 arise because J11 has more absolute magnetic flux at low latitudes due to its decreased diffusion, which tends to lead to greater helicity flux (except from diffusion, which is weaker in J11). Around Solar Minimum, the helicity fluxes from the two models are qualitatively more alike. The simulation whose helicity flux is larger at Solar Minimum varies from cycle to cycle, according to which simulation has the larger axial dipole moment. This is because both the helicity flux and axial dipole at Minimum are dominated by the high latitude (polar) field.

3.3.2 Net injection per solar cycle

Table 3.2 show the time-integrated helicity fluxes during each solar cycle, for the two models J11 and W18. Following Whitbread et al. (2017), we define Cycle 21 as the period 1976 May 1 to 1986 March 10, Cycle 22 as 1986 March 11 to 1996 June 1 and Cycle 23 as 1996 June 2 to 2008 August 3 (note this differs slightly from the simpler minima–defined cycles in Chapter 2). Concentrating on the net helicity flux (top two rows), we note that the sign of this net flux in W18 is negative in the Northern hemisphere and positive in the Southern for all three cycles, whilst in J11 it has the opposite sign in Cycles 21 and 22. We will show that this difference arises because the solar-cycle helicity flux is a signed quantity that involves much cancellation between contributions from different latitudes, which can be easily affected changes in the parameters governing the simulation.

In Figure 3.5 we break down the helicity fluxes down into their contributions in time and latitude (i.e., the surface integrals (3.21)–(3.24) are performed over longitude but not latitude). Figures 3.5(c) and (d) show that both W18 and J11 have the same qualitative behaviour, with strong contributions of both signs from the regions below about 55° latitude, and a weaker (but more consistent) contribution from the high-latitude polar field. In the Northern hemisphere, the high-latitude helicity flux is always negative, consistent with the Parker spiral. This is because the product $A_{0\phi}B_r$ for a polar–oriented dipole is always positive/negative in the northern/southern hemisphere, irrespective of the polarity of B_r: if the sign of B_r changes, then the sign of $\mathbf{A}_0$ must also change in line. As such,

	Cycle 21		Cycle 22		Cycle 23	
	North	South	North	South	North	South
Net (W18)	-4.33e46	3.70e46	-1.07e47	9.39e46	-2.27e46	2.61e46
(J11)	*6.72e45*	*-6.09e45*	*8.99e45*	*-6.02e45*	*-7.49e45*	*8.48e45*
(H-B)	-9.22e46	9.22e46	-9.42e46	9.42e46	-4.37e46	4.37e46
v_ϕ (W18)	-4.33e46	3.7e46	-1.08e47	9.40e46	-2.18e46	2.5e46
(J11)	*6.23e45*	*-5.38e45*	*8.43e45*	*-5.51e45*	*-8.01e45*	*9.08e45*
v_θ (W18)	9.23e43	-8.52e43	2.20e44	-1.32e44	2.94e44	-1.45e44
(J11)	*5.48e44*	*-7.67e44*	*5.95e44*	*-5.41e44*	*5.47e44*	*-6.31e44*
η (W18)	-1.03e43	1.03e43	-8.99e43	8.99e43	-8.84e43	8.84e43
(J11)	*-5.76e43*	*5.85e43*	*-3.10e43*	*3.25e43*	*-3.07e43*	*3.50e43*

Table 3.2 Solar-cycle-integrated helicity injection from each physical process [Mx^2], per cycle, for the W18 and J11 (italic) simulations. The results from Chapter 2 for the flux from rotation are also shown (labelled H-B).

the model dependence of the cycle-integrated flux in Table 2 must be associated with the balance between these differently signed contributions.

The positive and negative contributions from the butterfly wings arise not from Joy's law (like in the usual magnetic butterfly diagram) but simply from the fact that active regions are typically bipolar in the East-West direction. To illustrate this, figure 3.6(a,b,d) shows B_r, $A_{0\phi}$, and the differential rotation helicity flux integrand, where we have singled out two active regions R1 and R2, at CR3952 (April 1991) of J11. Region R1's radial field is stronger, so its quadrupolar $A_{0\phi}$ distribution dominates that from the global dipole (seen as positive (red) in areas without any active regions in (b)), leading to a product $A_{0\phi}B_r$ whose polarity is arranged North-South. This North-South pattern is the same for any strong active region, irrespective of the sign of B_r or the hemisphere. Region R2 does not show a quadrupolar helicity injection because its $A_{0\phi}$ is weaker than that from the global dipole. Even a fairly strong active region, located slightly below R1, is dominated by the quadrupole of R1. Since the helicity flux is approximately quadratic in B_r (given its presence in the expression for the magnetic vector potential), it is dominated by the strong regions, thus leading to the latitudinal sign pattern seen in the butterfly wings.

Additionally, in figures 3.6(c,e,f) we plot $A_{0\theta}$, and the helicity integrand for meridional velocity and supergranular diffusion respectively. The background vector potential from $A_{0\theta}$ is less well defined than $A_{0\phi}$, and as such for both R1 and R2 we see the same pattern in the meridional helicity flux integrand regardless of their field strength. Each of the three helicity fluxes seem to have a pattern that is quite unique: meridional velocity (qualitatively) appears to be a ninety-degree rotation of that from differential rotation, whilst the physical meaning of the helicity flux distribution from supergranular diffusion is not immediately obvious.

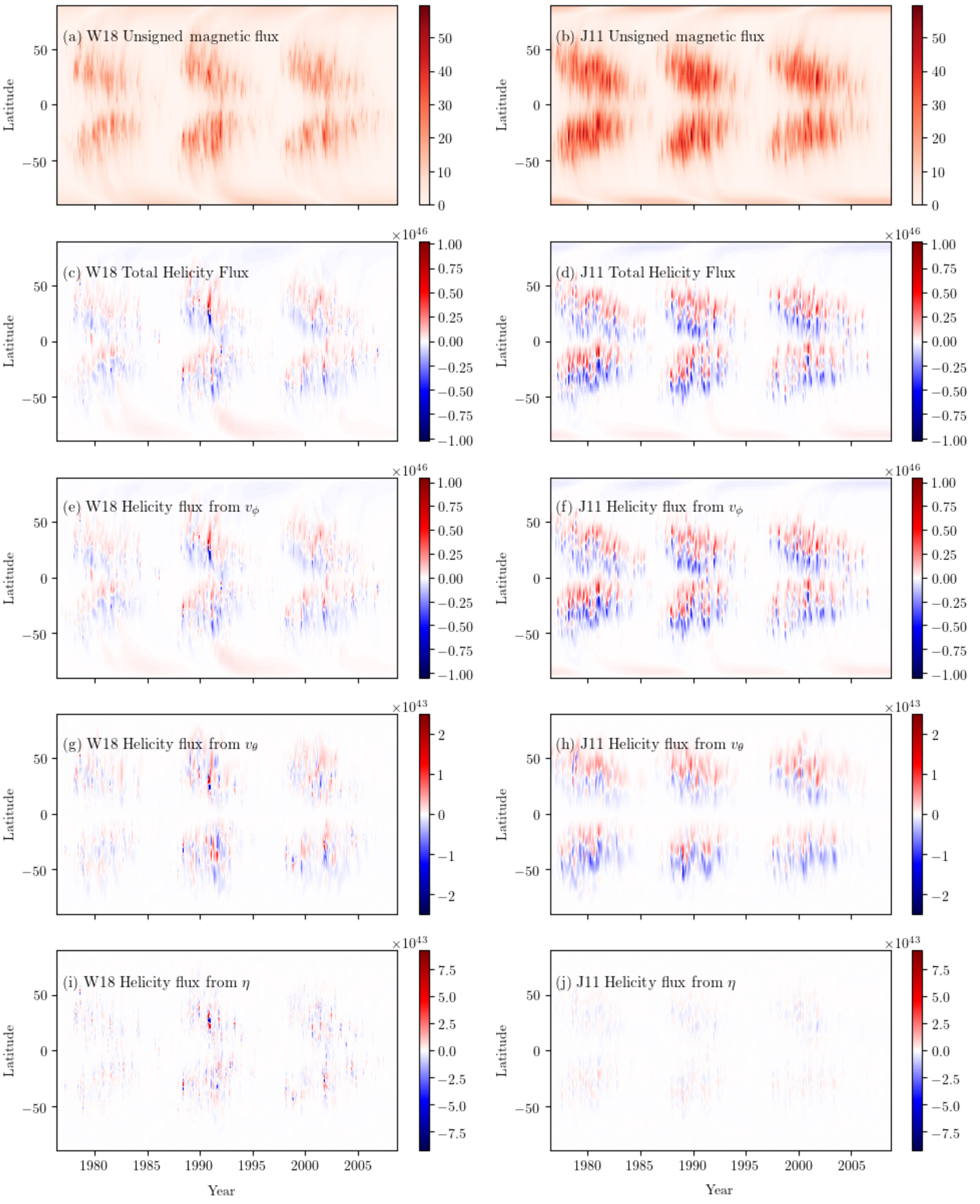

Fig. 3.5 Latitude-time distributions of longitude-averaged radial magnetic field (a,b) alongside longitude integrated total helicity flux (c,d), and helicity flux associated individually with differential rotation (e,f), meridional velocity (g,h) and supergranular diffusion (i,j) for W18 and J11 respectively. We stress that these latitudinal distributions are not in themselves physically meaningful, since there is typically significant cancellation between different latitudes. The same colour scales are used for W18 and J11. Units are G for (a,b) and $\mathrm{Mx}^2\,\mathrm{day}^{-1}$ for (c–j).

We find that the positive and negative helicity fluxes in each butterfly wing are not usually equal. Indeed, the net contribution over a solar cycle from latitudes $|\lambda| < 55^\circ$ is always opposite in sign to that from the high latitudes, being positive/negative in the Northern/Southern Hemisphere. This imbalance between latitudes arises because, later in the cycle, the equatorward polarity helicity fluxes tend to cancel across the equator, leaving an excess of the poleward polarities. Early in the cycle, there is little equatorial cancellation, and the net contribution tends to be opposite in sign because v_ϕ is slightly stronger nearer to the equator.

The net helicity flux in each hemisphere over a solar cycle is therefore a balance between oppositely signed contributions from high and low latitudes. We quantify this balance in Table 3.3 which shows means of the ratios

$$\begin{aligned} f_{N,|\lambda|<55}(t) &= \left|F_{N,|\lambda|<55}(t)\right| / \Big(\left|F_{N,|\lambda|<55}(t)\right| + \left|F_{N,|\lambda|>55}(t)\right| \Big), && (3.26) \\ f_{N,|\lambda|>55}(t) &= \left|F_{N,|\lambda|>55}(t)\right| / \Big(\left|F_{N,|\lambda|>55}(t)\right|\Big| + \left|F_{N,|\lambda|>55}(t)\right| \Big), && (3.27) \end{aligned}$$

and similarly for the Southern hemisphere. Notice that the high latitudes dominate for W18 in all cycles, explaining the net negative/positive helicity flux in the North/South. On the other hand, the low latitudes dominate for J11 during Cycles 21 and 22, explaining the opposite signs. This tendency for the low latitude butterfly wings to contribute more in J11 simply results from the stronger magnetic flux in that simulation, because of the lower supergranular diffusivity. This higher unsigned flux is evident in Figure 3.5(b) compared to Figure 3.5(a), as well as in Figure 3.4(a).

3.3.3 Comparison with earlier work

The third row of Table 3.2 shows the helicity fluxes estimated by Hawkes and Berger (2018) (Chapter 2 using low–harmonic WSO data), using the differential rotation profile of Berger and Ruzmaikin (2000). This profile is shown by the black dashed line in the right panel of Figure 3.2, and is seen to be close to those used in this thesis. The Hawkes and Berger (2018) helicity fluxes follow F_{v_ϕ} from the W18 model reasonably closely for Cycle 22, but are a factor two stronger for Cycles 21 and 23. These discrepancies can be attributed to the different spatial resolutions used for the two studies: in Hawkes and Berger (2018) the authors use only the first few degrees from the WSO spherical harmonic decomposition, and as such calculate the large scale winding without accounting for the contribution of active regions. Since active regions are important for the net helicity flux in our study, the Hawkes and Berger (2018) helicity flux is not necessarily directly comparable, but we include it for the sake of comparison.

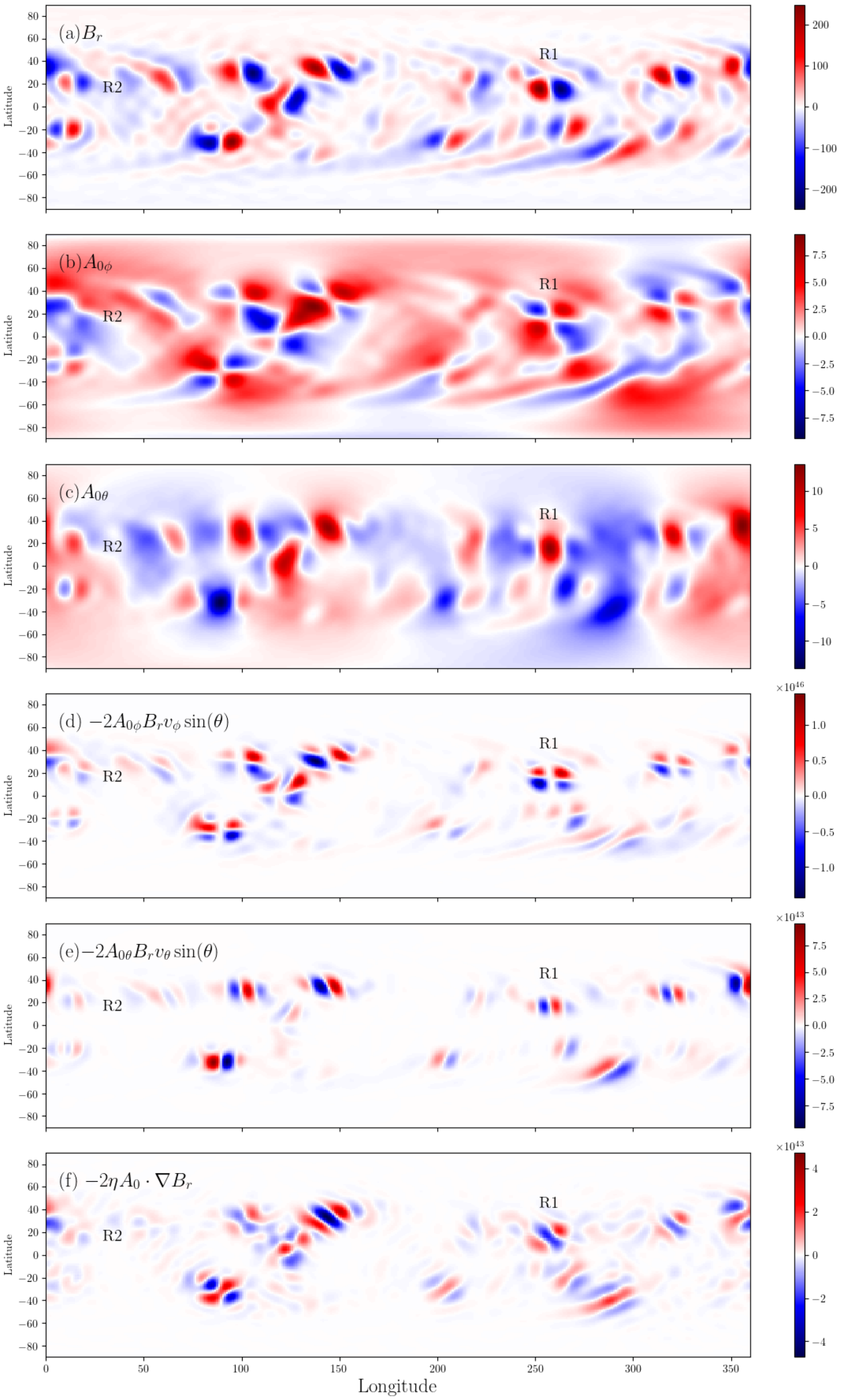

Fig. 3.6 Illustration of the source of helicity flux F_{v_ϕ} at CR3952 (April 1991) of J11. Panels show (a) B_r, (b) $A_{0\phi}$, (c) $A_{0\theta}$ and maps of helicity flux from (d) differential rotation, (e) meridional velocity and (f) supergranular diffusion.

	Cycle 21		Cycle 22		Cycle 23	
	North	South	North	South	North	South
$\lvert\lambda\rvert > 55$ (W18)	0.64	0.61	0.66	0.57	0.59	0.60
(J11)	*0.45*	*0.44*	*0.51*	*0.48*	*0.56*	*0.52*
$\lvert\lambda\rvert < 55$ (W18)	0.36	0.39	0.34	0.43	0.41	0.40
(J11)	*0.55*	*0.56*	*0.49*	*0.52*	*0.44*	*0.48*

Table 3.3 Mean of the ratios (3.26) and (3.27), indicating the relative size of the low- and high-latitude contributions to the helicity flux for W18 and J11 (italic).

3.4 Results for earlier Solar Cycles

Having demonstrated the basic pattern of helicity flux in surface flux-transport models, we now look at the full extent of the J11 simulation, covering 1700-2009 (twenty-seven complete solar cycles). The results are shown in Figure 3.7. We observe the same general behaviour as described in Section 3.3 across the entire simulation period, with the terms being ordered in magnitude as before. Having multiple cycles, however, enables us to consider the variation in cycle-integrated helicity flux from one cycle to the next.

In Figure 3.8 we plot cycle-integrated helicity flux against the strength (absolute value) of the end-of-cycle axial dipole moment for each cycle. Helicity fluxes above and below 55° latitude are shown separately, because they differ both in sign (as seen in Section 3.3) but also in the slope of their respective trends. The latter is expected because both high-latitude helicity flux and end-of-cycle axial dipole are determined by the strength of the high-latitude polar field. The end-of-cycle polar field is not a direct function of the cycle amplitude (strength of emerging active region magnetic flux), since it depends also on the orientation and locations of active regions (Jiang et al., 2014). Thus the high-latitude contribution causes the helicity flux to correlate better with axial dipole moment than with either cycle amplitude or cycle-integrated magnetic flux.

For comparison, Figure 3.8 also shows the W18 data points. Most of these do not deviate greatly from the J11 trend lines, except for one low-latitude contribution in the Northern hemisphere (for Cycle 22), which has the opposite sign. We found this to be associated with the more rapid rise to maximum of this cycle compared with Cycles 21 and 23 in W18, visible in Figure 3.4(a). The reason for the reversed sign of helicity flux is that early active regions are further from the equator, so that the corresponding part of the butterfly wing does not make a net positive contribution (as described in Section 3.3.2). Rather, the differential rotation gradient tends to win out early in the cycle and the net contribution is negative. As shown by Figure 3.9, this sign-reversal phenomenon occurs in all three W18 cycles. But it only beats the later contribution in Cycle 22, and only for the Northern hemisphere, owing to the stronger early flux emergence.

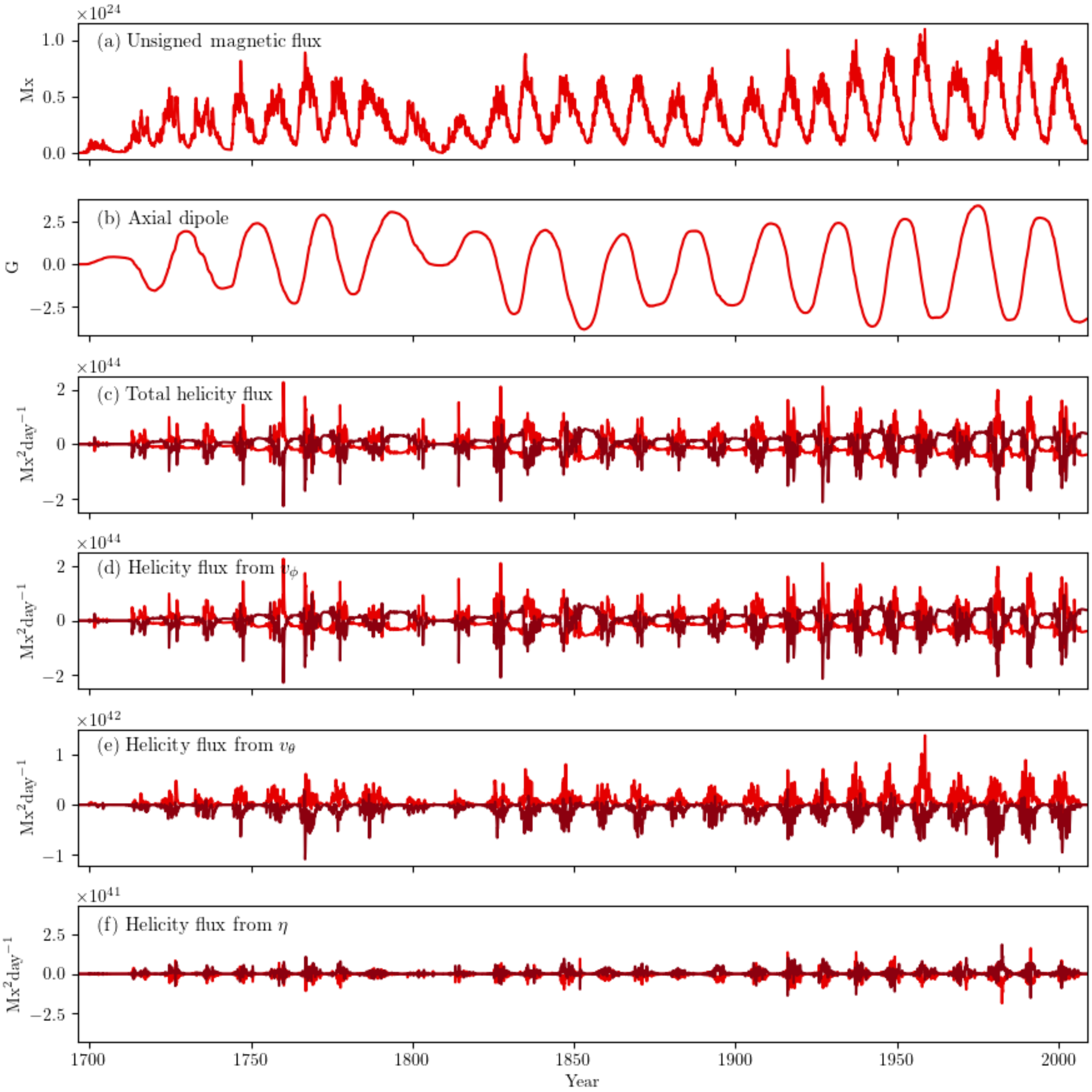

Fig. 3.7 Results for the full J11 model, showing unsigned magnetic flux (a), axial dipole moment (b), total helicity flux (c) and helicity flux from solar rotation (d), meridional velocity (e) and supergranular diffusion (f). In (c-f), light red shows the northern hemisphere and dark red the southern hemisphere.

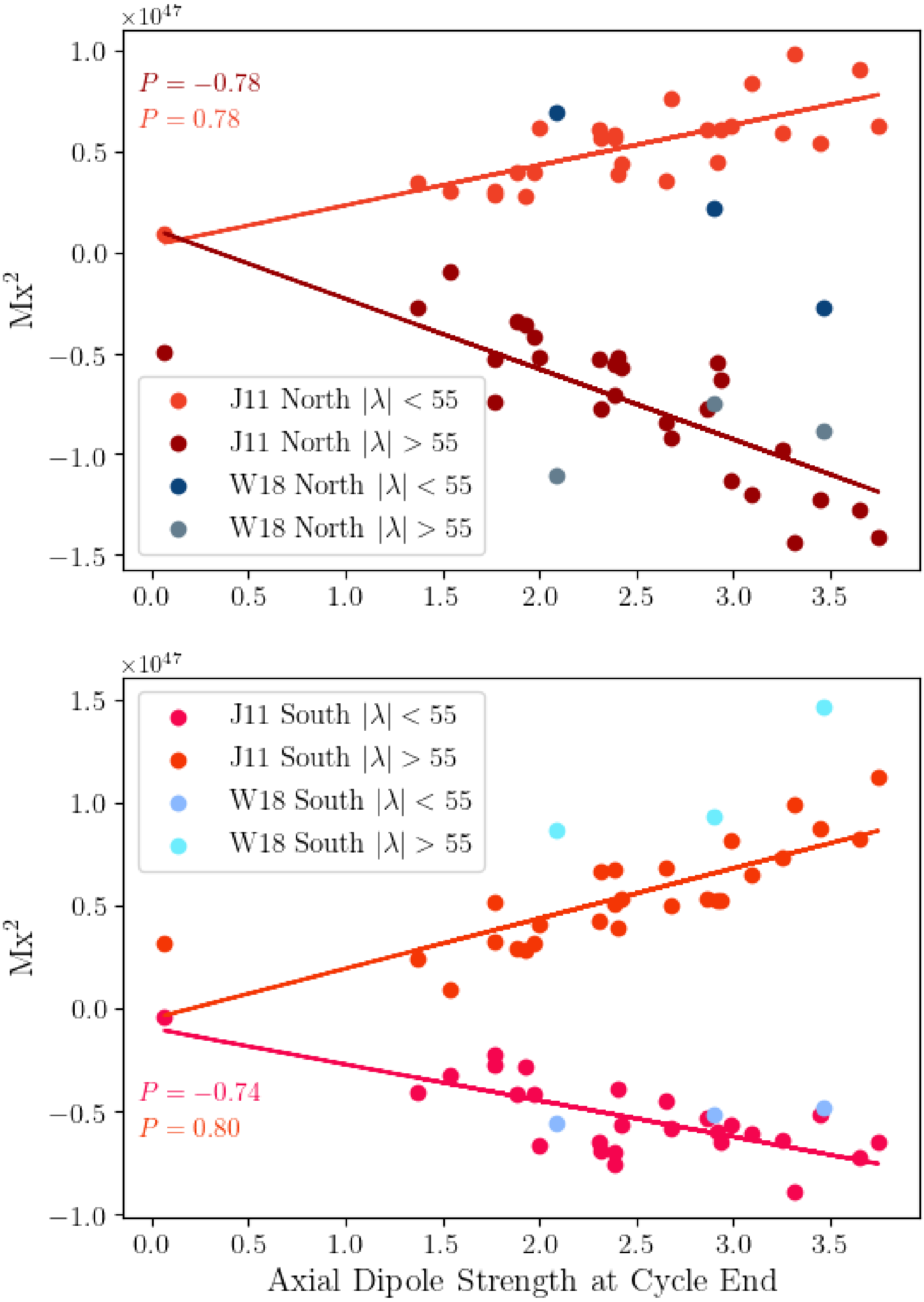

Fig. 3.8 Scatter plots of integrated helicity flux per cycle in each sub-hemisphere for both W18 and J11, plotted against the axial dipole strength (absolute value) at the end of each cycle. This time is defined as the time of minimum unsigned magnetic flux in figures 3.4(a) and 3.2(a). Lines of best fit and Pearson's correlation coefficient P are calculated for the J11 data only.

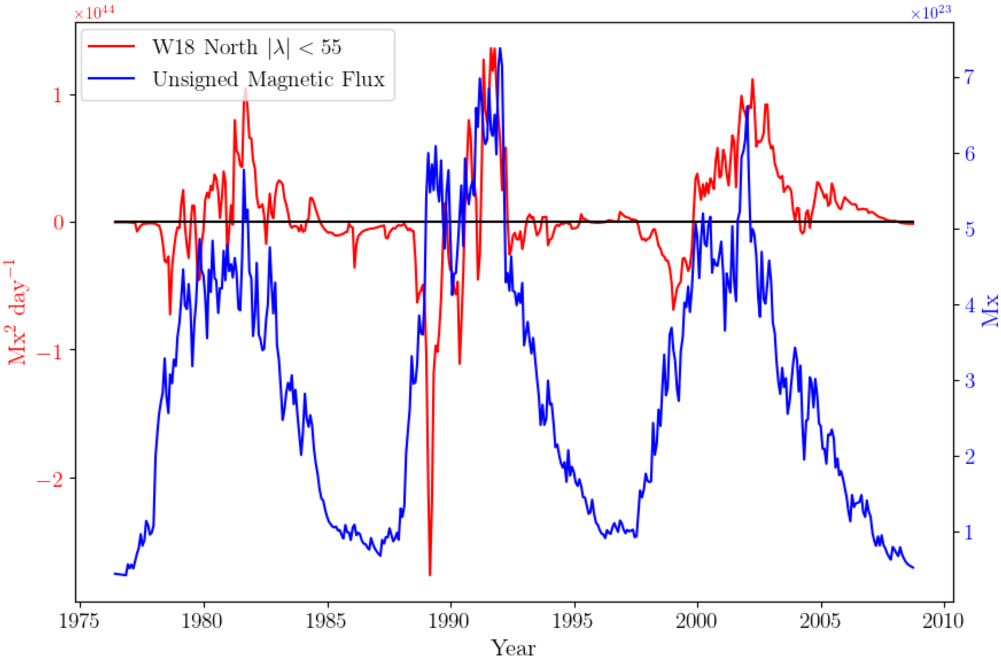

Fig. 3.9 Time variation of the $|\lambda| < 55^\circ$ helicity flux in the Northern hemisphere for W18 (red), compared to the unsigned magnetic flux (blue). The black line denotes the zero axis for helicity flux.

3.5 Comparisons with Wilcox Data

In Section 3.3.3, we calculated the integrated helicity per cycle from the helicity flux in Chapter 2 (Hawkes and Berger (2018)), which was itself calculated from low–harmonic WSO data. In this Section, we calculate the helicity fluxes associated with the WSO data, with all the harmonics available taken account of, and using the W18 velocity parameters. Note that we cannot calculate the flux associated with supergranular diffusion, as the Wilcox model is observational, rather than simulated. We immediately notice that the magnitude of the WSO unsigned magnetic field has a peak much lower ($\approx$ 8G) than that observed in the W18 and J11 models ($\approx$ 50G), and the peak magnitude is located in the polar regions, rather than active regions.

Although we do see the helicity flux patterns associated with the polar region, the active region detail is still almost completely lost. There is no butterfly wing activity beyond noisy behaviour at low latitudes.

Additionally, in Figure 3.11, we plot the helicity fluxes associated with differential rotation and meridional velocity in the full Wilcox model. We see none of the detailed, hemispheric–balanced behaviour from the surface flux transport models. The helicity flux from meridional velocity is almost identical between the two hemispheres, also in disagreement with the results obtained from the SFTM simulations. In figures 3.12 and 3.13, we plot the radial magnetic field distribution, with the magnetic vector potential overlaid, for the J11 and Wilcox models respectively, for the Carrington Rotation CR3952 in the J11 model, or CR1843 in the true frame (April 1991 for both).

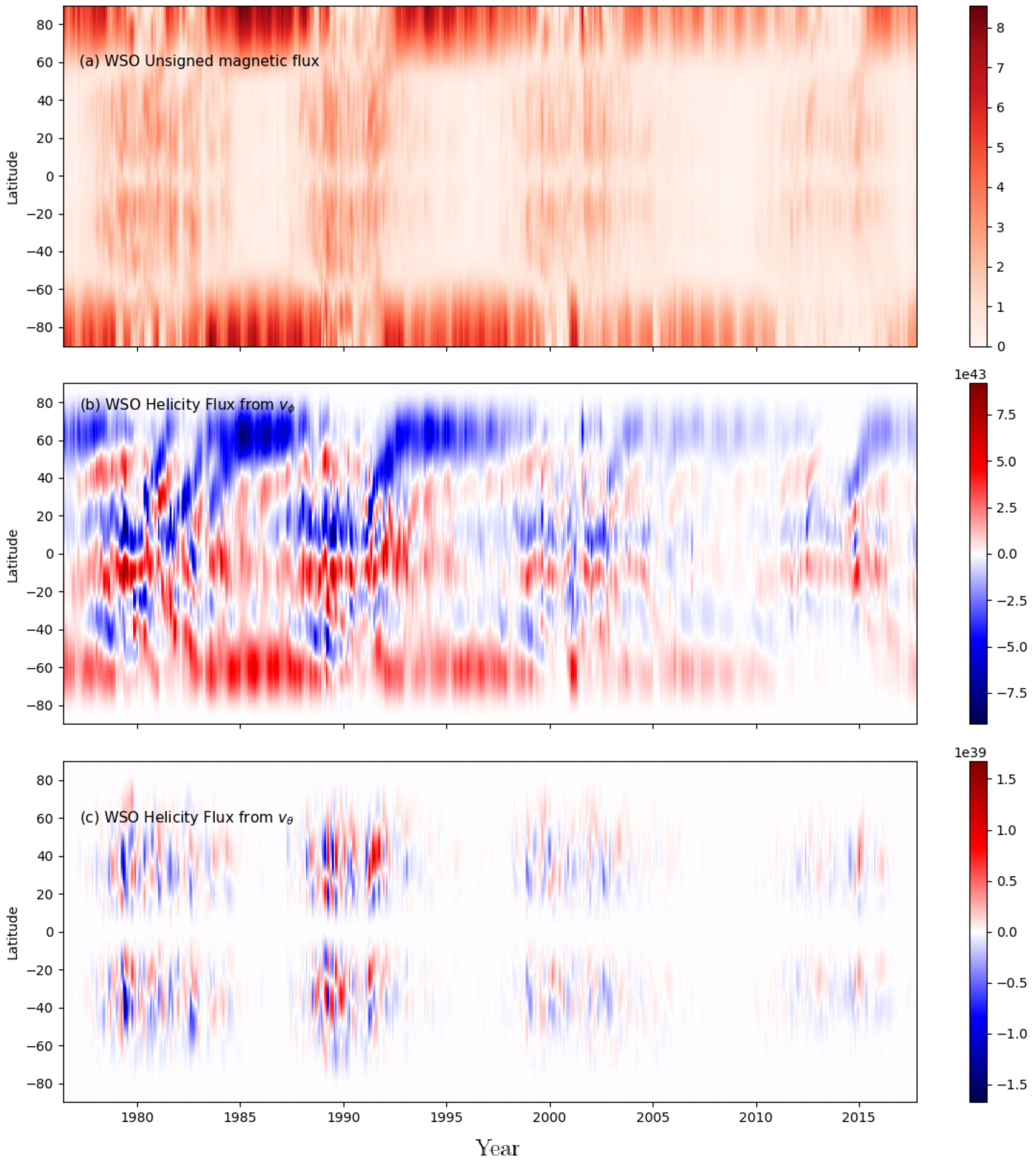

Fig. 3.10 Latitude-time distributions of longitude-averaged radial magnetic field (a) alongside longitude helicity flux from differential rotation (b) and meridional velocity (c), as calculated from the full WSO spherical harmonic expansion. Units are G for (a) and Mx^2 day^{-1} for (b,c).

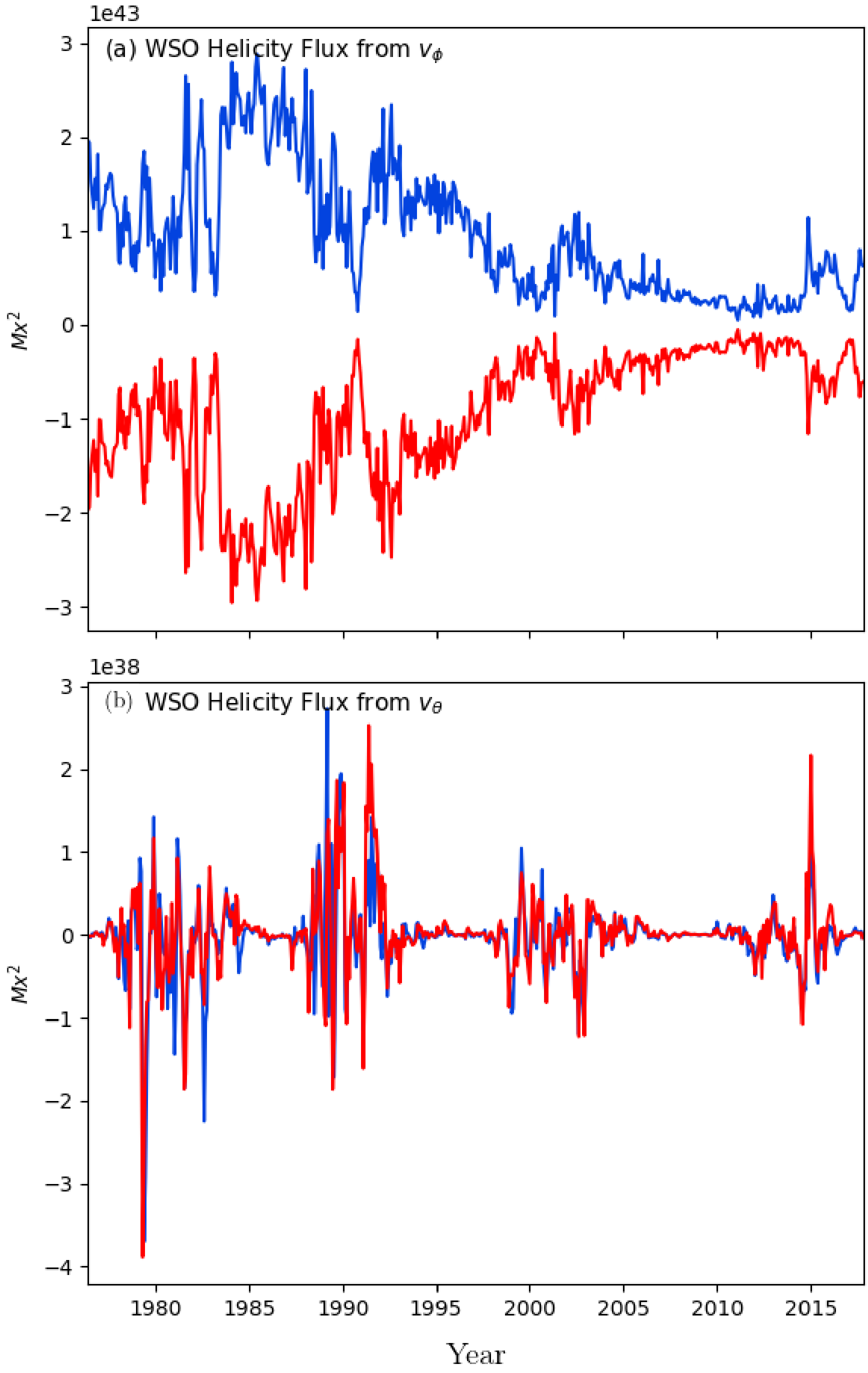

Fig. 3.11 Results for the full WSO harmonic decomposition, showing (a) helicity flux from differential rotation in the North (blue) and South (red), and (b) helicity flux from meridional velocity in the North (blue) and South (red).

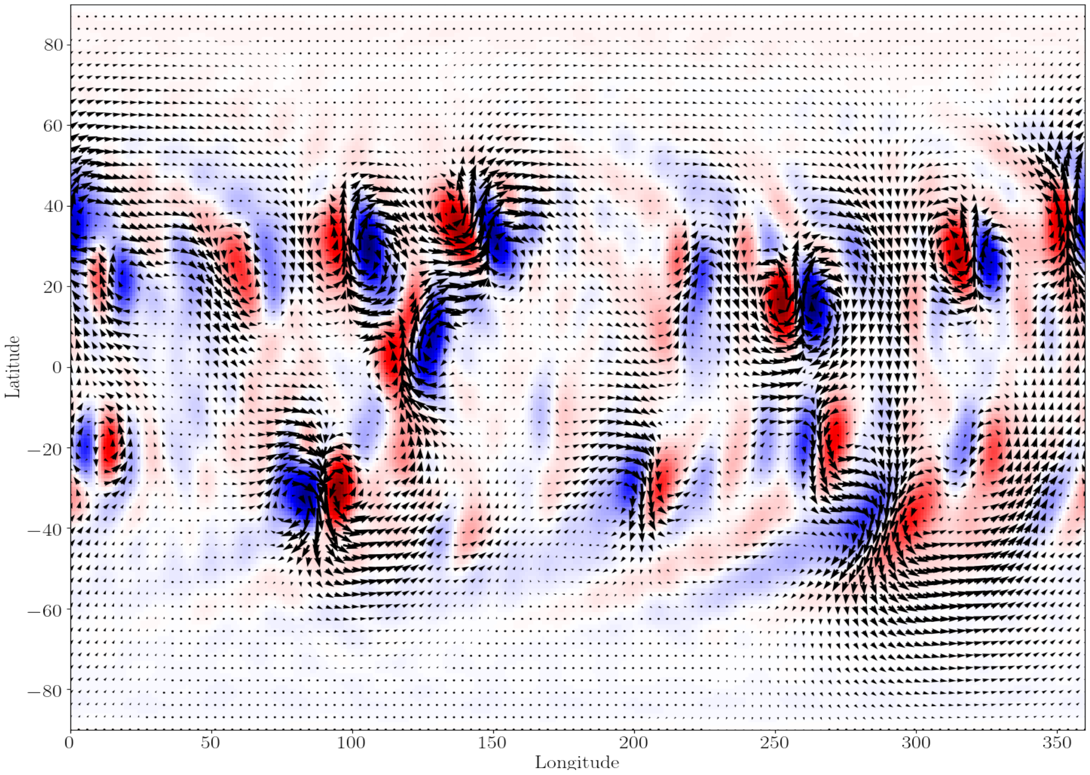

Fig. 3.12 Color map showing the distribution of B_r at CR3952 (April 1991) of J11 (as in Figure 3.6), with $\mathbf{A}_0$ overlaid.

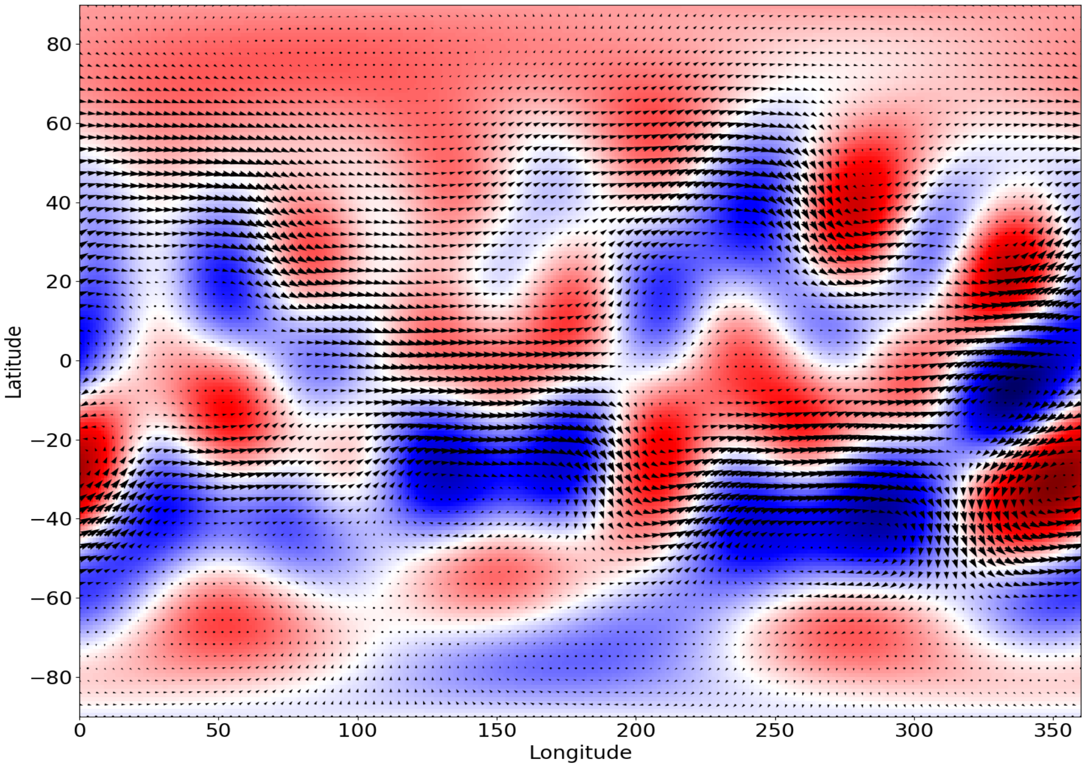

Fig. 3.13 Color map showing the distribution of B_r at CR1843 (April 1991) of Wilcox with $\mathbf{A}_0$ overlaid.

For this individual rotation, it is plausible that we could group the regions of oppositely signed magnetic flux in Figure 3.13 (Wilcox), but nowhere nearly as clearly as in that from the J11 simulation. Further, the active latitudes are less well defined, although the magnetic field strength does seem to peak at those latitudes (as opposed to the mean–field Figure 3.10(a). We propose that this analysis furthers the idea that Wilcox harmonics is best used to represent the larger scale magnetic fields, as employed in Chapter 2.

3.6 A Planar Bipole

In DeVore (2000), the author derives an analytical expression for the helicity injection associated with the insertion of a bipole, . They assume no background field, and that space is locally flat such that it can be treated as Cartesian. This work introduced the “deVore–Coulomb Gauge" (also introduced in Chapter 1):

$$\nabla \cdot \mathbf{A}_C = 0, \ \hat{\mathbf{n}} \cdot \mathbf{A}_C|_S = 0, \tag{3.28}$$

which is an additionally-constrained variant of the Coulomb gauge. Taking a scalar field, with potential form

$$\phi_c = B_0 d^3 \frac{x\cos\chi - y\sin\chi}{(x^2+y^2+(z+d)^2)^{3/2}}, \tag{3.29}$$

for a bipole with tilt angle χ, such that $\mathbf{B} = -\nabla\phi$, with

$$\mathbf{A}_C = \nabla \times \hat{\mathbf{z}} \int_z^\infty \phi_c \ \mathrm{d}z, \tag{3.30}$$

we have a well-described bipolar region with given tilt angle centred upon the origin of a two–dimensional Cartesian plane.

From these expressions, and the first term of equation (4.95), the authors were able to find an analytical expression for the helicity flux associated with the shear of differential shear: choosing a velocity vector of the form

$$\mathbf{v} = \Omega y \hat{\mathbf{x}}, \tag{3.31}$$

gives

$$\frac{\mathrm{d}H^{bmr}}{\mathrm{d}t}|_{t=0} = \frac{\pi\Omega B_0^2 d^4 \cos 2\chi}{8}. \tag{3.32}$$

Naturally, this expression is valid only at $t = 0$, and is shown to decay over a characteristic time $\tau^{bmr} \approx 2/|\Omega|$, giving a total helicity injection of

$$H_{bmr} \approx \frac{\tau^{bmr}}{2}\frac{\mathrm{d}H^{bmr}}{\mathrm{d}t}|_{t=0} \approx \mathrm{sgn}(\Omega)\frac{\pi}{32}\Phi^2\cos 2\chi, \tag{3.33}$$

where sgn denotes the sign function.

We now extend this to include meridional velocity. Taking

$$\mathbf{v} = u_\theta y \hat{\mathbf{y}}, \tag{3.34}$$

we have

$$\frac{\mathrm{d}H^{bmr}}{\mathrm{d}t}\Big|_{t=0,u_\theta} = \frac{\pi \sin(2\chi) B_0^2 d^4 u_\theta}{8}. \tag{3.35}$$

Then the ratio of the two fluxes is given by

$$\frac{\mathrm{d}H/\mathrm{d}t(\Omega)}{\mathrm{d}H/\mathrm{d}t(u_\theta)} = \frac{\Omega \cot(2\chi)}{u_\theta} \approx 20 \cot(2\chi). \tag{3.36}$$

Note that due to the scale of the analysis performed here (a small plane encompassing an active region) the radial factor making Ω into v_ϕ is dropped, making direct comparison less meaningful.

3.7 Hemispheric Balance of Helicity Fluxes

In this section we demonstrate analytically that the helicity fluxes associated with supergranular diffusion and differential rotation. In both cases, we make use of the gauge condition

$$\nabla \cdot \mathbf{A}_0 = 0 \Longleftrightarrow \frac{\partial(\sin(\theta) A_\theta)}{\partial \theta} + \frac{\partial A_\phi}{\partial \phi} = 0. \tag{3.37}$$

In this section we drop the subscript component of the $\mathbf{A}_0$ gauge notation for brevity under the assumption it is retained in meaning.

3.7.1 Differential Rotation

The helicity flux from differential rotation is

$$\begin{aligned} F_{v_\phi}(t) &= -2 \int_{r=R_\odot} A_\phi v_\phi B_r \,\mathrm{d}^2 x \\ &= -2R_\odot^3 \int_0^\pi \int_0^{2\pi} \Omega(\theta) \sin^2\theta A_\phi B_r \,\mathrm{d}\phi \mathrm{d}\theta. \end{aligned} \tag{3.38}$$

Now,

$$
\begin{aligned}
R_\odot \sin^2\theta A_\phi B_r &= \sin^2\theta \frac{1}{\sin\theta}\left[\frac{\partial}{\partial\theta}(\sin\theta A_\phi) - \frac{\partial A_\theta}{\partial\phi}\right] A_\phi \\
&= \frac{1}{2}\frac{\partial}{\partial\theta}\left(\sin^2\theta A_\phi^2\right) - \frac{\partial}{\partial\phi}\left(\sin\theta A_\phi A_\theta\right) + \sin\theta A_\theta \frac{\partial A_\phi}{\partial\phi} \\
&= \frac{1}{2}\frac{\partial}{\partial\theta}\left(\sin^2\theta A_\phi^2\right) - \frac{\partial}{\partial\phi}\left(\sin\theta A_\phi A_\theta\right) - \sin\theta A_\theta \frac{\partial}{\partial\theta}(\sin\theta A_\theta) \\
&\quad \text{[using (3.37)]} \\
&= \frac{1}{2}\frac{\partial}{\partial\theta}\left(\sin^2\theta A_\phi^2\right) - \frac{\partial}{\partial\phi}\left(\sin\theta A_\phi A_\theta\right) - \frac{1}{2}\frac{\partial}{\partial\theta}(\sin^2\theta A_\theta^2).
\end{aligned}
$$

Integration in ϕ reduces ϕ-derivative term to zero (by the periodicity of $\mathbf{A}$), such that $F_{v_\phi}(t)$ is given by

$$
F_{v_\phi}(t) = -R_\odot^2 \int_0^\pi \int_0^{2\pi} \Omega(\theta)\frac{\partial}{\partial\theta}\left(\sin^2\theta\left(A_\phi^2 - A_\theta^2\right)\right) \mathrm{d}\phi \mathrm{d}\theta. \tag{3.39}
$$

For the case of uniform rotation $\Omega(\theta) = \Omega_0$ (constant), we see that the integral vanishes. However, when Ω is a function of θ this is not the case, but we note that the flux is small because of the relative smallness of Ω_2 and Ω_4 as compared to Ω_0 (see equation (3.15)). As such, to leading order, the helicity flux associated with differential rotation is balanced between the hemispheres.

3.7.2 Supergranular Diffusion

$$
F_\eta = -2R_\odot\eta \int_0^{2\pi}\int_0^\pi \sin(\theta)\left(A_\theta\frac{\partial B_r}{\partial\theta} + \frac{1}{\sin(\theta)}A_\phi\frac{\partial B_r}{\partial\phi}\right)\mathrm{d}\phi\mathrm{d}\theta. \tag{3.40}
$$

We need only look at the integrand, such that we want to show

$$
\int_0^{2\pi}\int_0^\pi \sin(\theta)\left(A_\theta\frac{\partial B_r}{\partial\theta} + \frac{1}{\sin(\theta)}A_\phi\frac{\partial B_r}{\partial\phi}\right)\mathrm{d}\phi\mathrm{d}\theta = 0. \tag{3.41}
$$

We have

$$
\sin(\theta)A_\theta\frac{\partial B_r}{\partial\theta} + A_\phi\frac{\partial B_r}{\partial\phi} = \sin(\theta)A_\theta\frac{\partial B_r}{\partial\theta} + \frac{\partial(B_r A_\phi)}{\partial\phi} - \frac{\partial A_\phi}{\partial\phi}B_r, \tag{3.42}
$$

and note that

$$
\sin(\theta)A_\theta\frac{\partial B_r}{\partial\theta} = \sin(\theta)\frac{\partial(A_\theta B_r)}{\partial\theta} - \sin(\theta)B_r\frac{\partial A_\theta}{\partial\theta}, \tag{3.43}
$$

as well as

$$
\sin(\theta)B_r\frac{\partial A_\theta}{\partial\theta} = B_r\frac{\partial(\sin(\theta)A_\theta)}{\partial\theta} - \cos(\theta)B_r A_\theta, \tag{3.44}
$$

such that (substituting equation (3.44) into (3.43))

$$
\sin(\theta)A_\theta\frac{\partial B_r}{\partial\theta} = \sin(\theta)\frac{\partial(B_r A_\theta)}{\partial\theta} - B_r\frac{\partial(\sin(\theta)A_\theta)}{\partial\theta} + \cos(\theta)B_r A_\theta. \tag{3.45}
$$

Substituting (3.45) back into equation (3.42), our integrand becomes:

$$\sin(\theta)\frac{\partial(B_rA_\theta)}{\partial\theta}-B_r\frac{\partial(\sin(\theta)A_\theta)}{\partial\theta}+\cos(\theta)B_rA_\theta+\frac{\partial(B_rA_\phi)}{\partial\phi}-\frac{\partial A_\phi}{\partial\phi}B_r \tag{3.46}$$

$$=\sin(\theta)\frac{\partial(B_rA_\theta)}{\partial\theta}+\cos(\theta)B_rA_\theta+\frac{\partial(B_rA_\phi)}{\partial\phi}-B_r\left(\frac{\partial(\sin(\theta)A_\theta)}{\partial\theta}+\frac{\partial A_\phi}{\partial\phi}\right) \tag{3.47}$$

$$=\sin(\theta)\frac{\partial(B_rA_\theta)}{\partial\theta}+\cos(\theta)B_rA_\theta+\frac{\partial(B_rA_\phi)}{\partial\phi}\quad\text{[by (3.37)]} \tag{3.48}$$

$$=\frac{\partial(\sin(\theta)B_rA_\theta)}{\partial\theta}+\frac{\partial(B_rA_\phi)}{\partial\phi}. \tag{3.49}$$

The first integral term is zero due to the $\sin(\theta)$ term, and the second term is zero as B_rA_ϕ is periodic in ϕ. As such, $F_\eta = 0$ over the whole sphere. We stress that this is not at all obvious, given that the distribution of **B** is not regular across the photosphere.

3.8 Summary and Conclusions

To summarise, we have used surface flux transport models to estimate the amount of magnetic helicity injected into the solar corona through evolution of the large-scale magnetic field on the solar surface, on solar cycle time-scales. We find a consistent pattern whereby negative/positive helicity is systematically injected at high latitudes in the northern/southern hemisphere. In the lower-latitude wings of the magnetic butterfly diagram, the net helicity injection over a solar cycle is usually opposite to this in sign, unless the flux emergence is dominated by early active regions far from the equator. The overall helicity injection rate is therefore a balance between these high and low latitude contributions, and thus quite sensitive to the details of the flux transport model.

Using the 27-cycle J11 simulation driven by statistical active region emergence (Jiang et al., 2011), we have found that the rate of helicity injection in any given cycle correlates well with the end-of-cycle axial dipole moment. This is in agreement with the previous results of Chapter 2 (Hawkes and Berger (2018)) using lower resolution WSO magnetogram data, where we found a similar relation with the polar field for Solar Cycles 20-23. Compared to that study – which extended the earlier work of Berger and Ruzmaikin (2000) – the models in this chapter have higher spatial resolution for the magnetic field. We also include the helicity flux from meridional velocity and supergranular diffusion, although we have shown that this is essentially negligible in comparison with the flux from solar rotation.

We compared our results with that offered by the high–resolution Wilcox spherical harmonics (the lower–harmonics of which were employed in Chapter 2). We found that even when the full resolution of their data is employed, it still cannot resolve the intricacies needed to fully describe active region emergence and evolution. Their helicity fluxes did not show any sign of the intensive latitude dependence uncovered here: the helicity time–fluxes did not notably vary in structure when compared to the results of Chapter 2. The

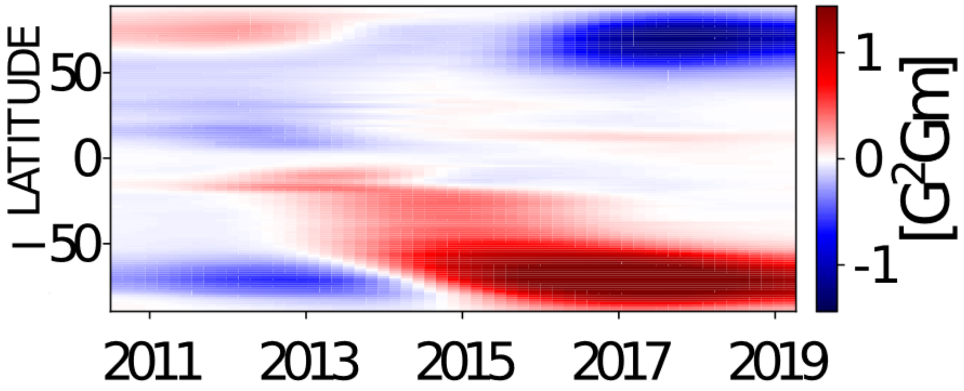

Fig. 3.14 Time–averaged large scale (their $\bar{\mathbf{A}} \cdot \bar{\mathbf{B}}$) as calculated by Pipin et al. (2019) (their Figure 5a, reproduced here).

order of magnitude of the fluxes from v_ϕ (as compared to J11 and W18) is fairly similar, but that from v_θ was notably lower. This is associated with the decreased θ–complexity of the vector potential that comes with a lower resolution magnetogram.

Finally, we provided a small number of analytical results regarding helicity fluxes both for individual AR's and entire-Sun regions. In particular, we proved that (perhaps unsurprisingly) helicity flux from uniform rotation (perhaps unsurprisingly) and supergranular diffusion (perhaps surprisingly) is balanced across the hemispheres. We also extended the results of DeVore (2000) to encompass meridional velocity, and calculated a rough ratio of fluxes.

Recently, Pipin et al. (2019) have published latitude-time maps of $\mathbf{A}_0 \cdot \mathbf{B}$ (they call the gauge $\mathbf{A}_P$) for 2010–2019 using vector synoptic magnetograms from the HMI instrument on Solar Dynamics Observatory. Whilst these show only the local helicity density in the solar photosphere (not the **flux** of helicity out of the Sun), they are nonetheless interesting to compare with our results. In particular, we compare with their Figure 5(a) (reproduced here in Figure 3.14) showing the longitude-averaged helicity density. At low latitudes, the helicity density shows a similar tendency to our helicity flux, namely net negative earlier in the cycle and net positive later in the cycle (cf. our Figure 3.9). However, at higher latitudes, the helicity density changes sign around 2014, following our sign pattern only in the first half of the cycle. Given the pioneering nature of these vector synoptic maps, and inherent uncertainties outside of active regions, it will be interesting to see whether this pattern is confirmed by other instruments.

We emphasize that we have computed only the flux of relative magnetic helicity out of the Sun. Once in the corona, the fate of this helicity depends on whether it is ejected onto a magnetic field line whose other end is open into the heliosphere, or one whose other end closes back to the solar surface. Depending on the relative injection at their two footpoints, closed field lines can store helicity within the corona, releasing it only in the form of sporadic coronal mass ejections (Bieber and Rust, 1995; Low, 1994). The details of this process require time-dependent modelling of the magnetic field structure in the corona, which is beyond the scope of this chapter. See Yeates and Hornig (2016) for some preliminary calculations in this regard.

Chapter 4

Spatial Scales and Locality of Magnetic Helicity

The research presented in this chapter has been published in the journal Astronomy and Astrophysics, under the title "Spatial Scales and Locality of Magnetic Helicity": see Prior et al. (2020). This work was the result of a close collaboration between myself and Chris Prior in particular. I was involved in developing the research idea, performed the vast majority of the data analysis and wrote large sections of the text. Work which is not my own has been labelled as so.

4.1 Introduction

As we have discussed in Chapter 1, magnetic helicity plays an important role in studies of MHD turbulence in general, and dynamo theories of magnetic energy generation in particular (*e.g* Blackman and Brandenburg (2003); Brandenburg et al. (2016); Sur et al. (2007); Vishniac and Cho (2001)). In a two scale kinematic dynamo, the large scale energy can increase exponentially. This poses a problem for magnetic helicity conservation. If the large scale magnetic helicity increases exponentially, then the small scale field must have an equal and opposite helicity which also blows up. Dissipation of the small scale helicity may not be physically feasible.

A solution to this problem lies in making the dynamo inhomogeneous – the dynamo operates in one region of space (e.g. the base of the convection zone in an interface dynamo) and excess magnetic helicity is carried away (Brandenburg, 2009; Vishniac and Shapovalov, 2013). However, to model this process properly, we need to be able to specify how helicity is spatially distributed.

Another area where helicity localization could be useful is in the study of solar activity. Many studies show how magnetic helicity can flow from the interior into active regions (*e.g.* Berger and Ruzmaikin (2000); Dalmasse et al. (2014); Kusano et al. (2002); Park et al. (2008); Pevtsov (2003); Prior and MacTaggart (2019)). A knowledge of how this helicity is distributed within an active region may help on the understanding and prediction of flares and coronal mass ejections. Scale dependence of magnetic helicity can also help in understanding the evolution of turbulence in the solar wind (Brandenburg et al. (2011)).

Whilst one can attempt to define helicity density as the quantity

$$H_{den} = \mathbf{A} \cdot \mathbf{B}, \tag{4.1}$$

this is in no sense gauge invariant, as gradient fields can be added to **A** without changing the magnetic field. Secondly, it does not represent spatially localised information: in a particular gauge such as Coulomb gauge, **A** is already an integral over the entire magnetic field, and is thus non-local. This has mathematical grounding – we've shown that helicity is associated with the Gauss linking number, for which we must take a double integral across all space. If we only have information about a small patch of field, there is no way of knowing how a field line within this patch goes on to twist and writhe around the rest of the field.

In Section 4.2 we will review various methods of obtaining localized or semi-localized measures of helicity. First, the relative helicity gives a gauge-invariant measure when the volume is not bounded by a magnetic surface. In general these measures are not additive in the sense that the helicity of all space may not equal the sum of helicities of subvolumes. Next, we show that absolute measures can be found for nested simply connected shells (e.g. concentric spheres). These measures do display additivity, but not in the sense that we would like. Third, we discuss Fourier decompositions of helicity, which help to provide information on how helicity behaves on various scales, but without information on locality. We also discuss field line helicities which measure how one chosen field line interlinks with all other lines. This quantity can be used to accurately quantify reconnection activity in magnetic fields (Prior and Yeates, 2018). The decomposition of helicity into contributions from individual fieldlines is still not localized.

In Section 4.3 we reintroduce the Winding Gauge $\mathbf{A}^W$, which is shown to measure the mean winding of fieldlines within a volume. We show that the winding gauge is infact merely a two–point winding–weighted correlation, which forms the basis of our definition of a gauge–free magnetic helicity, requiring no vector potential.

Section 4.4 provides a background to wavelet transforms and multiresolution analysis as a solution to the localisation problems. We also give a formal introduction of the full 3–D wavelet transform and its application to the helicity integral, with some illustrative examples. Further, we demonstrate how it is efficiently calculated numerically. Section 4.5 provides examples of how the wavelet multiresolution helicity formulation can be applied in practice. This includes a pair of twisted flux ropes which present a confusingly null spectral decomposition; the multiresolution helicity decomposition is shown to resolve the spatial separation of the system's entanglement. A second example of a pair of interlinked twisted flux ropes demonstrates how the decomposition can separate out the contributions from large scale linking and smaller scale twisting, as well as correctly assessing the localisation of helicity. We also demonstrate how the directionality component of a wavelet expansion can be useful, and consider whether the Fourier and Wavelet spectra should be in agreement. In Section 4.6 we consider the application of a double multiresolution wavelet decomposition to our geometric two-point correlation definition of helicity (if we decompose the magnetic field within the correlation vector). This is used to derive a linear helicity-energy decompositions for both magnetic and the field line helicity. Section 4.7 considers an example of a reconnecting magnetic braid, based on the numerical experiments. The field line helicity multiresolution analysis is utilised here. In particular we show that the field's twisted structure and its field line entanglement balance their helicity fluxes at differing spatial scales. Further we show that the growth and then decay in magnetic energy of this system is highly correlated with the field line helicity relaxation at the dominant spatial scales. In Section 4.8 we apply the multiresolution decomposition to helicity flux, with an application of a surface flux transport model, and finally conclude in Section 4.9.

4.2 Existing Helicity Decompositions

Suppose the volume V is not bounded by a magnetic surface ($\mathbf{B}\cdot\hat{\mathbf{n}}\neq 0$). Then, as we have previously discussed, this introduces a gauge dependence to the helicity integral: given some function Φ we can let $\mathbf{A}_G=\mathbf{A}+\nabla\Phi$, which induces a non-physical change in helicity corresponding to

$$H_G = H + \int_S \Phi\mathbf{B}\cdot\,\mathrm{d}\mathbf{S}, \tag{4.2}$$

which is only resolved if the magnetic field is closed.

4.2.1 Relative helicity

To circumvent this problem, as we have previously discussed, Berger and Field (1984) introduced a gauge invariant helicity referred to as relative helicity. Recall that relative helicity gives the helicity of our magnetic field $\mathbf{B}$ within some subvolume of space V relative to a second field $\mathbf{B}_0$ by taking the difference between the helicity of the fields when we integrate over all space, with the requirement that $\mathbf{B}\cdot\hat{\mathbf{n}}=\mathbf{B}_0\cdot\hat{\mathbf{n}}$ on the surface of V. This difference is independent of the details of the fields outside V. However, relative helicity is unsuitable for defining a local density as it does not have the property of additivity. If V is decomposed into subvolumes, the summation of relative helicities from each subvolume may not equal the total relative helicity if we considered the entirety of V. Further, the reference field may not be smooth across boundaries of sub-domains.

4.2.2 Absolute helicity

An alternate approach which allows for additivity within **concentric** shells is based on orthogonal field decompositions, for which an example in cylindrical geometries is given in Low (2015). For volumes bounded by arbitrary simply-connected surfaces, an generalised absolute helicity measure is given in Berger and Hornig (2018). The authors first generalize the toroidal-poloidal decomposition of magnetic fields (e.g. Moffatt (1978)) to geometries without the symmetry of a plane or a sphere. Within this decomposition, we have $\mathbf{B} = \mathbf{B}_P + \mathbf{B}_T$ where the poloidal field has no normal current, $\hat{\mathbf{n}} \cdot \mathbf{J_P} = 0$ and the toroidal field is divergence free and has no normal component, $\hat{\mathbf{n}} \cdot \mathbf{B_T} = 0$. Similarly, $\mathbf{A} = \mathbf{A}_P + \mathbf{A}_T$. In radially asymmetric geometries, the poloidal field can acquire an extra piece, the *shape field* $\mathbf{B}_S$. From this, the authors then define an absolute magnetic helicity

$$H_A = \int_{\mathrm{V}} (2\,\mathbf{A_P} \cdot \mathbf{B_T} + \mathbf{A_P} \cdot \mathbf{B}_S)\,\mathrm{d}^3\mathrm{x}. \tag{4.3}$$

The shape contribution can be zero for cases such as a sphere, as it possesses of the radial symmetry. This helicity can be calculated on successively larger shells, for example concentric spheres; the total helicity within some radius R will be the sum of the helicities of shells from $r = 0$ to $r = R$.

In the case of a cube, say, this expression allows us to properly calculate the helicity captured within any analytical domain: one definition of spatial helicity could be formed by continuous transformations in scale and shape, although this would not preserve additivity (as with relative helicity) as the cubes are not themselves nested. We will explore such a definition of localised helicity, and the shape field itself, in Chapter 5.

4.2.3 Fourier spectra

The splitting of magnetic fields into different scales is core to the study of many magnetohydrodynamical systems: Verma (2004) provides an in-depth review of turbulent magnetohydrodynamic fields, which have energy interchanges occurring across a spectrum of spatial scales. Following Blackman (2004, 2015); Subramanian and Brandenburg (2005), we can write the magnetic energy spectrum as

$$E_k = \int |\tilde{\mathbf{B}}|^2 k^2\,\mathrm{d}\Omega_\mathrm{k}, \tag{4.4}$$

where $k = ||\mathbf{k}||$, and Ω_k represents a shell in wave space given by all wavenumbers $k_- \leq k < k_+$ for which $k_\pm = ||\mathbf{k}|| \pm 0.5$. A tilde represents a vector field which has been Fourier transformed. In Fourier space, we have the direct relation $\tilde{\mathbf{A}} = -i\mathbf{k} \times \tilde{\mathbf{B}}/k^2$. We can thus write

$$H_k = \int (\mathbf{k} \times \tilde{\mathbf{B}}^*(\mathbf{k})) \cdot \tilde{\mathbf{B}}(\mathbf{k})\,\mathrm{d}\Omega_\mathrm{k}, \tag{4.5}$$

and as such we have a gauge invariant measure of magnetic helicity at scale $L = 2\pi/k$ which has the property of additivity (see for example Blackman and Brandenburg (2003); Brandenburg et al. (2016); Démoulin (2007); Moffatt (1978)). Note that this gauge invariance is limited to periodic or infinite domains, as these are the inherent restrictions to the Fourier transform.

It is important to note that the Fourier decomposition can produce counter–intuitive results. Consider an infinite system of flux tubes which are themselves infinite in z, and alternately twisted flux tubes the $x-y$ plane, but have a constant B_z everywhere. The Fourier transform of magnetic helicity would be zero at all scales (Asgari-Targhi and Berger, 2009). To see this, we note that as B_z is constant, it has power only at the $k=0$ (the mean) scale. Conversely, B_x and B_y have non–zero power everywhere except at $k=0$. As such, their product will always be zero. Alternatively, we can view the helicity as having net zero power at all fourier scales due to contributions from positively and negatively twisted flux tubes.

Additionally, the fourier spectrum offers no information regarding the locality at any scale. The windowed Fourier transform can help with this by convolving an envelope function with compact support on top of the infinite sinusoidal functions. Taking the Fourier transform using such a reduced analytic form gives an idea of the variations corresponding to scales at a given locality, but has two downsides (aside from the requirement of periodicity): the transformation does not provide an orthogonal basis, which is required to maintain additivity. Secondly, the window size is fixed, meaning we cannot separate intense fluctuations which are on smaller scales than the window size from weak contributions on the same scale as the window size.

4.2.4 Two point correlation functions

Helicity H_k can be related to the magnetic energy E_k via the transform of the two-point correlation tensor M_{ij}:

$$M_{ij}(\mathbf{X},\mathbf{x}) = B_i(\mathbf{X}-\mathbf{x})B_j(\mathbf{X}+\mathbf{x}). \tag{4.6}$$

In a periodic domain one can transform this function over the displacement $\mathbf{x}$ to obtain a skew-symmetric tensor function $\tilde{M}_{ij}(\mathbf{X},\mathbf{k})$ of both position and scale, and for isotropic (non–directional) turbulence this can be decomposed as

$$\tilde{M}_{ij} = \left[(\delta_{ij} - k^u_i k^u_j)2E_k - \mathrm{i}k^u_l \varepsilon_{ijl} k H_k\right]/8k^2\pi, \tag{4.7}$$

where k^u_i is the i^{th} component of the unit vector of $\mathbf{k}$ and ε_{ijk} the alternating tensor (Brandenburg et al., 2016; Roberts and Soward, 1975). So the energy is the trace of the tensor $\tilde{M}_{ij}$ and the helicity represented by the off-diagonal components. This is a potentially powerful relation relating the magnetic helicity and energy on a given Fourier shell at **each point** of space.

In this chapter, we intend to provide a decomposition of magnetic helicity which preserves this additivity and scale dependence, whilst also providing information about the spatial locality of terms contributing to the power at each scale. Key to our study is the lack of any assumptions about the boundary conditions of the magnetic field. One result is a variant of (4.7) which can retain information on the spatial distribution of the energy/helicity decomposition even in highly inhomogeneous systems.

4.2.5 Fieldline helicity

For a given field line γ we can define a field line helicity (Berger, 1988; Moratis et al., 2019; Prior and Yeates, 2014; Yeates and Hornig, 2013; Yeates and Page, 2018)

$$\mathscr{A}(\gamma) = \int_{\gamma} \mathbf{A}\cdot\mathbf{T}\,\mathrm{d}s, \tag{4.8}$$

where $\mathbf{T} = \mathbf{B}/||\mathbf{B}||$ is the unit tangent vector along the fieldline, and s is the arclength parameter of its curve. The fieldline helicity measures the average winding of all field lines around an individual field line, in a similar fashion to the winding gauge developed in Prior and Yeates (2014). If we imagine tracing the field lines between two planes, the field line helicity associated with a field line starting at each point (x_l, y_l) on some initial plane (typically taken as the lower boundary of a system) gives a two-dimensional density within that plane. This definition could be extended to three dimensions via vertical translations of the initial plane, but this would not preserve additivity (some lines would be counted multiple times, etc). Further, the quantity is not gauge invariant. There is a relative field line helicity version of this quantity, whose definition comes attached with various technical complexities (Moratis et al., 2019; Yeates and Page, 2018), but is an invariant for each individual field line. Further, there is some remaining gauge dependence.

4.3 Helicity is (almost) Winding

Given any integral representation for $\mathbf{A}$, the helicity integral becomes a double integral involving $\mathbf{B}$ evaluated at two different points. For example, in the Coulomb gauge with $\mathbf{A}$ expressed via the Biot-Savart law, helicity is written as

$$H = -\frac{1}{4\pi}\int_V \int_{V'} \frac{\mathbf{B}\cdot\mathbf{r}\times\mathbf{B}'}{r^3}\,\mathrm{d}^3x\,\mathrm{d}^3x'. \tag{4.9}$$

The integrand can be regarded as a two-point correlation function for the magnetic field (Subramanian and Brandenburg, 2005).

Recall that the winding gauge $\mathbf{A}^w$ (Prior and Yeates, 2014), given by

$$\mathbf{A}^w(x,y,z) = \frac{1}{2\pi}\int_{S_z} \frac{\mathbf{B}(x',y',z)\times\mathbf{r}}{r^2}\,\mathrm{d}x'\,\mathrm{d}y', \tag{4.10}$$
$$\mathbf{r} = (x-x', y-y', 0),$$

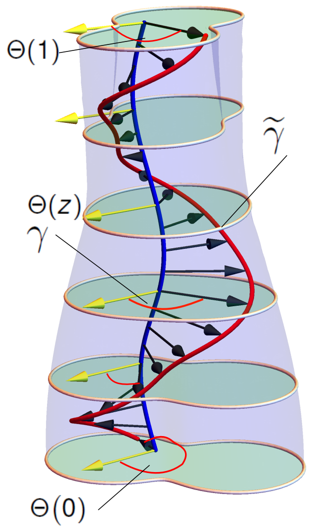

(a)

Fig. 4.1 Illustrations of the geometrical interpretation helicity through the winding number. The winding is defined by the mutual angle Θ between two curves γ and $\tilde{\gamma}$. The yellow arrows depict a fixed direction and the black arrows the joining vector of the two curves in a given plane S_z used to define Θ. This figure was created by Chris Prior, a co-author.

gives magnetic helicity the physically grounded definition of the flux-weighted average winding of all pairs of field line of **B** with each other, *i.e.*

$$
\begin{aligned}
H(\mathbf{B}) &= \frac{1}{2\pi}\int_V \int_{S_z} \mathbf{B}(x,y,z)\cdot \frac{\mathbf{B}(x',y',z)\times \mathbf{r}}{r^2}\ \mathrm{d}^2x\ \mathrm{d}^2x'\ \mathrm{d}z && (4.11)\\
&= \frac{1}{2\pi}\int_{z_0}^{z_1}\int_{S_z}\int_{S'_z} B_z(\mathbf{x})B_z(\mathbf{x}')\frac{\mathrm{d}}{\mathrm{d}z}\Theta(\mathbf{x},\mathbf{x}')\ \mathrm{d}^2x\ \mathrm{d}^2x'\ \mathrm{d}z. && (4.12)
\end{aligned}
$$

To see this, consider a volume V as in Figure 4.1 which can be sliced into parallel planes of $z =$ constant. The volume can either be infinite in x and y, or the volume can be magnetically closed apart from its top and bottom z–slices. Take two field lines γ and $\tilde{\gamma}$ of **B** that rise monotonically in z throughout $\mathscr{V}$, so that we can parametrize them as $\gamma = (\gamma_x(z),\gamma_y(z))$, $\tilde{\gamma} = (\tilde{\gamma}_x(z),\tilde{\gamma}_y(z))$.

Then, in any planar slice S_z, we can use the co-ordinates of the field lines to define the angle between the two curves within the plane,

$$
\Theta(\gamma,\tilde{\gamma},z) = \arctan\left(\frac{\gamma_y(z)-\tilde{\gamma}_y(z)}{\gamma_x(z)-\tilde{\gamma}_x(z)}\right). \qquad (4.13)
$$

Integrating the change in this angle Θ over the z planes, as we follow the curves from $z = z_0$ to $z = z_1$, is equal to the pairwise winding number

$$
\begin{aligned}
\mathscr{L}^W(\gamma,\tilde{\gamma}) &= \frac{1}{2\pi}\int_{z_0}^{z_1}\frac{\mathrm{d}}{\mathrm{d}z}\Theta(\gamma,\tilde{\gamma},z)\,\mathrm{d}z && (4.14)\\
&= \frac{1}{2\pi}\int_{z_0}^{z_1}\frac{(\gamma_2'-\tilde{\gamma}_2')(\gamma_1-\tilde{\gamma}_1)-(\gamma_1'-\tilde{\gamma}_1')(\gamma_2-\tilde{\gamma}_2)}{(\gamma_1-\tilde{\gamma}_1)^2+(\gamma_2-\tilde{\gamma}_2)^2}\,\mathrm{d}z. && (4.15)
\end{aligned}
$$

This can also be written as

$$\mathscr{L}^W(\gamma,\tilde{\gamma}) = \frac{1}{2\pi}\Big(\Theta(\gamma,\tilde{\gamma},z_1) - \Theta(\gamma,\tilde{\gamma},z_0)\Big) + N, \tag{4.16}$$

where z_0 and z_1 define the bottom and top boundaries of $\mathscr{V}$, and N counts the number of complete rotations between the curves as over the entire traversal. This means that $\mathscr{L}^W(\gamma,\tilde{\gamma})$ is invariant under any continuous deformation of the curves that does not move their end-points.

The relationship between winding angle and winding number was generalised in Berger and Prior (2006) to allow for curves which are not monotonic in z by splitting γ into n sections $\gamma^{(1)},\ldots,\gamma^{(n)}$. These subsections of the curve are defined as being bounded by the the $n-1$ turning points where $\mathrm{d}\gamma_z/\mathrm{d}z = 0$. For each section, one defines the indicator function

$$\sigma^{(i)} = \begin{cases} 1 & \text{if } \mathrm{d}\gamma_z^{(i)}/\,\mathrm{d}z > 0, \\ -1 & \text{if } \mathrm{d}\gamma_z^{(i)}/\,\mathrm{d}z < 0, \\ 0 & \text{otherwise.} \end{cases} \tag{4.17}$$

Then, by splitting $\tilde{\gamma}$ in a similar way, and defining $\widetilde{\sigma}^{(j)}$, we have that $\mathscr{L}^W(\gamma,\tilde{\gamma})$ is given by

$$\mathscr{L}^W(\gamma,\tilde{\gamma}) = \sum_{i=0}^{n}\sum_{j=0}^{\tilde{n}} \frac{\sigma^{(i)}\widetilde{\sigma}^{(j)}}{2\pi}\int_{z_{ij}^{\min}}^{z_{ij}^{\max}} \frac{\mathrm{d}}{\mathrm{d}z}\Theta(\gamma^{(i)},\tilde{\gamma}^{(j)},z)\,\mathrm{d}z, \tag{4.18}$$

where $[z_{ij}^{\min}, z_{ij}^{\max}]$ is the mutual range of z values (if any) shared by the curve sections $\gamma^{(i)}$ and $\widetilde{\gamma}^{(j)}$. Once again, $\mathscr{L}^W(\gamma,\tilde{\gamma})$ is invariant to any continuous deformation of the curves that fixes their endpoints on the boundaries. Note that we still require that the curves are entirely confined within the side boundaries of the volume.

The winding gauge then requires that the field can be composed of a set of planar surfaces $V = \{S_z | z \in [z_0, z_1]\}$, and that if the volume is finite in x or y then the field $\mathbf{B}$ is tangent on the side surfaces. For the absolute helicity introduced by Berger and Hornig (2018) (and in Section 4.2.2), the authors showed that this two–point correlation relation can be obtained from a poloidal-toroidal decomposition, and extended it to more general domains which can be constructed from sets of simply connected surfaces.

Recall that it was also shown in Prior and Yeates (2014) that any other choice of gauge, and hence reference field, gives a helicity measure which is equivalent to choosing to measure the angle Θ with respect to a varying direction, whose rotation is non physical in that it isn't associated with the magnetic field. In Figure 4.1, this corresponds to a non–physical rotation of the yellow reference direction.

Prior and Yeates (2014) also showed that the field line helicity can be written as

$$\mathscr{A}(\gamma) = \frac{1}{2\pi}\int_{\gamma}\int_{S_z'} \frac{\mathbf{T}\cdot\mathbf{B}(x',y',z(s))\times\mathbf{r}_\gamma}{r_\gamma^2}\,\mathrm{d}s\,\mathrm{d}x'\,\mathrm{d}y', \tag{4.19}$$

$$\mathbf{r}_\gamma = (x'-\gamma_x, y'-\gamma_y, 0),$$

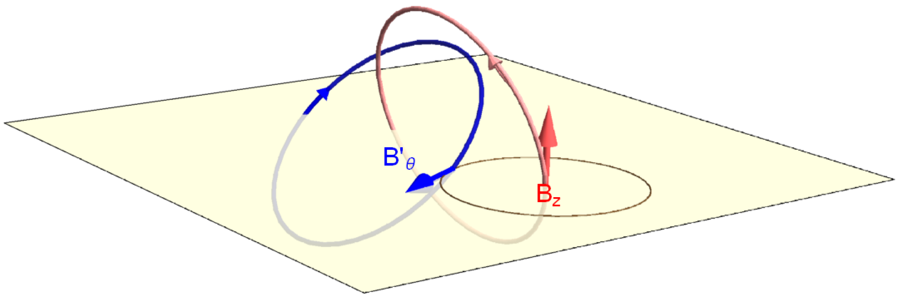

Fig. 4.2 Given two field lines, given in red and blue, product of B'_θ for the blue field line and B_z for the red line (according to the form associated with $\mathbf{B}\cdot\mathbf{r}\times\mathbf{B}'$ term) gives a measure of their mutual winding.

if the winding gauge is chosen, where $\mathbf{T} = \mathbf{B}/||\mathbf{B}||$.

4.3.1 A gauge independent measure of magnetic helicity

In (4.11), we note that the helicity is determined by a two–point correlation between $\mathbf{B}$ and $\mathbf{B}'$, given by $\mathbf{B}\cdot\mathbf{B}'\times\mathbf{r}$, which is equated directly with the field–weighted winding in (4.12) (also for the fieldline helicity in (4.19)). Thus, the two–point correlation measures the field–weighted entanglement of the magnetic field (see Figure 4.2), and is dependent only upon the magnetic field $\mathbf{B}$ itself. Even though such a definition was uncovered by use of the winding gauge (following the classical definition of magnetic helicity, $H = \int_V \mathbf{A}\cdot\mathbf{B}$), it still possesses all of the important properties which make magnetic helicity a well–conserved quantity worthy of study, based on only the interpretation as field–weighted winding rate $\mathrm{d}\theta/\mathrm{d}z$. In particular, it is invariant under ideal evolutions which vanish on the domain boundaries (Berger and Prior, 2006; Prior and Yeates, 2014) (i.e., magnetic flux does not exit the domain). And, crucially, it is well–conserved low plasma β relaxations (Russell et al., 2015). Neither of these properties require that we define a magnetic vector potential for the helicity.

As such, in this chapter we assert the two point correlation function as our fundamental definition of the magnetic helicity. To formally separate ourselves from the classical gauge definition, we define the following integral

$$\mathbf{C}(x,y,z) = \int_{S'_z} \frac{\mathbf{B}(x',y',z)\times\mathbf{r}}{r^2}\,\mathrm{d}x'\,\mathrm{d}y', \tag{4.20}$$

such that the product $\mathbf{B}\cdot\mathbf{C}$ then represents the total winding and field weighted two–point correlation of the field at a point (x,y) in the plane S_z with the whole field in that plane. If the magnetic field $\mathbf{B}$ is tangent on the side boundaries of the volume, then $\nabla\times\mathbf{C} = \nabla\times\mathbf{A}^w = \mathbf{B}$, and we can refer back to the classical magnetic helicity, but as we have discussed above $\mathbf{C}\cdot\mathbf{B}$ is a meaningful topological quantity even when this is not true.

We then have the following gauge–free, physically meaningful definitions of the helicity and field line helicity which place no requirements on the system's boundary conditions

$$H(\mathbf{B}) = \int_0^h \int_{S_z} \mathbf{B}\cdot\mathbf{C}\,\mathrm{d}x\,\mathrm{d}y\,\mathrm{d}z, \tag{4.21}$$

$$\mathscr{A}(\mathbf{B}) = \int_\gamma \mathbf{T}\cdot\mathbf{C}(\gamma)\,\mathrm{d}s. \tag{4.22}$$

Here, $[0,h]$ denotes the z range of the domain of interest. Further, in the style of (4.6), we can write

$$H = \int_0^h \int_{S_z} \int_{S_z'} M_W(\mathbf{x},\mathbf{x}')\,\mathrm{d}^2\mathrm{x}\,\mathrm{d}^2\mathrm{x}'\,\mathrm{d}z, \tag{4.23}$$

where

$$M_W(\mathbf{x},\mathbf{x}') = \frac{\mathbf{B}(\mathbf{x})\cdot\mathbf{B}(\mathbf{x}')\times\mathbf{r}}{r^2}, \tag{4.24}$$

is the two–point correlation scalar. We will often refer to $\mathbf{C}$ as the correlation function, to separate it meaningfully from $\mathbf{A}$, but strictly speaking only $\mathbf{B}\cdot\mathbf{C}$, or even M_W represent the true two–point correlation.

4.4 Helicity, Wavelets and Multiresolution Analysis

Now that we have established our measure of magnetic helicity, we move onto the task of spatially decomposing it. Crucially, our decomposition must be able to classify the magnetic helicity into components associated with regions of compact support within a given domain. Further, we require that this decomposition has a mathematically well–defined measure of scale, and that it possesses additivity. The latter is key to studies of magnetic helicity: the sum of the individual components must be representative of the whole. Clearly, the fourier transform is unsuitable and so we instead look to use a branch of signal analysis known as wavelet analysis, via a process known as multiresolution analysis.

We will focus on the set of wavelets known as discrete wavelets which form the discrete wavelet transform, in particular the multiresolution representation of this transform. There is also a continuous wavelet transform which is better suited for analytical functions or continuous signals, but we shall not use it here. For a more detailed introduction see *e.g.* Farge (1992) for a practical introduction in a fluid dynamic context, and Jawerth and Sweldens (1994) for more details on the underlying mathematics.

4.4.1 Haar wavelets

The Haar wavelets, in one dimension, are composed of a box function ϕ, known as the scaling function or father wavelet, which captures the mean behaviour of a function:

$$\phi(x) = \begin{cases} 1 & \text{if } 0 \le x \le 1, \\ 0 & \text{if } x > 1 \text{ or } x < 0, \end{cases} \tag{4.25}$$

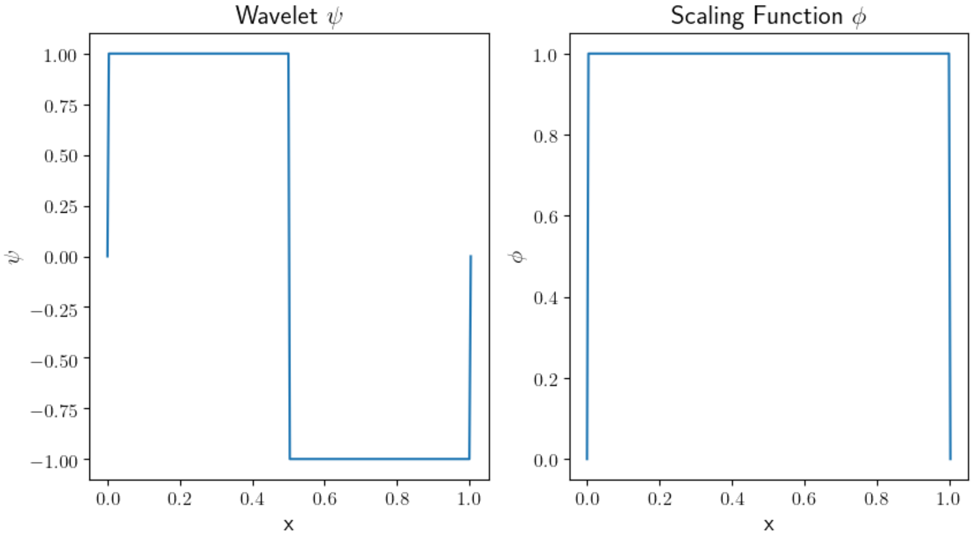

Fig. 4.3 Haar wavelet ψ and scaling function ϕ on the domain $[0,1]$ at scale 0.

and a simplistic step function ψ which captures the variation (4.26), which is known as the wavelet:

$$\psi(x) = \begin{cases} 1 & \text{if } 0 \leq x \leq 1/2, \\ -1 & \text{if } 1/2 < x \leq 1, \\ 0 & \text{if } x > 1 \text{ or } x < 0. \end{cases} \tag{4.26}$$

Neither the scaling or wavelet function are sufficient to describe a signal alone. We need only envisage a signal which embodies the properties of the scaling function, which the wavelet would be unable to classify (and vice–versa). Both functions are defined for all real x, and thus have the necessary compact support (they are fully localised). We plot them in Figure 4.3.

Then, the basic idea of a multiresolution analysis is that for some discrete signal on a domain $[0,1]$ (one can always scale this to any finite domain), we can choose a domain's spatial scales at which we wish to study the behaviour of the signal as factors of two *i.e.* $2^s, \ldots s \in 1,2,\ldots.$, as indicated in Table 4.1. For a given choice of scale s the functions (4.25)

Scale	Intervals (Locality)
0	$[0,1]$
1	$[0,\frac{1}{2}]$, $[\frac{1}{2},1]$
2	$[0,\frac{1}{4}]$, $[\frac{1}{4},\frac{1}{2}]$, $[\frac{1}{2},\frac{3}{4}]$, $[\frac{3}{4},1]$
3	$[0,\frac{1}{8}]$, $[\frac{1}{8},\frac{1}{4}]$, $[\frac{1}{4},\frac{3}{8}]$, $[\frac{3}{8},\frac{1}{2}]$, $[\frac{1}{2},\frac{5}{8}]$, $[\frac{5}{8},\frac{3}{4}]$, $[\frac{3}{4},\frac{7}{8}]$, $[\frac{7}{8},1]$

Table 4.1 Illustrative Examples of Scales and Locality

and (4.26) are mutually orthogonal and orthonormal with each other if suitably dilated and translated. A common notation, that we shall adopt, for these dilation/translation combinations is to write

$$\phi_{si}(x) = \sqrt{2^s}\phi\left(2^s x - i\right) \text{ and } \psi_{si}(x) = \sqrt{2^s}\psi\left(2^s x - i\right). \tag{4.27}$$

for a discretized domain into subsections indexed by i, each subsection of which has a compact support of width 2^{-s}. The statements of orthonormality and orthogonality can then be given as:

$$\int_0^1 \sqrt{2^s}\phi(2^s x - i)\sqrt{2^s}\psi(2^s x - j)\,\mathrm{d}x = 0, \tag{4.28}$$

$$\int_0^1 \sqrt{2^s}\phi(2^s x - i)\sqrt{2^s}\phi(2^s x - j)\,\mathrm{d}x$$
$$= \int_0^1 \sqrt{2^s}\psi(2^s x - i)\sqrt{2^s}\psi(2^s x - j)\,\mathrm{d}x = \delta_{ij}. \tag{4.29}$$

As such, wavelet analysis also provides us with a well-defined measure of scale s and locality i.

The Haar wavelet is designed to be orthonormal, such that

$$\int_0^1 \phi_{si}(x)\psi_{sj}(x)\,\mathrm{d}x = 0, \tag{4.30}$$

$$\int_0^1 \phi_{si}(x)\phi_{sj}(x)\,\mathrm{d}x = \int_0^1 \psi_{si}(x)\psi_{sj}\,\mathrm{d}x = \delta_{ij}. \tag{4.31}$$

One can also see some of these conditions can be extended for comparisons between scales,

$$\int_0^1 \phi_{si}(x)\psi_{s'j}(x)\mathrm{d}x = 0, \forall s' \geq s \text{ for } i \in 0,1,\ldots 2^s - 1 \text{ and } j \in 0,1,\ldots 2^{s'} - 1, \tag{4.32}$$

as well as

$$\int_0^1 \psi_{si}(x)\psi_{s'i'}(x)\mathrm{d}x = \delta_{\mathrm{ss'ii'}}. \tag{4.33}$$

Thus if we pick some base scale s_b the orthogonality conditions (4.31), (4.32) and (4.33) ensure it is possible to write

$$f(x) = \sum_{i=0}^{2^{s_b}-1} \langle \phi_{s_b i}|f\rangle\, \phi_{s_b i} + \sum_{s=s_b}^{\infty}\sum_{i=0}^{2^{s_b}-1} \langle \psi_{si}|f\rangle\, \psi_{si} \tag{4.34}$$

where

$$\langle g, f\rangle = \int_0^1 fg\,\mathrm{d}x. \tag{4.35}$$

for square integrable functions on $[0,1]$ (Jawerth and Sweldens, 1994). Daubechies et al. (1993) demonstrates that there are various other classes of functions ϕ and ψ with compact support which satisfy these conditions. The specific choice of ϕ and ψ can often be quite important for time series or image analysis (for discussions on the matter see *e.g.* Farge et al. (1996); Zhang et al. (2004)). However, the calculations we intend to perform depend less on the type of wavelet, and in what follows all example calculations use the Haar basis.

In practice the series (4.34) will be finite based on some maximum scale s_m, denoting the numerical resolution of the signal. It is also typical to choose $s_b = 0$, which prioritises the number of spatial scales used in the expansion, so that we have the following multiresolution approximation:

$$f(x) \approx \langle \phi_0 | f \rangle \, \phi_0 + \sum_{s=0}^{s_m} \sum_{i=0}^{2^s - 1} \langle \psi_{si}, f \rangle \, \psi_{si}. \tag{4.36}$$

We will use an equality sign for series such as (4.36) on the assumption it is understood this is actually an approximation due to the fact that our data is discrete.

4.4.2 Decomposing a function numerically

Numerically, wavelet co-efficients are calculated according to a filter methodology. The wavelet and scaling co-efficients are first resolved, simultaneously, at the the smallest possible spatial resolution n using a simplistic matrix multiplication. We provide an example of this below:

$$\begin{bmatrix} 1 & 1 & 0 & 0 & 0 & 0 & 0 & 0 \\ 1 & -1 & 0 & 0 & 0 & 0 & 0 & 0 \\ 0 & 0 & 1 & 1 & 0 & 0 & 0 & 0 \\ 0 & 0 & 1 & -1 & 0 & 0 & 0 & 0 \\ 0 & 0 & 0 & 0 & 1 & 1 & 0 & 0 \\ 0 & 0 & 0 & 0 & 1 & -1 & 0 & 0 \\ 0 & 0 & 0 & 0 & 0 & 0 & 1 & 1 \\ 0 & 0 & 0 & 0 & 0 & 0 & 1 & -1 \end{bmatrix} \cdot \begin{bmatrix} s_1 \\ s_2 \\ s_3 \\ s_4 \\ s_5 \\ s_6 \\ s_7 \\ s_8 \end{bmatrix} = \begin{bmatrix} s_{\phi_{n,0}} \\ s_{\psi_{n,0}} \\ s_{\phi_{n,1}} \\ s_{\psi_{n,1}} \\ s_{\phi_{n,2}} \\ s_{\psi_{n,2}} \\ s_{\phi_{n,3}} \\ s_{\psi_{n,3}} \end{bmatrix}. \tag{4.37}$$

Here, we are applying the Haar wavelet transform in matrix form (given by the left–most matrix) on a signal $S_8 = \{s_0, ..., s_8\}$, which gives us the wavelet co-efficients $s_{\phi_{n,0}}$ etc. The subscript $\phi_{n,0}$ refers to the co-efficient of the scaling function at spatial scale n (referring to the smallest scale) and index zero (in terms of its place along the axis). Note that we have used an orthogonal but not orthonormal filter for brevity.

Then, for each subsequent level of the expansion, we take advantage of the recursive nature of wavelets in terms of their scaling function. For the Haar wavelet, this takes the

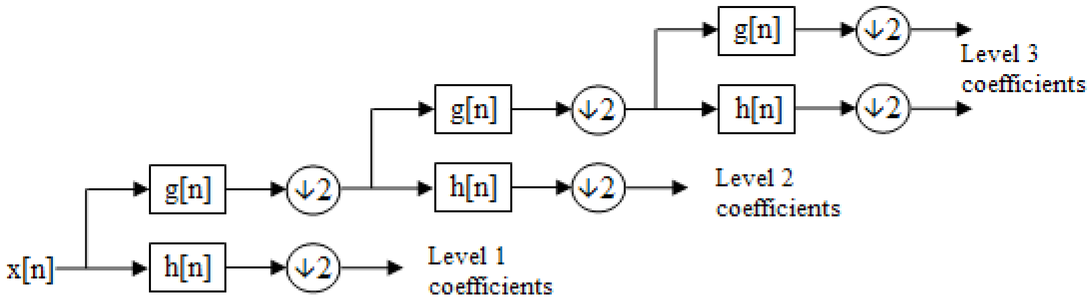

Fig. 4.4 Pictorial demonstration of the determination of wavelet co-efficients at each spacial scale. $g[n]$ and $h[n]$ refer to the recursive co-efficients of the scaling function and wavelet respectively (as per (4.38) and (4.39)). Level 1 corresponds to what we refer to as the n'th level of decomposition.

form

$$\psi(t) = \phi(2t) - \phi(2t+1) = \sum_n h[n]\psi(2t+n), \tag{4.38}$$

$$\phi(t) = \phi(2t) + \phi(2t+1) = \sum_n g[n]\psi(2t+n), \tag{4.39}$$

where a decreasing factor of t refers to a increasingly large spatial scale according to the definition given in (4.27). $g[n]$ and $h[n]$ are the recursive constants, in this case seen to be $\{1,-1\}$ and $\{1,1\}$ respectively, which can be seen from the structure of the wavelet and scaling functions shown in Figure 4.3. As such, we have

$$\begin{bmatrix} 1 & 1 & 0 & 0 \\ 1 & -1 & 0 & 0 \\ 0 & 0 & 1 & 1 \\ 0 & 0 & 1 & -1 \end{bmatrix} \cdot \begin{bmatrix} s_{\phi_{n,0}} \\ s_{\phi_{n,1}} \\ s_{\phi_{n,2}} \\ s_{\phi_{n,3}} \end{bmatrix} = \begin{bmatrix} s_{\phi_{n-1,0}} \\ s_{\psi_{n-1,0}} \\ s_{\phi_{n-1,1}} \\ s_{\psi_{n-1,1}} \end{bmatrix}, \tag{4.40}$$

for the next largest scale of the decomposition (scale $n-1$). This process is repeated, for a signal of any length, as many times as required, as Figure 4.4 shows pictorially. Note that, in that figure, Level 1 corresponds to our n'th level decomposition, etc.

In Figure 4.5 we plot the successive approximations of a generic function $f(x) = 10\cos(x) + 5\sin(x) + ((x)^3)/10.0 + \cos(2x) + 10\sin(3x)((2-x)^2)/4.0$, $0 \leq x \leq 2\pi$, chosen such that it does not posses periodicity (and as such cannot be accurately decomposed using a Fourier transform) by adding on each successive scale approximation. We took a numerical resolution of 128, which gives a wavelet expansion up to spatial scale 2^{-7}. Throughout this chapter, a spatial scale of 2^{-n} refers to a length scale of $L2^{-n}$, where L is the length scale of the whole volume of interest. In the first panel, we plot the analytic function, followed by the contribution from the scaling (mean) function, $\langle\phi_0|f(x)\rangle\,\phi_0(x)$, denoted by $f_\phi(x)$, and then we successively add on contributions from each scale decomposition (denoted by $f_{\psi,i}$ for the addition of the i'th scale).

Further, in Figure 4.6, we plot the coefficients themselves (without the wavelet term) from each individual scale (i.e. $\langle \psi_{si} | f(x) \rangle$)) for each s. Note that these co-efficients are not defined at every individual point, but for ranges of points, the width of which coincides with the scale under analysis.

4.4.3 Three dimensional Multiresolution Analysis

In a three-dimensional Cartesian domain V, we must expand the behaviour along each direction via a one dimensional multiresolution expansion (Jawerth and Sweldens (1994)). By writing each function as a multiresolution expansion we will encounter eight types of combinations (four in 2–D) for each scale s:

$$\psi^{\mu}_{slmn}(\mathbf{x}) = \begin{cases} \phi_{sl}(x)\phi_{sm}(y)\phi_{sn}(z) & \text{if } \mu = 1, \\ \psi_{sl}(x)\phi_{sm}(y)\phi_{sn}(z) & \text{if } \mu = 2, \\ \phi_{sl}(x)\psi_{sm}(y)\phi_{sn}(z) & \text{if } \mu = 3, \\ \phi_{sl}(x)\phi_{sm}(y)\psi_{sn}(z) & \text{if } \mu = 4, \\ \psi_{sl}(x)\phi_{sm}(y)\psi_{sn}(z) & \text{if } \mu = 5, \\ \psi_{sl}(x)\psi_{sm}(y)\phi_{sn}(z) & \text{if } \mu = 6, \\ \phi_{sl}(x)\psi_{sm}(y)\psi_{sn}(z) & \text{if } \mu = 7, \\ \psi_{sl}(x)\psi_{sm}(y)\psi_{sn}(z) & \text{if } \mu = 8. \end{cases} \tag{4.41}$$

$\mu = 1$ measures the mean term within the volume, and is direction–free. Then, $\mu = 2,...,7$ measure the variation from one corner of the volume (assumed to be a cuboid) to every other corner. The specific direction that each $\mu > 1$ corresponds to is given by the order of the ψ and ϕ terms, where the ϕ term acts only to localise and the ψ terms measure variation along a given axis.

Writing the respective coefficients as

$$f^{\mu}_{slmn} = \int_V f(\mathbf{x}) \psi^{*\,\mu}_{slmn}(\mathbf{x})\ \mathrm{d}^3x, \tag{4.42}$$

the ensuing multiresolution decomposition will be

$$f(\mathbf{x}) = f^1_0 \psi_0(\mathbf{x}) + \sum_{s=0}^{s_m} \sum_{l=0}^{2^s-1} \sum_{m=0}^{2^s-1} \sum_{n=0}^{2^s-1} \sum_{\mu=2}^{8} f^{\mu}_{slmn} \psi^{\mu}_{slmn}(\mathbf{x}), \tag{4.43}$$

see *e.g.* Farge et al. (1996).

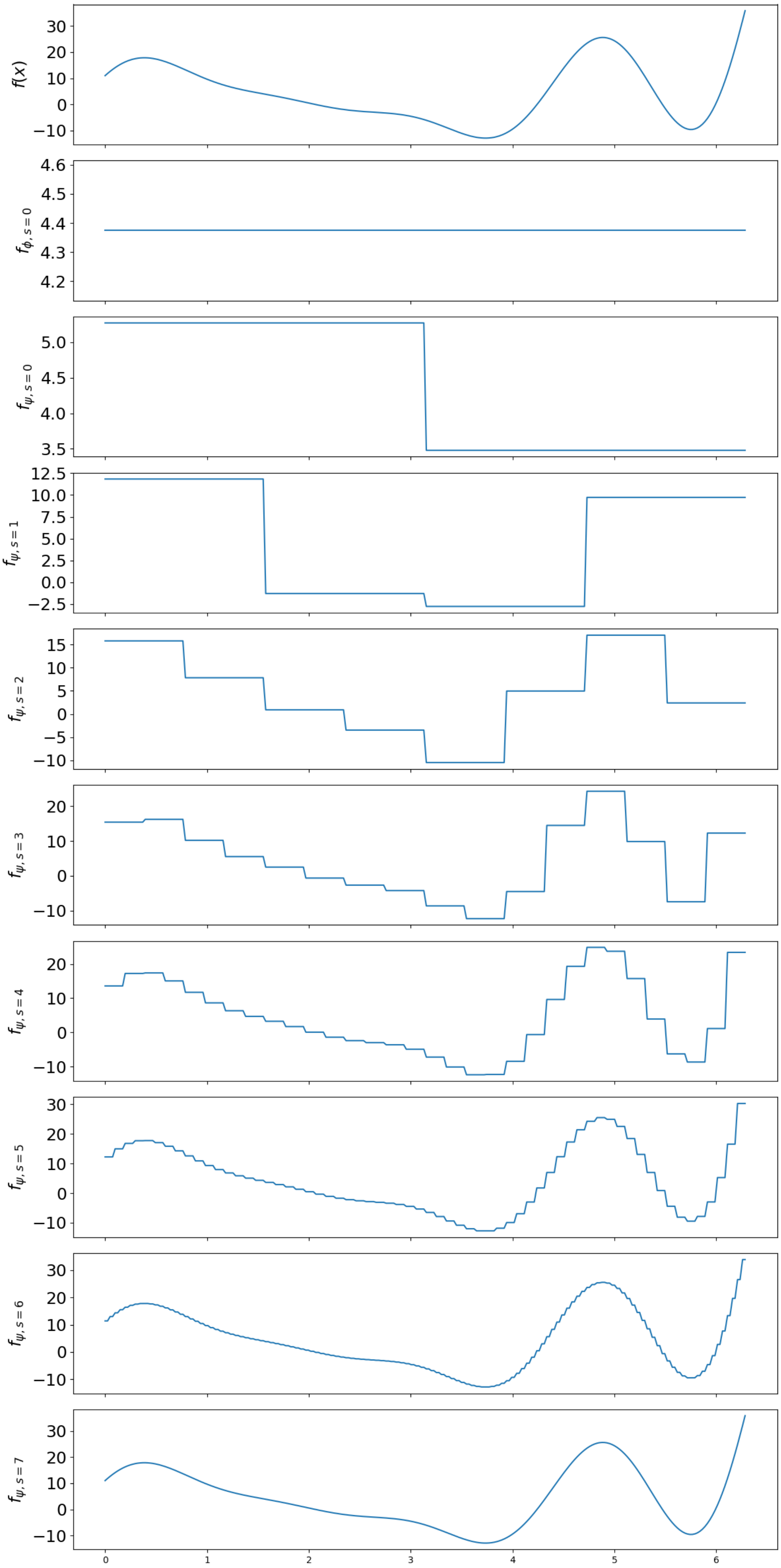

Fig. 4.5 Demonstrative example of the wavelet expansion as applied to a generic function $f(x) = 10\cos(x) + 5\sin(x) + x^3/10.0 + \cos(2x) + 10\sin(3x)(2-x)^2/4.0$. Each panel is given by successive addition of scales.

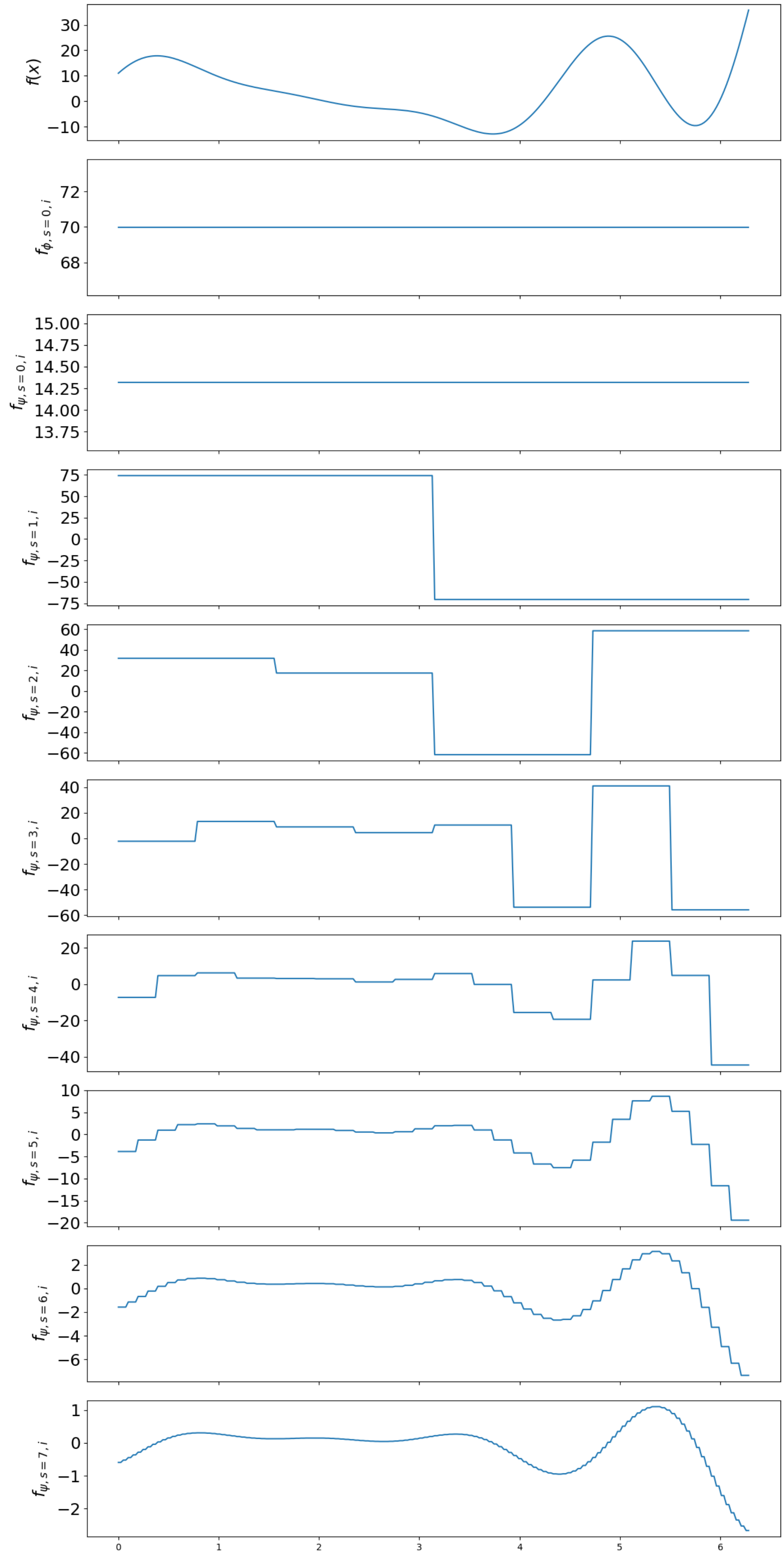

Fig. 4.6 Demonstrative example of the wavelet expansion as applied to a generic function $f(x) = 10\cos(x) + 5\sin(x) + x^3/10.0 + \cos(2x) + 10\sin(3x)(2-x)^2/4.0$. Each panel gives the wavelet co–efficient at each scale and locality.

Compacted notation

Unless otherwise specified, we will not be paying particular attention to the contributions of individual μ terms, thus for each l,m,n we shall assume the μ summation has been performed. We thus define an index k which, when summed over will be assumed to indicate a sum over l, m and n (or just l and n in 2-D). We then write (4.43) as

$$f(\mathbf{x}) = \sum_{s=0}^{s_m} \sum_{k=0}^{2^s-1} f_{sk} \psi_{sk}(\mathbf{x}). \tag{4.44}$$

Relative scale contributions

For a function f one can define the total (relative) contribution $Q_s(H)$ to the multiresolution decomposition at a scale s as

$$Q_s(H) = \sum_{k=0}^{2^s-1} f_{sk}. \tag{4.45}$$

Similarly we define the relative power $P_s(f)$ at scale s as:

$$P_s(f) = \frac{\sum_{k=0}^{2^s-1} |f_{sk}|}{\sum_{s'=0}^{s_m} \sum_{k=0}^{2^{s'}-1} |f_{s'k}|}. \tag{4.46}$$

4.4.4 Helicity formulae

Using multiresolution expansions (4.44), we can write the correlation function $\mathbf{C}$ (or, in the classical definition of magnetic helicity, $\mathbf{A}$), and $\mathbf{B}$, as

$$\mathbf{C} = \sum_{s=0}^{s_m} \sum_{k=0}^{2^s-1} \mathbf{C}_{sk} \psi_{sk}(\mathbf{x}). \tag{4.47}$$

Note that, for the delta function $\delta(\mathbf{x}-\mathbf{y})$,

$$\delta(\mathbf{x}-\mathbf{y})_{sk} = \langle \psi_{sk}(\mathbf{x}) | \delta(\mathbf{x}-\mathbf{y}) \rangle = \psi_{sk}(\mathbf{y}), \tag{4.48}$$

such that

$$\delta(\mathbf{x}-\mathbf{y}) = \sum_{s=0}^{s_m} \sum_{k=0}^{2^s-1} \psi_{sk}(\mathbf{y}) \psi_{sk}(\mathbf{x}). \tag{4.49}$$

Using the delta function, our expression for magnetic helicity can be written as

$$\begin{aligned}
H &= \int_V \mathbf{C}(\mathbf{x}) \cdot \mathbf{B}(\mathbf{x})\,\mathrm{dV} \\
&= \int_{V_x} \mathbf{C}(\mathbf{x}) \cdot \int_{V_y} \mathbf{B}(\mathbf{y})\delta(\mathbf{x}-\mathbf{y})\,\mathrm{d}^3\mathrm{x}\mathrm{d}^3\mathrm{y} \\
&= \int_{V_x} \mathbf{C}(\mathbf{x}) \cdot \int_{V_y} \mathbf{B}(\mathbf{y}) \sum_{s=0}^{s_m} \sum_{k=0}^{2^s-1} \psi_{sk}(\mathbf{y})\psi_{sk}(\mathbf{x})\,\mathrm{d}^3\mathrm{x}\,\mathrm{d}^3\mathrm{y} \\
&= \sum_{s=0}^{s_m} \sum_{k=0}^{2^s-1} \int_{V_x} \mathbf{C}(\mathbf{x})\psi_{sk}(\mathbf{x})\,\mathrm{d}^3\mathrm{x} \cdot \int_{\mathrm{V_y}} \mathbf{B}(\mathbf{y})\psi_{\mathrm{sk}}(\mathbf{y})\,\mathrm{d}^3\mathrm{y},
\end{aligned} \tag{4.50}$$

such that

$$H = \sum_{s=0}^{s_m} \sum_{k=0}^{2^s-1} \mathbf{C}_{sk} \cdot \mathbf{B}_{sk} = \sum_{s=0}^{s_m} \sum_{k=0}^{2^s-1} H_{sk}. \tag{4.51}$$

H_{sk} is then the helicity contribution at scale s at position $k = lmn$ (summing over all directions μ). This decomposition is admittedly still not fully localised, since the correlation integral $\mathbf{C}$ at a point (x,y,z) involves integration across planes of constant z of the domain. Thus the coefficient

$$\mathbf{C}_{sk} = \int_V \mathbf{C}\psi_{sk}\,\mathrm{d}V, \tag{4.52}$$

will include integration across all planes S_z containing the points (x,y,z) which have compact support from ψ_{sk}. As such the quantity $\mathbf{C}_{sk} \cdot \mathbf{B}_{sk}$ represents the winding correlation of the field in contained within the compact support of ψ_{sk} with the rest of the field in the planes containing ψ_{sk}, as indicated in Figure 4.7.

4.4.5 Classical Helicity

We wish to stress that the above expression (4.51) is equally valid for the classical definition of magnetic helicity:

$$H = \sum_{s=0}^{s_m} \sum_{k=0}^{2^s-1} \mathbf{A}_{sk} \cdot \mathbf{B}_{sk} = \sum_{s=0}^{s_m} \sum_{k=0}^{2^s-1} H_{sk}. \tag{4.53}$$

for a well–defined magnetic vector potential $\mathbf{A}$. Similarly, we can define a decomposition of relative helicity

$$\begin{aligned}
H_R &= \sum_{s=0}^{s_m} \sum_{k=0}^{2^s-1} (\mathbf{A}+\mathbf{A}_0)_{sk} \cdot (\mathbf{B}-\mathbf{B}_0)_{sk} \\
&= \sum_{s=0}^{s_m} \sum_{k=0}^{2^s-1} H_{R,sk}.
\end{aligned} \tag{4.54}$$

The physical intuition of local winding is, however, only retained when using the winding gauge $\mathbf{A}^W$.

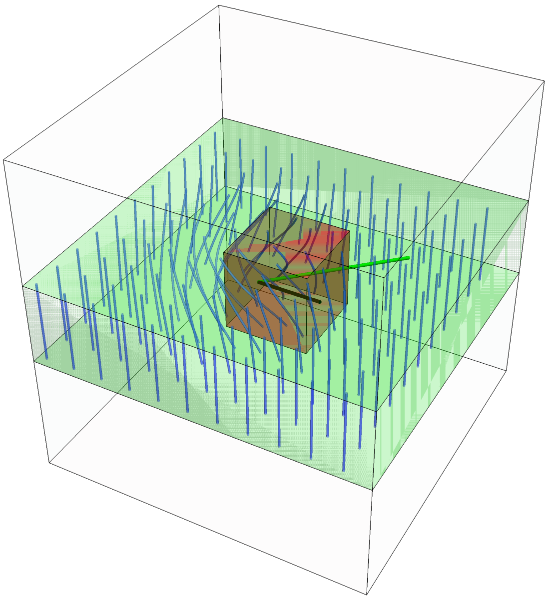

Fig. 4.7 The geometrical interpretation of the spatial contribution $\mathbf{C}_{sk} \cdot \mathbf{B}_{sk}$ of a spatial (wavelet) decomposition of the helicity. The red box represents the spatial sub-domain given by the triplet $k = lmn$. Each point in this red domain contributes a winding with the rest of the field in the plane in which it is contained. Because $\mathbf{C}_{sk} \cdot \mathbf{B}_{sk}$ is a sum over the whole red domain (by the form of $\mathbf{C}$), the entirety of the planes containing the red domain provide winding contributions to the sum, as indicated in the figure. This Figure was created by Chris Prior, the co–author.

4.4.6 Absolute Toroidal–Poloidal Helicity

We can also perform a multiresolution analysis on absolute helicity (introduced in Section 4.2.2), which has a physical interpretation similar to that of $\mathbf{C}$. The expression introduced in Section 4.2.2 (equation (4.3)) was suitable for a series of infinite Cartesian planes (with $\mathbf{B}_S = 0$), but practically the planes upon which our field lies are finite. In which case, we must take account of boundary terms. This can be done by properly expanding the sum

$$\begin{aligned} H_A &= \int_V (\mathbf{A_P} + \mathbf{A_T}) \cdot (\mathbf{B_P} + \mathbf{B_T})\ \mathrm{d}^3 x \\ &= \int_V (\mathbf{A_P} \cdot \mathbf{B_T} + \mathbf{A_P} \cdot \mathbf{B_P} + \mathbf{A_T} \cdot \mathbf{B_P})\ \mathrm{d}^3 \mathrm{x}, \end{aligned} \tag{4.55}$$

$(\mathbf{A_T} \cdot \mathbf{B_T} = 0)$ and as such

$$H_A = \sum_{s=0}^{s_m} \sum_{k=0}^{2^s-1} \left[\mathbf{A}_{\mathbf{P},sk} \cdot \mathbf{B}_{\mathbf{T},sk} + \mathbf{A}_{\mathbf{P},sk} \cdot \mathbf{B}_{\mathbf{P},sk} + \mathbf{A}_{\mathbf{T},sk} \cdot \mathbf{B}_{\mathbf{P},sk} \right],$$

following our notation. These boundary terms would be removed if we were to decompose along concentric shells, such as those making up a spherical geomtry, but we are currently limited to wavelet expansions in Cartesian space.

4.5 Multiresolution Analysis of Magnetic Helicity: Illustrative Examples

In this section we present examples which illustrate the benefits of the spatial decomposition offered by a multiresolution analysis of magnetic helicity. Unless otherwise stated, all quantities in this section have arbitrary units. Both examples are equally valid in either the winding–weighted two–point correlation regime introduced here, or by using the classical definition of helicity (with the winding gauge), as the magnetic field **B** is tangent at the side boundaries. Throughout the rest of this chapter, the zeroth spatial scale, which is unique (according to our use) in that it has contributions from both the scaling function and wavelet, is taken to be a sum over these two contributions.

Unless otherwise stated, all wavelet decompositions were calculated using PyWavelets, an open source module in Python (Lee et al., 2019). The numerical analysis and plotting of the outputs were also performed in Python.

4.5.1 Oppositely Twisted Flux Tubes

The first of our illustrative examples is that of a pair of oppositely twisted flux tubes whose vector field takes the form

$$\begin{aligned}\mathbf{B} = &\frac{100}{a}\exp\left[\frac{-((x+0.55)^2+y^2)}{a^2}\right](-y,x,0)\\ &-\frac{100}{a}\exp\left[\frac{-((x-0.55)^2+y^2)}{a^2}\right](-y,x,0)+(0,0,10),\end{aligned} \tag{4.56}$$

where we have chosen $a = 0.2$. This field (independent of z) is visualised for the domain $[-1,1]\times[-1,1]$, in Figure 4.8. Making an assumption of periodicity (which can be interpreted as an infinite repeating pattern of the form shown here), Fourier analysis indicates that that this magnetic field has zero overall helicity at every scale, even when the sum over $\mathbf{k} = k$ is taken with absolute values, as shown in Figure 4.9.

In contrast, in Figure 4.10, we plot the H_{sk} values for the wavelet multiresolution analysis of the magnetic helicity at spatial scales $r = 0 \to 6$ (along with the associated power $P_s(H)$). The plotting style is that of a "bubblegram": each sub-domain of helicity given by the multiresolution analysis is allocated a three-dimensional sphere at its centre. The radius of this sphere is dependent upon the absolute magnitude of the helicity of the sub-domain, and its color, red or blue, indicates a positive/negative sign respectively, with a gradient according to magnitude.

The bubblegrams indicate that the helicity is well localised in space in accordance with Figure 4.8, presenting with the correct sign of twist. It can be seen that the total helicity $Q_s(H)$ at each scale is zero. The absolute magnetic helicity power $P_s(H)$ is well localised in scale, as indicated in Figure 4.11. Peak magnetic helicity occurs at half the spatial scale of the domain, which is in agreement with the distribution of the twist in the magnetic field

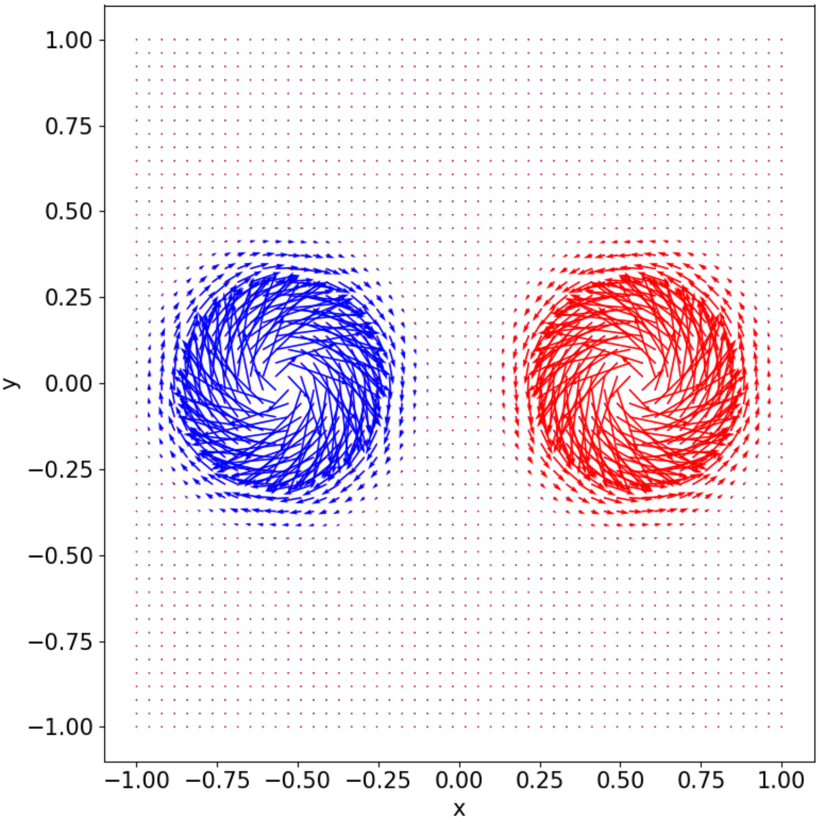

Fig. 4.8 Magnetic field vector plot of equation (4.56) at $z = 0$, red indicates positive twist, and blue indicates negative twist.

itself. Note that at the smallest spatial scales $2^{-5,6}$, the appearance of the bubblegram is distorted graphically due the frequency of data points, but we retain them for completion.

4.5.2 Linked Rings

The magnetic helicity associated with two flux tubes, with linking number $\mathscr{L}$, identical individual internal twists $\mathscr{T}$ and magnetic fluxes Φ is

$$H_L = 2(\mathscr{L} + \mathscr{T})\Phi^2, \tag{4.57}$$

following Berger (1999). A simple example of such linked rings, R_1 and R_2 can be parameterised as

$$R_1(r,\theta,\phi) = (R\cos(\theta) + r\cos(\theta)\cos(\phi), R\sin(\theta) + r\sin(\theta)\cos(\phi), r\sin(\phi)), \tag{4.58}$$

and

$$\begin{aligned} R_2(r,\theta,\phi) &= (C_x, C_y, C_z) \\ &\quad + (R\cos(\theta) + r\cos(\theta)\cos(\phi), -r\sin(\phi), R\sin(\theta) + r\sin(\theta)\cos(\phi)), \end{aligned} \tag{4.59}$$

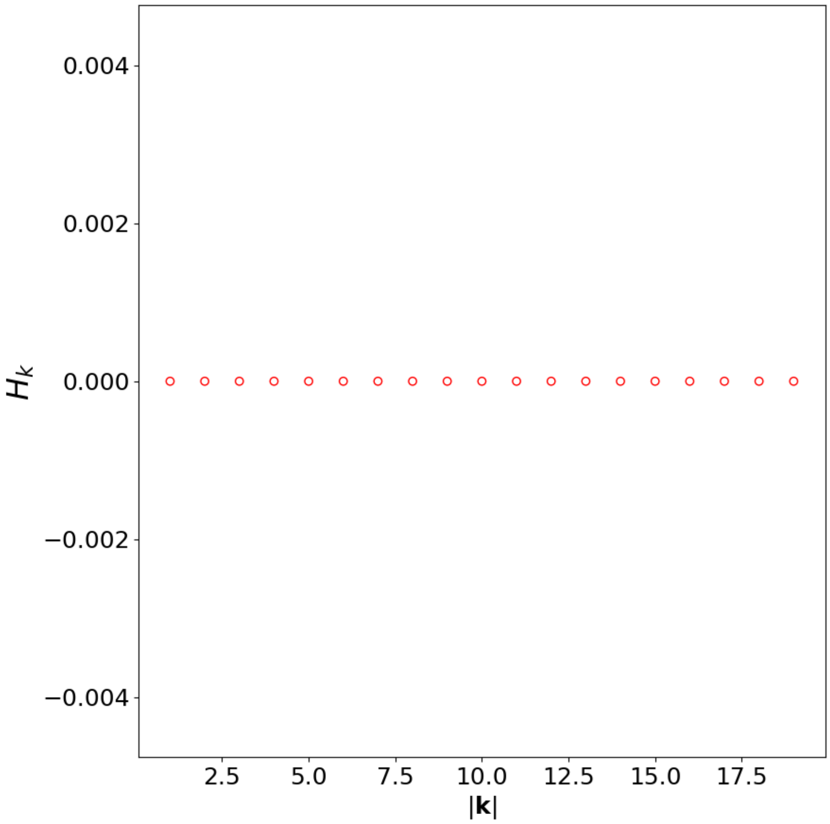

Fig. 4.9 Plot of fourier decomposition H_k of magnetic helicity of the vector field given in (4.56).

for major radius R, minor radius $r \in [0, r_m]$, toroidal angle θ and poloidal angle ϕ. The vector (C_x, C_y, C_z) defines the centre of R_2. An example with $r_m = 0.3$ and $R = 1$ is shown in Figure 4.12. We define the magnetic fields $\mathbf{B}_{R_i}$ of each ring as the sum of toroidal $\mathbf{B}_{R_it}$ and poloidal $\mathbf{B}_{R_ip}$ components, with

$$\begin{aligned}
\mathbf{B}_{R_1,t}(x,y,z) &= B_0\left(-\frac{y}{\sqrt{(x^2+y^2)}}, -\frac{x}{\sqrt{q_1}}, 0\right), \\
\mathbf{B}_{R_1,p}(x,y,z) &= \mathscr{T}B_0\left(\frac{xz}{r_{xy}}, -\frac{yz}{q_1}, 1-\frac{R}{\sqrt{q_1}}\right), \\
\mathbf{B}_{R_2,t}(x,y,z) &= B_0\left(-\frac{z}{\sqrt{q_2}}, 0, -\frac{x+1}{\sqrt{q_2}}\right), \\
\mathbf{B}_{R_2,p}(x,y,z) &= \mathscr{T}B_0\left(\frac{(x+1)y}{q_2}, -1+\frac{R}{\sqrt{q_2}}, \frac{yz}{q_2}\right),
\end{aligned} \tag{4.60}$$

where $q_1 = (x^2+y^2)$ and $q_2 = ((x+1)^2+z^2)$.

We choose $R = 1$ and $C_x = 1$, $C_y = C_z = 0$. Such an arrangement has an associated linking number of $\mathscr{L} = 1$, and if we assign $\mathscr{T} = -5$, $B_0 = 7$ and $r_m = 0.3$, there is a total magnetic helicity

$$H_{\mathscr{L}=1,\mathscr{T}=-5} = (2-10)\Phi^2 = -31.3, \tag{4.61}$$

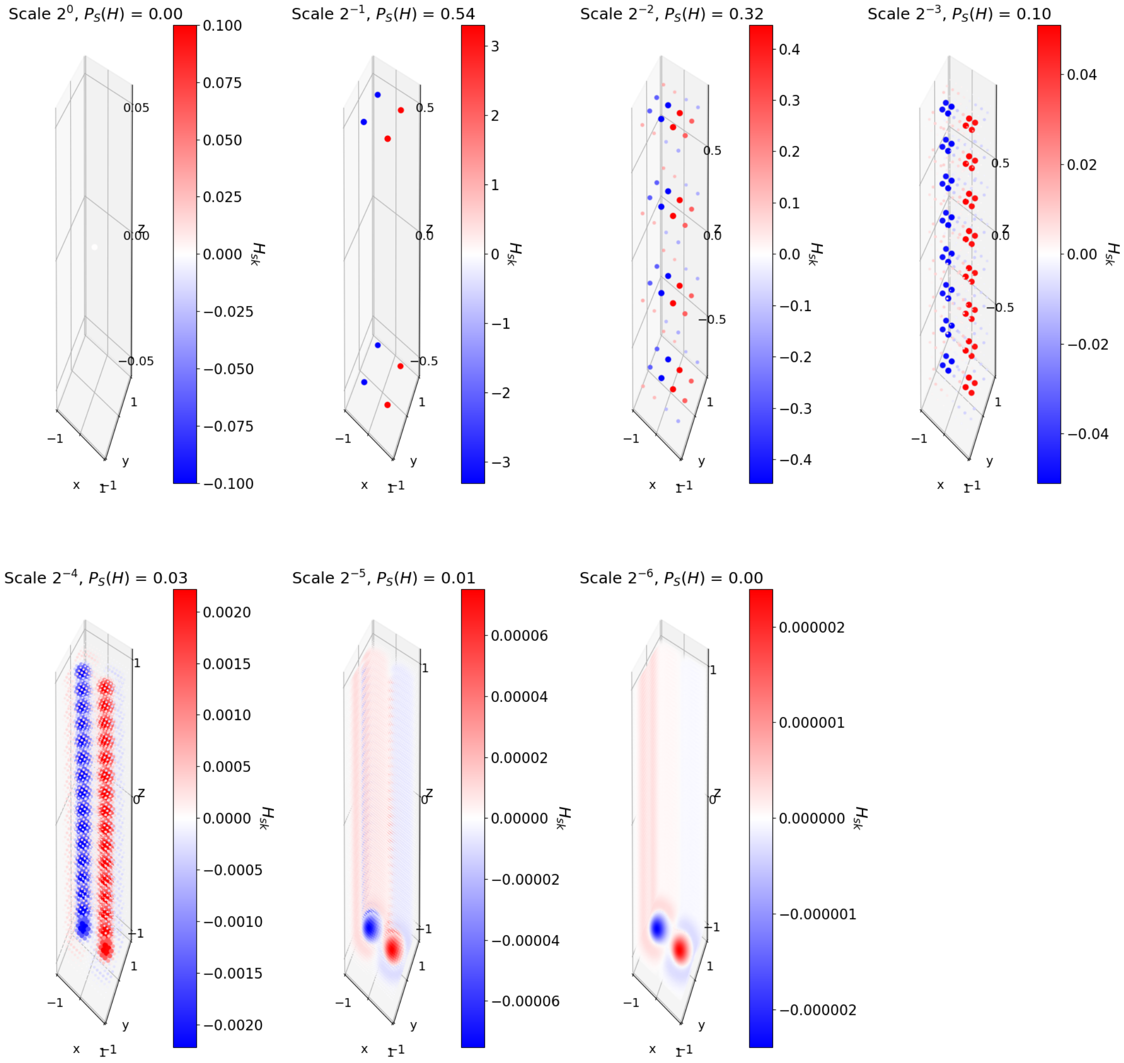

Fig. 4.10 H_{sk} for $s = 0 \to 6$ associated with the magnetic field distribution in equation (4.56). At the two smallest scales $2^{-5,6}$, the visual appearance of the bubblegram is distorted by the frequency of data points.

where $\Phi = 1.98$. In Figure 4.13, we plot the magnetic helicity coefficients H_{4k} associated with this magnetic field. The bubblegram indicates a distribution of magnetic helicity in correspondence to the distribution of the magnetic fields themselves, which we can attribute to the magnetic twist.

In Figure 4.14, we calculate the ratio of the multiresolution expansion of helicity with that of the analytical result, for both twisted and un–twisted rings, for which we define the measure

$$N_s(H) = \frac{\sum_{s'=0}^{s} Q_s(H)}{H_L}. \tag{4.62}$$

Naturally, $N_s \to 1$ as $s \to \infty$, as this is exactly the magnetic helicity. The distinction between the spatial scales at which this limit is approached is in agreement with the known scale separation between linking (large scale) and twist (small scale). We see in Figure 4.15 the regions of compact support for the Haar wavelet's at scales $s = 1, 2$. The $s = 1$ and

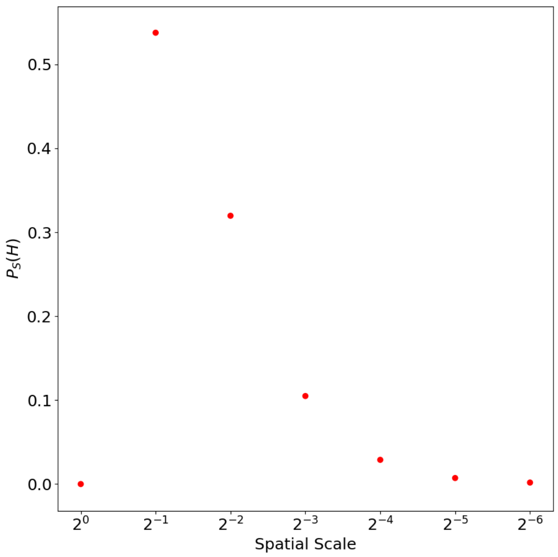

Fig. 4.11 $P_s(H)$ for the multiresolution helicity expansion of the field (4.56) at all spatial scales.

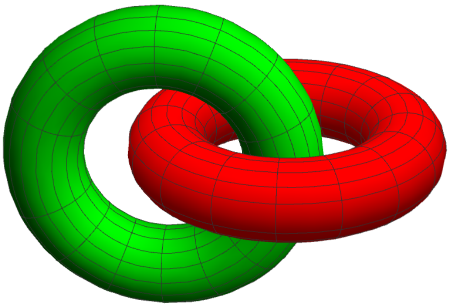

Fig. 4.12 Pictorial diagram of R_1 (red) and R_2 (green).

$s = 2$ scales tend to cover both tubes to some degree, whilst the scales $s = 3$ and higher generally only cover one tube. This is reflected in Figure 4.14 where we see the $\mathscr{T} = 0$ field is dominated by scales $s = 1,2$, as scales $s = 3$ and higher will reflect that on the single tube interior scale there is no complex topology. By contrast the $\mathscr{T} = -5$ case has a more balanced distribution across the scales.

4.5.3 Directionality

Recall that, as defined in (4.43), three–dimensional wavelets are inherently directional, and by summing over this variable we lose potentially useful information. This summation is performed for the goal of avoiding information overload, but here we demonstrate that the directional nature of wavelets can sometimes be easily interpreted.

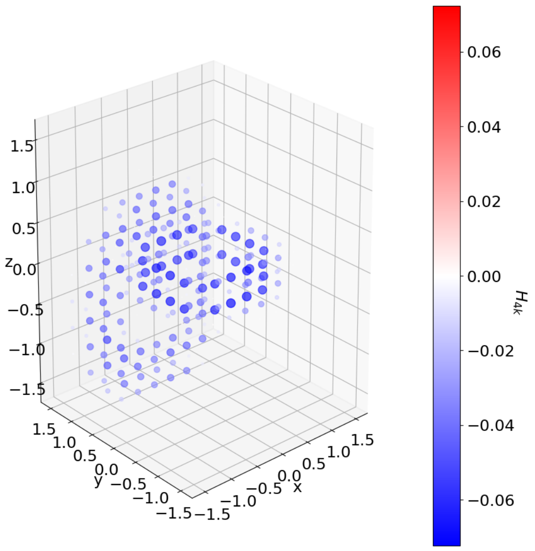

Fig. 4.13 H_{4k} for linked tubes with $\mathscr{T} = -5$.

We first define another analytical measure,

$$D_{\mu}(H) = \frac{\sum_{s=0}^{s_m} \sum_{k=0}^{2^s-1} |H_{sk}^{\mu}|}{\sum_{\mu'} \sum_{s=0}^{s_m} \sum_{k=0}^{2^s-1} |H_{sk}^{\mu'}|}, \tag{4.63}$$

which gives the absolute contribution from each direction over all scales. We will look at the strengths of each directional contribution in the Arnold-Beltrami-Childress (ABC) magnetic field/forcing, given by

$$\mathbf{B}_{ABC} = (C\cos(y) + A\sin(z), A\cos(z) + B\sin(x), B\cos(x) + C\sin(y)), \tag{4.64}$$

for constants A, B, C, and is such that $\mathbf{B}_{ABC} = \mathbf{A}_{ABC} = \nabla \times \mathbf{B}_{ABC}$. For this field, the directional variation of the magnetic field in each direction is uniquely defined by the constants (B, C, A) (in that order for axes x, y, z).

In Figure 4.16, we present $D_{\mu}(H)$ for a pair of ABC fields with different co-efficients for (B, C, A). The x–axis of this figure gives all possible directions, as previously established, in terms of a set three letters. For example, fmf denotes the father wavelet (scaling function) in the x and z directions, and the mother wavelet in the y direction, corresponding to a measure of the helicity associated with variation in the y–direction alone. Conversely, fmm would correspond to a measure of the helicity associated with variation in the y–z direction.

In the first example (4.16(a)) we choose $B = 0$, $C = A = 1$, and as such $D_{ffm} = D_{fmf} = 0.5$. All other directional contributions are zero (as we would expect). In the second (b) example, we take $B = 2$, $C = A = 1$, and as such (note that with $\mathbf{B}_{ABC} = \mathbf{A}_{ABC}$ we have $H \propto \mathbf{B}_{ABC}^2$) we find $D_{ffm} = D_{fmf} = 1/6$ and $D_{mff} = 4/6$, again in line with expectations.

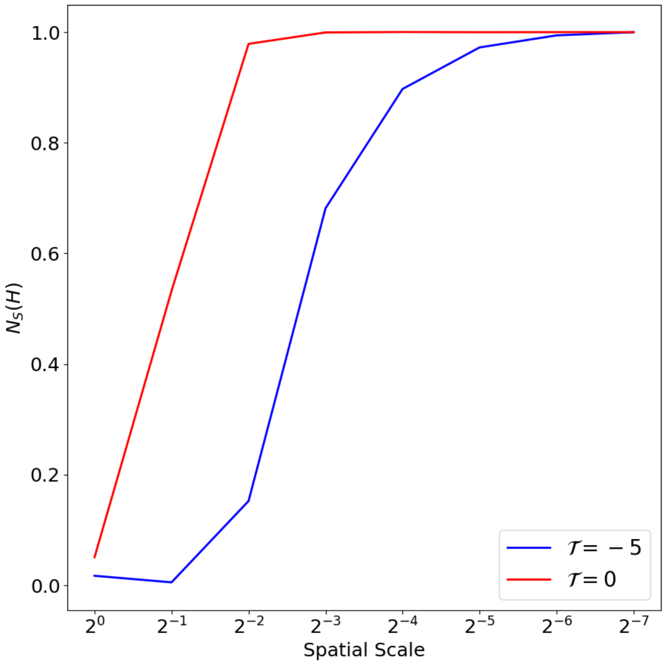

Fig. 4.14 $N_s(H)$ calculated for the two linked flux tubes, with either $\mathscr{T} = -5$ (blue) or without ($\mathscr{T} = 0$) internal twist (red).

4.5.4 Wavelet and Fourier Spectra

A great number of results have been established using the spectrum of helicity (and other quantities in general) obtained by taking the fourier transform. Recall that

$$H_k = \sum_{|\mathbf{k}|=k} \tilde{\mathbf{A}}^*(\mathbf{k}) \cdot \tilde{\mathbf{B}}(\mathbf{k}) \, \mathrm{d}\Omega_k, \tag{4.65}$$

for which we take $k_- \leq |\mathbf{k}| \leq k_+$, where $k_\pm = |\mathbf{k}| \pm 0.5$. This is already an inherent departure from the structure of a wavelet spectrum. Also,

$$Q_s(H) = \sum_{k=0}^{2^s-1} H_{sk}, \tag{4.66}$$

(for which wavelet $k = l,m,n$). At scale s, every component H_{sk} is of scale $(2^{-s}L)^3$ (for box length L) - i.e. every component in every direction is capturing variation at exactly one scale. In comparison, for the fourier spectrum, $k_- \leq |\mathbf{k}| \leq k_+$ represents a vector sphere in k–space. Take, for example, $|\mathbf{k}| = 4$. We could then have, say, $(k_x, k_y, k_z) = (0,0,4)$ or $(0,4,0)$ which correspond to drastically different scales of variation in the y and z directions. This, in some sense, implies that the wavelet spectra for a given scale Q_s versus H_k is more meaningful than its fourier counterpart, given that it corresponds to the same scale of variation in all directions.

We could circumvent this scale mixing by taking strictly $\mathbf{k} = (k,k,k)$, but this would result in a loss of the additivity condition for the fourier spectrum.

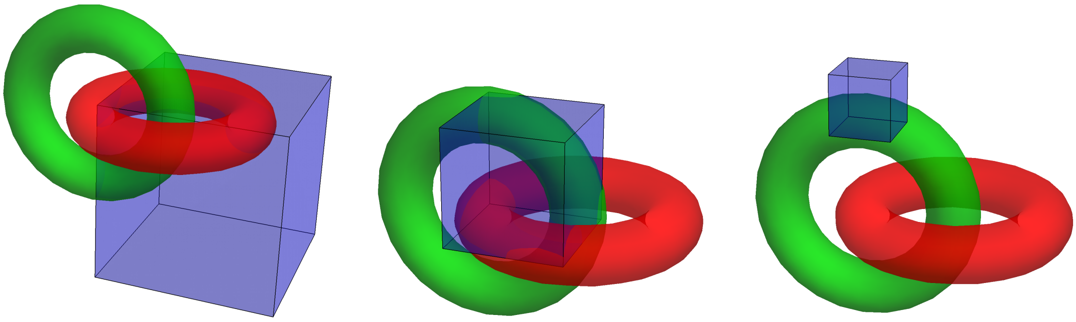

(a) Scale $s = 1$ (b) Scale $s = 2$ (c) Scale $s = 3$

Fig. 4.15 Pictorial figures indicating the contributing points of the density $\mathbf{A} \cdot \mathbf{B}$ at various scales for a Haar wavelet decomposition. (a) $s = 1$ and (b) $s = 2$ the overlap of the two tubes in the region of compact support is clear. (c) scale $= 3$ the region of compact support will generally only cover one tube. These figures were created by Chris Prior, the co-author.

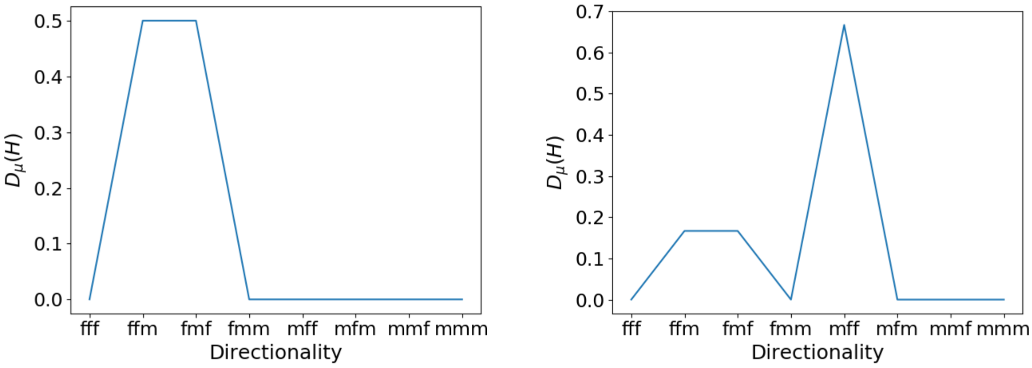

(a) $(B,C,A) = (0,1,1)$ (b) $(B,C,A) = (2,1,1)$

Fig. 4.16 $D_\mu(H)$ calculated for a pair of ABC fields.

In figures 4.17 and 4.18 we plot the wavelet and fourier spectra respectively for the *ABC* field $(B,C,A = (2,1,1)$, as in Figure 4.16(b)). There is no clear agreement between the two, even if we attempt to equate $k = 2\pi/L = 2\pi 2^{-s}$ (the latter of which represents the wavelet length scale). Both spectra, however, correctly sum to the total helicity.

4.6 Helicity, Energy and Topology

The result I present in this section (up to and including subsection 4.6.1) was first posed in a simplified form by the co-author, Chris Prior, as part of our collaboration. I was then intrinsically involved in the development of the result and its proof, and the presentation of the result as it is given here and within the aforementioned article.

The definition of localised helicity we have constructed in the previous subsections is still not entirely localised, as $\mathbf{C}$ contains an integral over each plane before its inclusion in the helicity volume integral. In this section we strive to overcome this barrier, and produce a fully localised measure of helicity.

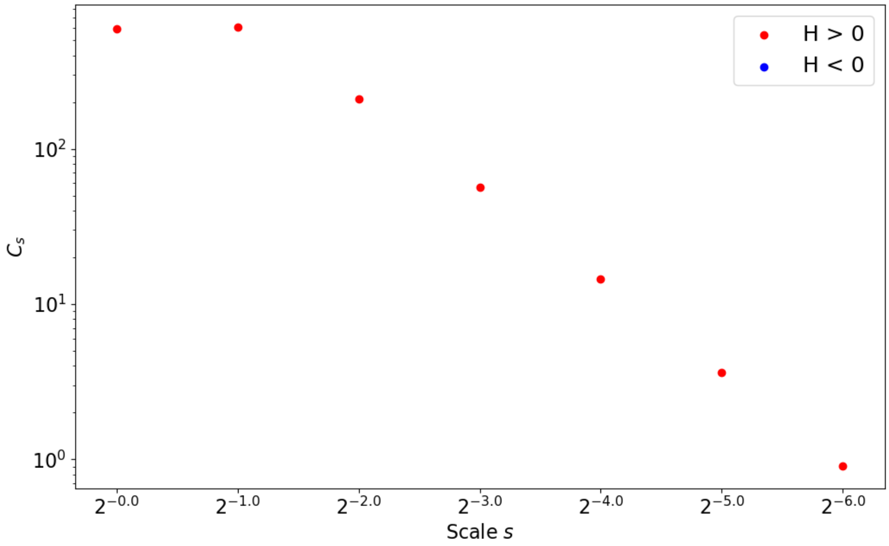

Fig. 4.17 Wavelet Spectrum Q_s for ABC field $(B,C,A) = (2,1,1)$.

By inserting a full three-dimensional mutli–resolution decomposition of the field **B** into the correlation function **C** (4.20) we obtain,

$$\begin{aligned}\mathbf{C}(x,y,z) &= \frac{1}{2\pi}\int_{S_z'}\sum_{s'=0}^{s_m}\sum_{k'=0}^{2^s-1}\psi_{sk}(x',y',z)\mathbf{B}_{s'k'}\times\frac{\mathbf{r}}{r^2}\,\mathrm{d}x'\,\mathrm{d}y',\\ &= \frac{1}{2\pi}\sum_{s'=0}^{s_m}\sum_{k'=0}^{2^s-1}\mathbf{B}_{s'k'}\times\int_{S_z'}\frac{\mathbf{r}}{r^2}\psi_{sk}(x',y',z)\,\mathrm{d}x'\,\mathrm{d}y', \qquad (4.67)\\ \mathbf{r} &= (x-x',y-y',0), \qquad (4.68)\end{aligned}$$

where we are able to place the summation in front of the integral given that each summation is finite, and can thus remove the $\mathbf{B}_{s'k'}$ term from within the integral as it is constant for each pair (s',k'). The parameter dependence of the wavelet function ψ indicates the integration is over only the in-plane functions of the 3-D wavelets. When we dot this expression with the magnetic field itself ($H = \int_V \mathbf{C}\cdot\mathbf{B}\,\mathrm{d}^3x$), we will obtain products of the form $\mathbf{B}_{s'k'}\cdot\mathbf{B}_{sk}$. We will thus attempt to extract magnetic energy.

First, in order to compare the helicity to the energy we must take account of the fact that magnetic helicity has an extra unit of length:

$$[H] = G^2m^4,$$
$$[E] = G^2m^3.$$

To account for this, note that if the planes S_z have x and y widths L and aL respectively then we can write $x = uL$ and $y = avL$ $(0 \leq u,v \leq 1)$ so that $\mathbf{r_L} = L(u-u',a(v-v'),0)$,

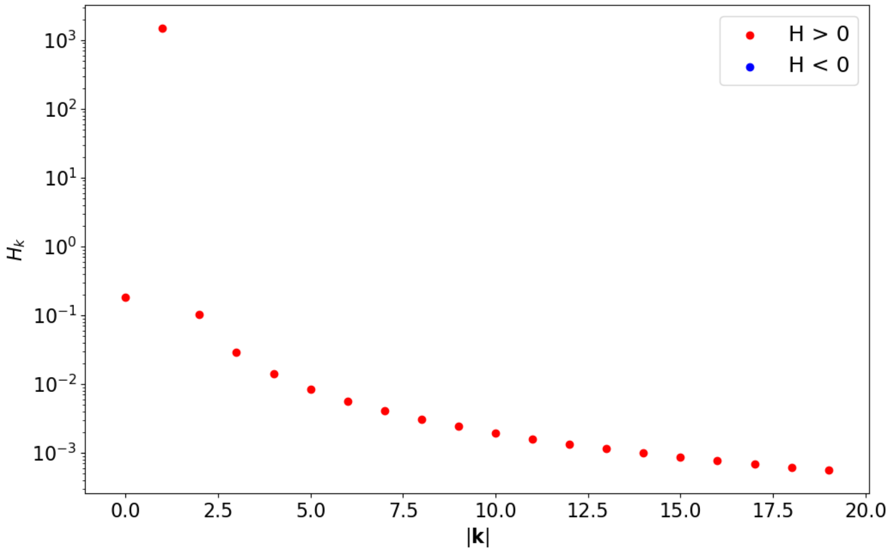

Fig. 4.18 Fourier Spectrum H_k for ABC field $(B,C,A) = (2,1,1)$.

then

$$\mathbf{C}(x,y,z) = \frac{L}{2\pi}\sum_{s'=0}^{s_m}\sum_{k'=0}^{2^s-1}\mathbf{B}_{s'k'} \times \int_{U_z'} \frac{a\mathbf{r_L}}{||\mathbf{r_L}||^2}\psi_{sk}(x(u'),y(v'),z)\;\mathrm{d}u'\;\mathrm{d}v', \tag{4.69}$$

where U_z' is the unit square. Inserting this into our expression for helicity (4.21) we obtain the helicity as an expansion in terms of the multiresolution expansion of the field **B** alone,

$$H = \frac{L}{2\pi}\sum_{s=0}^{s_m}\sum_{k=0}^{2^s-1}\sum_{s'=0}^{s_m}\sum_{k'=0}^{2^s-1}\mathbf{B}_{sk}\cdot\Bigg(\mathbf{B}_{s'k'} \\ \times\int_{z_0}^{z_1}\int_{S_z}\int_{U_z'}\frac{a\mathbf{r_L}}{||\mathbf{r_L}||^2}\psi_{sk}(x,y,z)\psi_{s'k'}(x(u'),y(v'),z)\Bigg)\;\mathrm{d}x\;\mathrm{d}y\;\mathrm{d}z\;\mathrm{d}u'\;\mathrm{d}v', \tag{4.70}$$

We first note that this expression can be represented in a quadratic form, but we first need to introduce some notation. Given that we have assumed a Cartesian domain $U_z' \times [0,h]$, with U_z' a unit plane at height z, then the quantity $W_i^{s'sk'k}$,

$$W_i^{s'sk'k} = \frac{L}{2\pi}\int_0^h\int_{S_z}\int_{U_z'}\frac{ar_L^i}{||\mathbf{r_L}||^2}\psi^*_{s'k'}(x(u'),y(v'),z) \\ \psi_{sk}(x,y,z)\;\mathrm{d}u'\;\mathrm{d}v'\;\mathrm{d}x\;\mathrm{d}y\;\mathrm{d}z. \tag{4.71}$$

is dependent only upon chosen wavelet and the length scale of the box, not the magnetic field itself. The cross-product in (4.68) can then be represented using a skew-symmetric matrix $\mathbf{M}_{ij}^{s'sk'k}$ which takes the form

$$\mathbf{M}_{ij}^{s'sk'k} = \begin{pmatrix} 0 & 0 & -W_2^{s'sk'k} \\ 0 & 0 & W_1^{s'sk'k} \\ W_2^{s'sk'k} & -W_1^{s'sk'k} & 0 \end{pmatrix}, \tag{4.72}$$

following the structure of the cross–product. Then, using the Einstein summation convention we have

$$H = \int_V \mathbf{A}^w \cdot \mathbf{B}\, \mathrm{d}V = \mathbf{M}_{ij}^{ss'kk'} B^{*j}_{s'k'} B^i_{sk}. \tag{4.73}$$

We note that in general the wavelet orthogonality relationships cannot be applied to (4.71) as the in-plane integrals are over different copies of U_z. However, the z integration is over the same domain so W_i will vanish if $n' \neq n$ ($z' \neq z$).

4.6.1 Helicity as a skew symmetric operator

The helicity is now being represented as product of the field at differing positions and scales through a skew-symmetric operator $\mathbf{M}$. In this case we can use the decomposition $\mathbf{M}_{ij}^{s'sk'k} = L\mathbf{I}_{ij}^{s'sk'k} + \mathbf{O}_{ij}^{s'sk'k}$, where $\mathbf{I}_{ij}^{s'sk'k}$ (the superscript labelling is for notational convenience) is the identity matrix and

$$\mathbf{O}^{s'sk'k} = \begin{pmatrix} -L & 0 & -W_2^{s'sk'k} \\ 0 & -L & W_1^{s'sk'k} \\ W_2^{s'sk'k} & -W_1^{s'sk'k} & -L \end{pmatrix}, \tag{4.74}$$

so that

$$H = L\mathbf{I}_{ij}^{s'sk'k} B^{*j}_{s'k'} B^i_{sk} + \mathbf{O}_{ij}^{s'sk'k} B^{*j}_{s'k'} B^i_{sk}. \tag{4.75}$$

Note that we have, in effect, simply added the identity and taken it away:

$$\mathbf{O}_{ij}^{s'sk'k} = \mathbf{M}_{ij}^{s'sk'k} - L\mathbf{I}_{ij}^{s'sk'k}. \tag{4.76}$$

The sum of contributions to the first term ($L\mathbf{I}_{ij}^{s'sk'k}$) for which $(s',k') = (s,k)$ give exactly the energy of the field, which we will extract.

We can decompose the sum (4.75) as follows

$$\begin{aligned} H &= L\mathbf{I}_{ij}^{s'sk'k} B^{*j}_{s'k'} B^i_{sk} + \mathbf{O}_{ij}^{s'sk'k} B^{*j}_{s'k'} B^i_{sk} \\ &= L\mathbf{I}_{ij}^{sskk} B^{*j}_{sk} B^i_{sk} + L\mathbf{I}_{ij}(1-\delta^{s's}\delta^{k'k}) B^{*j}_{s'k'} B^i_{sk} + \mathbf{O}_{ij}^{s'sk'k} B^{*j}_{s'k'} B^i_{sk} \\ &= L\mathbf{I}_{ij}^{sskk} B^{*j}_{sk} B^i_{sk} + N, \end{aligned} \tag{4.77}$$

where $\delta^{s's}$ is the Kronecker delta function, $\mathbf{I}_{ij}^{sskk} B^{*j}_{sk} B^i_{sk}$ is exactly the magnetic energy, and

$$N = L\mathbf{I}_{ij}(1-\delta^{s's}\delta^{k'k}) B^{*j}_{s'k'} B^i_{sk} + \mathbf{O}_{ij}^{s'sk'k} B^{*j}_{s'k'} B^i_{sk}, \tag{4.78}$$

contains additional topological information which constitutes the helicity.

We can thus write

$$H(\mathbf{B}) = LE(\mathbf{B}) + N(\mathbf{B}). \tag{4.79}$$

where N is the multiresolution representation of a functional of the field which contains the topological information through the quantities $W_i^{s'sk'k}$. Note that we have assumed the expansion of magnetic energy using wavelets:

$$\begin{aligned} E &= \frac{1}{2}\int_V \mathbf{B}\cdot\mathbf{B}\,\mathrm{d}^3x \\ &= \frac{1}{2}\sum_{s=0}^{s_m}\sum_{k=0}^{2^s-1}\mathbf{B}_{sk}\cdot\mathbf{B}_{sk}. \end{aligned} \tag{4.80}$$

4.6.2 Fieldline Helicity

Using (4.21) and (4.69), the fieldline helicity of a field line γ at scale s and position $k = lm$ can be written as

$$\begin{aligned} \mathscr{A}(\gamma) = \frac{L}{2\pi}\sum_{s'=0}^{s_m}\sum_{k'=0}^{2^s-1}\int_\gamma \frac{\mathbf{B}}{|\mathbf{B}|}\cdot(\mathbf{B}_{s'k'}(z))(s) \\ \times \int_{U_z'}\frac{a\mathbf{r_L}}{||\mathbf{r_L}||^2}\psi_{s'k'}(x(u'),y(v'),z)\,\mathrm{d}u'\,\mathrm{d}v'\,\mathrm{d}z \end{aligned} \tag{4.81}$$

where the summation over k implies a 2-D multiresolution decomposition, which is why the coefficient $\mathbf{B}_{s'k'}(z)$ of the multiresolution expansion has z dependence. Crucially, $B_{s'k'}$ is decomposed on each plane U_z, rather than in 3-D, meaning that $s'k'(z)$ denotes the contribution from U_z at a certain scale, locality and height, rather than from the entirety of V. The variable within the plane of interest (on which we plot our fieldline helicity distribution) is then $\mathbf{x}_0$, not k'. This causes some confusion with our notation, which we will correct in the next section. Under ideal evolutions $\mathscr{A}(\gamma)$ is preserved so the sum of $\mathscr{A}_s(\gamma)$ must be preserved and changes in $\mathscr{A}_s(\gamma)$ must be balanced across the scales.

4.7 Fieldline Helicity Evolution

A particular class of fields of significant interest in the solar physics community are braided fields for which $B_z > 0 \,\forall\, \mathbf{x} \in V$. In these cases, all field lines pass through the domain from the bottom to top boundary, and field lines γ can represented by the points $\mathbf{x}_0 \in S_0$ where they are rooted, such that $\mathscr{A}_{sk}(\gamma) \equiv \mathscr{A}_{sk}(\mathbf{x_0})$, where

$$\begin{aligned} \mathscr{A}_{sk}(\mathbf{x}_0) = \frac{L}{2\pi}\int_\gamma \frac{\mathbf{B}}{|\mathbf{B}|}\cdot(\mathbf{B}_{s'k'}(z))(s) \\ \times \int_{U_z'}\frac{a\mathbf{r_L}}{||\mathbf{r_L}||^2}\psi_{s'k'}(x(u'),y(v'),z)\,\mathrm{d}u'\,\mathrm{d}v'\,\mathrm{d}z. \end{aligned} \tag{4.82}$$

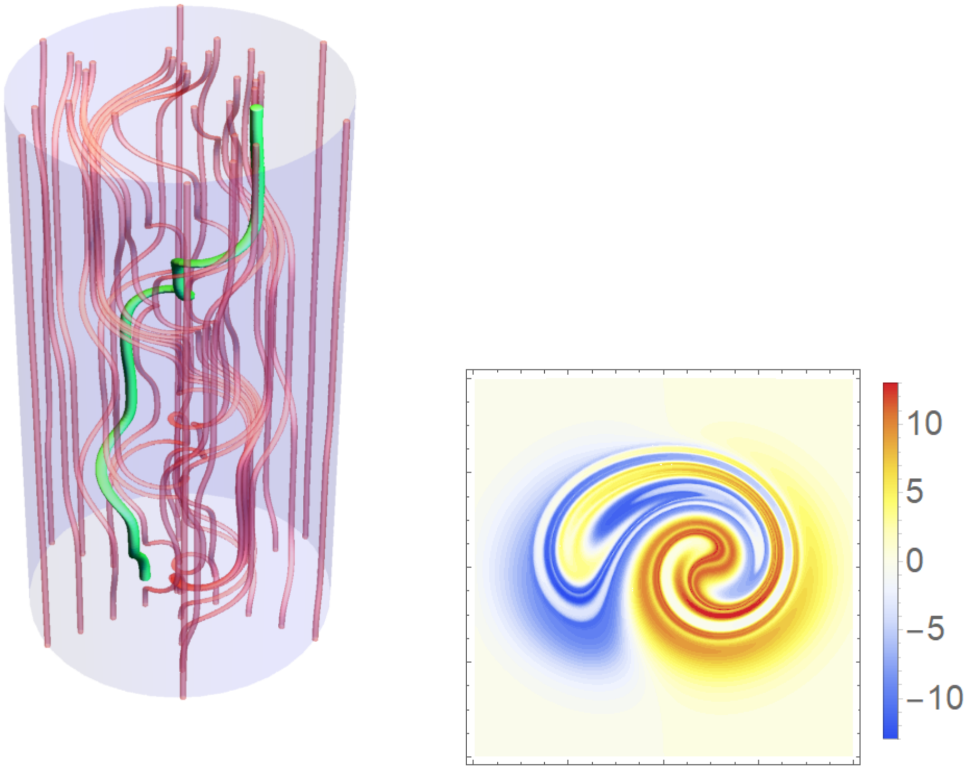

(a) (b)

Fig. 4.19 Figures indicating the entangled geometry of the braided field (4.87). (a) indicates a subset of the field lines in the region where the fields opposing twist units overlap. The field line helicity of the green field line indicated would have contributions due to its own complex geometry as well as its entanglement with the field. (b) the field line helicity distribution of (4.88) with $t = 0$, there is significant small scale structure indicating he field's complex entanglement. Panel (a) was created by Chris Prior, the co–author

As such (assuming $B_z > 0 \forall\, \mathbf{x} \in V$),

$$\begin{aligned} H(\mathbf{B}) &= \int_{S_0} \mathscr{A}(\mathbf{x_0})\ \mathrm{d}^2x \\ &= \sum_{s=0}^{s_m} \sum_{k=0}^{2^s-1} \int_{S_0} \mathscr{A}_{sk}(\mathbf{x_0})\ \mathrm{d}^2x. \end{aligned} \tag{4.83}$$

If the evolution is not ideal but such that the helicity is conserved (low plasma β relaxations) the distribution of $\mathscr{A}(\gamma)$ changes but the summation (4.83) is approximately preserved. In particular we have an alternative means of calculating the value of the operator $N(\mathbf{B})$.

$$\begin{aligned} N(\mathbf{B}) &= H(\mathbf{B}) - LE(\mathbf{B}) \\ &= \sum_{s=0}^{s_m} \sum_{k=0}^{2^s-1} \int_{S_0} \mathscr{A}_{sk}(\mathbf{x_0})\ \mathrm{d}^2x - LE. \end{aligned} \tag{4.84}$$

The advantage is that the field line helicity representation of N is additive in both s and k so, for example, we can decompose the contributions to N as the difference $H - LE$ at each scale s, and this decomposition is orthogonal.

4.7.1 Reconnection of a Dundee Braid

Following the the resistive MHD based braiding experiments in Russell et al. (2015); Wilmot-Smith et al. (2009, 2011), we define a field composed of exponential twist units $B_t(b_0, k, a, l, x_c, y_c, z_c)$ given by

$$\mathbf{B}_t(b_0, k, a, l, x_c, y_c, z_c) = \frac{2b_0k}{a}\exp\left(-\frac{(x-x_c)^2 + (y-y_c)^2}{a^2} - \frac{(z-z_c)^2}{l^2}\right)\mathbf{R}, \tag{4.85}$$

where

$$\mathbf{R} = (-(y-y_c), x - x_c, 0). \tag{4.86}$$

The parameter b_0 determines the strength of the field, a the horizontal width of the twist zones, l their vertical extent and k the handedness of the twist ($k = 1$ is right handed). The centre of rotation is (x_c, y_c, z_c). The braided field is then defined as a superposition of n pairs of positive and negative twists and a uniform vertical background field

$$\begin{aligned} \mathbf{B}_b(1, a, l, d, z_0, s_d, n) = \sum_{i=1}^{n} \Big[&\mathbf{B}_t(1, 1, a, l, -d, 0, z_0 + s_d(i-1)) \\ &+ \mathbf{B}_t(1, -1, a, l, 0, d, 0, z_0 + s_d(i-1)) \Big] + \hat{z}, \end{aligned} \tag{4.87}$$

where, d is the offset from the central axis, and s_d is the vertical spacing between consecutive twists (of the same sign) and z_0 the height of the first twist unit. In the literature this is sometimes referred to as a Dundee braid, which is a convention we shall follow. By altering the extent of the twist units (the parameters a and l) we can control the overlap the twist units. The field lines in the region of overlap show significant entanglement (Figure 4.19(a)) a property very well captured by the field line helicity distribution $\mathscr{A}(\gamma)$ (Figure 4.19(b)). The helicity of this field is (with a suitable choice of parameters) essentially zero owing to the balance of positive and negative twisting. It was found that under a high Reynold's number resistive MHD relaxation, for which the helicity is approximately conserved (Russell et al., 2015; Wilmot-Smith et al., 2011), that the field was able to simplify via localised reconnection into (roughly) a pair of oppositely twisted flux ropes. This process is a case of Taylor relaxation, which is solely dependent upon conservation of total magnetic helicity.

To keep matters simple in this first application of the multiresolution decomposition $\mathscr{A}_{sk}$, we define a rough analytic approximation of this relaxation process with the following parameterised magnetic field:

$$\mathbf{B} = \mathbf{B}_b(1, D_1(t), D_2(t), 1, -20, 8, 3), \tag{4.88}$$

where

$$\begin{aligned} D_1(t) &= \sqrt{2(1-t)}, & (4.89)\\ D_2(t) &= 2(1+2t). & (4.90) \end{aligned}$$

This field is considered in a domain $x, y \in [-4, 4]$, $z \in [-24, 24]$, these are the dimensions (and parameters for $t = 0$) used in Russell et al. (2015); Wilmot-Smith et al. (2009, 2011). As t increases the twisted units become more and more separated in the horizontal direction, as shown in Figure 4.20. The twist units with the same sign also merge vertically to form two non overlapping twisted flux tubes at $t = 1$. The decrease in overlap between the oppositely twisted units tends also reduces the complex field entanglement (we shall see this is not true for low t). It was checked numerically that the total helicity $H(\mathbf{B}, t)$ (essentially) remains zero for all t, a property designed to approximate the numerically observed conservation of helicity in the low plasma β MHD simulations. The Fourier expansion of the magnetic helicity of this field is zero throughout (even when an absolute magnitude sum is used).

In Figure 4.21, we present the field line distribution of the field line helicity decomposition $\mathscr{A}_s(\mathbf{x}_0)$. As we described earlier, it is important to note that these figures are not plots of 2-D k, but plots of $\mathbf{x}_0$. For a fieldline helicity the k variable denotes the spatial component of the decomposition within each plane U_z. As such, by summing over k (with the assumed z integration) for each individual fieldline we get a measure of the contribution from each scale for each individual field line: $\mathscr{A}_s(\mathbf{x}_0)$. This is functionally equivalent to $Q_s(\mathscr{A}_s)(\mathbf{x}_0)$ for *each* $\mathbf{x}_0$, in the way that we have previously defined Q_s, but here we will instead use this notation for referring to the sum over all fieldlines $\gamma \equiv \mathbf{x}_0$. The evolution of these distributions in time is shown at times $t = 0, 0.2, 0.4, 0.6, 0.8, 0.95$.

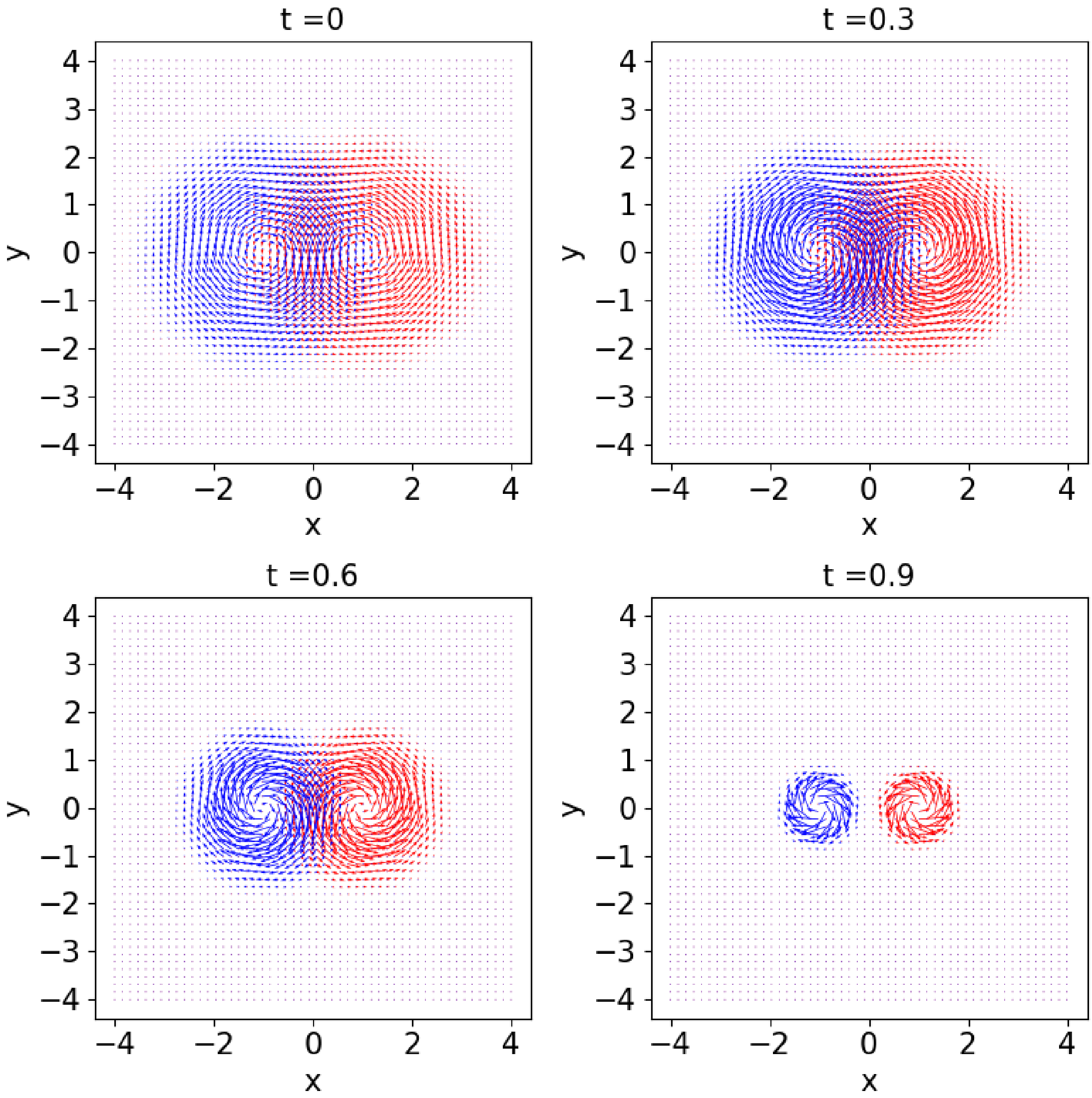

Fig. 4.20 Vector plot at four time steps $t = 0, 0.3, 0.6, 0.9$ at $z = 0$ of the magnetic field given by equation (4.88). Red (blue) denotes the positively (negatively) twisted regions.

At $t = 0$ all scale contributions $\mathscr{A}_s(\mathbf{x}_0)$ show (to varying degrees) the complex mixing pattern present in the full distribution. This is a result of the field line geometry (i.e. the geometry of the green curve in Figure 4.19(a)). This pattern disappears as the field lines reconnect and disentangle, which occurs at all scales. There is also a surrounding distribution which is most clear at the scales $s = 1, 2$, which persists through the evolution. To quantify the entanglement variation, we define a mixing parameter M as

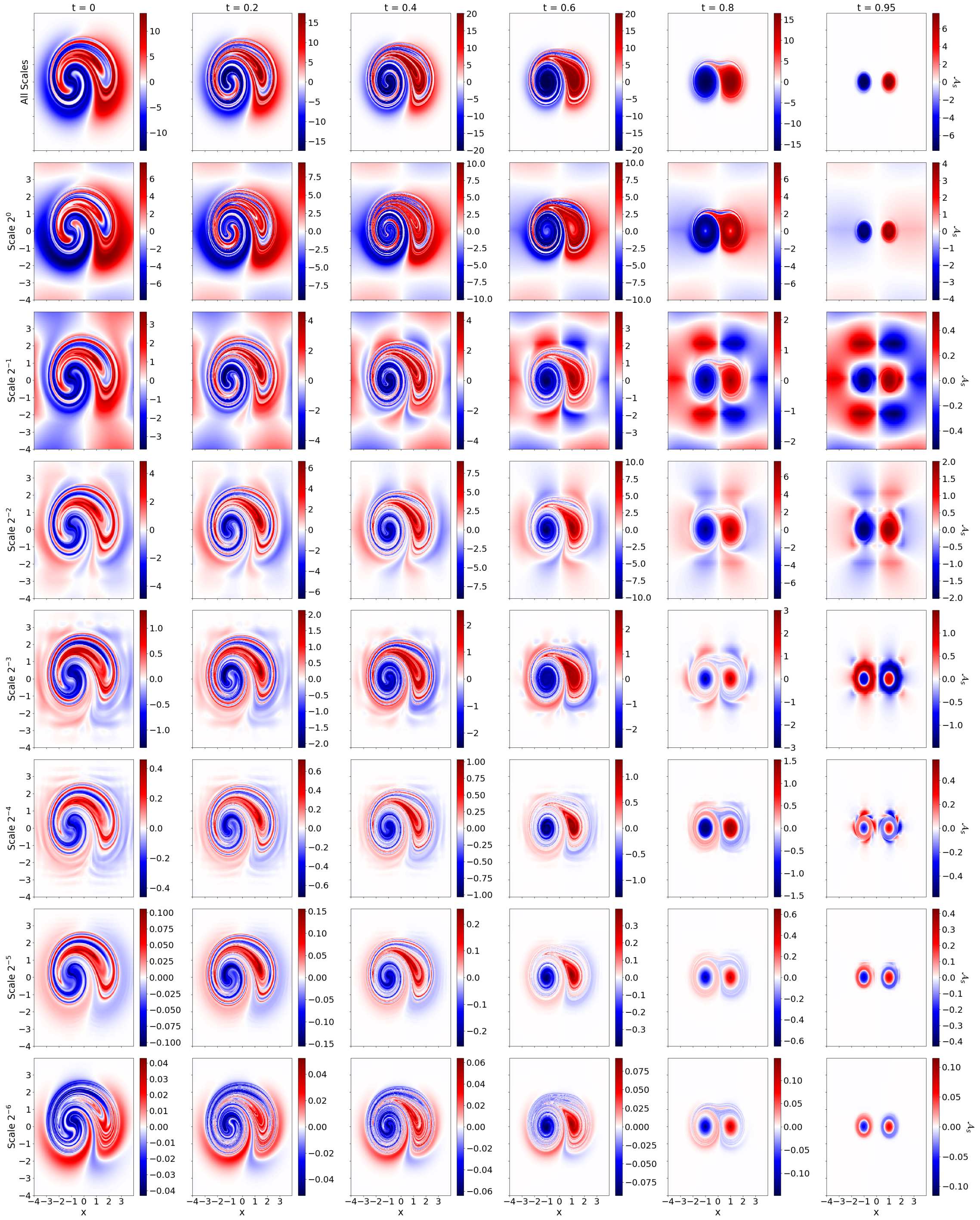

Fig. 4.21 Field line helicity $\mathscr{A}_s(\mathbf{x}_0)$ associated with time steps $t = 0, 0.2, 0.4, 0.6, 0.8, 0.95$ of an analytical reconnection simulation, in a domain $[-4,4]^2$ in x, y and $[-24,24]$ in z, with 400×400 field lines.

$$\mathrm{M} = |\nabla \mathscr{A}_{\mathrm{s}}| = \left(\left| \frac{\partial \mathscr{A}_{\mathrm{s}}(\mathbf{x}_0)}{\partial \mathrm{x}} \right|^2 + \left| \frac{\partial \mathscr{A}_{\mathrm{s}}(\mathbf{x}_0)}{\partial \mathrm{y}} \right|^2 \right)^{\frac{1}{2}}, \tag{4.91}$$

which will highlight the regions in which we see a rapid change in sign between positive and negative field line helicity $\mathscr{A}_s(\mathbf{x}_0)$. Admittedly this quantity will also capture simpler radial decay, but such contributions should be sufficiently weaker. Such a measure could be less meaningful in a system which is not as dichotomous as that which we have here (in that we are largely interested only in the sign of the twist, be that positive or negative, not its magnitude). The mixing associated with each scale, in the style of Figure 4.21, is shown in Figure 4.22. We see that the mixing actually increases at first up to $t = 0.4$ then it decays, and that the decay is more pronounced at larger length scales (smaller s).

In Figure 4.23 we plot the signed contribution $Q_s(\mathscr{A})$ as a function of scale for various t. Here we reinstate the use of Q_s, now referring to an *integral* over the $\mathscr{A}_s(\mathbf{x}_0)$, which we define as

$$Q_s(\mathscr{A}) = \int_{S_0} \mathscr{A}_s(\mathbf{x}_0)\,\mathrm{d}^2\mathrm{x}. \tag{4.92}$$

Note that this quantity effectively refers to the magnetic helicity at a given scale, due to the vertical field condition described earlier. This integral definition of Q_s, as opposed to a sum, is strictly for the use of fieldline helicity and its associated mixing parameter M.

There is always (approximately) as much negative as positive contribution, reflecting the total helicity conservation of the field. These values are dominated by the lower scales ($2^0 \to 2^{-2}$). Their relative magnitudes increase up to about $t = 0.4$ then decrease over time. It is interesting that the balance of positive and negative values is always maintained by the same scales (albeit with decreasing magnitudes). In Figure 4.24 we plot the absolute power $P_s(\mathscr{A})$ associated with each spatial scale for time steps $t = 0$ to $t = 0.95$, defined similarly to the new Q_s:

$$P_s(\mathscr{A}) = \frac{\int_{S_0} |\mathscr{A}_s(\mathbf{x})|\,\mathrm{d}^2\mathrm{x}}{\sum_{s'} \int_{S_0} |\mathscr{A}_{s'}(\mathbf{x})|\,\mathrm{d}^2\mathrm{x}}. \tag{4.93}$$

For early times the the values (mostly) decrease with s. However, as the twisting units separate and merge the scale $s = 2$ becomes more prevalent, reflecting the coherent development of the twisted flux ropes.

In figures 4.25 and 4.26 we see the total power normalised power across all scales of both the field line helicity $\mathscr{A}$ and the mixing M, respectively, as a function of time, given by

$$P_T(\mathscr{A}) = \frac{\int_{S_0} |\mathscr{A}_{s,T}(\mathbf{x},T)|\,\mathrm{d}^2\mathrm{x}}{\max_{T'} \int_{S_0} |\mathscr{A}_{s,T'}(\mathbf{x},T')|\,\mathrm{d}^2\mathrm{x}}. \tag{4.94}$$

Qualitatively the plots are very similar, showing a peak around 0.35 and then a relatively large drop as the twist units properly separate. The degree of mixing is determined by a ratio of the z decay and the $x-y$ overlap: if the z-decay is too weak, the two regions of twist will cancel and reduce the degree of mixing (assuming the twist regions overlap).

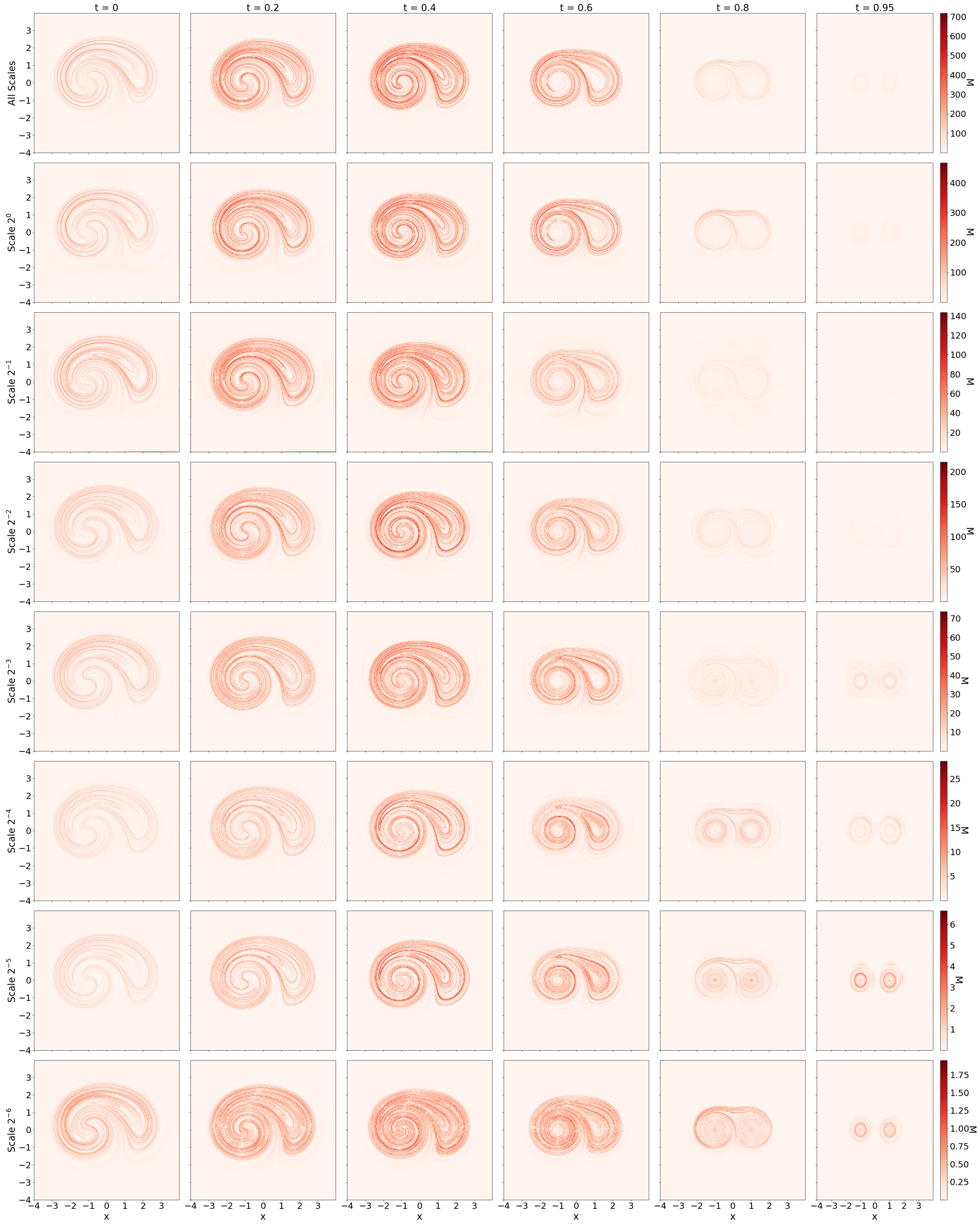

Fig. 4.22 Mixing M associated with time steps $t = 0, 0.2, 0.4, 0.6, 0.8, 0.95$ of an analytical reconnection field changing in time (4.88), in a domain $[-4,4]^2$ in x, y and $[-24,24]$ in z, with 400×400 field lines.

We can also directly compare the evolution of the fieldline helicity with that of magnetic energy, as shown in Figure 4.27, where we plot the absolute normalised magnetic energy against that of fieldline helicity, normalised within each scale ($P_T(\mathscr{A}_S)$ versus $P_T(E_S)$). Note that the multiresolution expansion of E was performed in all three dimensions ($k = lmn$), but the quantities will still be directly comparable.

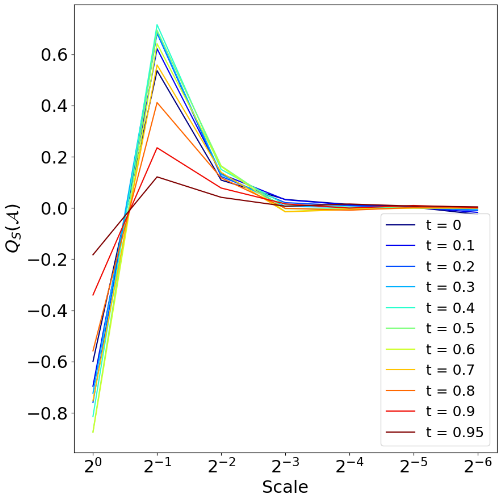

Fig. 4.23 Fieldline helicity power $Q_S(\mathscr{A}) \equiv \mathscr{A}_s$ attributed to each spatial scale, over time periods $t = 0$ to $t = 0.95$ for analytical reconnection via Dundee braids.

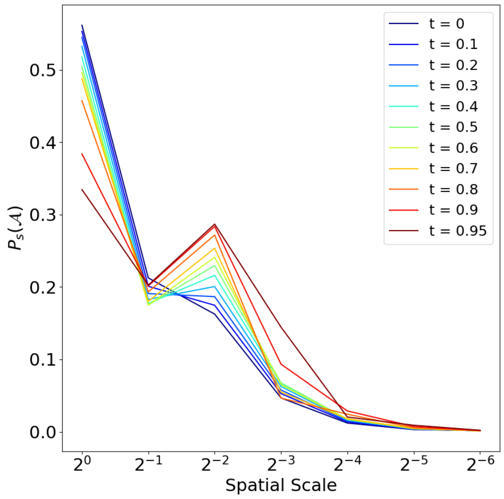

Fig. 4.24 Fieldline helicity absolute normalised power $P_S(\mathscr{A})$ attributed to each spatial scale, over time periods $t = 0$ to $t = 0.95$ for analytical reconnection via Dundee braids.

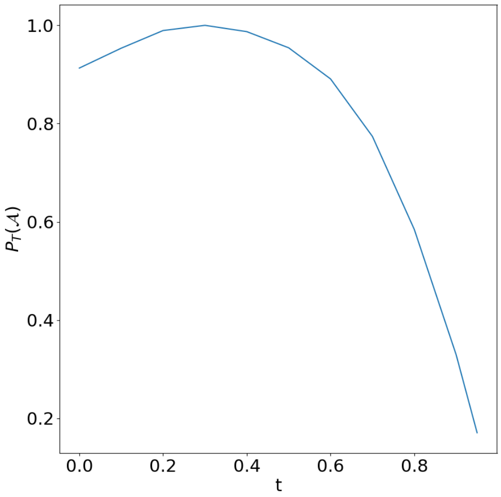

Fig. 4.25 $P_T(\mathscr{A})$ from $t = 0$ to $t = 0.95$.

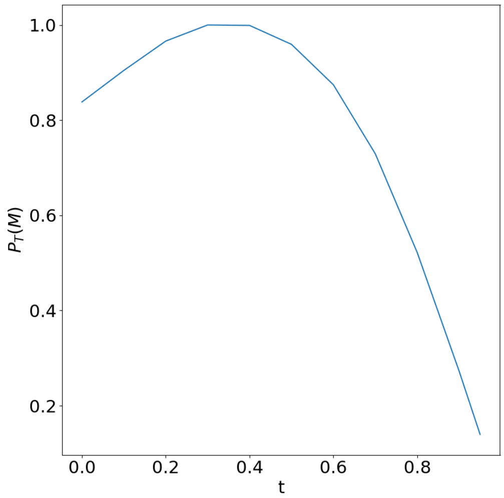

Fig. 4.26 $P_T(M)$ from $t = 0$ to $t = 0.95$.

The coefficient of correlation P between the two time series is seen to decrease as the spatial scale decreases in size: $P = [0.972, 0.904, 0.922, 0.752, 0.581, 0.576, 0.622]$ (in order of decreasing spatial scale). Their relative decay is most strongly aligned at scales $2^0 \rightarrow 2^{-2}$. Whilst the decay associated with fieldline helicity power is fairly consistent at all scales, the decay of magnetic energy is opposite to that of field line helicity at scales 2^{-5} and 2^{-6}. It is unsurprising that the scales $s = 0, 2$ are the most aligned, as we see in Figure 4.23 these are the dominant contributors to the field line helicity variations in the field. As the magnitude of these peaks rise (up to $t = 0.3$) and fall ($t > 0.3$) (Figure 4.23) so concurrently does the energy. This is a crucial observation: the variations in the the multiresolution decomposition of the field line helicity $\mathscr{A}_{sk}$ are intimately correlated with the variations in energy in the field.

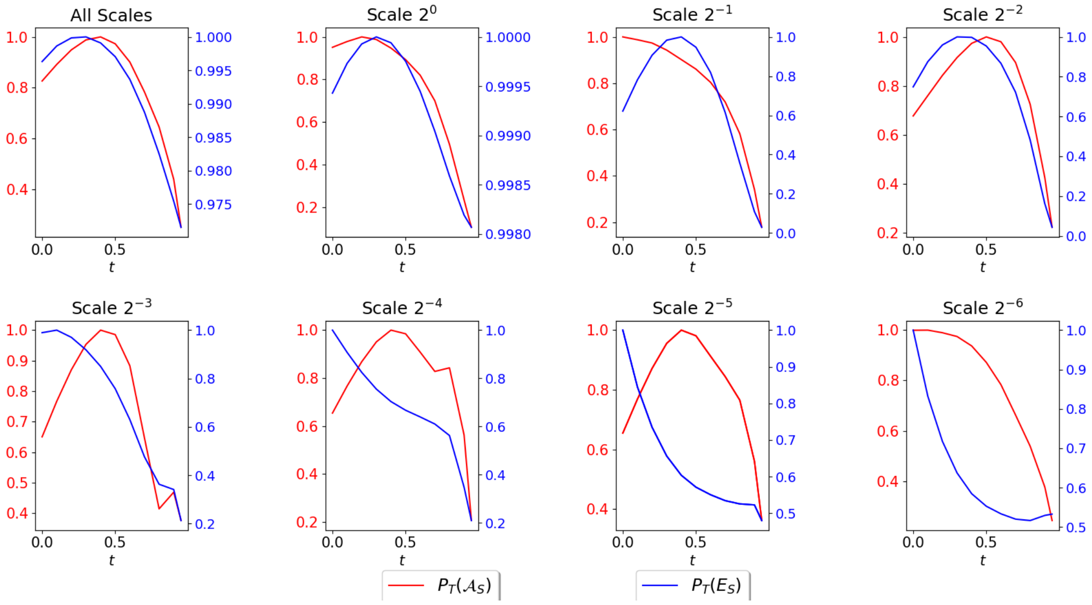

Fig. 4.27 P_T associated with the multiresolution analysis of fieldline helicity versus that attributed to the full three-dimensional decomposition of magnetic energy, where normalisation is scale dependent.

Note that spatial scales $2^{-1}, 2^{-2}$ (in the $x-y$ plane) corresponds to the distribution of twisted regions, and as such we would expect it to contain a large portion of the power. Scale 2^0 corresponds, for the fieldline helicity expansion, to the topological complexity of the line integrals themselves along each fieldline as there is only one-coefficient of B_{sk} filling each U_z (effectively the mean B_z). This relation between energy and topology was determined analytically in Section 4.4.4 for the winding gauge, and as such we should also hope to observe it in true resistive relaxation simulations.

4.8 Flux of Magnetic Helicity

Recall that the flux of magnetic helicity is defined by

$$\frac{\mathrm{d}H}{\mathrm{d}t} = -2\int_V \mathbf{E}\cdot\mathbf{B}\,\mathrm{d}^3\mathrm{x} + 2\int_S \left((\mathbf{A}_0\cdot\mathbf{v})\mathbf{B} + (\mathbf{A}_0\cdot\mathbf{B})\mathbf{v}\right)\cdot\hat{\mathbf{n}}\,\mathrm{d}^2\mathrm{x}, \tag{4.95}$$

for the reference field $\mathbf{A}_0$ uniquely defined by the appropriate boundary conditions of magnetic field $\mathbf{B}$, and velocity field $\mathbf{v}$. As is stated throughout this thesis, the second expression can be interpreted as the sum of two individual fluxes: the effect of twisting motions on the boundary, and secondly the movement of magnetic field through the boundary. As usual, the first term representing dissipation is neglected.

Wavelet analysis allows us to define a fourth measure of helicity flux, giving an indication of how helicity moves spatially within the volume. An intuitive example of this could be a study of a coronal loop expanding through a simulated region, for which the twist associated with the flux rope would be seen to move spatially. Multiresolution analysis measures helicity as a set of coefficients H_{sk} attributed to a given scale and spatial domain (with compact support). We can then simply define

$$\frac{\mathrm{d}H_{t,sk}}{\mathrm{dt}} = \frac{H_{t,sk} - H_{t-\delta t,sk}}{\delta t}, \tag{4.96}$$

in the form of a finite difference approximation, for the multiresolution analyses of two adjacent time snapshots.

Further, we can (via a $\delta(\mathbf{x}-\mathbf{y})$ separation) apply the standard wavelet decomposition on each term of the analytical measure of flux. For instance,

$$\frac{dH}{dt}_{sk} = 2\int_S (\mathbf{A}_0\cdot\mathbf{v})(\mathbf{x})\,\psi_{sk}(\mathbf{x})\,\mathrm{d}^2\mathrm{x}\cdot\int_\mathrm{S}\mathrm{B_r}(\mathbf{y})\,\psi_\mathrm{sk}(\mathbf{y})\,\mathrm{d}^2\mathrm{y} = 2\sum_{\mathrm{s=0}}^{\mathrm{s_m}}\sum_{\mathrm{k=0}}^{2^\mathrm{s}-1}(\mathbf{A}_0\cdot\mathbf{v})_\mathrm{sk}\mathrm{B}_\mathrm{r,sk}, \tag{4.97}$$

where we note that the z-spatial co-ordinate has been dropped again ($k = lm$). This is a multiresolution form of the helicity flux used in studies of the solar helicity flux through the hemisphere (see, for example, Chapters 2 and 3). Using the surface flux transport model simulations of Jiang et al. (2011) (J11 in Chapter 3), we calculate the helicity flux associated with seven spatial scales in Figure 4.28. This data covers their simulations for Solar Cycles 21 and 22, where time is counted from the beginning of cycle 21. As each cycle develops, the helicity flux associated with the largest scale ($2^{-1,-2}$ in $(\cos(\theta),\phi)$, which equates to a hemispherical split), drops in line with an increase in helicity flux associated with B_r of a smaller scale. This can be interpreted as the decreasing relative importance of polar (large scale) field relative to small-scale emerging active regions. This behaviour is seen to repeat over the course of two solar cycles (the end of the figure corresponds to the end of Cycle 22).

4.9 Summary and Conclusions

We have demonstrated how a multiresolution decomposition can be applied to the magnetic helicity and field line helicity, crucial topological quantities in astrophysical applications of the MHD equations. Our novel approach was compared to spectral (Fourier) helicity decompositions, which demands periodic domains, the likes of which is rarely seen in realistic observations and simulations. The method of multiresolution analysis has some significant advantages over this purely spectral approach:

1. It requires no periodicity conditions on the domain thus has a far wider range of potential applications.

2. It yields information on the spatial decomposition of helicity in the field, this is particularly useful for fields with significant heterogeneity of their entanglement.

On the first point the we have circumnavigated any issues regarding gauge choice by instead using a concrete geometrical definition of helicity which combines the results of Prior and

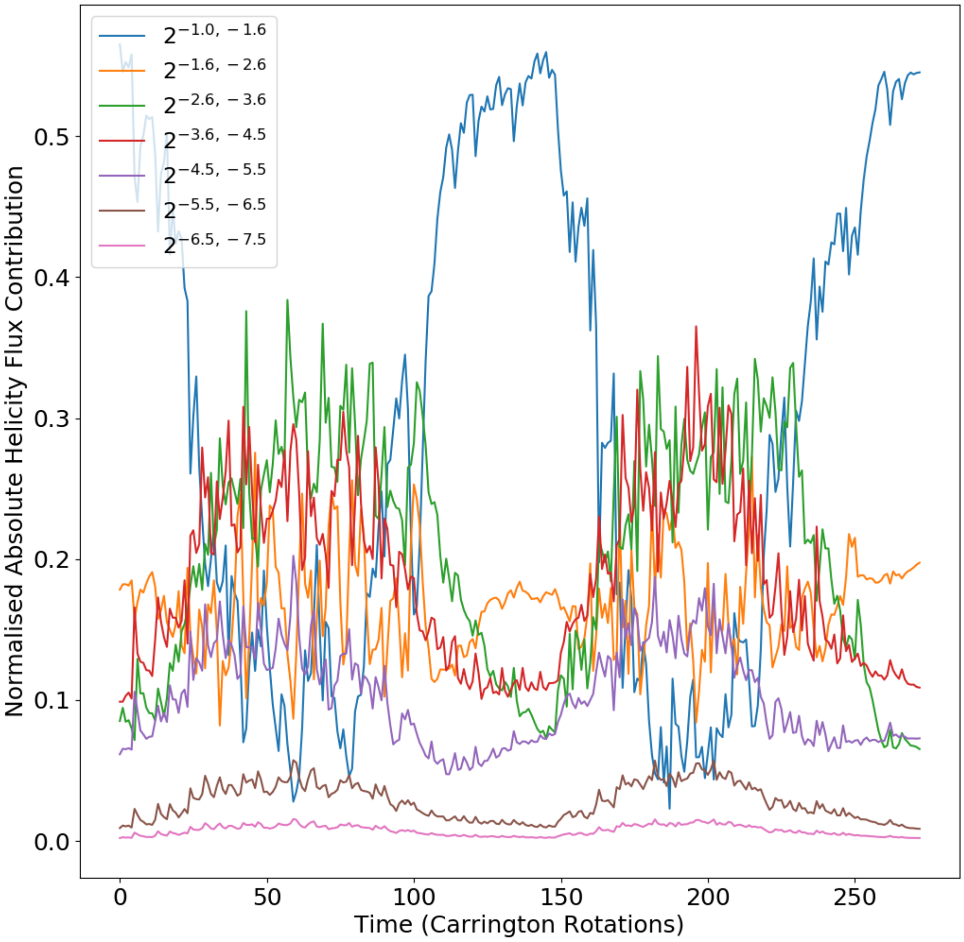

Fig. 4.28 Helicity flux dH/dt_{sk} of equation (4.97) for a portion of the simulations of Jiang et al. (2011), scale $2^{-a,b}$ refers to spatial scale $2^{-a}2$ in $\cos(\theta)$ and $2^{-b}2\pi$ in ϕ. Carrington rotations are counted from the beginning of Solar Cycle 21.

Yeates (2014) and Berger and Hornig (2018) to give a topologically meaningful definition of the helicity which depends only on the magnetic field **B** and the physically–meaningful winding between its fieldlines, represented as a two–point correlation vector **C**. It was also shown that helicity can be written as the product of components of the multiresolution expansions of **C** and the magnetic field **B**.

We have given an explicit geometrical interpretation of the coefficients H_{sk} (at scale s and position vector k), whether one chooses to decompose **B** inside **C** or not. We demonstrated this method on an intuitive example, with the mutliresolution analysis correctly identifying the opposing twisting two flux tubes, where the Fourier decomposition does not.

By using a purely geometrical definition of the helicity we were able to show that helicity can be written as a linear sum:

$$H(\mathbf{B}) = LE(\mathbf{B}) + N(\mathbf{B}), \tag{4.98}$$

where the operator N is a sum over various contributions to the total winding (entanglement) of the field from the various scales and spatial components of the multiresolution expansion of the field **B**. The characteristic length scale L was required to balance units. This decomposition not only places no requirement on the boundary conditions of the field but gives information about the spatial distribution of contributions to this sum.

We further showed that the field line helicity $\mathscr{A}(\gamma)$, the average entanglement of the field line γ with the rest of the field, can be composed into both spatial and scale components using a multiresolution analysis (see equation (4.81)). Under an ideal evolution, when the distribution of field line helicity is conserved, this decomposition could be used to provide insight as to how the field's topology redistributes both spatially and across scales *i.e.* flux ropes kinking/expanding or buoyantly rising through the photosphere and out of the Sun.

As an illustrative example, we applied the field line helicity decomposition to an analytic representation of a resistively relaxing magnetic braid whose total helicity is conserved (mimicking well known numerical experiments of low plasma β resistive MHD relaxation). In this case the spatially integrated sum of the field line helicity at each scale, which is equal to the helicity in this case (and is hence conserved), indicated that the conservation was maintained by a varying balance of entanglement on scales which reflected the varying field line entanglement, and the twisted structure of the underlying magnetic field. It was also seen that the variance in these contributions strongly correlated with the variations in energy of the field during its relaxation. Further, we introduced a simplistic quantitative definition of mixing which can be applied to any dichotomous system. The mixing of the aforementioned system was also seen to vary in line with fieldline helicity (as another measure of topological complexity).

Finally, we demonstrated how to apply this multiresolution decomposition to helicity fluxes through a planar boundary. An example application of this to the helicity flux associated with shear in a surface flux transport model over two solar cycles is used to indicate the analysis separates the varying contributions from the large-scale polar field and the smaller scale active region contributions to the cycle variation.

If a vector potential definition of the helicity is used, then the winding gauge of Prior and Yeates (2014) was recommended to be consistent with the rest of the results. The helicity can still be written as a sum of the components of multiresolution expansions, where the vector potential $\mathbf{A}$ replaces $\mathbf{C}$. However, this methodology reintroduces the gauge–defined boundary conditions. Other vector potential gauges, such as the Coulomb gauge, do not have such a well–defined physical meaning. For open magnetic fields, when using the classical gauge definition of helicity, we also demonstrated that the decomposition can be applied to relative helicity.

There is enormous potential for the application of this work, in a range of simulated and observation–driven MHD fields. It remains to be seen whether the two–point correlation helicity measure will ever take precedent over the classical vector potential definition. Of particular interest will be to apply these techniques to resistive MHD simulations akin to our analytic example. Even outside of MHD, such as in the study of tornadoes, can the vorticity at different scales be of potential interest.

One downside of this work is that we have chosen a preferred direction, z. Although we can choose z arbitrarily, we cannot have it correspond to more than one direction simultaneously. Thus, the natural choice for future extension is to generalise such that we are averaging across all three possible choices of z. It would also be of interest to explore how to decompose the two–point correlation captured within the toroidal–poloidal methods introduced in Berger and Hornig (2018) as they are applicable to spherical domains. This would also require a generalisation of wavelets to non–uniform grids.

Chapter 5

Localised Helicity contributions from Asymmetric Volumes

5.1 Introduction

In Chapter 4 we introduced a novel method which separates magnetic helicity in terms of its local contributions from variations within the magnetic field. Key to the novelty of that methodology was the retention of additivity across the whole space, and a lack of boundary assumptions. In the introduction to that method (Section 4.1), we discussed the concept of absolute helicity, introduced by Berger and Hornig (2018), which is applicable to all simply connected volumes (no holes). In this chapter, we will first investigate how the toroidal–poloidal gauge is affected by the choice of geometry, and then secondly attempt to define a localised helicity density. The choice of geometry in particular will be a consistent theme throughout the chapter. Our localised helicity density will consist of a series of absolute helicity values calculated by maximising the filling of the domain of interest with geometries of differing shapes and scales. The definition of scale will closely follow that established in the wavelet methodology, as shall be described.

The concept of calculating helicity within geometries which themselves fill the larger domain is not entirely novel; in Longcope and Malanushenko (2008) the authors define a relative helicity density within space-filling shapes. However, they require that each subvolume is defined by a magnetic surface ($\mathbf{B}\cdot\hat{\mathbf{n}} = 0$). In their work, subvolumes at the outer edges of the domain also require special attention. As we will show, there are no such constraints on our method.

In Section 5.2, we introduce the mathematical framework posed by Berger and Hornig (2018) for a generalised toroidal–poloidal decomposition, with a particular interest in how the asymmetry of the geometry affects the calculation of absolute helicity, as managed by a shape field. This is followed by a description of how to solve the inverse curl problem (previously described in chapters 2 and 3) for a surface geometry which is non–orthogonal and curvilinear, in Section 5.3. Section 5.4 has us study how magnetic helicity presents itself when the toroidal poloidal formalism has it be contained within the geometry itself, rather than in the magnetic field.

We then move on to studying how to define a magnetic helicity density for a variety of geometries. In particular, we will choose these geometries to be deformations of a sphere, for which we define surface co–ordinates for a few geometries of interest in Section 5.5. We then apply our methodologies to a constrained field as a test case in Section 5.6, and an ABC field in 5.7. Finally, in Section 5.8 we perform a simple study of the strength of this shape–field helicity for a number of simplistic shapes, and conclude in Section 5.9.

5.2 Methodology

We first review the mathematics behind the toroidal–poloidal decomposition, following Berger and Hornig (2018) (BH18). We write the magnetic field $\mathbf{B}$ in terms of its poloidal and toroidal components,

$$\mathbf{B} = \mathbf{B}_T + \mathbf{B}_P, \tag{5.1}$$

where $\mathbf{B}_T$ and $\mathbf{B}_P$ are the toroidal and poloidal components respectively. In the BH18 formalism, the magnetic field is decomposed in this way upon a series of concentric shells (surfaces) which cumulatively make up the volume of interest. This space of shells is fully described by a co-ordinate system (u,v,r), for which (u,v) describes the surface of each shell, whilst r determines which shell is being considered. As such, r is taken to be constant on each shell.

Upon each shell, the toroidal and poloidal components are then defined such that

$$\mathbf{B}_P(r)\cdot\hat{\mathbf{n}}(r) = B_n(r), \tag{5.2}$$
$$\mathbf{B}_T(r)\cdot\hat{\mathbf{n}}(r) = 0, \tag{5.3}$$

and

$$(\nabla\times\mathbf{B}_P(r))\cdot\hat{\mathbf{n}}(r) = 0, \tag{5.4}$$
$$(\nabla\times\mathbf{B}_T(r))\cdot\hat{\mathbf{n}}(r) = J_n(r). \tag{5.5}$$

Qualitatively, then, the poloidal field encompasses the entirety of the normal component of the magnetic field (with respect to the concentric shell), whilst the toroidal field encompasses the normal current, J_n. We will often drop the (r) notation for brevity, but it is assumed to be ubiquitous.

T and P, the poloidal and toroidal flux functions respectively, are solutions of a pair of Poisson equations:

$$\Delta_{||}P = -B_n, \tag{5.6}$$

and

$$\Delta_{||}T = -J_n, \tag{5.7}$$

where $\Delta_{||}$ is the two-dimensional surface Laplacian ($\Delta_{||}P = -\nabla^2 \hat{\mathbf{r}} P$). On a cartesian plane (x,y,z), the solution to (5.6) could then be written as

$$P(x,y) = \frac{1}{2\pi} \int \int B_n(\mathbf{x}') \ln|\mathbf{x} - \mathbf{x}'| \mathrm{d}^2\mathrm{x}, \tag{5.8}$$

$(u = x, v = y)$ and similarly for (5.7). These expressions can also be written as

$$\mathbf{B}_P = \nabla \times \mathscr{D}^{-1} B_n \tag{5.9}$$

$$\mathbf{B}_T = \mathscr{D}^{-1} J_n, \tag{5.10}$$

where $\mathscr{D}$ is the normal curl operator:

$$\mathscr{D}\mathbf{B} = \hat{\mathbf{n}} \cdot \nabla \times \mathbf{B}, \tag{5.11}$$

such that $\mathscr{D}^{-1}$ is the inverse normal curl operator. The magnetic vector potentials are defined similarly:

$$\mathbf{A}_P = \mathscr{D}^{-1} B_n, \tag{5.12}$$

$$\mathbf{A}_T = T\hat{\mathbf{r}}. \tag{5.13}$$

It is known that the linking of the either the toroidal or poloidal field with themselves is zero ($H(\mathbf{B}_T, \mathbf{B}_T) = H(\mathbf{B}_P, \mathbf{B}_P) = 0$)), such that the contribution to the absolute helicity (as termed by BH18) upon each concentric domain, for either a sphere or an infinite Cartesian plane, is given by

$$H_A(r) = 2 \int_{S_r} \mathbf{A}_P(\mathbf{x}, r) \cdot \mathbf{B}_T(\mathbf{x}, r) \, \mathrm{d}^2\mathrm{x}. \tag{5.14}$$

This expression applies equally well to open and closed magnetic fields: if we were to calculate the magnetic helicity of some reference potential field (as to subtract its magnetic helicity in the manner given by relative helicity), we would find it is always zero. This is due to the fact that

$$\mathbf{B}_{0,T} = 0, \tag{5.15}$$

as $\nabla \times \mathbf{B}_0 = \mathbf{J}_0 = \mathbf{0}$ for a potential field. The total absolute helicity contained within the entire volume of shell-radius R (or some subdomain) for a spherical or planar (symmetric) domain is then given by

$$H_V = \int_0^R H_A(r) \, \mathrm{d}r. \tag{5.16}$$

5.2.1 Asymmetric Geometries

The BH18 formalism of absolute helicity is designed to function not only for the standard spherical and planar cases, but also for any simply connected domain. In such cases, the boundary between a poloidal field and a toroidal field is not so clearly defined, as we shall see.

For example, imagine a tube resembling a incomplete figure of eight, such that it doesn't quite complete itself, as in Figure 5.1 (similar to that posed by Berger and Field (1984)). We can easily consider these ends to be closed (either by a simple plane, or hemispherical cap), and as such we ensure that there are no holes, and the tube is thus simply connected.

Now, further imagine that there is a magnetic field threading through the entire geometry, emerging from one end and then re-entering the tube at the other end (such that the magnetic field is itself a complete figure of eight). We can further define this magnetic field to be always normal to the cross section of the tube. In this case, at every point along the tube the magnetic field either has no toroidal component (at the two ends, where the field can be treated as potential: $J_n = 0$), or no poloidal component (along the remainder of the of the tube, where $B_n = 0$). By (5.14) and (5.16), this would indicate that the absolute helicity is zero. However, such a magnetic field distribution clearly has helicity, due to its writhe (self-crossing). This deeper subtlety was the focus of BH18, and it is prevalent (to differing degrees) for all geometries which are radially asymmetric.

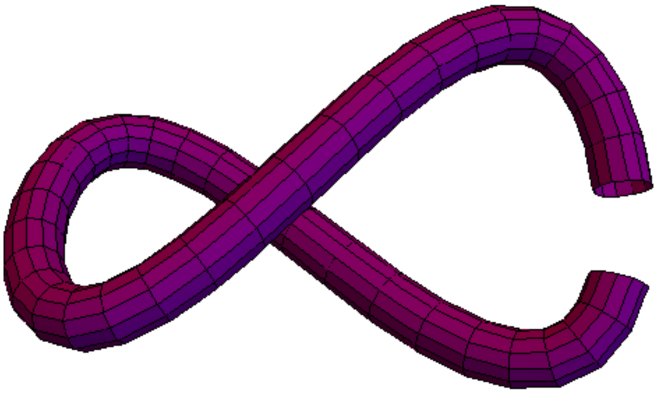

Fig. 5.1 Pictorial example of an incomplete figure of eight.

We must thus check that the two components (poloidal and toroidal) of the magnetic field remain well-defined for any asymmetric domain. We can continue to define the toroidal field as the inverse curl of the current, which is well-defined as all of the toroidal field lines within each concentric shell must close.

For the poloidal field, however, BH18 found that if one attempts to define $\mathbf{A}_P$ as in equation (5.12), the resulting poloidal field ($\mathbf{B}_P = \nabla \times \mathbf{A}_P$) might not necessarily be a two-gradient within the shell-surface (as is required to fulfil $\hat{\mathbf{n}} \cdot \nabla \times \mathbf{B_P} = 0$). In this case, asymmetries associated with the shell's structure have caused an additional, unwanted toroidal field to appear:

$$J_{P,n} = \hat{\mathbf{n}} \cdot (\nabla \times \nabla \times \mathbf{A}_P) = -\hat{\mathbf{n}} \cdot \Delta \mathbf{A}_P, \tag{5.17}$$

where Δ is the standard Laplacian (for a given geometry). They thus conclude that an additional term in the expansion of the magnetic field is required: the shape field, $\mathbf{B}_S$. We define

$$\mathbf{B}_P = \tilde{\mathbf{B}} + \mathbf{B}_S, \tag{5.18}$$

where $\tilde{\mathbf{B}} = \nabla \times \mathscr{D}^{-1} B_n$ (for symmetric domains $\tilde{\mathbf{B}} = \mathbf{B}_P$), with $\tilde{\mathbf{A}} = \mathscr{D}^{-1} B_n$, such that the shape field $\mathbf{B}_S$ acts to negate the effects of asymmetry:

$$\mathbf{B}_S = \mathscr{D}^{-1}\left(-\hat{\mathbf{n}} \cdot \nabla \times \tilde{\mathbf{B}}\right). \tag{5.19}$$

Qualitatively, then, the toroidal shape field is exactly opposite to that of the unwanted toroidal component of $\tilde{\mathbf{B}}$.

The absolute magnetic helicity associated with a series of concentric asymmetrical shells within a volume containing a magnetic field is then given by the sum of the linking of the toroidal field and the poloidal, plus the linkage of the poloidal field with the shape field (acting to correct the first term of the sum):

$$H_A = 2\int_0^R \int_{S_r} \tilde{\mathbf{A}}(r) \cdot \mathbf{B}_T(r)\, \mathrm{d}^2x\, \mathrm{d}r + \int_0^R \int_{S_r} \tilde{\mathbf{A}}(r) \cdot \mathbf{B}_S(r)\, \mathrm{d}^2x\, \mathrm{d}r. \tag{5.20}$$

5.3 Solving the inverse curl problem

As in Chapter 3 (Section 3.2.1), the magnetic vector potentials associated with the toroidal-poloidal decomposition are solutions of a Poisson equation. In some complex geometries the solutions to this problem are not so trivial, and in this section we detail our numerical methodology. In particular, the vector spaces for which this work is applicable are assumed to be non–orthogonal and curvilinear, so we will not explicitly state the indexed equations used, only describe them qualitatively.

We focus on the solution to the problem $\tilde{\mathbf{A}} = \mathscr{D}^{-1} B_n$, but the ideas naturally translate to the solution for both the toroidal and shape field. The two conditions on $\tilde{\mathbf{A}}$ are still that it is solenoidal ($\nabla \cdot \mathbf{B} = 0$) and $\mathscr{D}\tilde{\mathbf{A}} = B_n$, such that

$$\nabla \cdot \tilde{\mathbf{A}} = 0, \tag{5.21}$$

and

$$(\nabla \times \tilde{\mathbf{A}}) \cdot \hat{\mathbf{n}} = B_n. \tag{5.22}$$

We will choose our surface coordinate systems to resemble that of a sphere ($u = \theta, v = \phi$). This has topological grounding: an asymmetrical simply connected surface is simply the result of deformation applied to a sphere (which has constant curvature), where this deformation is the root cause of the shape field associated with such asymmetrical surface. Choosing a fixed co-ordinate system also maximises the generality of the numerical code. Co-ordinate lines will then be representative of latitude and longitude lines. Given a resolution in θ of n_θ, and ϕ of n_ϕ, which we index by l, m respectively, for every vertex defined by a specific value of (l, m), we have a curl and divergence equation.

As in the previous chapters (2 and 3), for n_θ latitude lines and n_ϕ longitude lines forming vertices, each of which has two components (given by $\tilde{\mathbf{A}}_\theta$ and $\tilde{\mathbf{A}}_\phi$ along the vertex lines), there are $2n_\theta n_\phi$ unknowns. Further, at the polar points ($\theta = 0, \pi$) we have two co–ordinate singularities, such that $\mathbf{r}(\theta,\phi) = \mathbf{r}(0,\phi) = \mathbf{r}(0)$ (and similarly for $\theta = \pi$). As such, at these points we have $\sqrt{g} = 0$, where g is the determinant of the spatial metric, and we cannot properly resolve the partial differential equations at this point. Instead, we choose to start our co-ordinate system at $\delta\theta$ (where $\delta\theta = \theta/n$), and end at $\pi - \delta\theta$ (with $n'_\theta = n_\theta - 2$ latitude lines).

As in the earlier chapter of this thesis, to resolve the polar magnetic flux which we have disregarded, recall that if at every vertex, bar one, we have fulfilled the divergence equation ($\nabla \cdot \mathbf{B} = 0$), then we must have also fulfilled it at the final, unevaluated vertex. The final divergence equation is then null, and we instead use it to properly resolve the poles. This final divergence equation is taken as a line integral around the co–ordinate line $\theta = \delta\theta$, such that it encloses the un–evaluated polar point, which (by Stokes' theorem) must equal the polar flux, and as such the polar flux is properly accounted for.

Finally, we check that the net flux out of each surface is zero (to again ensure divergence–free fields) for our numerical approximations of a magnetic field. If this is not fulfilled, we simply take the difference and spread it across every face as a function of the relative area of that face.

Writing this system as a matrix, we can treat it as sparse for the sake of numerical efficiency (as the majority of equations only refer to a small number of unknowns each). To check, calculating the sparsity of our matrix, given by the ratio of co-efficients equal to zero to the total number of co-efficients, gives a value of 0.992 (indicating an extremely sparse matrix). The numerical codes used to solve, assess, and plot these systems were written in both Python and Mathematica (with agreement between the two).

The vector derivatives of equations (5.21) and (5.22), in a geometry which is neither assumed to be orthogonal nor linear, are given by

$$\nabla \cdot \boldsymbol{A} = \frac{1}{\sqrt{g}} \frac{\partial}{\partial q^i} (\sqrt{g} A^i), \tag{5.23}$$

$$(\nabla \times \boldsymbol{A})^k = \frac{\varepsilon^{ijk}}{\sqrt{g}} \frac{\partial A_j}{\partial q^i}, \tag{5.24}$$

respectively, where ε^{ijk} is the fully three–dimensional Levi–Civita symbol, are heavily dependent upon the metric tensor g_{ij} (for which $g = \det g_{ij}$). We have chosen not to expand the curl equation (5.24) using Stokes' theorem due to the added complexity of a non–orthogonal curvilinear co–ordinate system. Note that these expressions are dependent upon both the contravariant (A^i) and covariant (A_j) expansions of a vector and covector respectively. The covariant vector is the more physical of the two, as it changes in–line with the co-ordinate system (under, for example, a rotation), but both sets of expansion are necessary. The metric tensor (in three–dimensions) is most commonly written

$$g_{ij} = \begin{pmatrix} \mathbf{e}_i \cdot \mathbf{e}_i & \mathbf{e}_i \cdot \mathbf{e}_j & \mathbf{e}_i \cdot \mathbf{e}_k \\ \mathbf{e}_j \cdot \mathbf{e}_i & \mathbf{e}_j \cdot \mathbf{e}_j & \mathbf{e}_j \cdot \mathbf{e}_k \\ \mathbf{e}_k \cdot \mathbf{e}_i & \mathbf{e}_k \cdot \mathbf{e}_j & \mathbf{e}_k \cdot \mathbf{e}_k \end{pmatrix},$$

where

$$\mathbf{e}_i = \frac{\partial \mathbf{r}}{\partial q^i}, \tag{5.25}$$

is the covariant basis vector defined on the co-ordinate system $(\theta,\phi,r) = (q^0,q^1,q^2)$, with

$$\mathbf{r} = x(\theta,\phi,r)\hat{\mathbf{x}} + y(\theta,\phi,r)\hat{\mathbf{y}} + z(\theta,\phi,r)\hat{\mathbf{z}}. \tag{5.26}$$

The metric tensor defines both distance within a vector space, and the line element

$$\begin{aligned} ds^2 &= g_{ij}dq^i dq^j \\ &= g_{00}d\theta d\theta + g_{11}d\phi d\phi + g_{22}drdr + 2g_{12}d\phi dr + 2g_{01}d\theta d\phi + 2g_{02}d\theta dr, \end{aligned} \tag{5.27}$$

for some infinitesimal change $(d\theta, d\phi, dr)$. Note the use of Einstein summation notation.

The interchange between a contravariant and covariant expansion is facilitated by lowering and raising of indices via the metric tensor,

$$A_j = g_{ij}A^i. \tag{5.28}$$

We must note that whilst there is no A^r component, as the poloidal vector potential is in effect a toroidal vector field (the curl of a toroidal field is a poloidal vector field, and vice–versa) , there could be an A_r component, given by

$$A_r = g_{\theta r}A^\theta + g_{\phi r}A^\phi, \tag{5.29}$$

which is non–zero when the metric is non-diagonal due to a lack of orthogonality in our co-ordinate system. The other two covariant components are given by

$$A_\theta = g_{\theta\theta}A^\theta + g_{\phi\theta}A^\phi, \tag{5.30}$$

$$A_\phi = g_{\theta\phi}A^\theta + g_{\phi\phi}A^\phi. \tag{5.31}$$

When calculating magnetic helicity, we must take the dot product of a vector potential with a curled quantity, and as such need a properly generalised dot product. This is given by

$$\boldsymbol{A} \cdot \boldsymbol{B} = g_{ij}A^i B^j. \tag{5.32}$$

Naturally

$$\boldsymbol{dl}_{(\theta_1,\phi_1),(\theta_2,\phi_2)} = (\theta_2 - \theta_1, \phi_2 - \phi_1, 0), \tag{5.33}$$

is the vector (determined by the resolution) going from (θ_1, ϕ_1, r) to (θ_2, ϕ_2, r). Finally, upon the surface of each individual shell making up our domain, the area element is given by the first fundamental form:

$$dA = \int\int \sqrt{g_{00}g_{11} - g_{10}^2}\mathrm{d}\theta\mathrm{d}\phi. \tag{5.34}$$

Throughout this chapter, unless otherwise specified, we will perform our calculations at the following resolution:

$$n_\theta = 82, \tag{5.35}$$

$$n_\phi = 82, \tag{5.36}$$

$$n_r = 16. \tag{5.37}$$

5.4 Where is the Writhe?

Before looking at how the BH18 formalism can be applied to produce a measure of helicity density, we will first consider the illustrative motivator for the shape field given in Section 5.2.1, where we introduced an incomplete, but crucially closed, figure of eight. In this section, we will model this geometry to see how the numerical result compares with the theoretical hypothesis.

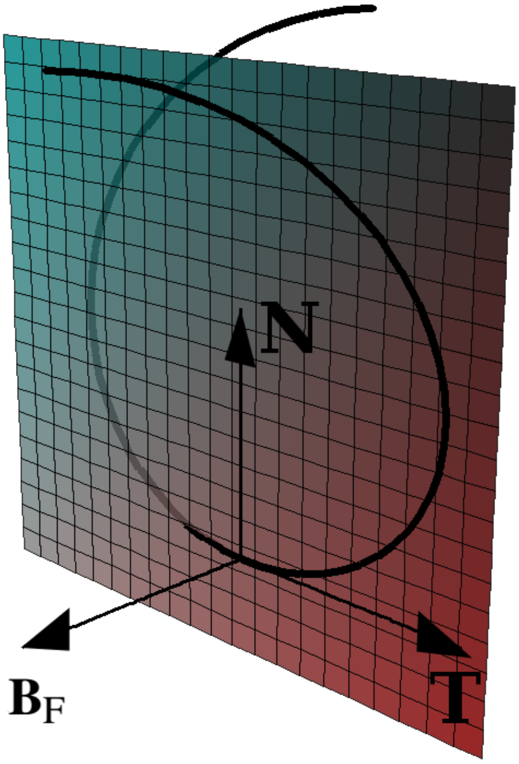

Fig. 5.2 Pictorial representation of the Frenet Serret frame, displaying each of the three Frenet-Serret vectors.

The tubular section of the figure of eight can be generated using a Frenet-Serret frame, which is made up of three vectors; the tangent vector to the curve **T**, the normal to the tangent, **N**, and the binormal $\mathbf{B}_F$. **T** follows the standard definition of a tangent vector, pointing in the direction of traversal. **N** is the derivative of **T**, with respect to the arc length parameter along the curve. Finally, $\mathbf{B}_F$, is formed by taking the cross product of **T** and **N**. Specifically, $\mathbf{B}_F$ is the normal to the plane defined by unit vectors **T** and **N**, within which the curve lies at any given instant. All three vectors are shown pictorially in Figure 5.2 for a generic example curve.

The expressions defining the frenet frame are given by

$$\begin{aligned} \frac{\mathrm{d}\mathbf{T}}{\mathrm{ds}} &= \kappa\mathbf{N}, \\ \frac{\mathrm{d}\mathbf{N}}{\mathrm{ds}} &= -\kappa\mathbf{T}+\tau\mathbf{B}_F, \\ \frac{\mathrm{d}\mathbf{B}_\mathrm{F}}{\mathrm{ds}} &= -\tau\mathbf{N}, \end{aligned} \tag{5.38}$$

where s is the arc length parameter of the curve, τ is the torsion of the curve, given by

$$\tau = -\mathbf{N}\cdot\frac{\mathrm{d}\mathbf{B}_\mathrm{F}}{\mathrm{ds}}, \tag{5.39}$$

and κ is the curvature, given by

$$\kappa = ||\frac{\mathrm{d}\mathbf{T}}{\mathrm{ds}}||. \tag{5.40}$$

In this framework, the tubular section can be parameterised as

$$\mathbf{r}_{Tube}(\theta,\phi) = \mathbf{T}(\theta)+r\cos(\phi)\mathbf{N}(\theta)+r\sin(\phi)\mathbf{B}_F(\theta), \tag{5.41}$$

where the original curve f_8 is given by

$$f_8(\theta) = \left(\cos(2.2\theta),\sin(4.4\theta),\frac{\sin(2.2\theta)}{3}\right), \tag{5.42}$$

for $0.1\pi \leq \theta \leq 0.9\pi$. We must also otherwise close the ends of the figure of eight, else we would produce a geometry with holes. We choose to close the ends with hemispheres, given by

$$\mathbf{r}_{\mathrm{End1}}(\theta,\phi) = r\sin(5\theta)\cos(\phi)\hat{\mathbf{x}}+r\sin(5\theta)\sin(\phi)\hat{\mathbf{y}}+r\cos(5\theta)\hat{\mathbf{z}}, \tag{5.43}$$

where r_{End1} denotes the $\theta = 0.1\pi$ end ($0 \leq \theta \leq 0.1\pi$). r_{End2} is defined similarly.

The ends of the tubular section are not aligned with the standard cartesian co-ordinate system (x,y,z), and as such we must align the hemispheric geometry with the co-ordinate system (**N**, **T**, $\mathbf{B}_\mathbf{F}$). This is done using the Euler angles (α,β,γ): on a sphere these are known as pitch, tilt and roll, and can be used relocate any one point on the sphere to any other point. In Figure 5.3, we show the three angles pictorially for translating from one co-ordinate system $(\mathbf{x},\mathbf{y},\mathbf{z})$ to another $(\mathbf{X},\mathbf{Y},\mathbf{Z})$.

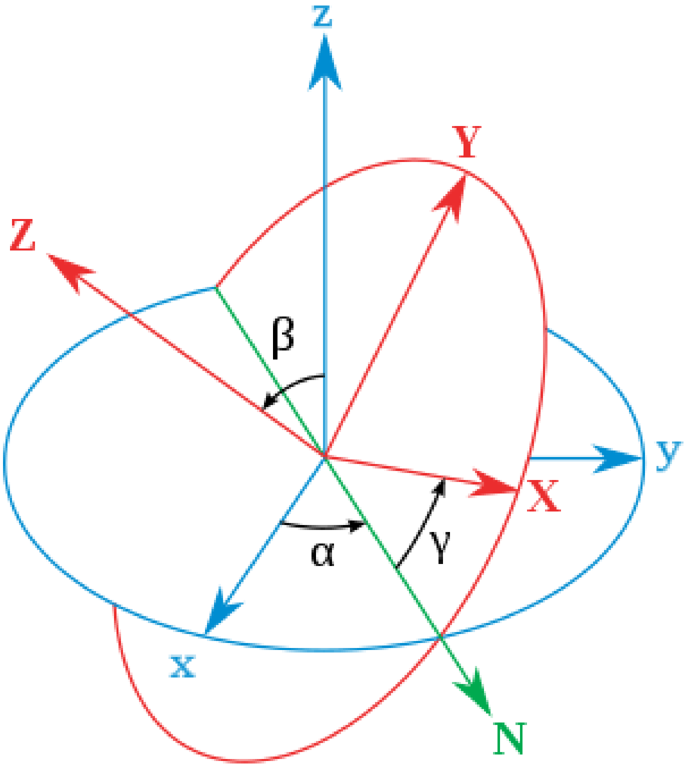

Fig. 5.3 Pictorial representation of the Euler angles for transforming to a frame $(\mathbf{X},\mathbf{Y},\mathbf{Z})$ from another frame $(\mathbf{x},\mathbf{y},\mathbf{z})$.

To transform into the new coordinate system, one first rotates around the **z** unit vector (of the original Cartesian co-ordinate system) by angle α, then around **x** by angle β, and finally around **z** again by angle γ. We calculate these angles according to the formulae

$$\alpha = \arccos\left(\frac{-\mathbf{Z}_y}{\sqrt{1-\mathbf{Z}_z^2}}\right), \tag{5.44}$$

$$\beta = \arccos(\mathbf{Z}_z), \tag{5.45}$$

$$\gamma = \arccos\left(\frac{\mathbf{Y}_z}{\sqrt{1-\mathbf{Z}_z^2}}\right), \tag{5.46}$$

where $\mathbf{Z}_y$ denotes the y component of the vector defining the new **z** unit vector, etc. The transformation between frames can then be written

$$\mathbf{R}_{\mathrm{F8}} = \mathrm{R}_z(\gamma)\mathrm{R}_x(\beta)\mathrm{R}_z(\alpha), \tag{5.47}$$

for the standard three-dimensional rotation matrices around the x and z Cartesian axes. Taking $\mathbf{R}_{\mathrm{F8}}\mathbf{r}_{\mathrm{End1}}$ applied to each end, and taking account of the proper origin, we arrive at the geometry as shown in Figure 5.4. Here, green denotes the tubular geometry whilst red and blue are the two hemispheric caps.

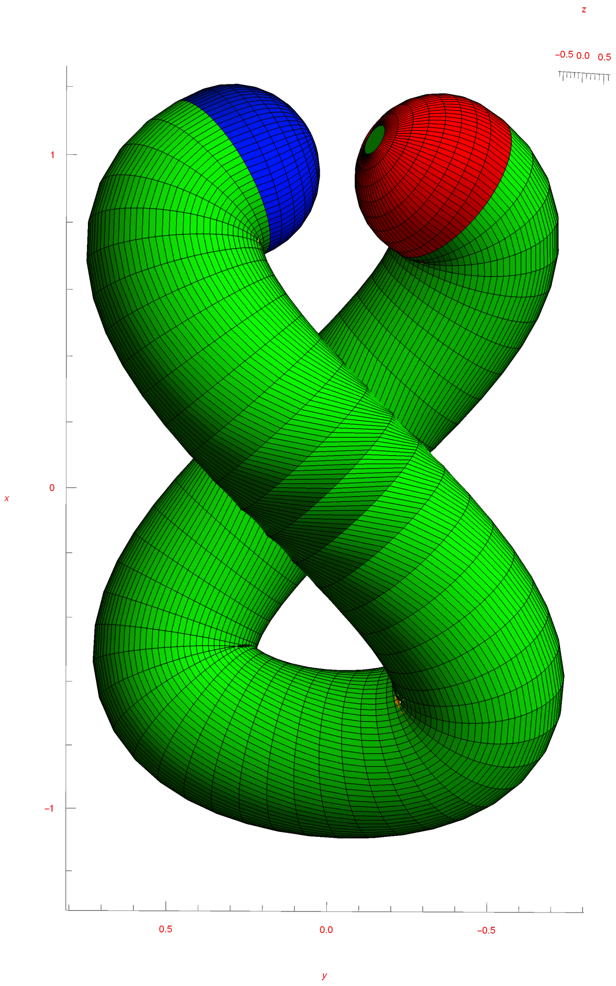

Fig. 5.4 Figure of Eight geometry as used in gauge calculations with hemispheric caps. Green denotes the tubular portion of the geometry, whilst red and blue denote the change in co-ordinate systems to the hemispheres.

In our original thought experiment, we envisaged a magnetic field which takes the form of a complete figure of eight. By aligning this magnetic field with our incomplete figure of eight geometry, then we should be able to measure the magnetic helicity associated with its writhe (self-crossing). Given the nature of our incomplete figure of eight, the magnetic field will emerge ($B_n > 0$) from one hemispherical cap, and then re–enter the closed domain at the other cap ($B_n < 0$). We assume that the magnetic field is exactly normal to these hemispherical caps, such that from the perspective of a toroidal–poloidal decomposition, it is a potential field at the caps. As such, we take

$$\mathbf{B}_{\mathrm{F8}} \cdot \hat{\mathbf{r}} = \begin{cases} 1 & \forall\ 0 \leq \theta < 0.1\pi, \\ 0 & \forall\ 0.1\pi \leq \theta < 0.9\pi, \\ -1 & \forall\ 0.9\pi \leq \theta < \pi, \end{cases}$$

with $\mathbf{B}_{\mathrm{F8}} \cdot \hat{\theta} = \mathbf{B}_{\mathrm{F8}} \cdot \hat{\phi} = 0$ on the caps. Thus, $\mathbf{B}_{\mathrm{F8,T}} = 0$ and $\nabla \times \mathbf{B}_{\mathrm{F8}} = \mathbf{J}_{\mathrm{F8}} = \mathbf{0}$ on the caps, accordingly. Elsewhere, along the tube, $\mathbf{B}_{\mathrm{F8}}$ is exactly toroidal.

In the case of a magnetic flux tube of radius 0.3 and magnetic flux $\Phi_{\mathrm{F8}} = 0.28$ we would expect (if it were embedded in a Cartesian volume) a magnetic helicity of $H_{\mathrm{F8}} = L_{\mathrm{F8}}\Phi_{\mathrm{F8}}^2 = 0.079$ (with $L_{\mathrm{F8}} = 1$).

Comparatively, by applying our methodology to this problem, with the magnetic field being largely enclosed by the incomplete figure of eight, we find that

$$\begin{aligned} H_A &= 2\int_0^r \int_0^\pi \int_0^{2\pi} \tilde{\mathbf{A}} \cdot \mathbf{B}_T \,\mathrm{d}\phi\,\mathrm{d}\theta\,\mathrm{dr} + \int_0^{\mathrm{r}} \int_0^\pi \int_0^{2\pi} \tilde{\mathbf{A}} \cdot \mathbf{B}_{\mathrm{S}} \,\mathrm{d}\phi\,\mathrm{d}\theta\,\mathrm{dr} \\ &= 0 + 0.071, \end{aligned}$$

which is accurate to within 90% of the theoretical result. We tested this for a variety of magnetic field strengths, and found the results to be consistent (we believe a higher resolution would improve the result). As such, we have demonstrated that the shape field is exactly contributing to the overall helicity in specialised geometric cases. Additionally, the helicity associated with linking has shown to be contained within the linking tubes themselves, not arbitrarily between the two linked regions (otherwise our integration within the tube would not capture it).

In Figure 5.5 we present a vector plot of the shape field associated with the above calculation, the implications of which are not immediately obvious. The regions in which we see circulation are clearly the points for which $J_{P,n}$ were most intense. These seem to occur where the tube experiences the most curvature/torsion (as we would expect), which presumably overall captures the total writhe of the geometry which corresponds to the linking.

5.5 A Local Helicity Density

Now that we have established the theoretical underpinning of the toroidal–poloidal decomposition, and in particular that of the shape field, we move to look at how it can be used to define a space–filling magnetic helicity density within a given domain of interest. We must also ensure that at no point do we double–count a portion of the magnetic field in our calculations.

The Kepler Conjecture states that the tightest possible packing of spheres has a density of 74.05%, using the most efficient lattice. This volume coverage will likely vary for

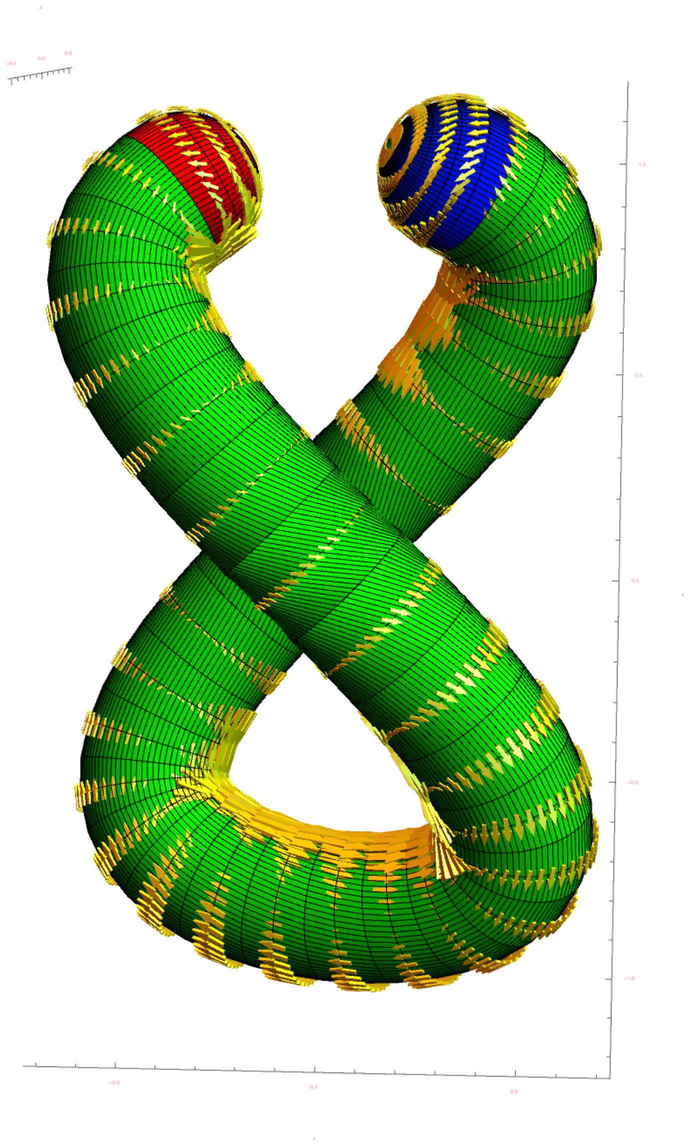

Fig. 5.5 Vector (yellow) plot of the shape field associated with a Figure of Eight with a potential field linking the two ends.

different geometries, such as cylinders, or even in the extreme case of non-overlapping figures of eight. As such, we choose to follow the convention established by the wavelet decomposition in the previous chapter: we will fill the domain of interest with a number of **non-overlapping** shapes, such as cubes or spheres, at a range of scales. We will again choose these scales to be factors of two, such that $L_s = 2^{-s}L$, where L is the domain length and L_s is the length of the largest concentric shell of a given domain at scale s. Note that we do not refer to the radius of a given shell, as our formalism has the radius being constant across the shell (when the Cartesian radius may in fact vary for, say, a cube).

As an example, consider a periodic magnetic field data cube, with $x_{\min} = y_{\min} = z_{\min} = 0$ and $x_{\max} = y_{\max} = z_{\max} = 2\pi$. Then, at scale $s = 0$, there will be exactly one value of absolute helicity ‘density’ (it has no spatial variation) calculated from a series of, say, cubic concentric shells centred at the midpoint of the domain, (π, π, π). When using concentric shells that have a cubic surface, this value of absolute helicity should correspond to the total helicity of the data cube, but if were to employ spherical shell surfaces, then we would naturally miss some of the volume (how this missing volume affects the calculations of an absolute helicity density is considered in the following section). At scale $s = 1$ there will be exactly eight values of absolute helicity, calculated from geometries of volume $(L/2)^3$ centred at $(\pi/2 + d_x\pi, \pi/2 + d_y\pi, \pi/2 + d_z\pi)$, where $d_{x,y,z} = \{0, 1\}$. This pattern is held consistently regardless of the surfaces being used.

By studying how the absolute helicity varies in space with decreasing spatial scale we will be able to learn about the scales and localities of the helicity structures within the magnetic field. Unlike the wavelet decomposition, this measure will not be additive, but it has a more intuitive physical meaning as the 'helicity in a box', whereas wavelets could tell us about the helicity associated with magnetic field that varies at a certain scale and locality.

As specified earlier, we will perform the calculations of absolute helicity at the following numerical resolution:

$$n_\theta = 82, \tag{5.48}$$

$$n_\phi = 82, \tag{5.49}$$

$$n_r = 16, \tag{5.50}$$

for the largest spatial scale ($s = 0$), but then each resolution parameter will be multiplied by a factor of

$$\frac{1}{5/2(s+1)}, \tag{5.51}$$

for all subsequent scales. We found that altering each of the resolutions by up to ±20% made no discernible difference.

To begin with, we detail the geometries with which we are interested, and show how to represent them in a spherical-esque coordinate system.

5.5.1 Geometries

Sphere

A sphere of radius r is properly described by the spatial vector

$$\mathbf{r} = r\sin(\theta)\cos(\phi)\hat{\mathbf{x}} + r\sin(\theta)\sin(\phi)\hat{\mathbf{y}} + r\cos(\theta)\hat{\mathbf{z}}, \tag{5.52}$$

with metric tensor

$$g_{ij} = \begin{pmatrix} r^2 & 0 & 0 \\ 0 & r^2\sin(\theta) & 0 \\ 0 & 0 & 1 \end{pmatrix}.$$

Although a sphere is mathematically symmetric in the radial direction, a numerical approximations of a sphere will have an associated shape field due to restrictions in resolution.

The shape field then quantifies how far (geometrically) our sphere of resolution n is from a true sphere.

Spherical Cube

The vast majority of dynamo, and in general MHD, simulations (including those studied in this article) are of a cuboid structure, with flat edges associated with either magnetic surfaces and or free or periodic boundaries. Thus, outside of Fourier analysis, it has been difficult to probe the distribution of helicity within these simulations. As we discussed in the previous chapter, spectral methods can also be inherently misleading. One could attempt to fill the simulation volume with spheres, and calculate the relative helicity of each sphere, but (as we discussed earlier) these are inherently non-space filling nor additive.

A cube is an inherently complex shape; at the corners there is an nonfinite amount of curvature contained in an infinitesimal space, or in other words a discontinuity. Our co-ordinate system will therefore itself be discontinuous. We take the coordinate system, modelled upon that of a distorted sphere:

$$\boldsymbol{r} = \begin{cases} \Theta r\hat{\mathbf{x}} + \Theta r\tan(\phi)\hat{\mathbf{y}} + f(\theta,r)\hat{\mathbf{z}} & \forall\ 7\pi/4 < \phi \leq \pi/4, \\ \Theta r\cot(\phi)\hat{\mathbf{x}} + \Theta r\hat{\mathbf{y}} + f(\theta,r)\hat{\mathbf{z}} & \forall\ \pi/4 < \phi \leq 3\pi/4, \\ -\Theta r\hat{\mathbf{x}} - \Theta r\tan(\phi)\hat{\mathbf{y}} + f(\theta,r)\hat{\mathbf{z}} & \forall\ 3\pi/4 < \phi \leq 5\pi/4, \\ -\Theta r\cot(\phi)\hat{\mathbf{x}} - \Theta r\hat{\mathbf{y}} + f(\theta,r)\hat{\mathbf{z}} & \forall\ 5\pi/4 < \phi \leq 7\pi/4, \end{cases}$$

where

$$\Theta = \begin{cases} 4\frac{\theta}{\pi} & \forall\ 0 \leq \theta \leq \pi/4, \\ 1 & \forall\ \pi/4 \leq \theta \leq 3\pi/4, \\ 4\frac{\pi-\theta}{\pi} & \forall\ 3\pi/4 \leq \theta \leq \pi, \end{cases}$$

and

$$f(\theta,r) = \begin{cases} r & \forall\ 0 \leq \theta \leq \pi/4, \\ r(-4\frac{\theta}{\pi}+2) & \forall\ \pi/4 \leq \theta \leq 3\pi/4, \\ -r & \forall\ 3\pi/4 \leq \theta \leq \pi. \end{cases}$$

Figure 5.6 shows how this decomposition resembles a sphere.

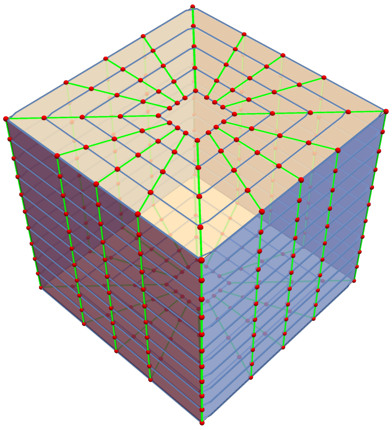

Fig. 5.6 Co-ordinate lines of a spherical co-ordinate representation of a cube.

Half Sphere

As we demonstrated in chapters 2 and 3, the helicity associated with a dynamo (in those cases, the Sun) is best represented on a hemispherical basis. A closed hemisphere, in the style of a sphere, can be written

$$\boldsymbol{r} = \begin{cases} r\sin(\theta)\cos(\phi)\hat{\mathbf{x}} + r\sin(\theta)\sin(\phi)\hat{\mathbf{y}} + r\cos(\theta)\hat{\mathbf{z}} & \forall\ 0 \leq \theta < \pi/2 \\ r\cos(\phi)(-2\Theta+2)\hat{\mathbf{x}} + r\sin(\phi)(-2\Theta+2)\hat{\mathbf{y}} & \forall\ \pi/2 \leq \theta < \pi, \end{cases}$$

where again $\Theta = \theta/\pi$. However, this geometry is not sufficiently three-dimensional in the equatorial plane, as it can be approximated by polar co–ordinates due to the parallel nature of r and Θ. This would result in $\sqrt{g} = 0$ due to the parallel nature of $\hat{\mathbf{r}}$ and $\hat{\boldsymbol{\theta}}$. As such, we choose

$$\boldsymbol{r} = \begin{cases} r\sin(\theta)\cos(\phi)\hat{\mathbf{x}} + r\sin(\theta)\sin(\phi)\hat{\mathbf{y}} + r\cos(\theta)\hat{\mathbf{z}} - \frac{r}{2}\hat{\mathbf{z}} & \forall\ 0 \leq \theta < \pi/2 \\ r\cos(\phi)(-2\Theta+2)\hat{\mathbf{x}} + r\sin(\phi)(-2\Theta+2)\hat{\mathbf{y}} - \frac{r}{2}\hat{\mathbf{z}} & \forall\ \pi/2 \leq \theta < \pi, \end{cases}$$

such that the centre of the hemisphere moves down at a rate half of that at which its volume is expanding, ensuring the geometries are nested. This is a numerical 'trick' to ensure continuity of a three-dimensional metric - the field which we assume to act on the surface of each substructure need not depend on the spatial variables.

Large scale magnetic fields, such as those describing the geomagnetic field of the Earth, are often written in terms of a spherical harmonic expansion. A large number of these functions Y_l^m have equatorial symmetry, such that the helicity associated with a symmetric component of a magnetic field would sum to zero, despite the magnitude of this contribution. By treating the hemisphere's separately, we overcome this cancellation. Further, by including the equatorial plane in the calculation of $\tilde{\boldsymbol{A}}$, we can enhance our estimate of helicity both contained in each hemisphere and how it is transferred between hemispheres. In such an example, we would calculate the normal field at each face according to the original expression (i.e. without the $-r/2\,\hat{\mathbf{z}}$ term).

5.6 A Constrained Field Example

In Smiet et al. (2015), the authors derive an analytical expression for a magnetic field given by the evolved state of an initially knotted, but consistently well–constrained magnetic field. This evolution is performed in a resistive MHD regime in a periodic box of length $2\pi l_0$, where l_0 is some characteristic length parameter. Naturally, as their simulations progress, the field simplifies (reducing magnetic energy). They find that the final form of the magnetic field lies upon a set of nested toroidal magnetic surfaces, and can be described by the following expression in Cartesian coordinates:

$$\mathbf{B}(x,y,z,r_0,a,\omega_1,\omega_2) = \frac{4r_0^4\sqrt{a}}{\pi(r_0^2+r^2)^3}\Big(2(\omega_2 r_0 y - \omega_1 xz), \\ -2(\omega_2 r_0 x + \omega_1 yz), \omega_1(-r_0^2+x^2+y^2-z^2)\Big)^T. \qquad (5.53)$$

Here, r_0 defines the radius of the smallest nested toroid, for which the field lines wind around ω_1 times in the poloidal direction (“the short way around") and ω_2 times in the toroidal direction (“the long way around") (note that these are not the same ’toroidal’ and ’poloidal’ which are the subject of this chapter), and a is a unit correction constant, which will be set to one.

In Figure 5.7, we plot this field for $r_0 = 1.1$, $\omega_1 = 0.17$, and $\omega_2 = 0.19$ (an example given by the original article) using a simplistic Runge Kutta code. It is clear to see that the field is well constrained within a short range of the origin (restricted by the r^6 term in the denominator), as well as being a well-twisted structure, indicating the presence of magnetic helicity. These parameters will be used throughout this study unless otherwise stated.

The work of the Smiet et al. (2015) paper is a particularly good test case as they have calculated an expression for the magnetic helicity of the total field for any set of parameters, given by

$$H = \int_0^\infty \int_0^\pi \int_0^{2\pi} \frac{4ar_0^7\omega_1\omega_2}{\pi^2(r_0^2+r^3)^3} r^2\sin(\theta)\; d\phi d\theta dr = ar_0^4\omega_1\omega_2. \qquad (5.54)$$

Note that the integration over all space allows us to use the classical definition of helicity. Further, their article states that the constants are strictly positive, meaning that we have a strictly positive helicity. This does not however imply that the helicity is everywhere positive. The distinction between helicity signs and magnitude at different scales is the very purpose of this work.

In Figure 5.8 we plot the ratio of the absolute magnetic helicity contained within a spherical geometry of spherical radius r with that of the analytical expectation above, as a

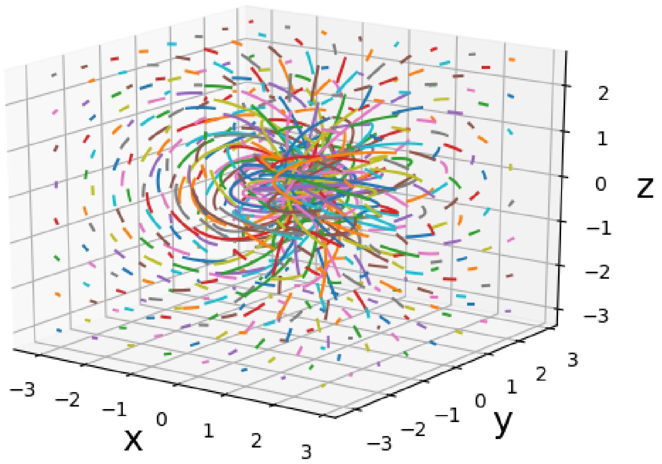

Fig. 5.7 Runge Kutta plot of the field given by equation 5.53, with parameters $r_0 = 1.1$, $\omega_1 = 0.17$, and $\omega_2 = 0.19$. Each coloured line indicates an individually seeded field-line with a fixed step length (giving variable length).

secondary test case. Each individual line corresponds to a randomised set of parameters r_0, ω_1, ω_2. As we approach $r \approx 2$, these lines approach unity, as we would expect, indicating again that the methodology of this work is correctly calculating magnetic helicity. The rate at which unity is reached is naturally dependent upon the parameters themselves, as they alter the inherent structure of the magnetic field. The value of $r_{unity} \approx 2$ is predicted in Figure 5.7, where (for $r > 2$), we see $|\mathbf{B}|$ approach zero.

In figures 5.9 and 5.10 we plot bubblegrams (as described for the wavelet methodology in Chapter 4) of the absolute magnetic helicity as a function of space, for scales $s = 0, 1, 2, 3, 4$, using spherical and cuboid domains respectively, as described in Section 5.5. As we have previously described, scale 2^0 ($s = 0$) should correspond to the total helicity of the field, which corresponds to $H_K = 0.04729043$ for this set of parameters. In this case, the spherical domains have captured 98% of the theoretically expected helicity, whilst the cuboid domain captured 90% of the total helicity, which is admittedly contrary to our expectation. One likely explanation for this is linked to the necessity of a finite numerical resolution: a cuboid will assign a greater weighting (relative to its total resolution) to the field at the outer edges of the domain (which has been shown to be asymptotically zero). A sphere will approach these boundaries more slowly (except for along the equator), and as such a greater weighting is placed where the field is non–trivial. We will attempt to demonstrate this below.

The two choices of domain (spherical and cuboid) are in agreement that the vast majority of the magnetic helicity is on the scale of the domain. At scales 2^{-2} onwards, we see that there is a an increasingly amount of small scale absolute magnetic helicity located

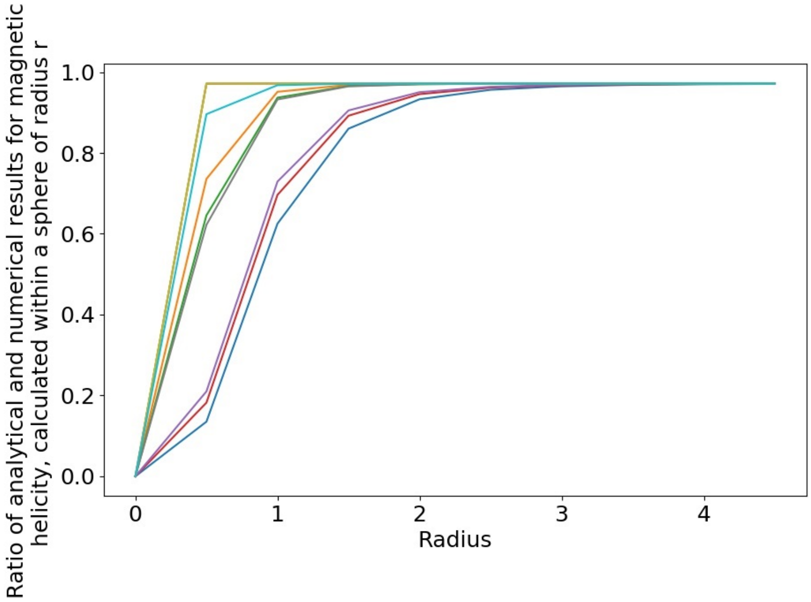

Fig. 5.8 Value of the ratio between the magnetic helicity calculated within spheres centred on the origin, and the analytical expression of (5.54), where each line was generated by a set of randomised parameters for r_0, ω_1 and ω_2.

in one corner of the knotted field. This is contrary to what one might expect having looked at only the field line distribution, which implied that the helicity is entirely centred on the origin at all scales. The amplitude of this helicity implies that is likely numerical noise, however.

In Figure 5.11, we plot the ratio of the helicities at each locality, as a function of scale, between the results obtained for a sphere and cuboid. This ratio is given by

$$\frac{|H_A(x,y,z,s)[\text{Sphere}]|}{|H_A(x,y,z,s)[\text{Cube}]|} \tag{5.55}$$

where (x,y,z) is the centre of a given locality, which is held consistent for both the sphere and cube, being dependent only upon the domain itself (as described in Section 5.5). The locality index (LI) advances by one for each subsequent locality considered. Thus, $\text{LI} = 0$ corresponds to the single value of absolute helicity considered at $s = 0$. Then, $1 \leq \text{LI} \leq 8$ corresponds to the eight localities of volume $(L/2)^3$ required to maximally fill the domain at scale $s = 1$, etc. The colour coding within the figure indicates which portions of the LI correspond to which spatial scale: there is no locality information in the index itself, it acts only to compare the helicity at the same centrality, regardless of where that centrality is.

Although initially above one (see the discussion above), the ratio does settle well below unity, at around 0.4. The pattern does appear cyclic, likely associated with how close the locality associated with each index is to the origin (where the magnitude of the magnetic field is most intense). At the smaller scales, the differences in relative weighting of the field becomes less important, which are also the scales where we see the cube out-perform the sphere (based on the positive–definite nature of magnetic helicity in this case).

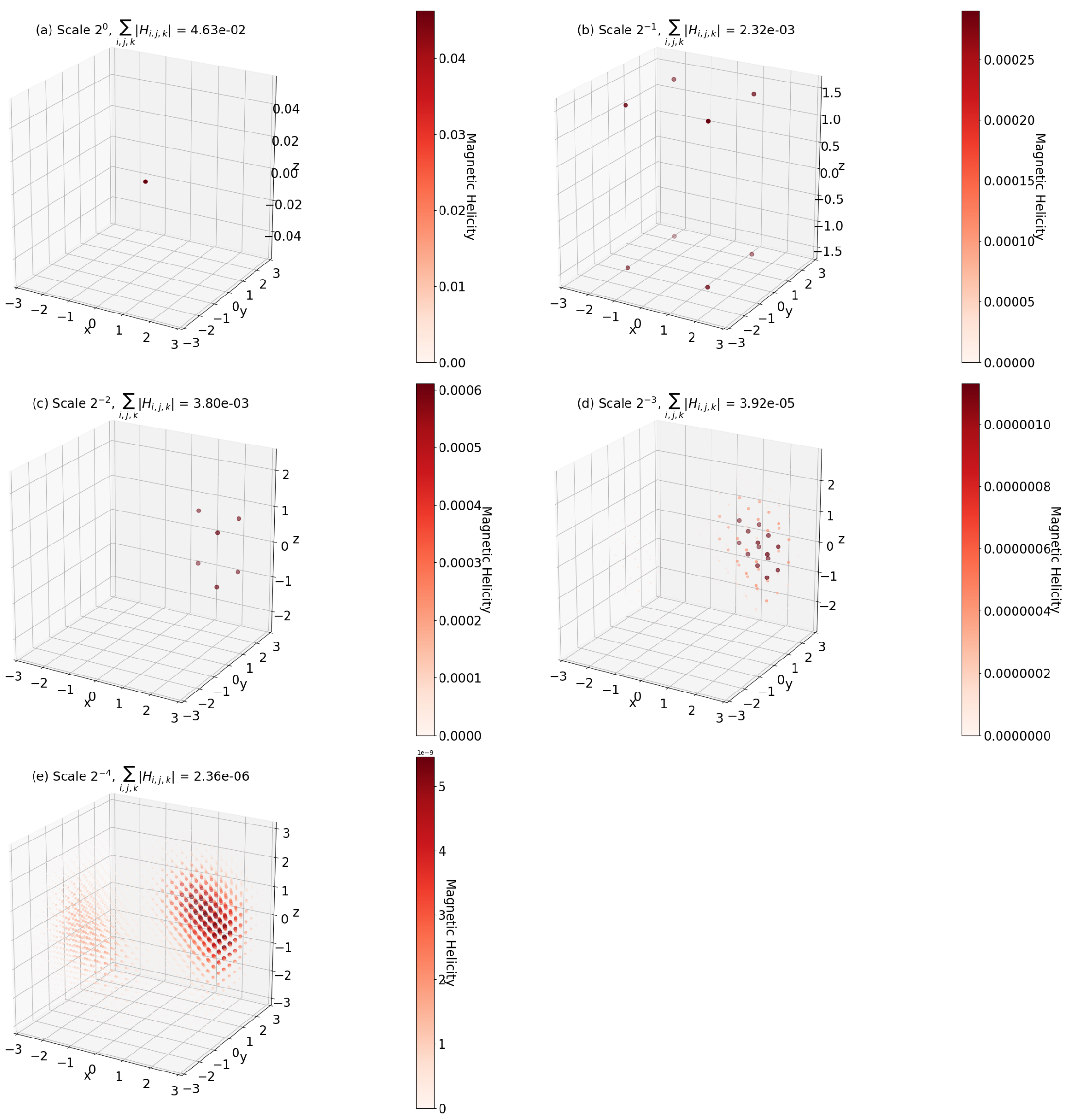
(a) Scale 2^{0}, $\sum_{i,j,k}|H_{i,j,k}|$ = 4.63e-02

(b) Scale 2^{-1}, $\sum_{i,j,k}|H_{i,j,k}|$ = 2.32e-03

(c) Scale 2^{-2}, $\sum_{i,j,k}|H_{i,j,k}|$ = 3.80e-03

(d) Scale 2^{-3}, $\sum_{i,j,k}|H_{i,j,k}|$ = 3.92e-05

(e) Scale 2^{-4}, $\sum_{i,j,k}|H_{i,j,k}|$ = 2.36e-06

Fig. 5.9 Helicity as a function of space at scale $s = 0, 1, 2, 3, 4$, calculated using the toroidal poloidal density applied to spherical domains, for the knotted field described in equation (5.53).

Finally, in Figure 5.12, we plot the relative contribution of the shape field helicity to the total absolute helicity,

$$H_S = \frac{|\int_0^r \int_0^\pi \int_0^{2\pi} \tilde{\mathbf{A}} \cdot \mathbf{B}_S \, \mathrm{d}\phi \, \mathrm{d}\theta \, \mathrm{d}r|}{|H_A|}, \tag{5.56}$$

for both the cuboid (blue) and sphere (red) calculations. As we would expect, the shape field associated with the spherical case, whilst non-zero, offers a much smaller contribution than that in the cuboid case (with a maximum of 2% compared to 35%). The mean relative contribution of the shape fields from the sphere and cuboids are 0.58% and 14.2% respectively.

Again, the shape field contribution appears to demonstrate cyclic behaviour, for which the two methods themselves are roughly in sync (although there appears to be a small

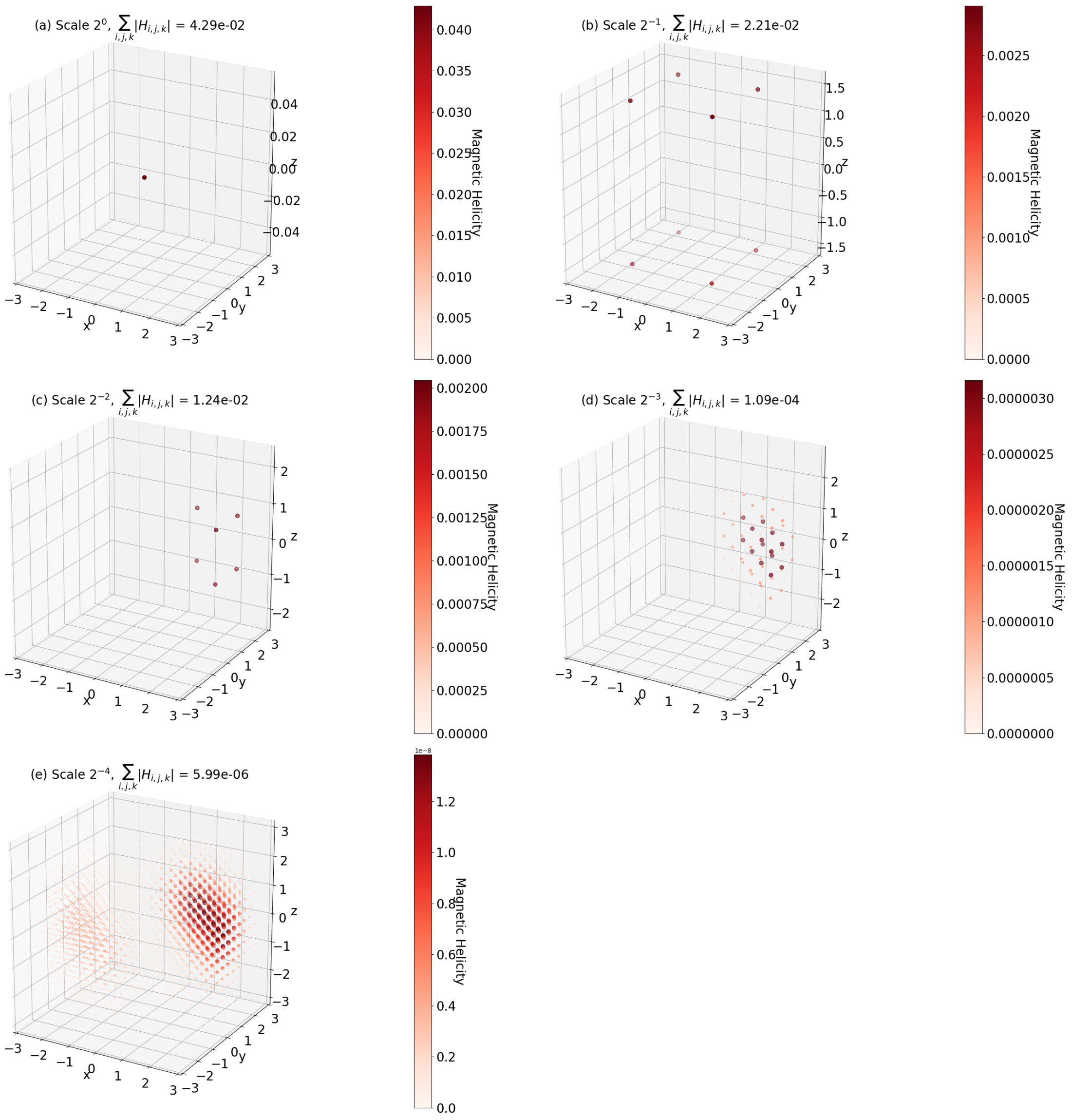

Fig. 5.10 Helicity as a function of space at scale $s = 0, 1, 2, 3, 4$, calculated using the toroidal poloidal density applied to cuboid domains, for the knotted field described in equation (5.53).

deviation in the cuboid case during the maxima). This is likely associated the specific magnetic field distribution at the given locality.

It is important to note that direct comparisons of shape field here would not be rigorous: the differing structure of the two geometries means that the magnetic field through each face ($B_n(\theta, \phi)$) is different for both the sphere and cuboid, even assuming they are centred at the same locality. We will test this more rigorously later in this chapter. In the next section, we apply our methods to a forcing which is known to be able to produce a magnetohydrodynamical dynamo.

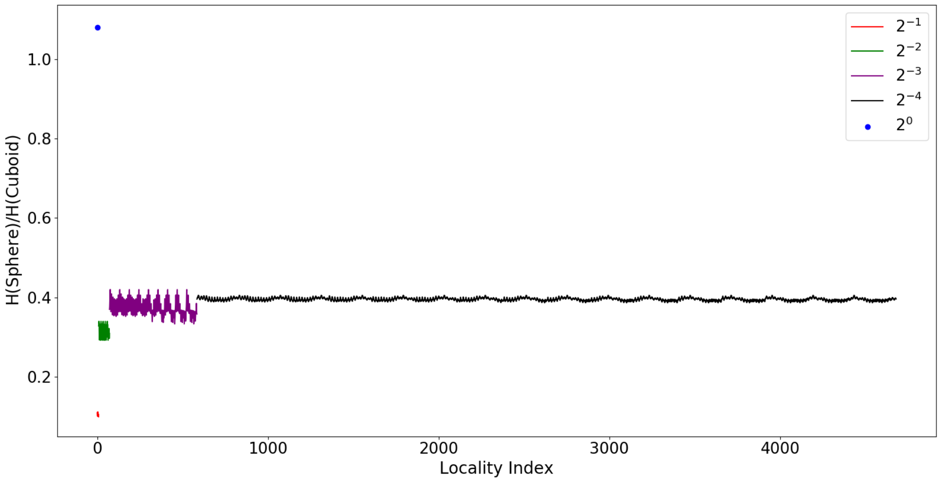

Fig. 5.11 Ratio of helicity contained within a sphere versus that of a cube at each locality and scale. Colour indicates the scale which the index refers to.

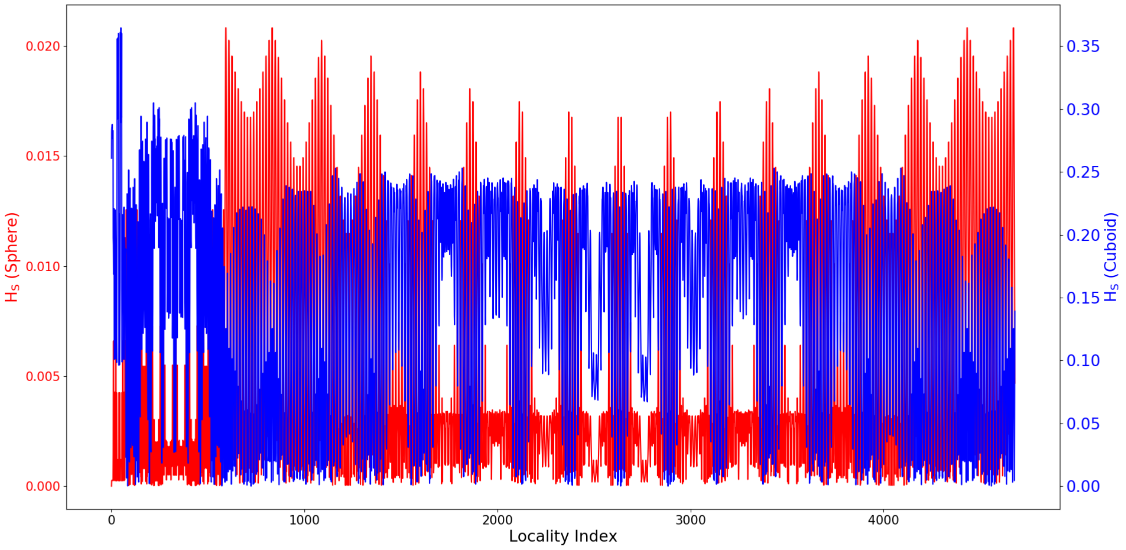

Fig. 5.12 Ratio of magnitude of helicity contributed by the shape field to that of the linking of the toroidal and poloidal fields, for both the sphere (red) and cuboid (blue) case.

5.7 ABC Field

The future impact of this work is the potential to be able to analyse the localised density and scale of helicity within complex MHD simulations and observations, as both a function of space and scale. Recall from the previous chapter, the Arnold-Beltrami-Childress (ABC) magnetic field/forcing is given by

$$\mathbf{B}_{ABC} = (C\cos(y) + A\sin(z), A\cos(z) + B\sin(x), B\cos(x) + C\sin(y)), \tag{5.57}$$

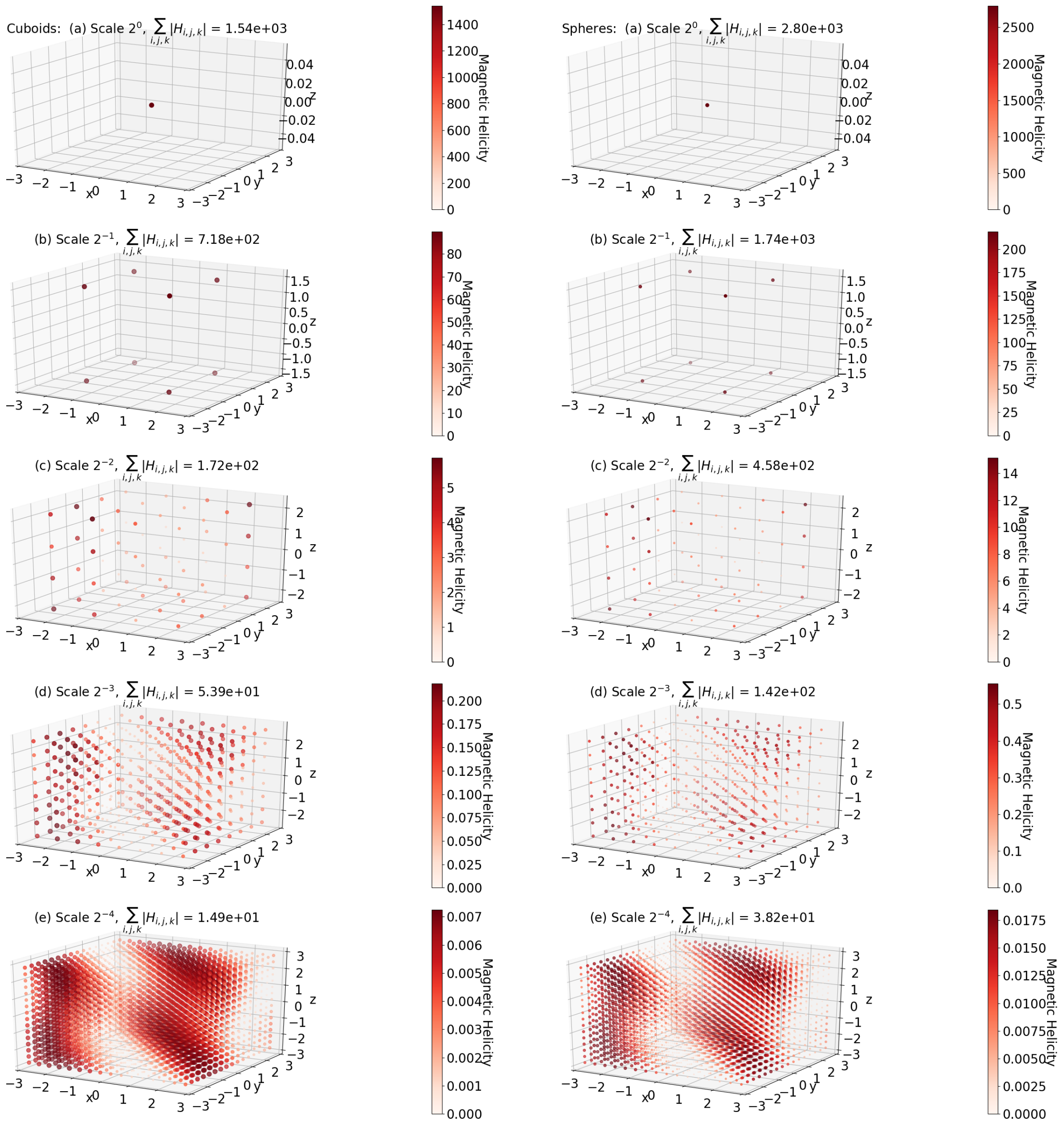

Fig. 5.13 Magnetic helicity associated cuboid (left) and spherical (right) domains with decreasing scale (down), as applied to an ABC field with $A = 3$, $B = 2.5$, $C = 4.5$.

for constants A, B, C, and is such that $\mathbf{B}_{ABC} = \mathbf{A}_{ABC} = \nabla \times \mathbf{B}_{ABC}$. In this section, I apply our methodology to such a magnetic field.

The ABC field is of particular interest as it has a positive definite helicity “density", as $\nabla \times \mathbf{B} = \mathbf{B}$, such that $\mathbf{A} = \mathbf{B}$, and

$$\mathbf{A} \cdot \mathbf{B} = |\mathbf{B}|^2. \tag{5.58}$$

Integrating over all space gives a total magnetic helicity

$$H_{ABC}(A, B, C) = 8\pi^3 (A^2 + B^2 + C^2). \tag{5.59}$$

Taking $A = 3$, $B = 2.5$, $C = 4.5$, we have $H_{ABC} = 2802$, we apply our methodology (from both spheres and cubes side–by–side) in Figure 5.13, with cuboids on the left and spheres on the right. Further, in Figure 5.14, we plot the ratio between the values of absolute

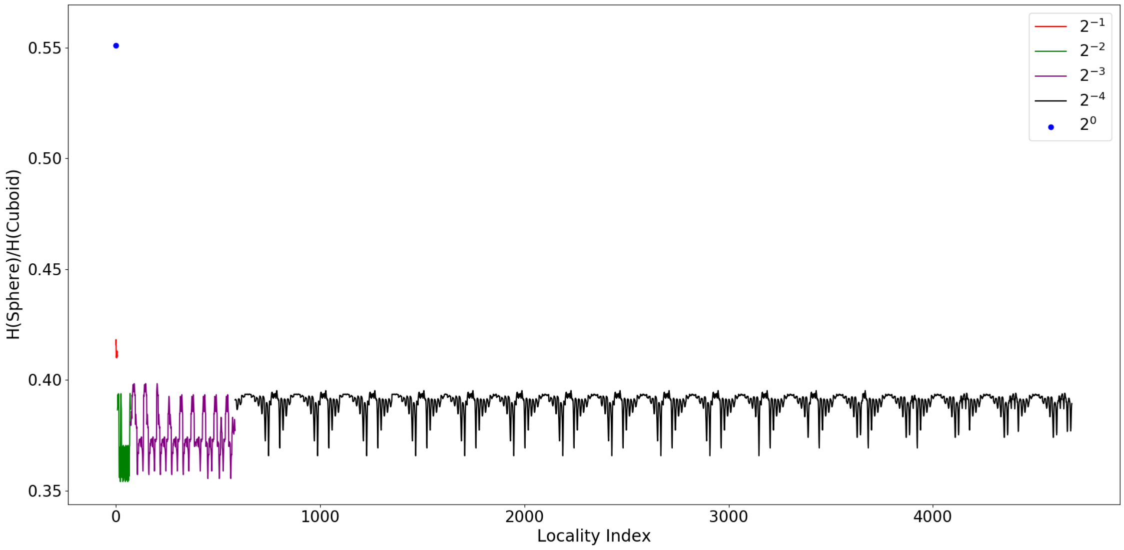

Fig. 5.14 Ratio of magnetic helicity as captured by spherical and cuboid domains, as a function of locality through all scales.

helicity associated with each locality (as in Figure 5.11). The results in this case are more in line with expectations, lending credence to our theory regarding the resolution weighting theory when considered alongside the unconstrained nature of the ABC field. The largest spatial scale in the cube case captures basically the entire helicity structure (99.8%), whilst the spherical example massively underperforms (55%). This value is in line with a basic estimation of the ratio between a spherical and cubic volume of the same radii;

$$\frac{4/3\pi r^3}{(2\pi)^3} = 0.52, \tag{5.60}$$

(taking into account of the inhomogeneity of the ABC field). The structure of the ABC field can be seen at scales 2^{-3} and 2^{-4} The ratios in Figure 5.14 show that the cube consistently outperforms the sphere at all scales. Finally, in Figure 5.15, we plot the value of the magnetic helicity from the shape field associated with each locality at each scale for both the sphere and cube. We see no notable change from that of the previous example (a constrained, knotted field).

5.8 Asymmetry Contributions

In sections 5.6 and 5.7 we have demonstrated that the shape field, on average, behaves as we would expect when comparing its relative contribution to the absolute helicity associated with cuboid and spherical domains. However, we noted that the comparisons were not precisely rigorous, due to the disparities between the values of B_n on the faces (due to the geometrical differences). We circumvent this problem by defining $\mathbf{B}$ as a function of (θ, ϕ) (referring to the general spherical-decomposition used throughout this chapter). Spherical harmonics are a well known example of such functions, which we will make use of in this

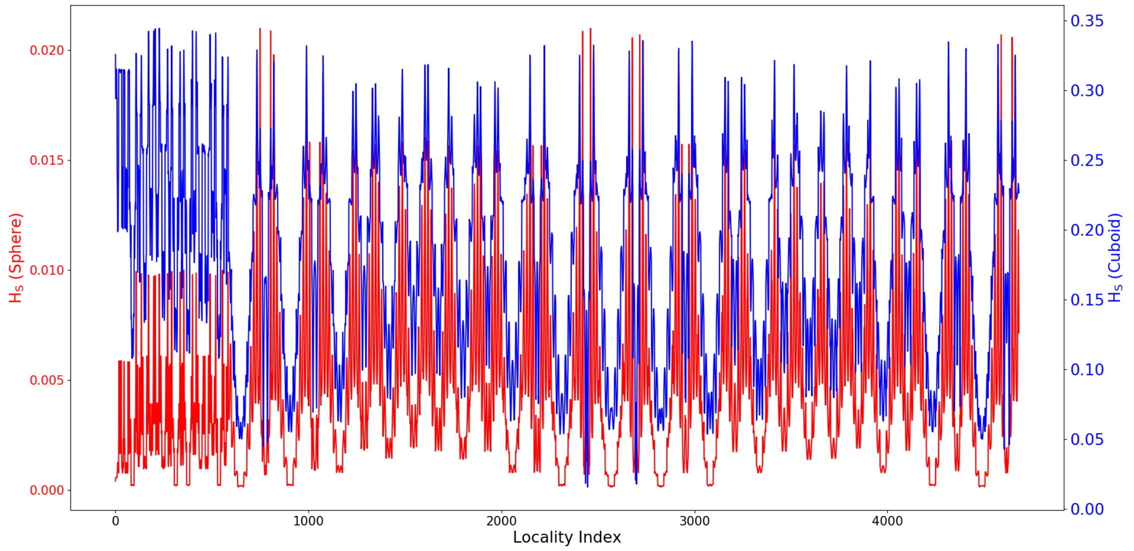

Fig. 5.15 Magnitude of shape field as a function of locality for both spheres and cubes, as applied to the ABC field.

subsection. They are especially useful in this context as they fulfil

$$\int_S Y_l^m \,\mathrm{d}\theta\mathrm{d}\phi = 0, \tag{5.61}$$

the divergence free condition. As such, we choose

$$B_n(\theta,\phi) = Y_l^m(\theta,\phi), \tag{5.62}$$

with $\mathbf{B}_\theta = \mathbf{B}_\phi = 0$. This admittedly does not resolve the disparity between the areas of individual face-elements, but is otherwise an improvement to the previous comparisons.

In figures 5.16, 5.18 and 5.20 we plot $\tilde{\mathbf{B}}$ associated with $B_n = Y_5^2(\theta,\phi)$ alongside their respective $\mathbf{B}_S$ in figures 5.17, 5.19 and 5.21 for the spherical, cubic and cylindrical geometries respectively. Note that in this case, we take $n_r = 3$ (the minimum number required to calculate a central-difference curl), but n_θ and n_ϕ remain unchanged. The vectors associated with each vector field are given in yellow, with the magnetic field indicated by blue/red (positive/negative), against a neutral green background. Further, in Table 5.1, we give the values of

$$\int_S \tilde{\mathbf{B}}\cdot\tilde{\mathbf{B}}\,\mathrm{d}\theta\mathrm{d}\phi, \tag{5.63}$$

and similarly for the shape field $\mathbf{B}_S$, and the ratio between the two for the spherical, cubic, half sphere, figure of eight and cylindrical geometries.

Demonstrably, in all cases for which the shape field is non-zero (in a notable sense), it is most intense around the regions for which the geometries experience the most intense curvature. This is as we would expect, and in line with the results of Section 5.4. In this ideal case, we find the shape field associated with the sphere to be extremely small in magnitude (although not necessarily small in terms of its helicity contribution), as

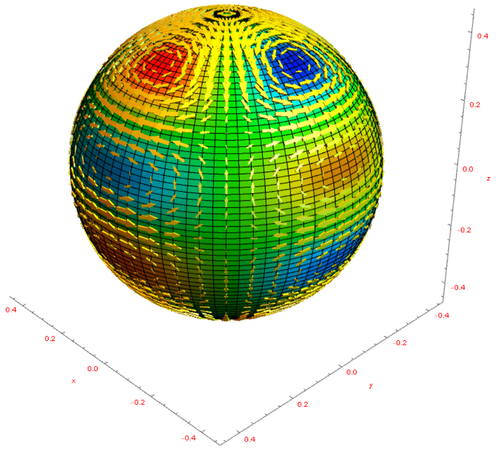

Fig. 5.16 Vector potential $\tilde{\mathbf{B}}$ on a sphere for $B_n = Y_5^2$

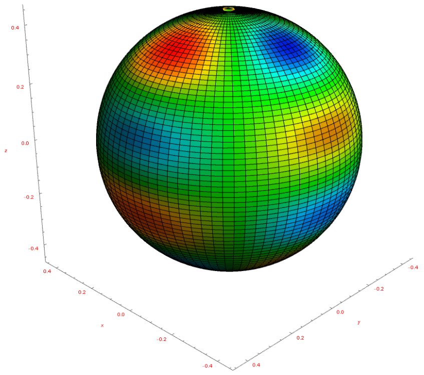

Fig. 5.17 Shape field $\mathbf{B}_S$ on a sphere for $B_n = Y_5^2$

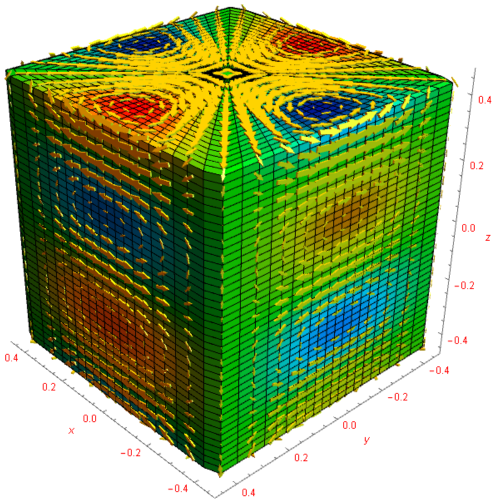

Fig. 5.18 Vector potential $\tilde{\mathbf{B}}$ on a cube for $B_n = Y_5^2$

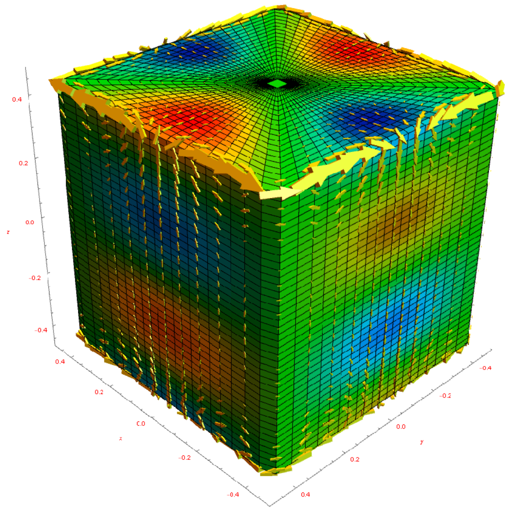

Fig. 5.19 Shape field $\mathbf{B}_S$ on a cube for $B_n = Y_5^2$

Geometry	$\tilde{\mathbf{B}}$ Integral ($\times 10^{-2}$)	$\mathbf{B}_S$ Integral ($\times 10^{-2}$)	Ratio
Sphere	1.13	3.74×10^{-7}	3.29×10^{-7}
Cube	3.32	0.461	0.138
Half Sphere	5.64	0.552	0.098
Figure of Eight	32.2	41.1	1.28
Cylinder	12.1	2.04	0.17

Table 5.1 Values of $\tilde{\mathbf{B}}$ integral and $\mathbf{B}_S$ integral according to a magnetic field Y_5^2, which is fixed in (θ, ϕ) rather than in (x, y, z).

compared to previous results for the constrained knotted field, and ABC field. The magnitude of the shape field in the cube geometry is also lower, perhaps implying that magnitude is not a perfect measure of relative importance of helicity contribution, in this

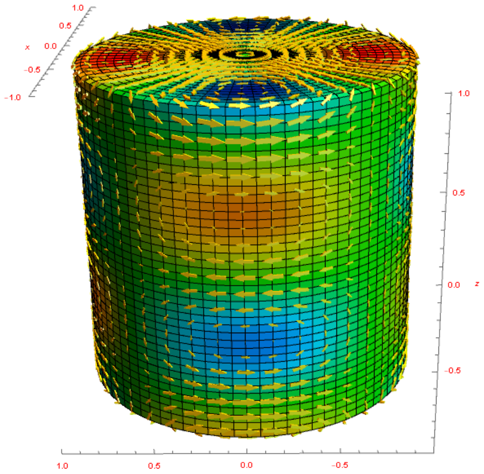

Fig. 5.20 Vector potential $\tilde{\mathbf{B}}$ on a cylinder for $B_n = Y_5^2$

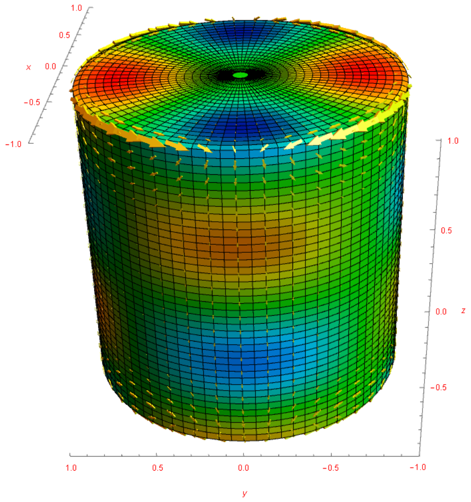

Fig. 5.21 Shape field $\mathbf{B}_S$ on a cylinder for $B_n = Y_5^2$

case. This is especially notable for the figure of eight, where the magnitude ratio is close to one, whilst the relative contribution of the shape field is 100%.

We note in particular that the magnitude of the shape field for the cylinder is bigger than that from the cube geometry, despite the cube geometry appearing to have additional discontinuities. This, combined with the notable smallness of the shape field magnitude for the half–sphere, illustrates the importance of radial symmetry when considering the importance of the shape field, not just the degree of discontinuity. We then, in figures 5.22 and 5.23, plot the ratio between the absolute helicities contained within cylinders, and the relative contribution to absolute helicity from the shape field for the cylinder, for the ABC field, both as compared to the case when using cubic shells, as an additional data point. The ratio of absolute helicity captured by cylinders, as compared to cubes, is extremely close to the ratio of their volumes:

$$\frac{2\pi^4}{(2\pi)^3} = 0.79. \tag{5.64}$$

The relative contribution to the shape field in the case of the cylinder is, in this case, very slightly lower than that of the cuboid.

5.9 Summary and Conclusions

We have computed numerically the theoretical concepts proposed in Berger and Hornig (2018), in which a magnetic field within a generic magnetic is decomposed into its poloidal ($B_r = 0$) and toroidal ($J_r = 0$) components upon a series of concentric shells making up said geometry. We have performed the first numerical calculations of the shape field

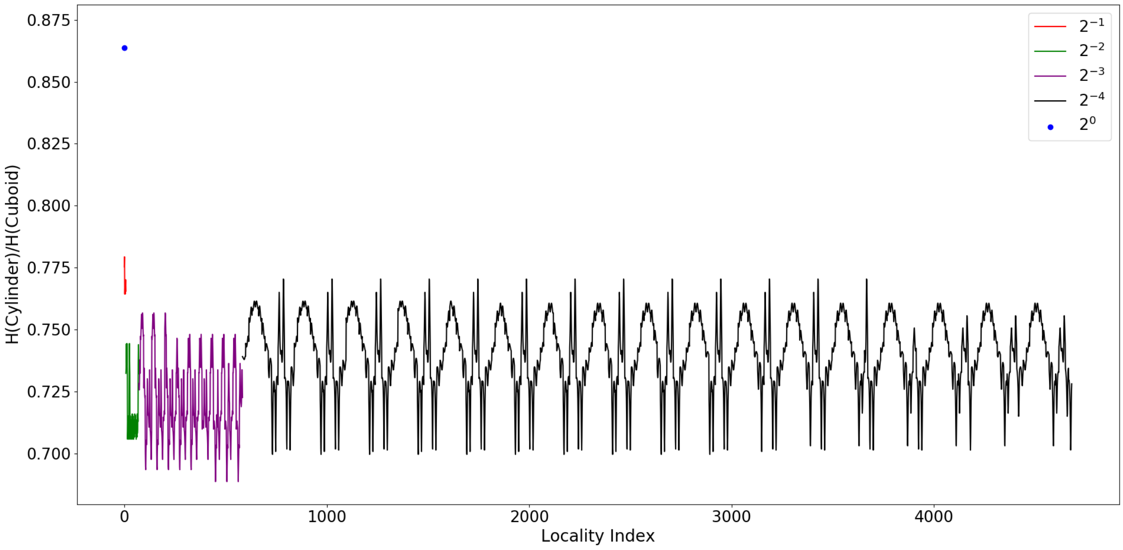

Fig. 5.22 Ratio of magnetic helicity as captured by cylindrical and cuboid domains, as a function of locality through all scales.

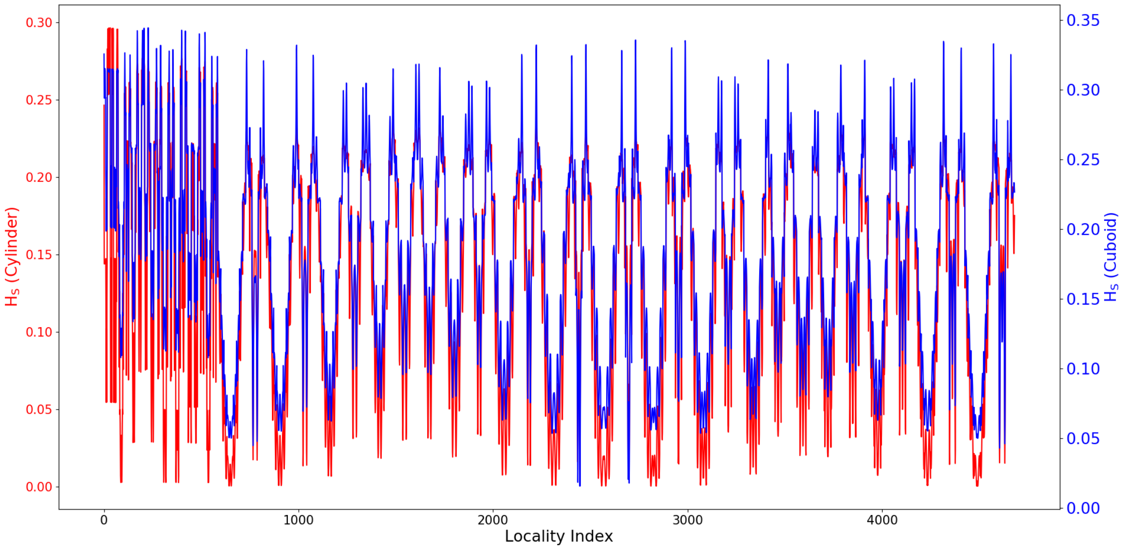

Fig. 5.23 Magnitude of shape field contribution to magnetic helicity as a function of locality for both cylinders and cubes, as applied to the ABC field.

associated with radial asymmetries within these shells, which we found indeed highlight their asymmetries, and are seen to make notable contributions to the balancing of the overall helicity. In particular, in the illustrative example of an incomplete figure of eight, which is completed by a potential field, we found that the shape field alone captures the writhe associated with its crossing. This showed that writhe is contained along fieldlines, rather than (say) at some generic point between the two crossing fieldlines.

We also showed that the generalisability of the toroidal–poloidal decomposition allows it to be used as a helicity density in a variety of circumstances. In particular, the geometries used to define said density can offer information about the field, by comparing the helicity densities calculated using differing geometries. This definition of density is not as rigorously well–defined as that of proposed in Chapter 4, but the intuition as the 'helicity in a box' could be useful for certain subsets of field. Further, it is unrestricted by the wavelet requirement (at least in three–dimensions) to a cubic domain.

Finally, as a point of interest (and to some degree a numerical check) we calculated the magnitude of the shape field associated with a small range of theoretically relevant geometries for a fixed magnetic field which depended only on the co-ordinate decomposition, not the locality (to ensure cross–comparison).

Chapter 6

Summary, Conclusions and Further Work

The aim of this thesis was to first establish magnetic helicity as a meaningful quantity in context of the solar dynamo and, with such a context as a motivator, develop theoretical results which will enable further, more detailed study. In particular, we were motivated by the concept of alpha quenching, which indicated that magnetic helicity is directly related to both the function of the solar cycle, and the ability for the dynamo to transfer energy between states.

In Chapter 2, we demonstrated that whilst the polar field was a good indicator of the strength of the next solar cycle, being the field which is wrapped up by the omega effect, large–scale magnetic helicity flux was in most cases statistically superior. Physically, this is because the amount of magnetic field being wrapped up *is* the helicity flux, but also because we must take account of magnetic field below the polar field cap.

In particular, we found that a hemispherical splitting of both magnetic helicity flux and sunspot number offered the best statisical correlation. There is, however, a lack of data available for such comparisons. To obtain a significant number of data points we resorted to reconstructions of the magnetic field, but these were found to be too noisy and unreliable.

In Chapter 3, we studied the helicity flux associated with shear motions on the Sun in more detail using the output of a pair of surface flux transport models. They offered a good comparison through the differences in the flux emergence term: one model employed magnetogram–filtered emergence, whilst the latter used semi–synthetic sunspot number data. The latter model allows a much longer simulation time.

Surface flux transport models offer a higher spatial resolution than that used in the previous chapter. Helicity fluxes were also calculated for the shear effects of meridional velocity and supergranular diffusion. However, these additional helicity fluxes proved to be largely negligible outside of solar minima, as compared to that due to differential rotation. The spatial resolution used within this chapter was shown to be unachievable by the observational data used in Chapter 2.

We found that even a hemispherical splitting may not be sufficient: magnetic helicity flux is oppositely signed in the polar regions as compared to the active latitudes, and the overall helicity flux as a function of time is a delicate balance between these two latitudes. We also presented some analytical results on the overall balance of helicity flux associated with differential (uniform) rotation and turbulent supergranular diffusion. The physicality of the latter case is not immediately clear, and we believe this should be the focus for a small exploratory project.

Finally, we showed that this high–resolution helicity was highly correlated with the axial dipole moment for the semi–synthetic simulation of the solar magnetic field, over the period 1700 – 2009. This is in agreement with the results obtained in Chapter 2.

In Chapter 4, the main result of this thesis, we demonstrated that the gauge and boundary conditions can be circumvented using an appropriate two–point correlation measure of winding, inspired by the winding gauge. Further, as a step beyond the scale measures offered by the Fourier analysis, we showed that a wavelet decomposition offers a physically meaningful spatial and scale localisation of helicity, whilst retaining the crucial feature of additivity. In particular, the localising nature was shown to be physically meaningful dependent upon the degree of decomposition which we apply to the magnetic field.

By doubly decomposing the magnetic field within the two–point correlation measure, we were able to analytically separate helicity into contributions from magnetic energy and topology. This relationship was also demonstrated for an analytic duplication of magnetic reconnection. In the future, it is extremely important that this relationship is tested for true MHD simulations.

Comparisons were made with fourier methods, for which we concluded that the latter offered a less well–specified measure of scale. A physically meaningful spatial decomposition of helicity has important consequences for the study of the α effect in solar dynamo theory, and of MHD turbulence in general. We believe that the wavelet decomposition is more powerful and intuitive than the currently used fourier methods, and as such there is a great deal of comparative work to be done, and further exploratory analysis on existing simulation work. To do this comparative work, a more thorough comparison of Fourier and Wavelet spectra must be performed.

Finally, in Chapter 5 we explored a more simplistic measure of localised helicity, in terms the helicity contained with a series of non–overlapping geometries. These geometries can be both curvilinear and non–orthogonal: asymmetries within the geometry were shown to affect the value of helicity, and we calculated these contributions numerically for the first time, as compared to the contribution from the magnetic field itself. We also demonstrated that the writhe–helicity associated with a self–crossing flux tube is located at the points of intense torsion.

References

Arnol'd, V. and Khesin, B. (1998). Topological Magnetohydrodynamics *Springer*.

Asgari-Targhi, M. and Berger, M. A. (2009). Writhe in the stretch-twist-fold dynamo. *Geophysical and Astrophysical Fluid Dynamics*, 103(1):69–87.

Balogh, A., Hudson, H., and Kristof, P. (2016). The Solar Activity Cycle: Physical Causes and Consequences. *Springer*.

Baumann, I., Schmitt, D., and Schussler, M. (2006). A necessary extension of the surface flux transport model. *Astronomy and Astrophysics*, 446(1):307–314.

Berger, M. (1988). An energy formula for nonlinear force-free magentic fields. *Astronomy and Astrophysics*, 201:355.

Berger, M. and Field, G. (1984). The topological properties of magnetic helicity. *Journal of Fluid Mechanics*, 147:133–148.

Berger, M. and Prior, C. (2006). The writhe of open and closed curves. *Journal of Physics A: Mathematical and Theoretical*, 39:8321–8348.

Berger, M. A. (1984). Rigorous New Limits on Magnetic Helicity Dissipation in the Solar Corona. *Geophysical and Astrophysical Fluid Dynamics*, 30(1-2):79–104.

Berger, M. A. (1999). Introduction to magnetic helicity. *Plasma Physics and Controlled Fusion* 167.

Berger, M. A. and Hornig, G. (2018). A generalized poloidal – toroidal decomposition and an absolute measure of helicity. *Journal of Physics A: Mathematical and Theoretical* , 51.

Berger, M. A. and Ruzmaikin, A. (2000). Rate of helicity production by solar rotation. *Journal of Geophysical Research*, 105:10481–10490.

Bieber, J. W. and Rust, D. M. (1995). The Escape of Magnetic Flux from the Sun. *The Astrophysical Journal*, 453:911.

Blackman, E. G. (2004). How spectral shapes of magnetic energy and magnetic helicity influence their respective decay timescales. *Plasma Physics and Controlled Fusion*, 46(2):423–430.

Blackman, E. G. (2015). Magnetic Helicity and Large Scale Magnetic Fields: A Primer. *Space Science Reviews* 188:59-91.

Blackman, E. G. and Brandenburg, A. (2002). Dynamic Nonlinearity in Large-Scale Dynamos with Shear. *The Astrophysical Journal*, 579(1):359–373.

Blackman, E. G. and Brandenburg, A. (2003). Doubly Helical Coronal Ejections from Dynamos and Their Role in Sustaining the Solar Cycle. *The Astrophysical Journal*, 584:L99.

Brandenburg, A. (2009). The critical role of magnetic helicity in astrophysical large-scale dynamos. *Plasma Physics and Controlled Fusion*, 51(12).

Brandenburg, A., Petrie, G. J. D., and Singh, N. K. (2016). Two-scale analysis of solar magnetic helicity. *The Astrophysical Journal*, 21.

Brandenburg, A. and Sandin, C. (2004). Catastrophic alpha quenching alleviated by helicity flux and shear. *Astronomy and Astrophysics*, 427(1):13–21.

Brandenburg, A., Subramanian, K., Balogh, A., and Goldstein, M. (2011). Scale-dependence of magnetic helicity in the solar wind. *The Astrophysical Journal.*, 734.

Cameron, R. and Schussler, M. (2015). The crucial role of surface magnetic fields for the solar dynamo. *Science*, 347:1333.

Cameron, R. H., Jiang, J., Schmitt, D., and Schüssler, M. (2010). Surface flux transport modeling for solar cycles 15-21: Effects of cycle-dependent tilt angles of sunspot groups. *The Astrophysical Journal*, 719(1):264–270.

Cattaneo, F. and Hughes, D. W. (1996). Nonlinear saturation of the turbulent alpha effect. *Physical Review E - Statistical Physics, Plasmas, Fluids, and Related Interdisciplinary Topics*, 54(5):4532–4535.

Centeno, R. (2012). The naked emergence of solar active regions observed with SDO/HMI. *The Astrophysical Journal*, 759(1).

Chapman, G. A., Cookson, A. M., and Dobias, J. J. (1997). Solar Variability and the Relation of Facular to Sunspot Areas during Solar Cycle 22. *The Astrophysical Journal*, 482(1):541–545.

Charbonneau, P. (2005). Dynamo Models of the Solar Cycle. *Living Reviews in Solar Physics*, 2:1–83.

Choudhuri, A. R. (2010). Flux-transport and mean-field dynamo theories of solar cycles. *IAU Symposium*, page 100.

Choudhuri, A. R., Chatterjee, P., and Jiang, J. (2007). Predicting solar cycle 24 with a solar dynamo model. *Physical Review Letters*, 98:1–4.

Dalmasse, K., Pariat, E., Démoulin, P., and Aulanier, G. (2014). Photospheric Injection of Magnetic Helicity: Connectivity-Based Flux Density Method. *Solar Physics*, 289(1):107–136.

Daubechies, I., Meyer, Y., Lemerie-Rieusset, P. G., Techamitchian, P., Beylkin, G., Coifman, R., Wickerhauser, M. V., and Donoho, D. (1993). Wavelet transforms and orthonormal wavelet bases. *Different perspectives on wavelets*, 47:1–33.

Démoulin, P. (2007). Recent theoretical and observational developments in magnetic helicity studies. *Advances in Space Research*, 39(11):1674–1693.

Démoulin, P., Janvier, M., and Dasso, S. (2016). Magnetic Flux and Helicity of Magnetic Clouds. *Solar Physics*, 291:531–557.

DeVore, C. R. (2000). Magnetic Helicity Generation By Solar Differential Rotation. *The Astrophysical Journal*, 539:944–953.

Dikpati, M., de Toma, G., and Gilman, P. A. (2006). Predicting the strength of solar cycle 24 using a flux-transport dynamo-based tool. *Geophysical Research Letters*, 33(5):10–13.

Ding, Y., Hong, Q., and Wang, H. (1987). A Statistical Study of the Spiral Spots on the Solar Disc. *Solar Physics*, 107:221–231.

D'Silva, S. and Choudhuri, A. R. (1993). A theoretical model for the tilts of bipolar magnetic regions. *Astronomy and Astrophysics*, 272:621–633.

Farge, M. (1992). Wavelet transforms and their applications to turbulence. *Annual review of fluid mechanics*, 24(1):395–458.

Farge, M., Kevlahan, N., Perrier, V., and Goirand, E. (1996). Wavelets and turbulence. *Proceedings of the IEEE*, 84(4):639–669.

Ferreira, S. E. S. and Potgieter, M. S. (2004). Long-Term Cosmic-Ray Modulation in the Heliosphere. *The Astrophysical Journal*, (1999):744–752.

Finn, J. and Antonsen, T. M. (1985). Magnetic Helicity: What Is It and What Is It Good For? *Comments Plasma Phys. Control. Fusion. 111*, (9):111.

Frisch, U., Pouquet, A., Léorat, J., and Mazure, A. (1975). Possibility of an inverse cascade of magnetic helicity in magnetohydrodynamic turbulence. *Journal of Fluid Mechanics*, 68(4):769–778.

Frohlich, C. (2013). Total solar irradiance: What have we learned from the last three cycles and the recent minimum? *Space Science Reviews*, 176:237–252.

Georgoulis, M. K., Rust, D. M., Pevtsov, A. A., Bernasconi, P. N., and Kuzanyan, K. M. (2009). Solar Magnetic Helicity Injected into the Heliosphere: Magnitude, Balance, and Periodicities Over Solar Cycle 23. *The Astrophysical Journal*, 705:L48–L52.

Gnevyshev, M. (1963). The Corona and the 11-Year Cycle of Solar Activity. *Soviet Astronomy* , 7(3):401–412.

Gopalswamy, N., Makela, P., Yashiro, S., and Akiyama, S. (2018). Long-term Solar Activity Studies using Microwave Imaging Observations and Prediction for Cycle 25. *Journal of Atmospheric and Solar-Terrestrial Physics* , Preprint:1–94.

Hathaway, D. H. (2009). Solar cycle forecasting. *Space Science Reviews*, 144:401–412.

Hawkes, G. and Berger, M. A. (2018). Magnetic Helicity as a Predictor of the Solar Cycle. *Solar Physics*, 293(7):109.

Hawkes, G. and Yeates, A. (2019). Hemispheric injection of magnetic helicity by surface flux transport. *Astronomy and Astrophysics*, 138(631):1–10.

Henwood, R., Chapman, S. C., and Willis, D. M. (2010). Increasing lifetime of recurrent sunspot groups within the greenwich photoheliographic results. *Solar Physics*, 262:299–313.

Hoyt, D. V. and Schatten, K. H. (1998). Group Sunspot Numbers: A new solar activity reconstruction. *Solar Physics*, 181:491–512.

Hubbard, A. and Brandenburg, A. (2012). Catastrophic Quenching in alpha-omega Dynamos Revisited. *The Astrophysical Journal*, 748(1):51.

Jawerth, B. and Sweldens, W. (1994). An overview of wavelet based multiresolution analyses. *SIAM review*, 36(3):377–412.

Jiang, J., Cameron, R. H., Schmitt, D., and Schüssler, M. (2011). The solar magnetic field since 1700. I. Characteristics of sunspot group emergence and reconstruction of the butterfly diagram. *Astronomy and Astrophysics*, 528:82.

Jiang, J., Cameron, R. H., Schmitt, D., and Schüssler, M. (2011). The solar magnetic field since 1700. II. Physical reconstruction of total, polar and open flux. *Astronomy and Astrophysics*, 528:A83.

Jiang, J., Chatterjee, P., and Choudhuri, A. R. (2007). Solar activity forecast with a dynamo model. *Monthly Notices of the Royal Astronomical Society*, 381:1527–1542.

Jiang, J., Hathaway, D. H., Cameron, R. H., Solanki, S. K., Gizon, L., and Upton, L. (2014). Magnetic Flux Transport at the Solar Surface. *Space Science Reviews*, 186(1-4):491–523.

Moraitis, K., Pariat, E., Valori, G. and Dalmasse, K., (2019). Relative magnetic field line helicity. *Astronomy and Astrophysics*, 624:A51.

Kusano, K., Maeshiro, T., Yokoyama, T., and Sakurai, T. (2002). Measurement of magnetic helicity injection and free energy loading into the solar corona. *The Astrophysical Journal*, 577(1):501.

LaBonte, B. J., Georgoulis, M. K., and Rust, D. M. (2007). Survey of Magnetic Helicity Injection in Regions Producing X-Class Flares. *The Astrophysical Journal*, 671(1):955–963.

Lee, G. R., Gommers, R., Waselewski, F., Wohlfahrt, K., and O'Leary, A. (2019). PyWavelets: A Python package for wavelet analysis. *Journal of Open Source Software*, 4(36):1237.

Leka, K. D., Barnes, G., and Wagner, E. L. (2017). Evaluating (and Improving) Estimates of the Solar Radial Magnetic Field Component from Line-of-Sight Magnetograms. *Solar Physics*, 292(2).

Longcope, D. W. and Malanushenko, A. (2008). Defining and Calculating Self-Helicity in Coronal Magnetic Fields. *The Astrophysical Journal*, 674(2):1130–1143.

Low, B. C. (1994). Magnetohydrodynamic processes in the solar corona: Flares, coronal mass ejections, and magnetic helicity. *Physics of Plasmas*, 1(5):1684–1690.

Low, B. C. (2015). Field topologies in ideal and near-ideal magnetohydrodynamics and vortex dynamics. *Science China Physics, Mechanics & Astronomy*, 58.

Lowder, C. and Yeates, A. (2017). Magnetic Flux Rope Identification and Characterization from Observationally Driven Solar Coronal Models. *The Astrophysical Journal*, 846:106.

Makarov, V. I. and Tlatov, A. G. (2000). The large-scale solar magnetic field and 11-year activity cycles. *Astronomy Reports*, 44:759–764.

Moffatt, H. K. (1969). The degree of knottedness of tangled vortex lines. *Journal of Fluid Mechanics*, 35:117–129.

Moffatt, H. K. (1978). Magnetic field generation in electrically conducting fluids. *Cambridge University Press*, page 337.

Munoz-Jaramillo, A., Balmaceda, L. A., and Deluca, E. E. (2013). Using the dipolar and quadrupolar moments to improve solar-cycle predictions based on the polar magnetic fields. *Physical Review Letters*, 111(4):1–5.

N. R. Sheeley, J. (2008). A Century of Polar Faculae Variations. *The Astrophysical Journal*, 680:1553.

NOA (2019). Solar cycle 25 prediction panel announcement april 2019. https://www.weather.gov/news/190504-sun-activity-in-solar-cycle. Accessed: 2019-09-30.

Pariat, E., Démoulin, P., and Berger, M. A. (2005). Photospheric flux density of magnetic helicity. *Astronomy and Astrophysics*, 439(3):1191–1203.

Pariat, E., Leake, J. E., Valori, G., Linton, M. G., Zuccarello, F. P., and Dalmasse, K. (2017). Relative magnetic helicity as a diagnostic of solar eruptivity. *Astronomy and Astrophysics*, 601:1–15.

Park, S.-H., Lee, J., Choe, G.-S., Chae, J., Jeong, H., Yang, G., Jing, J., and Wang, H. (2008). The variation of relative magnetic helicity around major flares. *The Astrophysical Journal*, 686(2):1397.

Parker, E. N. (1955). Hydromagnetic Dynamo Models. *The Astrophysical Journal*, 122(1950):293.

Parker, E. N. (1993). A Solar Dynamo surface wave at the interface between convection and nonuniform rotation. *The Astrophysical Journal*, (408):707–719.

Petris, G., Petrone, S., and Campagnoli, P. (2009). Dynamic linear models with R. *Springer*.

Petrovay, K. (2010). Solar Cycle Prediction. *Living Reviews in Solar Physics*, 7.

Pevtsov, A. (2003). Helicity Evolution in emerging active regions. *The Astrophysical Journal*, 593(2000):1217–1225.

Pipin, V. V., Pevtsov, A. A., Liu, Y., and Kosovichev, A. G. (2019). Evolution of Magnetic Helicity in Solar Cycle 24. *The Astrophysical Journal*, 877(2):L36.

Pouquet, A., Frisch, U., and Léorat, J. (1976). Strong MHD helical turbulence and the nonlinear dynamo effect. *Journal of Fluid Mechanics*, 77(2):321–354.

Priest, E. (2014a). The Basic Equations of Magnetohydrodynamics (MHD), page 74–106. *Cambridge University Press*.

Priest, E. (2014b). Dynamo Theory. *Cambridge University Press*: 281–305.

Prior, C., Hawkes, G., and Berger, M. A. (2020). Spatial scales and locality of magnetic helicity. *Astronomy & Astrophysics*, 635:A95.

Prior, C. and MacTaggart, D. (2019). Interpreting magnetic helicity flux in solar flux emergence. *Journal of Plasma Physics*, 85(2).

Prior, C. and Yeates, A. R. (2014). On the helicity of open magnetic fields. *The Astrophysical Journal*, 787(2).

Prior, C. and Yeates, A. R. (2018). Quantifying reconnective activity in braided vector fields. *Physical Review E*, 98(1):013204.

Roberts, P. and Soward, A. (1975). A unified approach to mean field electrodynamics. *Astronomische Nachrichten*, 296(2):49–64.

Russell, A. J., Yeates, A. R., Hornig, G., and Wilmot-Smith, A. L. (2015). Evolution of field line helicity during magnetic reconnection. *Physics of Plasmas*, 22(3):032106.

Sanchez, S. and Fournier, A. (2014). A mean-field Babcock-Leighton solar dynamo model with long-term variability. *Annals of the Brazilian Academy of Sciences*, 86:11–26.

Schatten, K. H., Scherrer, P. H., Svalgaard, L., and Wilcox, J. M. (1978). Using dynamo theory to predict the sunspot number during solar cycle 21. *Geophysical Research Letters*, 5.

Smiet, C. B., Candelaresi, S., Thompson, A., Swearngin, J., Dalhuisen, J. W., and Bouwmeester, D. (2015). Self-Organizing Knotted Magnetic Structures in Plasma. *Physical Review Letters*, 115(9):1–11.

Snodgrass, H. B. and Ulrich, R. K. (1990). Rotation of the Doppler Featuring the Solar Photosphere. *The Astrophysical Journal*, 351(Bruning 1988):309–316.

Subramanian, K. and Brandenburg, A. (2005). Magnetic helicity density and its flux in weakly inhomogeneous turbulence. *The Astrophysical Journal*, 648(1):71–74.

Sur, S., Shukurov, A., and Subramanian, K. (2007). Galactic dynamos supported by magnetic helicity fluxes. *Monthly Notices of the Royal Astronomical Society*, 377(2):874–882.

Taylor, J. B. (1974). Relaxation of toroidal plasma and generation of reverse magnetic fields. *Physical Review Letters*, 33:1139–1141.

Temmer, M., Rybák, J., Bendík, P., Veronig, A., Vogler, F., Otruba, W., Pötzi, W., and Hanslmeier, A. (2006). Hemispheric sunspot numbers R n and R s from 1945–2004: catalogue and N-S asymmetry analysis for solar cycles 18–23. *Astronomy and Astrophysics*, 447(2):735–743.

Usoskin, I. G. (2005). A History of solar activity over millennia. *Living Reviews in Solar Physics*, 5:1–88.

Vainshtein, S. I. and Cattaneo, F. (1992). Nonlinear restrictions on Dynamo action. *The Astrophysical Journal*, (393):165–171.

van Driel-Gesztelyi, L., Démoulin, P., and Mandrini, C. H. (2003). Observations of magnetic helicity. *Advances in Space Research*, 32:1855–1866.

Vaquero, J. M. and Gallego, M. C. (2002). Evidence for a sunspot in a.d. 939 in an arabian source. *Solar Physics*, 206:209.

Verma, M. K. (2004). Statistical theory of magnetohydrodynamic turbulence: Recent results. *Physics Reports*, 401(5-6):229–380.

Vishniac, E. T. and Cho, J. (2001). Magnetic helicity conservation and astrophysical dynamos. *The Astrophysical Journal*, 550(2):752.

Vishniac, E. T. and Shapovalov, D. (2013). Properties of magnetic helicity flux in turbulent dynamos. *The Astrophysical Journal*, 780(2):144.

Whitbread, T., Yeates, A. R., and Muñoz-Jaramillo, A. (2018). How many active regions are necessary to predict the solar dipole moment? *The Astrophysical Journal*, 863.

Whitbread, T., Yeates, A. R., Muñoz-Jaramillo, A., and Petrie, G. J. D. (2017). Parameter optimization for surface flux transport models. *Astronomy and Astrophysics*, 607:A76.

Wilmot-Smith, A., Hornig, G., and Pontin, D. (2009). Magnetic braiding and quasi-separatrix layers. *The Astrophysical Journal*, 704(2):1288.

Wilmot-Smith, A., Pontin, D., Yeates, A., and Hornig, G. (2011). Heating of braided coronal loops. *Astronomy and Astrophysics*, 536:A67.

Woltjer, L. (1958). A Theorem on Force–Free Magnetic Fields. *Proceedings of the National Academy of Sciences*, 44(6):489–491.

Yeates, A. and Hornig, G. (2013). Unique topological characterization of braided magnetic fields. *Physics of Plasmas*, 20(1):012102.

Yeates, A. R. (2015). Source of a Prominent Poleward Surge During Solar Cycle 24. *Solar Physics*, 290(11):3189–3201.

Yeates, A. R., Baker, D., and van Driel-Gesztelyi, L. (2015). Source of a Prominent Poleward Surge During Solar Cycle 24. *Solar Physics*, 290(11):3189–3201.

Yeates, A. R. and Hornig, G. (2016). The global distribution of magnetic helicity in the solar corona. *Astronomy and Astrophysics*, 594:A98.

Yeates, A. R. and Page, M. H. (2018). Relative field-line helicity in bounded domains. *Journal of Plasma Physics*, 84(6).

Zhang, T., Sun, H., and Wu, P. (2004). Wavelet denoising applied to vortex flowmeters. *Flow measurement and Instrumentation*, 15(5-6):325–329.

Alfvén , H (1942). Existence of Electromagnetic-Hydrodynamic Waves *Nature*, 10.1038/150405d0